To my Parents…

ELECTROCHEMICAL IMPEDANCE SPECTROSCOPY BASED CHARACTERIZATION AND MODELING OF ELECTROCHEMICAL ENERGY STORAGE SYSTEMS

A DISSERTATION SUBMITTED TO

THE GRADUATE SCHOOL OF ENGINEERING AND SCIENCE

OF BILKENT UNIVERSITY

IN PARTIAL FULFILLMENT OF THE REQUIREMENTS FOR

THE DEGREE OF

DOCTOR OF PHILOSOPHY

IN

CHEMISTRY

By

Mohammed Ahmed Mohammed Zabara

October 2021

ELECTROCHEMICAL IMPEDANCE SPECTROSCOPY BASED CHARACTERIZATION AND MODELING OF ELECTROCHEMICAL ENERGY STORAGE SYSTEMS

By Mohammed Ahmed Mohammed Zabara

October 2021

We certify that we have read this dissertation and that in our opinion it is fully adequate, in scope and in quality, as a dissertation for the degree of Doctor of Philosophy.

Burak Ülgüt (Advisor)

Şefik Süzer

Salim Erol

Selmiye Alkan Gürsel

Damla Eroğlu Pala

Approved for the Graduate School of Engineering and Science:

Ezhan Karasan

Director of the Graduate School

ABSTRACT

ELECTROCHEMICAL IMPEDANCE SPECTROSCOPY BASED CHARACTERIZATION AND MODELING OF ELECTROCHEMICAL ENERGY STORAGE SYSTEMS

Mohammed Ahmed Mohammed Zabara

Ph.D. in Chemistry

Advisor: Burak Ülgüt

October 2021

In this thesis, first we demonstrate the characterization of the electrochemical processes in primary Lithium batteries utilizing Electrochemical Impedance Spectroscopy (EIS). We develop Galvanostatic-EIS at discharge technique which provide linear and stable impedance data of primary Li batteries in wide frequency range. The obtained data is further investigated by variation of the electrolyte composition. The results reveal the electrochemical processes associated with impedance response at different frequency regions. The impedance response is then assigned to the corresponding anodic and cathodic charge transfer plus the interfacial processes. Further, we investigate the temperature dependence of the impedance of the batteries which reveals the activated processes and allow for the calculation of their activation energies.

Along with the linear impedance response, we also investigate the non-linear response obtained from the primary Li batteries. We show that non-linearity can be used to detect the degree of the passivation of the Li anode. We also show the non-linear response at different States-of-Charge and with temperature change.

Second, we utilize linear impedance data in modeling the voltage response of the primary Li batteries. We apply previously developed EIS based Zero-free-parameter modeling approach to predict the voltage response of the primary Li batteries for the desired applications. We improve the method to account for the voltage delay phenomena which is an outcome of using metallic Li in the anode.

We further utilize the same modeling method to predict the voltage response of hybrid unmanaged secondary Li-ion batteries supercapacitor systems under real-life setarious. We develop the method to first predict the current distribution among the parallel connected hybrid systems utilizing differential evolution optimization algorithm. Then with the accurate impedance of each system the voltage response is predicted. We validate the modeled results with experimental measurements which shows high accuracy for various hybrid Li-ion supercapacitor systems.

Finally, utilizing the modeled results we present design rules for hybridization based on the gains obtained in different parameters such as, peak current, power and total energy. Moreover, the improvements in size and cost of hybridization with different supercapacitor capacities are studied which also contribute in determining the best combination of the Li-ion battery supercapacitor hybrid system.

Keywords: Electrochemical Impedance Spectroscopy, primary Li batteries, Solid Electrolyte Interface, equivalent circuit analysis, non-linear harmonics.

ÖZET

ELEKTROKİMYASAL ENERJİ DEPOLAMA SİSTEMLERİNİN ELEKTROKİMYASAL EMPEDANS SPEKTROSKOPİSİ TABANLI KARAKTERİZASYONU VE MODELLENMESİ

Mohammed Ahmed Mohammed Zabara

Kimya, Doktora Tezi

Danışman: Burak Ülgüt

Ekim 2021

Bu tezde ilk olarak, Elektrokimyasal Empedans Spektroskopisi (EIS) kullanan birincil Lityum pillerdeki elektrokimyasal süreçlerin karakterizasyonunu gösteriyoruz. Geniş frekans aralığında birincil Li pillerin doğrusal ve kararlı empedans verilerini sağlayan deşarj tekniğiyle Galvanostatik-EIS geliştiriyoruz. Elde edilen veriler, elektrolit bileşiminin varyasyonu ile ayrıca araştırıldığında sonuçlar, farklı frekans bölgelerindeki empedans yanıtının türünü ortaya koymaktadır. Empedans tepkisi daha sonra ilgili anodik ve katodik yük transferine ve arayüzey süreçlerine atanmıştır. Ayrıca, sıcaklıkla aktive olan süreçleri ortaya çıkaran ve aktivasyon enerjilerinin hesaplanmasına izin veren pillerin empedansının sıcaklığa bağımlılığını araştırıyoruz.

Lineer empedans yanıtının yanı sıra, birincil Li pillerden elde edilen doğrusal olmayan yanıtı da araştırıyoruz. Li anodunun pasifleşme derecesini tespit etmek için doğrusal olmayanlığın kullanılabileceğini gösterdik. Ayrıca, farklı Şarj Durumlarında ve sıcaklık değişimi ile doğrusal olmayan tepkiyi de gösteriyoruz.

İkinci olarak, birincil Li pillerin voltaj yanıtını modellemede doğrusal empedans verilerini kullanıyoruz. İstenen uygulamalar için birincil Li pillerin voltaj tepkisini tahmin etmek için önceden geliştirilmiş EIS tabanlı Sıfırsız parametre modelleme yaklaşımını uyguluyoruz. Anotta metalik Li kullanmanın bir sonucu olan voltaj gecikmesi olgusunu hesaba katan yöntemi geliştirdik.

Aynı modelleme yöntemini, hibrit ikincil Li-ion pil süper kapasitör sistemlerinin gerçek yaşam setari altında voltaj tepkisini tahmin etmek için de kullanıyoruz. Diferansiyel evrim

optimizasyon algoritmasını kullanarak paralel olarak bağlı hibrit sistemler arasındaki akım dağılımını ilk önce tahmin etmek için yöntemi geliştiriyoruz. Daha sonra her sistemin doğru empedansı ile voltaj yanıtı tahmin edilir. Modellenen sonuçları, çeşitli hibrit Li-iyon süper kapasitör sistemleri için yüksek doğruluk gösteren deneysel ölçümlerle doğruladık.

Son olarak, modellenen sonuçları kullanarak, tepe akımı, güç ve toplam enerji gibi farklı parametrelerde elde edilen kazanımlara dayalı hibridizasyon için tasarım kuralları sunuyoruz. Ayrıca, Li-ion pil süper kapasitör hibrit sisteminin en iyi kombinasyonunun belirlenmesine de katkıda bulunan farklı süper kapasitör kapasiteleriyle hibridizasyonun boyutundaki ve maliyetindeki iyileştirmeler incelenmiştir.

Anahtar sözcükler: Elektrokimyasal Empedans Spektroskopisi, birincil Li piller, Katı Elektrolit Arayüzü, eşdeğer devre analizi, doğrusal olmayan harmonikler.

Acknowledgement

I am extremely grateful to my supervisor, Assoc.Prof.Burak Ülgüt for his precious advice, continuous support, and patience during my PhD study.

I would like to thank my thesis defense committee with special thanks to my thesis monitoring committee for their valuable contribution.

My deep appreciation to my family who made my PhD journey full of joy and contentment. I am always thankful to my parents, Ahmed and Bushra, whose love and guidance are with me in whatever I pursue. Special cheers go to my beloved wife Roqiah who was always supportive, caring and patient. Similar feelings to my two wonderful children, Fatima and Alhasan who provided unending inspiration.

Many thanks to my lab mates, Can Berk Uzundal whose contribution is much appreciated, Gözde Karaoğlu for her teamwork and elated spirit in the lab, Musa Zakaria and Berk Delibaş who together we contributed in advancing lab projects.

My sincere gratitude goes to the scholarship provided by Bilkent University \ Department of Chemistry and funding from TÜBİTAK under the project number 118Z739.

Contents

List of Figures

List of Tables

Chapter 1
Introduction

The demand for high-performance energy storage systems is growing. This is attributed to the large increase in the electric energy storage dependent applications. On one hand, there are clean technologies that convert various forms of energy into electricity by means of environment friendly yet intermittent methods such as, solar and wind. On the other hand, there is the electrification trajectory that governments are trying to achieve by electrifying various forms of transportation. Moreover, there is the ongoing increase of dependence on electronics such as, laptops and cellphones which all require wireless electric power sources [1]–[3].

Electric energy storage is mostly achieved through Electrochemical Energy Storage (EES) devices which utilize different electrochemical processes for the aim of energy storage. Various EES technologies are in active use and under continuous development. Examples of these technologies include batteries, supercapacitors, fuel cells and flow batteries. Depending on the requirements of the field and the application used; different types, sizes and shapes of EES devices are utilized. Studying, understanding and developing characterization and modeling methods for the existing and developing EES systems is an important part in the field of their research and development. The aim is to meet the high-performance demand for their applications in a safe, reproducible and predictable manner [4]–[7].

In employing any of the EES devices in a specific application, there exist fundamental questions related to their best utilization for the application. High-level of understanding

of the electrochemical process taking place inside these systems is essential for their best utilization. Accurate characterization and modeling methods which are able to predict and simulate the response of the systems under any tailored application are needed.

This thesis presents studies on the development of both characterization and modeling methods for EES systems. For electrochemical characterization, we employ Electrochemical Impedance Spectroscopy (EIS) technique which contain information regarding the charge and mass transfer phenomena inside the studied EES devices. For performance modeling, we introduce EIS based modeling methodologies which are experimentally validated that provide correct and accurate response predictions of the EES systems under any tailored applications with high accuracy and low complexity.

In this chapter, fundamental knowledge is presented regarding the electrochemical processes taking place on the characterized and modeled systems. Next, description of the used EES systems will be provided. Following that, basics of EIS and how it is utilized in characterizing various EES is presented. Finally, an introduction to EES systems' performance modeling is made.

1.1. Electrochemical Energy Storage Systems

In EES devices the electrical energy is stored by means of electrochemical reactions. Electrochemical reactions are distinguished from other chemical reactions by the transfer of electric charge between atoms, molecules or different interfaces. The charge transferred can be in the form of electrons or ions. Examples of these processes' ranges from a single electron oxidation/reduction reaction to multiple electron transfer and ion transport reactions through different interfaces.

Electrochemistry is the branch of chemistry that studies the different charge and mass transfer processes through different materials. Understanding the principle of charge transfer is crucial for understanding the energy storage mechanisms in different EES devices. Since the invention of the first battery by Volta, theories regarding the

thermodynamics and the kinetics of these electrochemical processes are well established [8], [9]. Similarly, electrochemical characterization methods with various characterization capabilities are developed and used regularly for testing and studying electrochemical systems.

Mostly used current EES systems are batteries and supercapacitors. In principle, batteries store energy in the form of chemical energy through electrochemical reactions and supercapacitors exchange the energy through electrostatic and capacitive interactions. These two different mechanisms give batteries and supercapacitors different properties. The performance of each system is evaluated by how much energy they can store, energy density, and how fast they can release the energy, power density. Those two parameters are represented in Ragone plot which has each parameter at its axes shown in Figure 1.

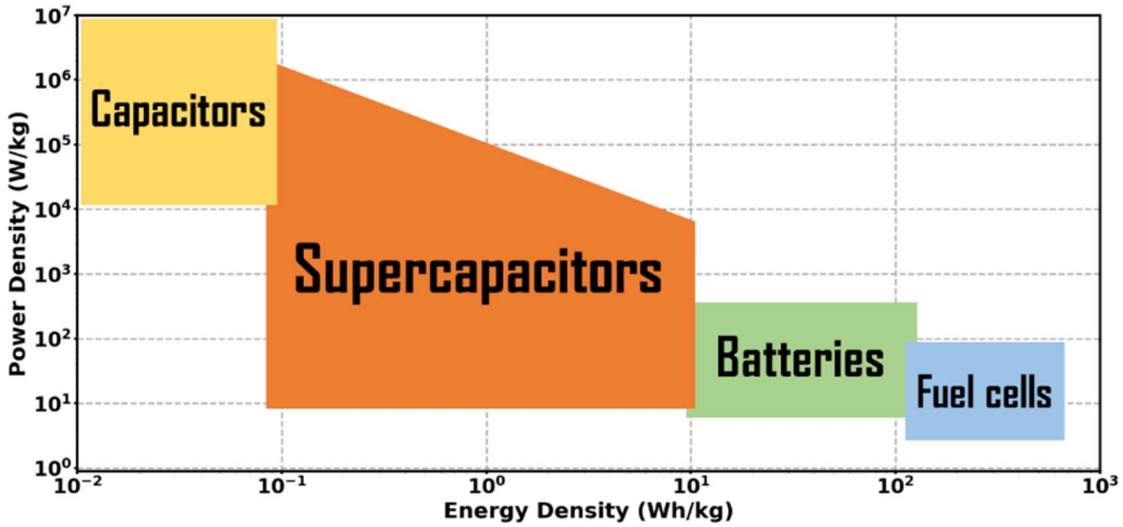

Figure 1. Ragone plot in gravimetric energy and power densities for most used Electrochemical Energy Storage Systems

As can be seen, batteries are high energy density systems but are slow in terms of storing and providing the stored energy. On the other hand, supercapacitors are fast in charge and discharge but suffer from their low energy density. The ideal EES system should provide both properties which will take its place at the right top of the Ragone plot.

To achieve the goal of having high performance EES devices with both properties, two research and development approaches can be followed:

The first, is to increase the energy densities and the specific power of both batteries and supercapacitor systems. This can be achieved through the development of new materials and the enhancement of the electrochemical processes. For example, in the state-of-the-art Li-ion batteries the utilization of the metallic Li anode should double the existing energy density [9]. Unwanted electrochemical processes such as, inhomogeneous Li plating and dendrite formation are what prevent the usage of such anode material [10], [11]. Understanding these processes and bringing solutions to prevent their occurrence is what many researchers are aiming to reach.

The second is to hybridize batteries and supercapacitors by parallel connection which will provide high specific power when needed from the supercapacitor with high total energy density from battery. This strategy is proven to bring the high performance and is what many applications are achieving to use. However, there exists issues related to the best choice of battery and supercapacitor for specific application and the understanding of the power distribution among the two systems when parallel connected and operated. The solutions which are developed are based on introducing management systems which are based on convertors and complex electronics which still cannot fully utilize the systems.

1.2. Aim of the Thesis

In this work, aiming for the development of high-performance battery supercapacitor systems we follow the mentioned two approaches;

First, we study the highest energy density Li-based batteries utilizing EIS technique. The aim is to deconvolute the charge and mass transfer processes and to contribute in more understanding of the electrochemical processes of these systems.

Second, we develop performance modeling methods for the Li-based batteries and the hybrid parallel connected battery/supercapacitor systems. The aim of the methods is to

determine the best combination of battery/supercapacitor for intended applications and to evaluate the performance under tailored applications.

Before going through the details of the characterization and modeling methods developed and the obtained results, an introduction on the types of systems used in the study with brief explanation of the important electrochemical processes taking place is provided in this chapter.

1.3. Electrochemical Processes in Energy Storage Devices

EES devices are constructed as a combination of four main components, two electrodes (anode and cathode), the electrolyte and the separator shown in Figure 2. The function of the EES is to store electricity in the form of electric charges. The charges are stored through electrochemical processes which involves oxidation/reduction reactions along with possible bond formation/destruction, intercalation, phase changes etc. All the components must be electrically connected to allow for the flow of the charges throughout the system. This flow is achieved through the heterogenous charge transfer process in solid media and through mass transport processes in liquid and interfacial environments. Ultimately, the energy difference between the states in which charges are in different electrodes is known as the free energy difference, which can be expressed as potential when scaled with the number of charges transferred.

The type of electrodes determines the function and the properties of the EES device. For example, in primary Lithium batteries, Lithium metal is used as the anode with different porous materials as the cathode. The function of the electrolyte is to carry the charge carriers, ions, between the electrodes. Though, in special cases it can be also used as the cathode active materials such as, Lithium Thionyl Chloride battery. The separator is used to prevent the direct contact between the electrodes and in special cases to prevent the movement of specific ions. The existence of the solid electrodes and the liquid electrolyte in direct contact results in the formation of electrode electrolyte interface where the electrochemistry is taking place.

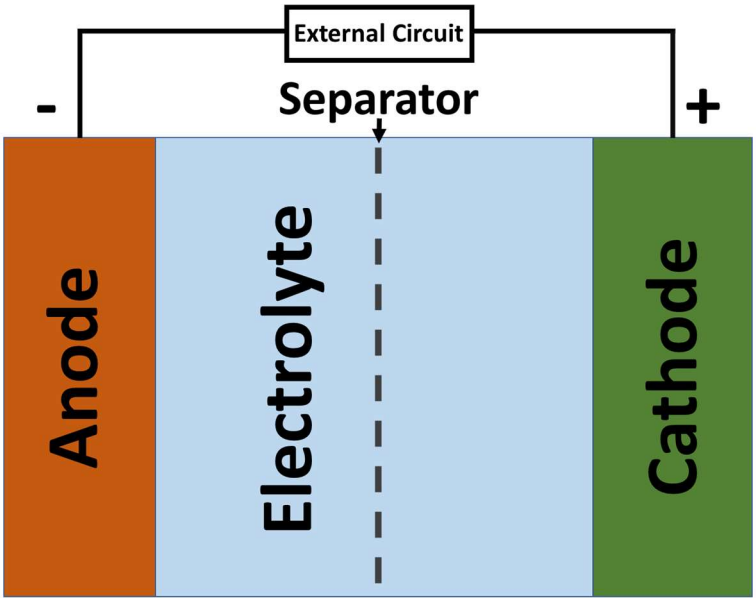

Figure 2. Main components of Electrochemical Energy Storage systems

The mechanisms in which the storage of the charges happen at the electrodes can be divided into two types:

The first, and the less complex, is electrochemical double layer charging. This process is happening on the surface of the electrode without any charge transfer involvement. It forms as the result of accumulation of charges with different signs at the surface of the solid electrode and the liquid electrolyte. This process is how supercapacitors operate.

The second, is through what is known as Faradaic reactions or charge transfer reactions which involves electrochemical reactions in different forms. This process takes place not only at the surface but also at the bulk of the active materials of the porous electrodes. It involves charge transfer through different interfaces and other processes such as bond formation and destruction or intercalation/deintercalation processes. These processes are the responsible for the energy storage and conversion in batteries, fuel cells and flow batteries.

Although this simple description of the storage mechanisms in EES devices is correct, there are more details regarding the processes at each component. The existence of more than one interface which is unique to the type active materials and the electrolytes used requires deep understanding of the various charge and mass transfer mechanisms taking place which are dependent to each other. Brief description of these phenomena will be covered in this section.

1.3.1. Fundamental Concepts

To understand the different electrochemical processes at the EES devices, the fundamentals of some thermodynamic and kinetic terms should be covered. These terms will be used throughout the thesis to explain the processes and to interpret the data obtained from the experiments. In this section, a brief description is provided with respect to their use in the EES systems. Detailed explanations for the terms are well-elaborated in different electrochemistry and electrochemical methods books.

The term which indicates the feasibility of the EES to provide energy are called potential or voltage of the device which describe the thermodynamic state of the systems. Important terms related to the potential are:

- *Cell Potential* is what causes the EES to force charge carriers through an outside load. It is defined as the difference of energy that the charge faces when moved between the two terminals or the amount of work needed to move the charges between the terminals. Each charge transfer process at the electrodes of the EES has a certain potential with a reference electrode. The difference in the reduction potentials of the processes inside the EES gives a potential value known as the cell potential. The potential of the cell is the most important thermodynamic value which is related to the Gibbs free energy (in Joules/mole) by the following equation:

$$E = -\frac{\Delta G}{nF}$$

where, n is the number of electrons, F is the Faraday's constant = 96,485 C/mol and E is the potential measured in Volts. From this equation we can infer that any positive potential between the terminals of the EES will have a negative Gibbs free energy difference resulting in spontaneous reactions. These reactions will allow for the flow of the electrons if the terminals are connected to a load.

- *Open Circuit Potential* is the measured potential at the terminals of the EES system at rest without the connection to any power source or load. It is the potential at equilibrium or when the system moves toward equilibrium state from a previous non-equilibrium state.
- *Overpotential* is the extra amount of potential that is provided to the system beyond the equilibrium potential. Overpotential is required due to the kinetic limitations which is needed to overcome certain activation barrier of an electrochemical process. In batteries for example, overpotential has to be applied for charging which should be higher than the open circuit potential of the battery at its terminals.

Beside the thermodynamic description of the system by potential, the kinetics of the flow of the charges are described by current which is defined as:

- *Current* is the measurement of the rate of electron flow between the terminals of the EES system. Its unit is coulomb per second (Amperes).
- *Maximum Continuous Current* is the highest current that can be drawn from the EES without causing loss or degradation of the active materials. The value changes by changing the capacity, geometry and the type of the EES system.

Having knowledge about the voltage and the current of an EES device enables the determination of the amount of energy and power the device can provide. The terms used for describing the storage properties of the EES are as follows:

- *Energy density* is the amount of energy which can be stored per mass, called gravimetric energy density, or volume, called volumetric energy density, of an EES device. Its unit is Wh/kg for gravimetric and Wh/L for volumetric energy density. Power can be calculated by multiplying the voltage by the current and Energy can be calculated as the

integral of power over time. Depending on the importance of the mass or volume of the intended application one of these parameters is used.

- *Power density* is the measurement of the amount of power the EES device can provide instantly. It is defined as the power capacity per kilogram W/kg of the EES device.
- *Capacity* is the measurement of how many hours the EES device can provide a constant current above a certain voltage which is defined as the cutoff voltage. Its unit is ampere-hour (Ah) in which 1Ah is 3600Coulomb. It can be also defined in Watt-hour (Wh) in which 1Wh is 3600J since W = V x A.
- *C-rate* is the measure of the discharge current relative to the maximum capacity of the EES device. It is used to normalize the discharge current against the different capacities of the EES devices. 1C rate represent the discharge of the device in one hour by the specific discharge current. If the capacity of the battery is 100mAh 1C rate current is 100 mA.

Moreover, the measurement term for the amount of the energy contained in the EES from the defined maximum value is called the state-of-charge:

- *State-of-Charge* is the measure of the amount of the stored energy relative to the total energy of the battery. As 100% State-of-Charge (SoC) represent a full device 50% SoC represent the remaining of the half of the total energy of the device.
- *Self-discharge* is the reduction in the energy of the EES device due to unwanted internal mechanisms at open circuit without the connection to any load.

These above terms will be used in describing the electrochemical processes and in the interpretation of the obtained results. In the following sections, we describe the mechanisms and the electrochemical processes responsible for the charge storage in the EES devices.

1.3.2. Double Layer Capacitance

Electrochemistry happens at interfaces. Any electrode that is immersed in an electrolyte forms an interface which experiences unique properties due to the drastic change in the physical state. On one hand, the charge movement in solid state electrode such as metallic electrodes or porous carbon electrodes is based on the movement of free electrons or holes as the atoms are still. On the other hand, the charge movement in the electrolyte is achieved through the movement of the solvated negative and positive ions in an abundance of the solvent molecules. Because of the coulombic interaction between the electrode's charge carriers and the electrolyte ions, an attraction between the unlike charges at solid electrolyte interfacial region. This attraction forms what is known as the Electric Double Layer. This is the same also for solid electrolyte. The charge carriers with the opposite charges will be attracted at the interfaces forming a double layer with different charges. Although the environment of the charge carriers differs in solid electrolyte than liquid electrolytes, which will change the mass transport properties of the ions, the resultant capacitive behavior is similar.

The columbic attraction results in the formation of oppositely charge mediums. The formation and the composition of the double layer is well studied. On the electrode surface, there is an accumulation of electrons or holes. The electrolyte side of the double layer is proposed to be made of several layers. The inner layer which is closest to the surface of the electrode is made of solvent molecules or specifically adsorbed molecules and ions. In electrochemistry literature, this inner layer is named as compact, Helmholtz or Stern layer. The second layer is thought to be made of solvated ions which are known to be non-specifically adsorbed. The position of the electrical center of these two layers are named Inner Helmholtz Plane (IHP) and Outer Helmholtz Plane (OHP). The ions are then distributed from the OHP to the bulk solution in a layer called the diffuse layer.

The electric double layer represents a capacitor since it is composed of two oppositely charged layers separated by a specific distance. Similarly, a parallel-plate capacitor is constructed by two plates separated by distance. For any capacitor, the equation for the capacitance is as follows:

$$C = \varepsilon_0 \varepsilon \frac{A}{d}$$

where ε is the permittivity of the dielectric medium used between the two plates and ε_0 is for air, A is the area of the palates and d is the distance between the plates.

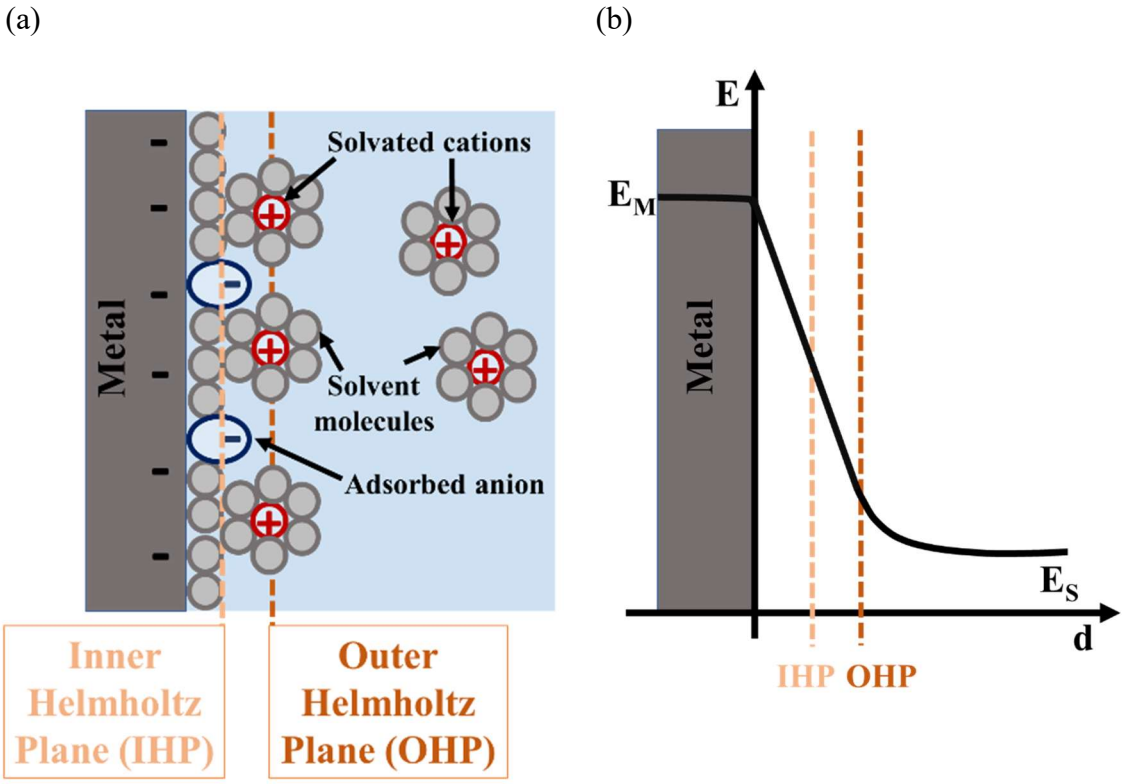

Figure 3. (a) Electric Double Layer (EDL) model illustration as proposed and developed by Helmholtz Gouy, Chapman and Stern, (b) Simplified illustration of the potential behavior at the EDL with respect to the distance from the metal surface

As the equation indicates, the capacitance is directly proportional to the surface area of the electrodes and the inversely proportional to the distance between the ions and the electrode's surface. Keeping in mind that the distance between the ions and the electrode is almost constant with a very small scale of 1 to 10 Angstroms depending on the type and size of the ion, increasing the surface area of the electrodes is the key to increase the capacitance. The use of porous carbon electrodes with very high surface area results in high

capacitance, in a range of hundreds to thousands of Farads in single supercapacitor, and forms what is known as supercapacitors. Supercapacitors are made of positive and negative electrodes where each has an electric double layer of their own, thus a supercapacitor cell is actually made of two capacitors connected in series.

(a)

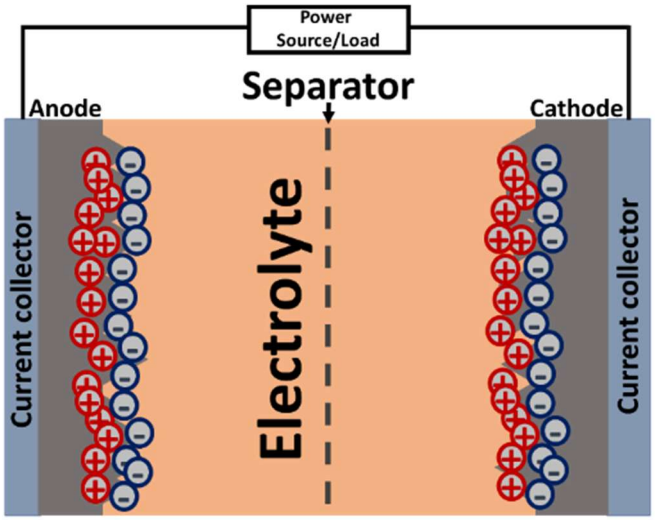

(b)

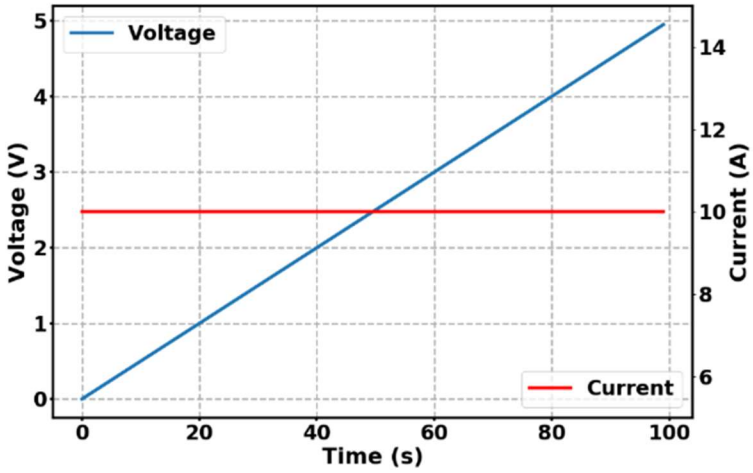

Figure 4. (a) Supercapacitor structure scheme (b) Typical charge curve for a capacitor

The relation between the voltage of an idealized capacitor and the charge follows linear relation as:

$$V = \frac{Q}{C}$$

where Q is the charge in Coulomb and C is the capacitance in Farads.

The most important property of the capacitor is its ability to store and release the charges in very fast time scales. This is due to its simple double layer charging mechanism. However, the amount of energy that can be stored is limited to the surface area of the electrodes. Though with the development of the highly active surface area materials, there exist a wide range of supercapacitor with capacities ranging from milli Farads to kilo Farads.

1.3.3. Charge Transfer Processes

Beside the double layer charging mechanism for storing electrical energy, there are different mechanisms of charge transfer which in general store charges by electrochemical reactions. We will consider batteries in demonstration of the charge transfer processes since they are studied in this thesis. For example, in batteries when the active material is oxidized or reduced the charges are stored in the as part of the core structure of the material.

In EES systems these processes take place at the active materials which are well-defined. The conversion of one form of the active material into another by means of electrochemical reaction occur around a specific potential. The equation that governs the relation between the ratio of the two forms of active materials to the electrochemical potential is the Nernst equation.

In a typical EES system when discharged, oxidation of the active material takes place at the anode and reduction at the cathode. When charged, the reversed is happening. For a primary system, non-rechargeable, there is only the former situation because of the irreversibility of the chemistry. The maximum amount of work which can be obtained from

the total reaction is related to the change in the Gibbs free energy which is also related to the reaction potential as:

$$W_{max} = \Delta G = -nFE$$

For instance, if we assume an EES cell with the following reaction which is the summation of the anodic and cathodic reaction:

Anodic reaction: $aA \rightleftharpoons cC + ne^-$

Cathodic reaction: $bB + ne^- \rightleftharpoons dD$

Overall reaction: $aA + bB \rightleftharpoons cC + dD$

We can express the change of the Gibbs free energy of the cell's reaction as:

$$\Delta G = \Delta G^0 + RTln\frac{{a_A}^a {a_B}^b}{{a_C}^c {a_D}^d}$$

where ΔG^0 is the standard Gibbs free-energy change that can be obtained from the Gibbs free energy of formation $= \Delta G^0{}_{f(rxn)} = -\frac{E^0}{nF}$.

R is the gas constant 8.314 J/K.mol, T is the temperature in Kelvin.

Nernst equation of the potential of the cell is obtained if the above equation is divided by $-nF$ which can be used for relating the potential of the cell to the reaction components:

$$E = E^0 - \frac{RT}{nF} ln\frac{{a_A}^a {a_B}^b}{{a_C}^c {a_D}^d}$$

in which F is the Faraday's constant 96485 C/mol and n is the number of electrons.

From the above equation we can estimate that the potential of the cell will not change drastically as the amount of the active material change due to the logarithmic relationship. The cell will operate at narrow potential window until one of the active species runs out and then the potential will have drastic change. Though for most of the electrochemical

reactions some components will have unity activity due to their solid or liquid states and will not contribute in the Nernst equation. Mostly the ionic and the dissolved species will contribute in the cell potential.

(a)

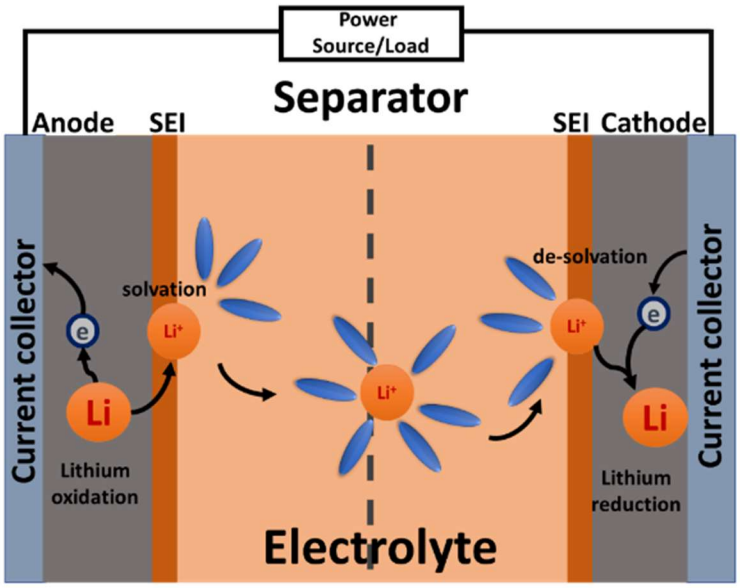

(b)

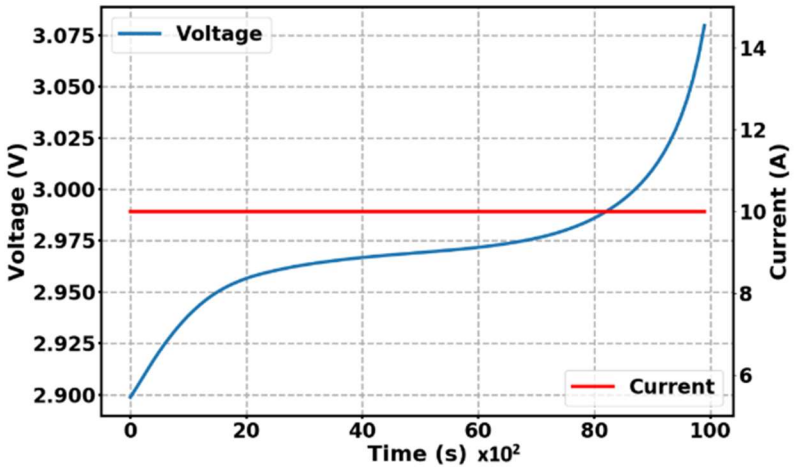

Figure 5. (a) Illustration of charge and mass transfer processes in Lithium Battery (b) Charging voltage curve of battery

The cell reaction will take place if the terminals are connected to a load or a power source. The amount of current that can be obtained from the cell reaction will be determined by

the slowest electrochemical process in the cell. Usually, the rate determining step in EES devices is the mass transport of ions.

The kinetics of the anodic and the cathodic charge transfer can be described with Butler-Volmer model which relates the current density of the reaction to the overpotential of the electrochemical reaction. The overpotential here is the electrode potential minus the equilibrium potential for the reaction.

The Butler-Volmer equation relate the current density of the charge transfer processes exponentially to the overpotential. The equation is as follows:

$$i_{CT} = i_0 \left\{ e^{\frac{(1-\alpha)nF\eta}{RT}} - e^{\frac{-\alpha nF\eta}{RT}} \right\}$$

where i_0 is the exchange current density, F is Faraday's constant, T is temperature in Kelvin, R is gas constant, α is the transfer coefficient which can range from 0 to 1, n is number of electrons involved and η is the overpotential ($E - E^0$) which measures the degree of polarization from the equilibrium potential.

The equation indicates that the current will increase exponentially as we draw more voltage from the device. This is actually the case at small current values. However, for large currents the increase reaches constant value which is due to the mass transport limitation in the systems. This indicates that ions in the solution cannot reach the electrode with higher rate.

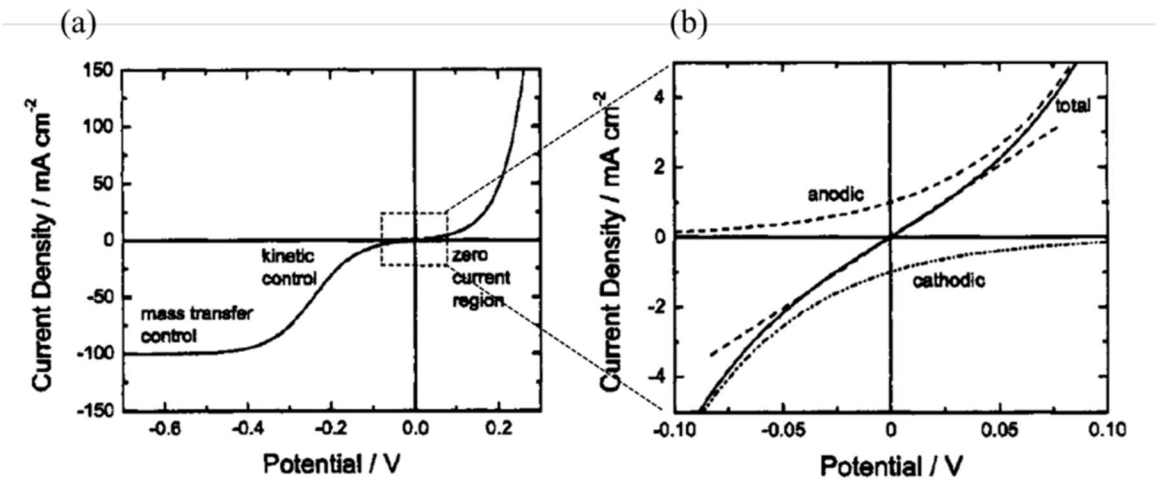

Figure 6. (a) Expanded representation of Butler Volmer behavior with mass-transfer control at cathodic potentials and kinetic control at the anodic potentials (b) Expanded representation of near zero current region, reproduced with permission from [12]

The resistance that arises from the kinetically-controlled charge transfer process is called charge transfer resistance. If we assume that the overpotential is very small and though the current density i_{CT} is zero. We can write from the Butler-Volmer the following equation for the charge transfer resistance:

$$R_{CT} = \frac{RT}{nFi_0}$$

This charge transfer resistance has exponential temperature relation since it is a thermally activated process which is represented by the Arrhenius equation as:

$$\frac{1}{R_{CT}} = A_0 e^{\frac{-E_a}{RT}}$$

in which A_0 is the frequency factor, E_a is the activation energy of the charge transfer process.

Charge transfer processes are responsible for the charge storage in batteries. For instance, the anodic process in Li-based batteries involve the oxidation of Li to Li-ion at discharge.

After oxidation the electrons are transferred to the load through the current collector. At the same time the Li-ions are transported to the cathode through the electrolyte.

1.3.4. Mass Transport Processes

Ion movement inside the EES devices takes place in two forms either by diffusion or by migration. Diffusion is caused by the concentration gradient and migration is by the effect of electric field. The driving force for the movement of the ions are the electric field formed by the change in the electric potential between the two electrodes. The change in the concentration at the electrode surface due to the transform of one species to another by the electrochemical reaction is what causes the diffusion.

The transport of the ions is not only taking place at the electrolyte. It also involves the diffusion of the ions at the solid electrolyte interfaces. Typically, this makes the mass transport processes the rate limiting processes. The rate capability is defined as the capability to preserve the capacity as the current density increases.

The migration and diffusion are described by Nernst-Planck equation in one dimension can be written as:

$$J(x) = -D\frac{\partial C(x)}{\partial x} - DC\frac{zF}{RT}\frac{\partial \emptyset(x)}{\partial x}$$

where $J(x)$ is the flux at the distance x from the surface, D is the diffusion coefficient, C is the concentration, z is the charge, $\frac{\partial C(x)}{\partial x}$ and $\frac{\partial \emptyset(x)}{\partial x}$ are the concentration and the potential gradient. The first part describes the diffusion which is caused by the concentration gradient and the second part the migration caused by the electric potential gradient. Although modeling and the calculations of the mass transport of the ions in the EES devices are more complex they are based on the above equation.

1.3.5. Solid Electrolyte Interface

The EES devices such as most batteries are composed of solid electrodes and liquid electrolytes in direct contact. For example, in Li-ion batteries the anode is made of graphite which is in contact with organic solvents and Li salt. This leads to side reactions resulting in the formation of layers at the electrode electrolyte interface. The side reactions can occur instantaneously when in direct contact or it can occur when the voltage is applied or drawn from the device. In fact, the formation of such layers is inevitable which contribute hugely in the performance of the EES device.

The first observation of the formed interfaces was made when Li metal electrode was studied in non-aqueous electrolytes in the late 1970s. The term Solid Electrolyte Interface (SEI) was introduced as the passivation layer formed on the top of Li metal. However, this layer has the unique property of electronic insulation and yet Li-ion conduction. Studies in the literature revealed that the SEI forms and grows until dense and compact multilayer is formed which prohibit the conduction of electrons and the reaction with the electrolyte. In the end, the SEI reaches a stable form governing the stability of the battery.

The SEI composition, thickness and properties varies from one battery chemistry to another. This is because the layer is formed from the product of the reaction of the active materials with the electrolyte. In the last four decades, several studies were made to understand the composition, the mechanisms of formation and the effect of the SEI in the battery's performance. As Wang et al. mentioned in their review on modeling the anode SEI for lithium-ion batteries "SEI is still regarded as the most important but least understood (component) in rechargeable Li-ion batteries" [13][14]

In this thesis, we study the effect of the SEI on the Li-based batteries and we model its effect on its performance. The SEI on metallic Li anode is the key for its stability and hence understanding the Li-ion transport processes through the SEI is crucial for their utilization.

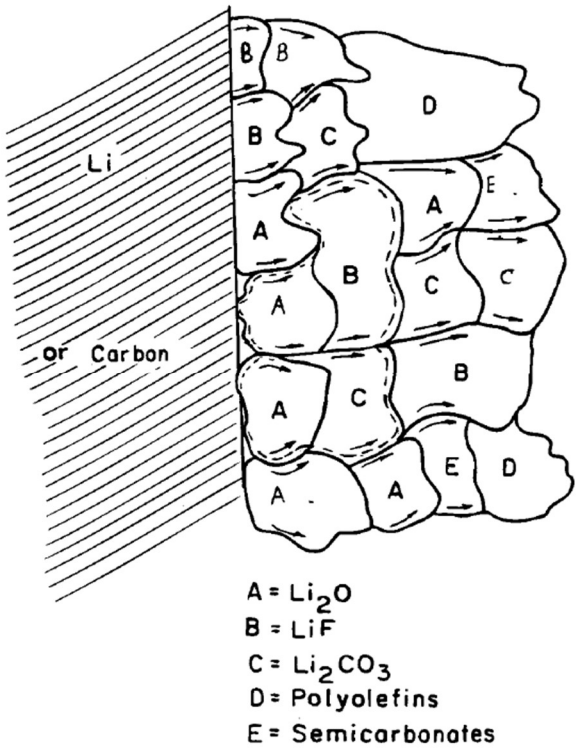

Figure 7. Schematic representation of the Mosaic model presented by Paled et. al. for the Solid Electrolyte Interface reproduced with permission from [15]

1.3.6. Electrochemical Impedance

All the electrochemical processes mentioned previously are the consequence of charge carrier movement. For example, an oxidation/reduction reaction results in electrons hopping from one medium to another. In another scenario, formation of the electric double layer requires the arrangement of the charges at the solid electrolyte interface. This movement by the charge carriers is faced by impedance (resistance). The characteristic of the resulting impedance is unique for every electrochemical process. Moreover, every process has time scale that is different from another. For example, mass transport processes are much slower compared to charge transfer ones. This is due to the involvement of ion movement in the former while electron hoping in the later. This difference in time-scales enables us to study each process at its time scale by applying corresponding excitation signals.

The technique used for studying the electrochemical impedance is called Electrochemical Impedance Spectroscopy which excite the electrochemical system with alternating signals at various frequencies and measuring the resultant response. Electrochemical Impedance Spectroscopy is used to study the electrochemical processes in the EES devices by determining their impedance. The impedance parameters are then used to extract information about the properties of the processes.

In this thesis, we use Electrochemical Impedance Spectroscopy to characterize and model various EES devices. The details of the Electrochemical Impedance Spectroscopy technique and how it is used are given in the following sections.

1.4. Electrochemical Impedance Spectroscopy for Electrochemical Energy Storage Devices

Since the introduction 1980s, Electrochemical Impedance Spectroscopy (EIS) technique has developed to become a fundamental tool in electrochemical research. EIS is used widely in studying various EES systems. It is a very powerful technique which enables the researcher to gain knowledge about the fast charge transfer processes, the interfacial processes and the slow mass transport processes in one measurement that is in-situ and nondestructive. It can also be used to probe various statuses of the EES devices such as, the State-of-Charge and the State-of-Health. Moreover, it is considered the main electrochemical technique for obtaining the physical parameters used for modeling the behavior of the EES devices.

In our work, we utilize EIS for understanding the various electrochemical processes in Li-based batteries and hybrid battery/supercapacitor systems. We further use the obtained EIS data to simulate and model the behavior of these systems under various conditions. Here we present the fundamentals of the technique and its applications which will benefit the reader when presenting the obtained results in the following chapters.

1.4.1. Fundamentals of Electrochemical Impedance Spectroscopy

Although EIS involves complex mathematical computation involving real, imaginary and frequency domain analysis, it is based on a simple concept that is impedance. Impedance is a wider and more general concept of a resistance which is the ability to resist the flow of electrical current. The mathematical expression for computing impedance is based on Ohm's law which states the impedance to be the ratio between the voltage and the current.

$$Z(t) = \frac{V(t)}{I(t)}$$

The word electrochemical in EIS indicates the electrochemical medium that the resistance of the current flow takes place which involve the charge and mass transfer processes of the charge carriers. Usually, the word spectroscopy is used in chemistry to infer the interaction of light with material. However, in EIS it means the utilization of wide range of frequencies in the alternating excitation signal. As we will see the response of the EIS is shown in a spectrum from Mega Hertz to Milli Hertz.

The two main variables in electrochemistry are voltage and current. Electrochemical analysis involves the excitation of the systems with one and measurement of the other. The excitation signal in EIS is an alternating sine-wave with certain amplitude applied at several points in a frequency range. If the excitation is achieved through a voltage signal and the response is measured as current the measurement is named Potentiostatic-EIS. If the reverse is performed it is named Galvanostatic-EIS.

The sinusoidal excitation signal involves two parameters, the amplitude of the wave and its frequency. In a conventional potentiostatic-EIS measurement, the excitation is made with small voltage amplitude V_A (in Volts) applies at frequency f (expressed in Hz = 1/s). The signal V(f) can be expressed as:

$$V(f) = V_A \sin(2\pi f)$$

The response signal will be a measured current signal at the same frequency I(f) with amplitude I_A and shifted in phase ($\emptyset$) which can be written as:

$$I(f) = \mathrm{I}_A \sin(2\pi f + \emptyset)$$

The expression of the excitation voltage signal in the x-axis and the response current signal in the y-axis will give us an ellipse shape figure known as the Lissajous plot shown in Figure 8(b). The analysis of the Lissajous give indications about the linearity and stability of the measurement. Impedance can also be calculated geometrically from the parameters of the ellipse and the way it rotates.

The ratio between the voltage and the current signals will give us the impedance. However, because we have two variables the impedance is expressed as a complex number with two components real and imaginary:

$$Z(f) = \frac{V(f)}{I(f)} = \frac{V_A \sin(2\pi f)}{\mathrm{I}_A \sin(2\pi f + \emptyset)} = Z_r + iZ_i$$

Therefore, impedance is expressed in terms of a magnitude with absolute value (Z) and a phase shift (∅) which both can be computed as:

$$Z = |Z_r + iZ_i| \quad \text{and} \quad \emptyset = \arctan\left(\frac{Z_r}{Z_i}\right)$$

The expression of the impedance can be done in two different representations. The first is called the Bode plot which have the frequency in its x-axis and the absolute impedance or the phase shift in the y-axis. The second is called Nyquist plot which shows the real impedance component in the x-axis and the negative of the imaginary impedance in the y-axis. The details of these plots are explained in the interpretation of the EIS section.

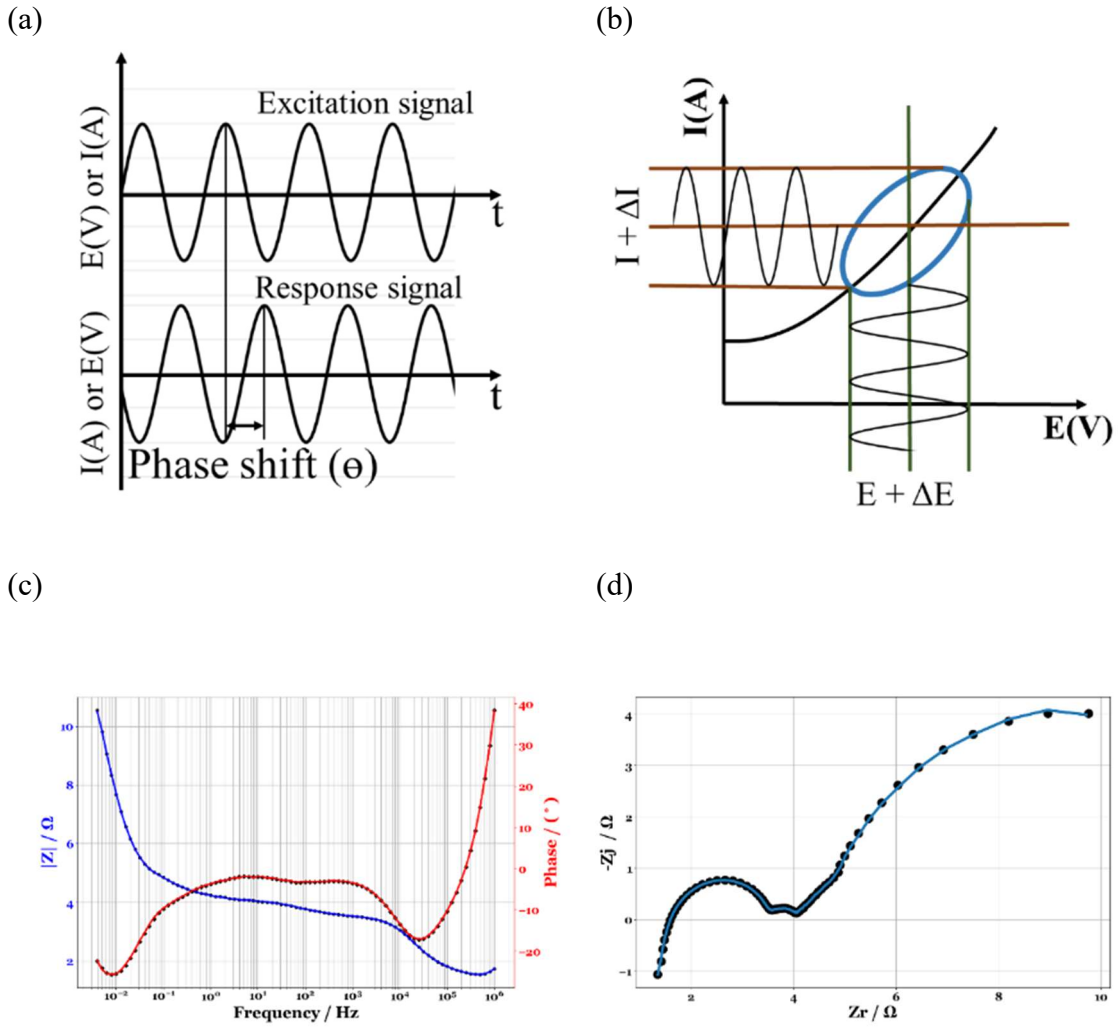

Figure 8. (a) Excitation and response signals in Electrochemical Impedance Spectroscopy measurement (b) Lissajous plot resulting from drawing excitation signal vs. response signal (c) Bode plot showing the modulus impedance and the phase shift vs. frequency and (d) Nyquist plot demonstrating the negative of the imaginary impedance vs. real impedance

1.4.2. Validation of the Electrochemical Impedance Data

The excitation of any electrochemical system with a sinusoidal signal will result in an impedance response which may represent the real impedance of the system or maybe an

artifact. Obtaining accurate and reliable EIS data for the studied systems requires the fulfillment of three conditions namely, linearity, stability and causality.

As we have shown earlier, the relationship between the current and the voltage in the electrochemical systems are non-linear in nature. For example, in a reversible kinetically limited system, the current to voltage relationship is governed by Butler-Volmer equation which are related by an exponential rather than linear relation. Linearity is achieved by the excitation with relatively small amplitudes signals which results in a pseudo-linear relation as shown Figure 9(a).

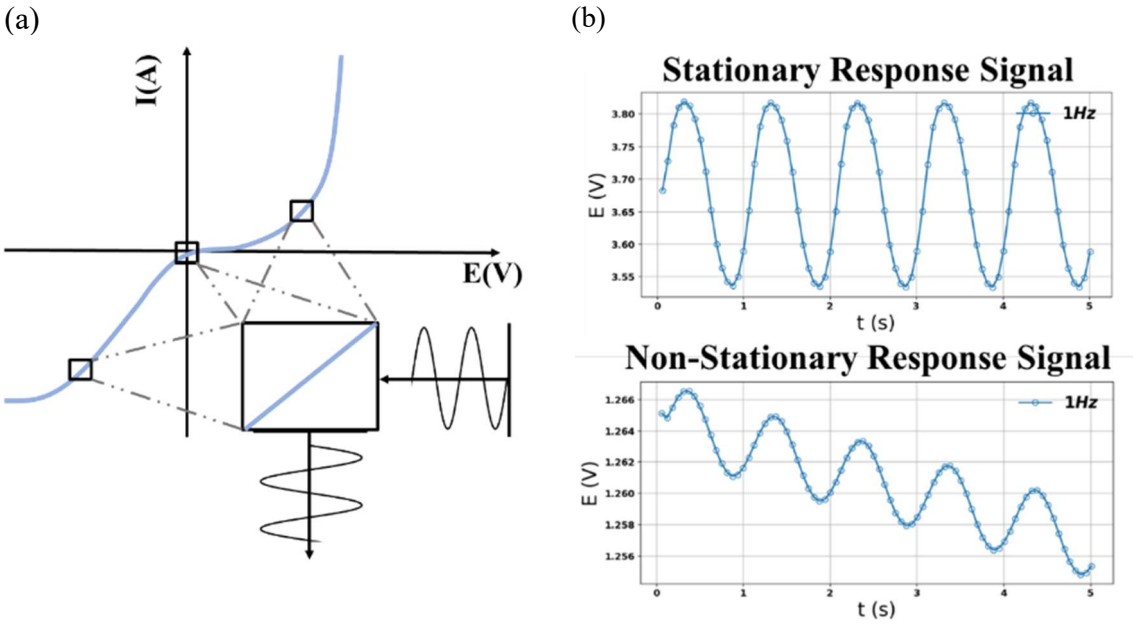

Figure 9. (a) Achieving linearity in EIS measurements by reducing the amplitude of the excitation signal, (b) Stationary vs. Nonstationary response signal in EIS measurements

Stability depends on the time scale of the measurement. Electrochemical systems can achieve stability within the EIS measurement period. Stability can be defined as the invariance in the system's impedance during the time scale of the measurement. Another similar concept is stationarity which is related to the Direct Current (DC) level of the response signal. It can be defined as the invariance in the DC voltage response in the

galvanostatic measurements or the current in potentiostatic measurement being zero. The change in the DC voltage value during the measurement in a galvanostatic measurement is called voltage drift.

Causality is achieved by being confident that the impedance response is coming from the system not from noise. Namely, the excitation is causing the response, if the excitation is taken away, the response should go away as well.

To check for the fulfillment of the mentioned conditions, further analysis is needed on the obtained EIS data. There are mainly two analysis methods used for the validation. The first method is the compatibility test of the EIS data with the Kramers-Kronig relations. The Kramers-Kronig relations relate the real and the imaginary component of the obtained EIS data. Any deviation in Kramers-Kronig compatibility test will indicates the presence of non-linearity and/or non-stability in the data. Kramers-Kronig relation is as follows:

$$Z_r(\omega) = Z_{r,\infty} - \frac{2}{\pi}\int_0^{\infty} \frac{xZ_j(x) - Z_j(\omega)}{x^2 - \omega^2} dx$$

Which indicates that the real component of the impedance can be predicted from function of the imaginary component if the conditions of linearity and stability are met. However, as can be seen from the relation it involves the integration from zero to infinity which is not suitable for direct application. Instead, approximation is implemented by fitting the data to generic Kramers-Kronig compatible circuit elements.

The second is by checking for the presence of high order Harmonics in the response signal. This involves the transformation of the obtained time domain response signal to the frequency domain by means of Fourier Transform. In a linear and stable response, the frequency domain should only contain one signal, named Fundamental signal, with high amplitude at the corresponding frequency of the excitation. Other signals in the frequency domain should be having low amplitudes in the noise level of the signal. The presence of high-order harmonics at the multiple of the fundamental signal frequency is an indication of the presence of non-linearity and/or non-stationarity in the obtained data.

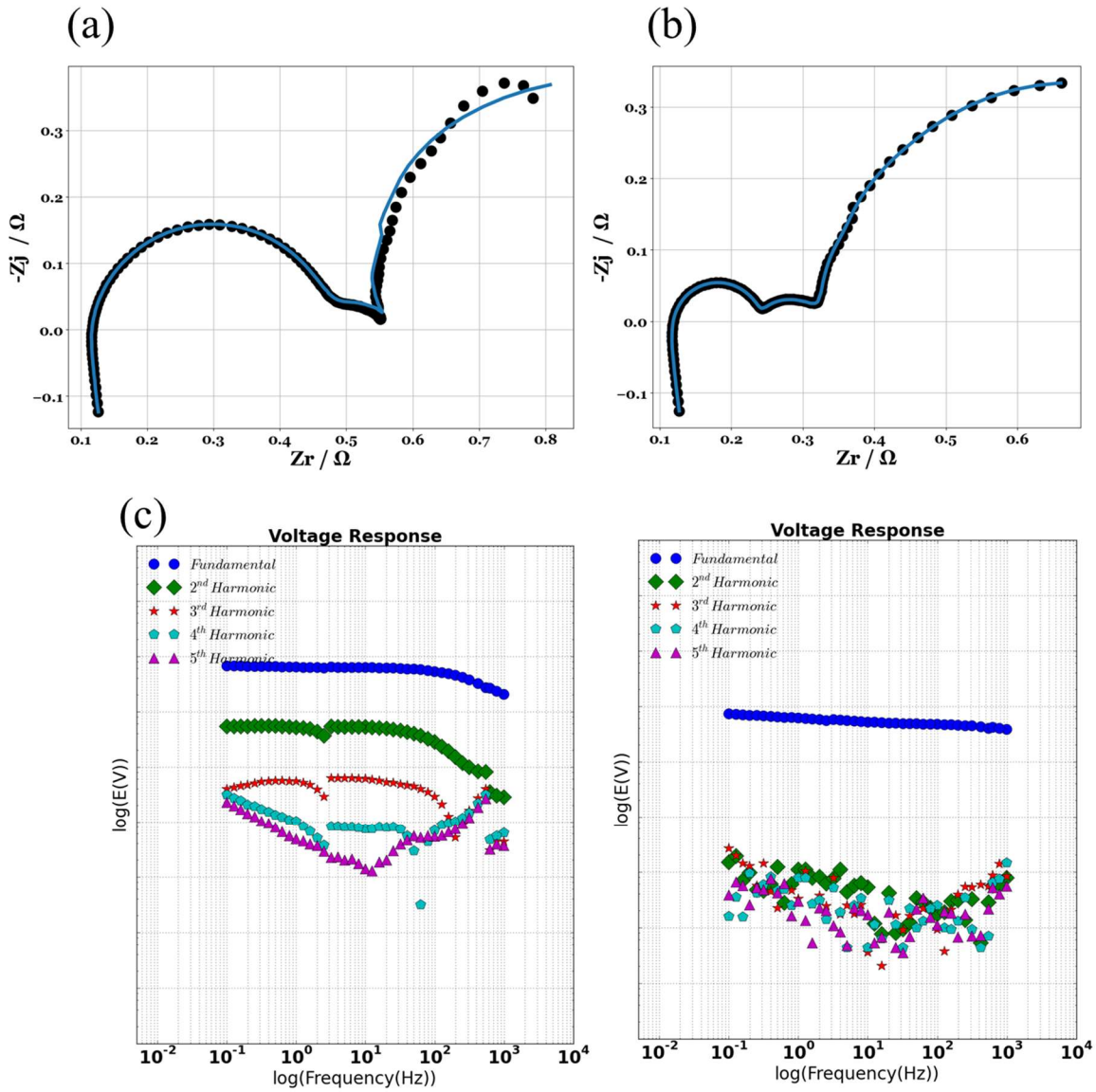

Figure 10. (a) Nyquist plot showing Kramers-Kronig incompatible data at the low frequency region, (b) Nyquist plot with Kramers-Kronig compatibility, (c) Harmonic spectrum of linear(left) and non-linear(right) voltage responses

1.4.3. Interpretation of the Electrochemical Impedance Spectra

The EIS response of EES devices is complex and involves various responses at different frequency regions. It is due to the nature of the EES which is composed of several interfaces

with electrochemical process interconnected with each other. This makes the interpretation of the EIS data of the EES systems challenging and requires careful assignments. As we have demonstrated in the fundamental of the electrochemical processes in the EES section, there are double layer capacitance, charge transfer, mass transfer and interfacial process which take place at different time scales inside any EES device. The impedance response of these processes can be resistive, capacitive and diffusive or the combination of all three. In this section we try to break down these EIS responses with presenting their theoretical origins and data demonstration.

To simplify the impedance interpretation, an electric circuit analogy is used for every electrochemical process. These are known as equivalent circuit models where a resistive behavior such as charge transfer resistance is modeled by an electric resistor and a capacitive behavior such as the double layer capacitance as a capacitor. The relationship between the voltage and the current is well established in the equivalent circuit models which makes the calculations and the interpretations of the EIS data easier.

- Resistor (R):

The basic impedance response for any electrochemical phenomena is the resistance of charge flow. The resistance is against the flow of electrons or ions in solid and liquid states. Resistance is the simplest impedance response which follows Ohm's law with a linear relation between the voltage excitation and the current response or vice versa.

$$Z_R = \frac{V}{I}$$

where Z_R is the resistive impedance, V is the voltage and I is the current.

As can be seen from the equation, there is no time dependence in the resistance response so it is frequency independent. Therefore, there is no change in the phase angle between the excitation and the response signal which will show zero phase angle at all frequencies in the Bode plot. In the Nyquist plot since there is no imaginary components, the resistance value appears as a point in the x-axis with no values in the y-axis.

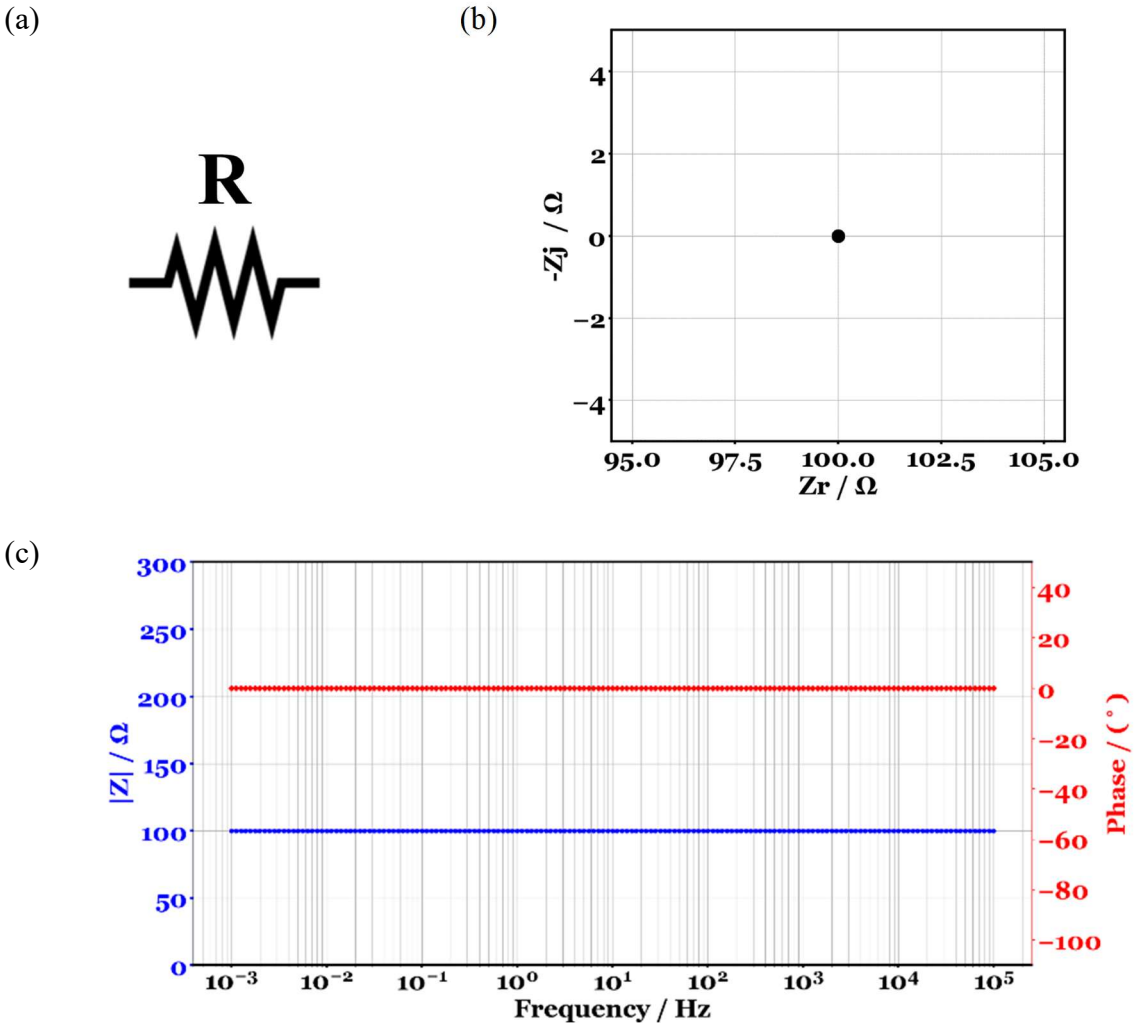

Figure 11. (a) Equivalent circuit symbol for a resistor, impedance response of R in (b) Nyquist plot, (c) Bode plot showing the modulus impedance and the phase angle

- Capacitor (C):

Capacitive processes that involve charge accumulation can be modeled as an electric capacitor in which the current is a time-dependent function of voltage. The relation between the current and the voltage is as follows:

$$I = C\frac{dV}{dt}$$

in which I is the current in Amps, C is the capacitance in Farads, V is the voltage in Volts and t is time in seconds.

The impedance relation to the capacitance is time dependent which varies by changing the frequency of the excitation signal. The impedance equation for the capacitor is as follows:

$$Z_C = \frac{1}{i\omega C}$$

where Z_C is capacitive impedance, i is imaginary number = $\sqrt{-1}$, ω is the angular frequency $\omega = 2\pi f$, and C is the capacitance.

As can be seen, the capacitive impedance is inversely proportional to the frequency. As frequency decreases, the value of the impedance increases which shows a straight line with an increasing slope as we move to lower frequencies in the Bode plot. The phase angle between the voltage and the current in an ideal capacitor is -90 degrees as shown in the Bode plot. Since there is no real component in the capacitive impedance, the response in the Nyquist plot appears as a straight line with increasing values in the y-axis at the origin of the x-axis.

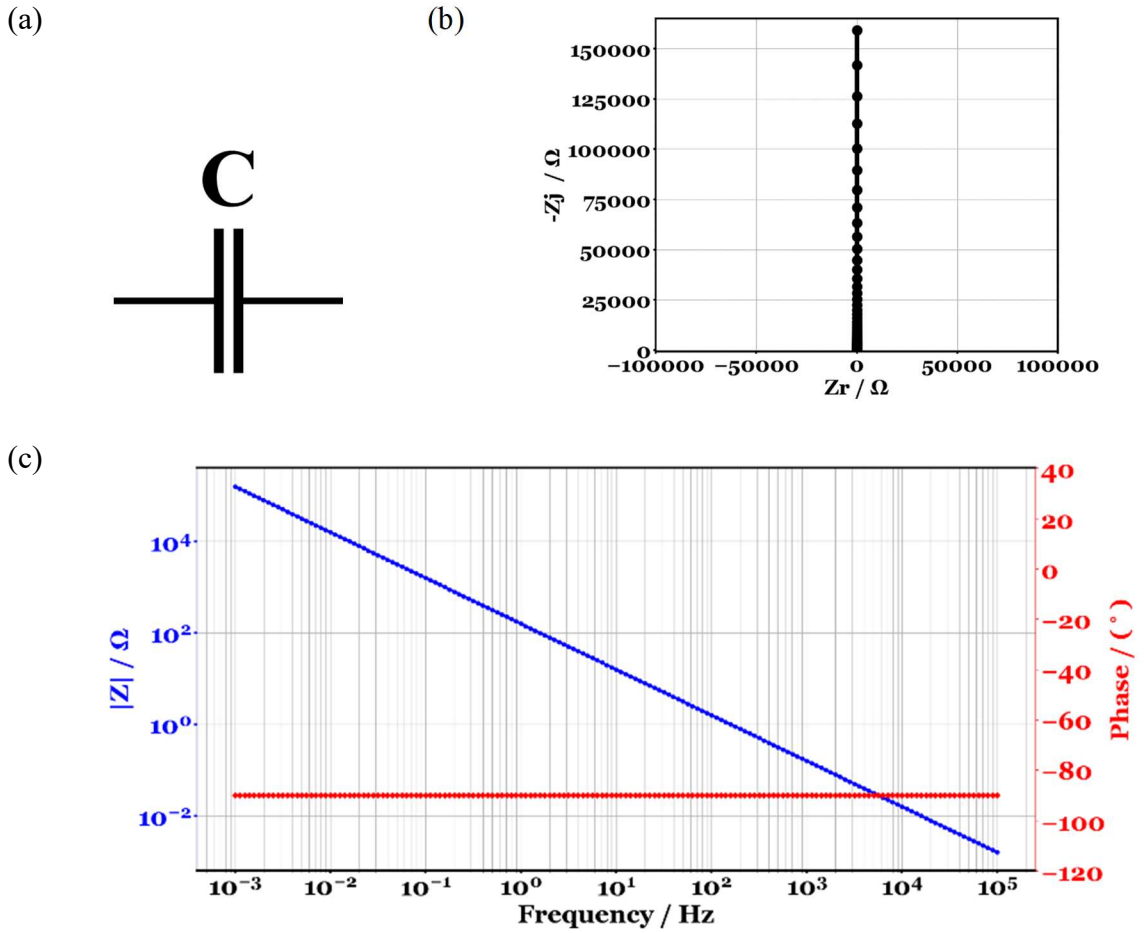

Figure 12. (a) Equivalent circuit symbol for a capacitor, impedance response of C in (b) Nyquist plot, (c) Bode plot showing the modulus impedance and the phase angle

- Resistor with Capacitor (RC):

All electrochemical processes happen as a combination of resistance and capacitance. The combination takes place in which each process occurs at different time scale which shows parallel response in the equivalent circuit analogy or both processes occur at the same time which shows series connection.

For example, for every capacitive process there is a resistance for the flow of the charges that takes place at the same time of the capacitive process. The equivalent circuit here is a resistance and a capacitance connected in series as shown in Figure 13. The impedance

response for such processes can be calculated by the series combination of the resistive impedance with the capacitive one. The equation of the series connection is as follows:

$$Z = Z_R + Z_C = R + \frac{1}{i\omega C}$$

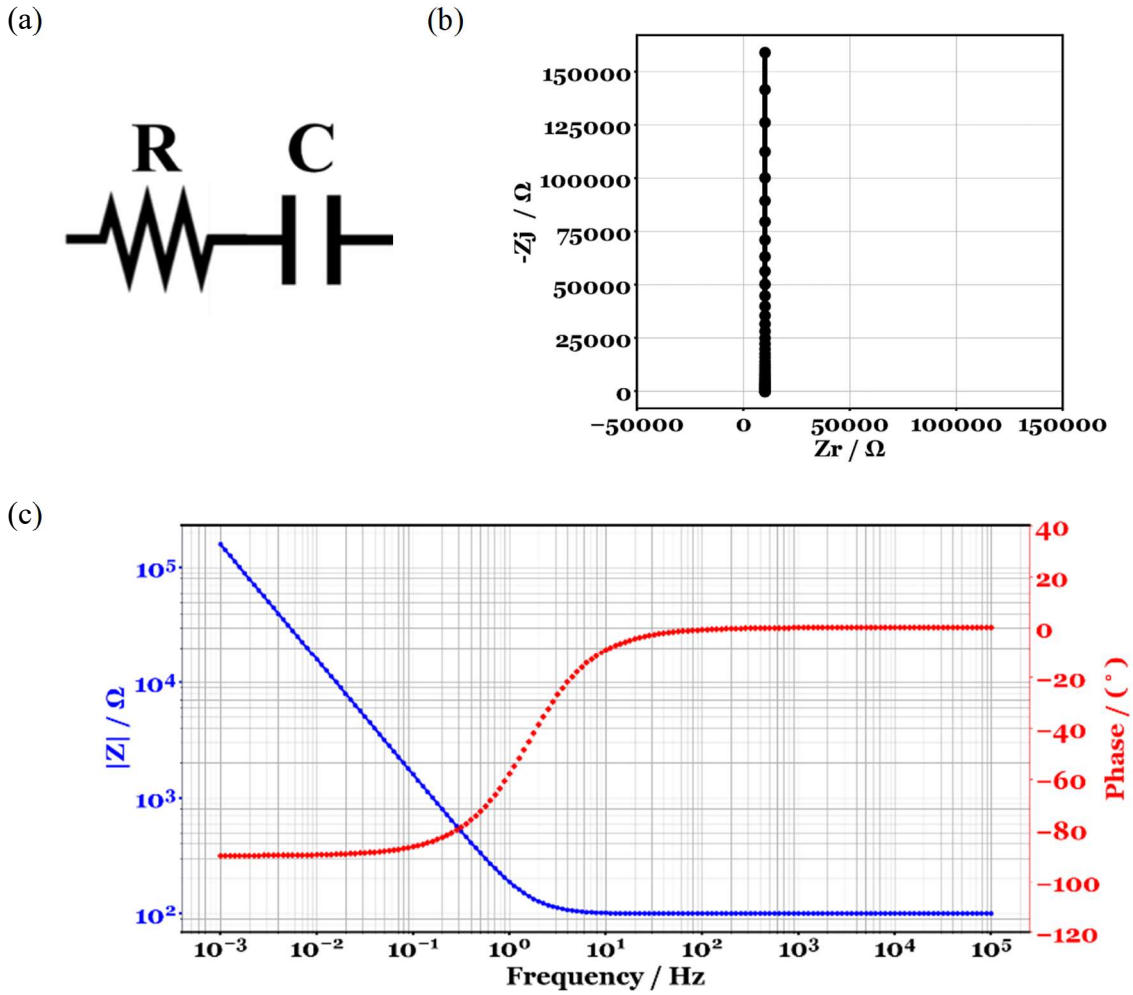

Figure 13. (a) Equivalent circuit symbol for a resistor connected in series to a capacitor, impedance response of RC in (b) Nyquist plot, (c) Bode plot showing the modulus impedance and the phase angle

The other combination of resistive and capacitive processes is what occur for charge transfer at every electrode electrolyte interface. It is the parallel combination of the formed double layer capacitance and the charge transfer resistance. The equation for the impedance is as follows:

$$\frac{1}{Z} = \frac{1}{Z_R} + \frac{1}{Z_C} = \frac{1}{R} + i\omega C = \frac{1 + i\omega RC}{R}$$

$$Z = \frac{R}{1 + i\omega RC}$$

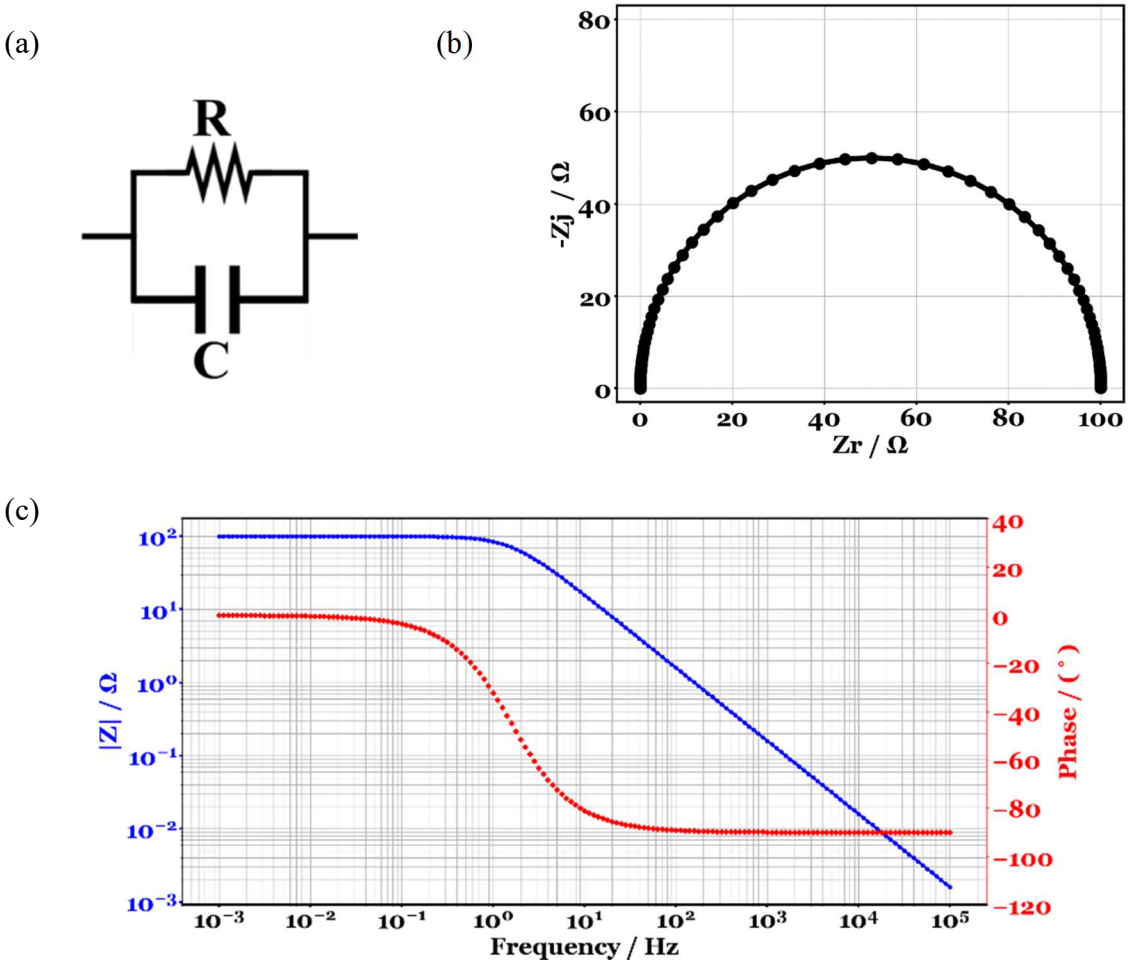

Figure 14. (a) Equivalent circuit symbol for a resistor connected in parallel to a capacitor, impedance response of RC in (b) Nyquist plot, (c) Bode plot showing the modulus impedance and the phase angle

- Simplifie Randles' Circuit ($R_S - R_{CT} \parallel C_{DL}$)

The parallel combination of the charge transfer resistance and the double layer capacitance also involve a resistance for the charge flow through the solution and can be assumed to

contain every other resistance in the system such as contact resistance. This resistance is connected in series with the parallel connected RC. The resulting equivalent circuit is called Randles' circuit which is used for modeling the behavior of the electrochemical processes and its impedance response.

$$Z = Z_{Rs} + Z_{RC} = Rs + \frac{R}{1 + i\omega RC}$$

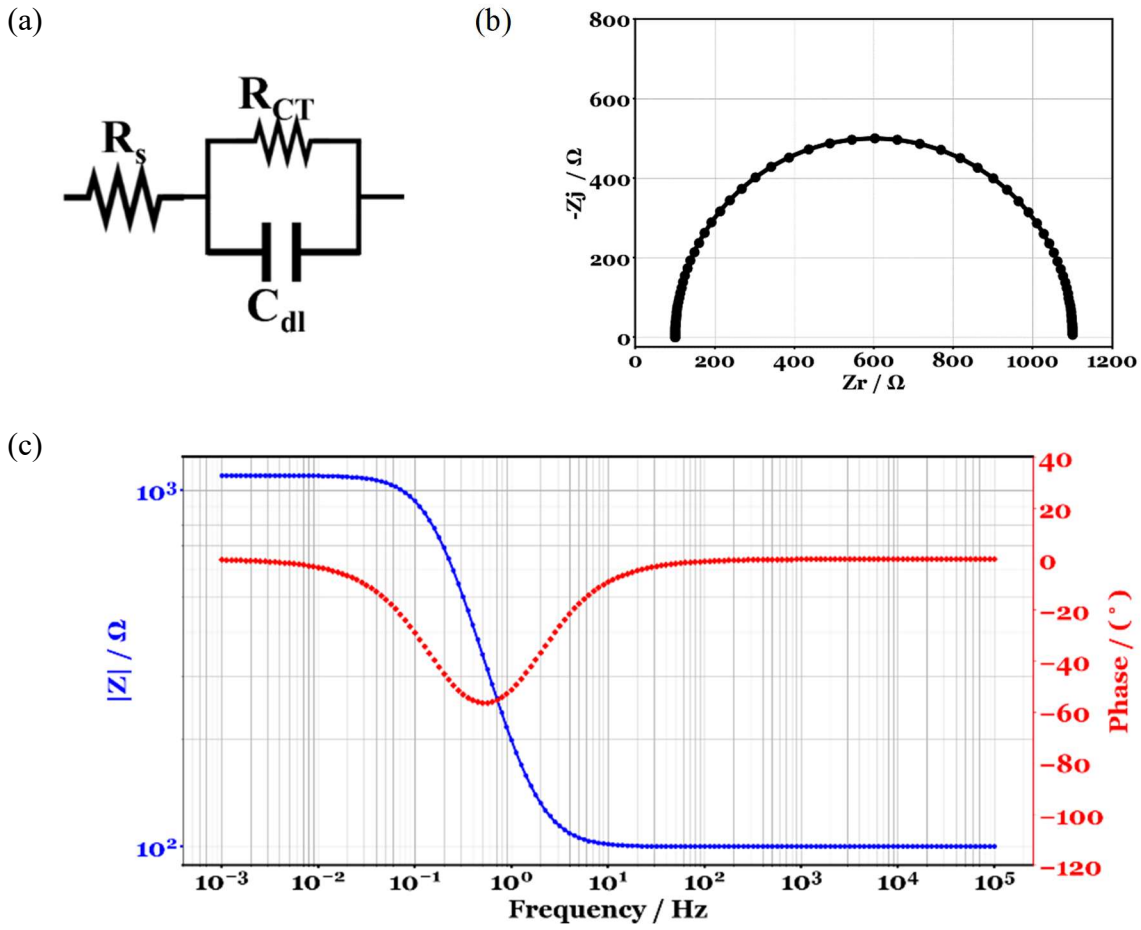

Figure 15. (a) Equivalent circuit symbol for a Randle's equivalent circuit, impedance response of R_S – R_{CT} | C_{DL} in (b) Nyquist plot, (c) Bode plot showing the modulus impedance and the phase angle

- Diffusion, Warburg Element (W)

The impedance response of the mass transport processes, diffusion, in liquid medium is modeled by Warburg element. This diffusion impedance is related to the frequency by square root relation as follow [16]:

$$Z_w = \frac{\sigma}{\sqrt{\omega}} - \frac{\sigma i}{\sqrt{\omega}}$$

where σ is the Warburg coefficient with units of Ohm/$\sqrt{s}$.

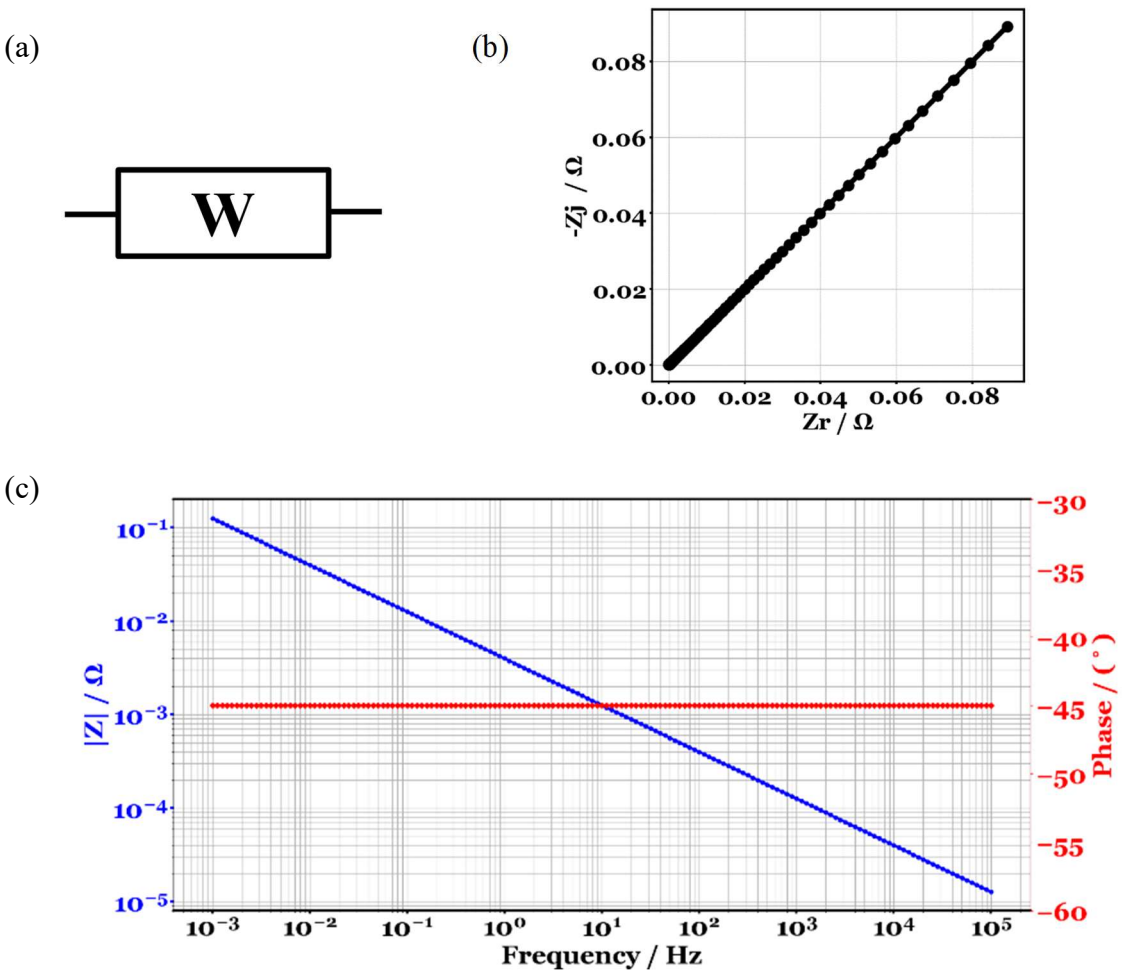

Figure 16. (a) Equivalent circuit symbol for a Warburg element, impedance response of W in (b) Nyquist plot, (c) Bode plot showing the modulus impedance and the phase angle

As can be seen from the equation Warburg impedance is inversely proportional to the square root of frequency and in Nyquist plots it gives a straight line with a phase of 45°. In Bode plot it exhibits phase shift of -45° at all frequencies.

- Inductor (L)

The inductive behavior is observed in EIS at very high frequency regions. This due to the direct proportionality of the inductive impedance to the frequency. The equation is as follows:

$$Z_C = i\omega L$$

in which L is the inductance in Henry. Since there is no real component in the inductive impedance it will show only imaginary values with phase angle of 90°.

The inductive behavior is usually seen at >100kHz frequencies and is mostly originating from the instrument or the connections. It is also observed originating from the metallic parts of the electrochemical systems. The inductance at these regions usually does not represent any electrochemical processes of the systems.

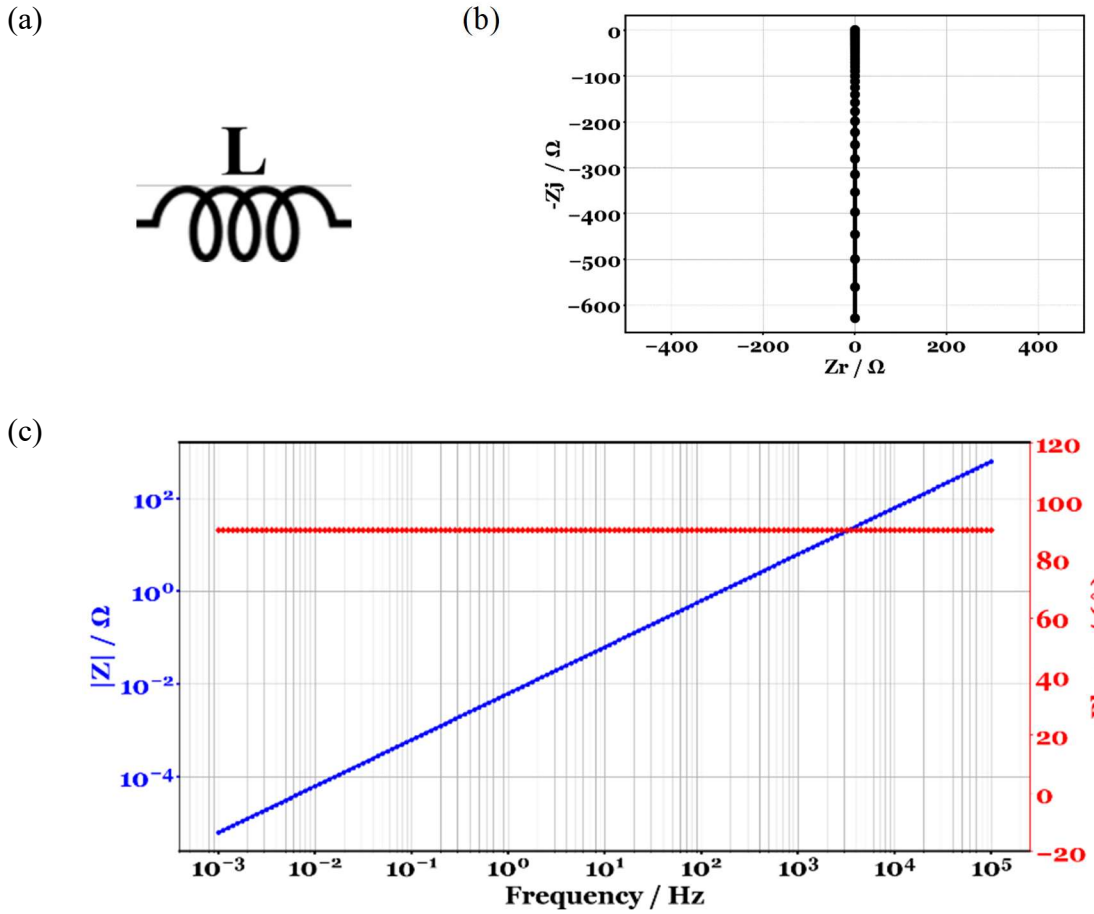

Figure 17. (a) Equivalent circuit symbol for an inductor, impedance response of L in (b) Nyquist plot, (c) Bode plot showing the modulus impedance and the phase angle

- Constant Phase Element (CPE)

Real electrochemical systems are composed of highly porous materials aimed for the increase in the surface area which results in high electrochemical activity. The capacitive behavior of these electrodes deviates from ideal capacitor behavior and requires compensation to correctly represent the impedance of the system. For this purpose, an equivalent circuit element called Constant Phase Element (CPE) is introduced. In the CPE a new parameter is presented called alpha (α) which compensate for the deviation from ideality. Its value ranges from zero to one. The equation for the CPE impedance is as:

$$Z_{CPE} = \frac{1}{(i\omega)^{\alpha} Q}$$

where Q is the CPE coefficient (Ohm-1 sα). As can be seen the value of alpha determines the meaning of Q in the CPE element. Q will equal to capacitance (C) if alpha is one and Warburg diffusion element (W) is alpha is 0.5.

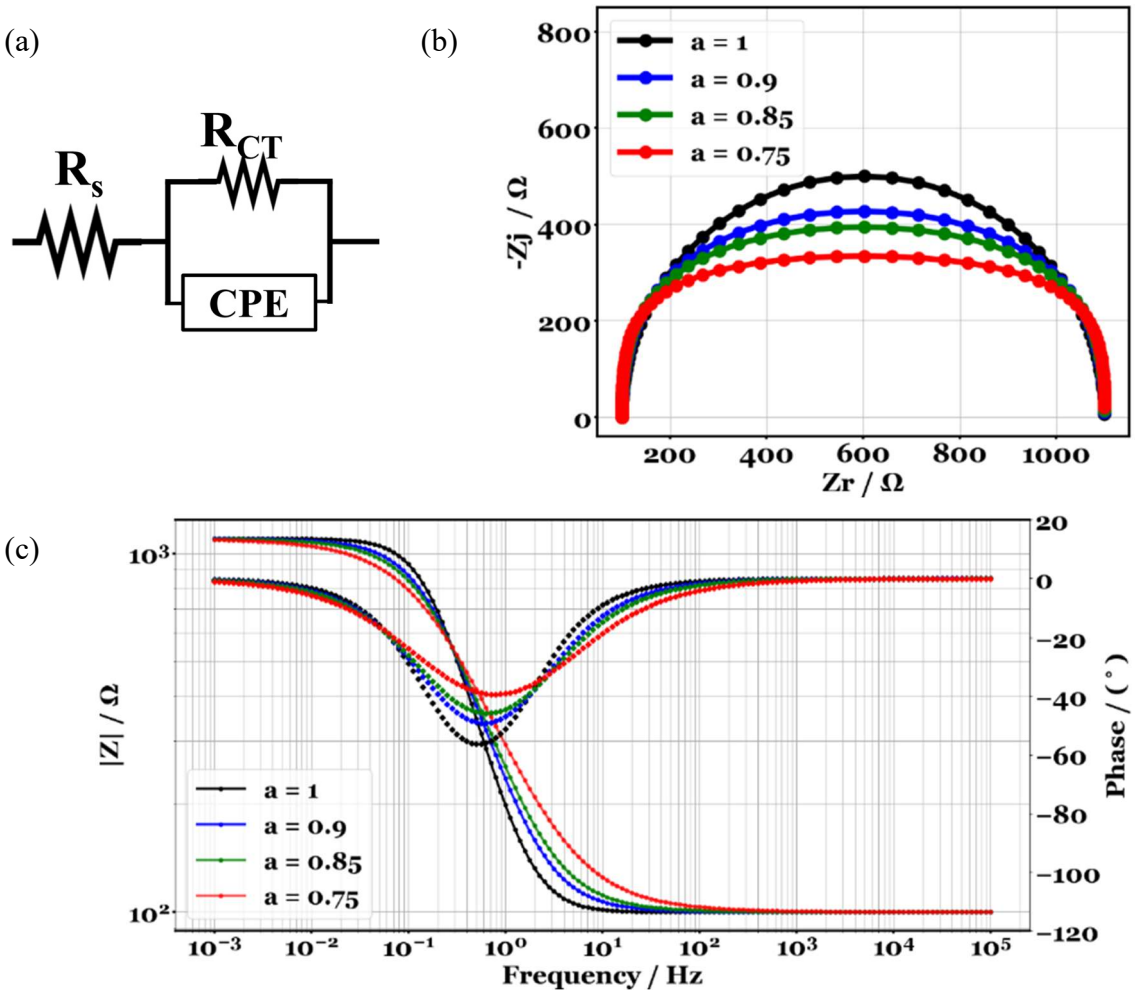

Figure 18. (a) Equivalent circuit for a Constant Phase Element, impedance response of CPE in (b) Nyquist plot, (c) Bode plot showing the modulus impedance and the phase angle with four different a values(1, 0.9, 0.85, 0.75)

1.4.4. Non-linear Harmonic Analysis in Electrochemical Impedance Spectroscopy

The presence of non-linearity and non-stationarity in the impedance data is unwanted when the impedance data is used to extract the parameters of the system such as, charge transfer resistance and double layer capacitance. Their presence will render the data incompatible with any equivalent circuit fitting as the circuit elements are linear and stationary. However, the origins of the non-linearity and the non-stationarity in the impedance data should be understood and interpreted by the researcher. In fact, recently there are several studies which investigates the reasons for their observations and attempts have been made to correlate their presence to kinetic and mechanistic reasons [17]–[20].

The method used for the investigation of non-linearity and non-stationarity in the impedance data is through the analysis of the response sinusoidal signal in the frequency domain. The transfer of the signal from time to frequency domain is achieved mathematically through Fourier Transform. Typically, the time domain response signals at each frequency are obtained and transformed to the frequency domain and components of each signal is analyzed. The components of the sinusoidal signals at the frequency domain are in the form of definite amplitude single points at certain frequencies called Harmonics. Linear and stationary signals give no higher harmonics than their fundamental signal at the frequency of the sinusoidal wave. Non-linearity and non-stationarity appear as high order harmonics with frequencies that are multiples of the fundamental frequency.

In order to analyze the response signal in the frequency domain, Fourier Transform is used which is a mathematical tool for transforming periodic functions of time into a function of frequency. It resolves the periodic function of time into an equivalent infinite summation of sine waves and cosine waves. The resulting infinite series is the Fourier Series which can be expressed in exponential form as:

$$x(t) = \sum_{n=-\infty}^{\infty} c_n \, e^{-in\omega t}$$

Where, n = sample number, ω = angular frequency = 2πf, c_n are the Fourier series coefficients.

Fourier Transform is used to solve for the coefficients c_n. The result is a group of coefficients which are function of frequency and can be obtained by the following sum:

$$c_f = \sum_{n=0}^{N-1} x_n \, e^{-i2\pi f n/N}$$

Where, N = number of samples, n = sample number, x_n = value of the input signal at n, f = frequency = 0,1,2,3,….,N-1 and c_f = coefficient value.

For a Linear Time-Invariant signal, the value of the coefficients will have power only at the corresponding frequency of the analyzed current or voltage signal. The rest of the coefficients will have minimal power which represents the noise level of the signal.

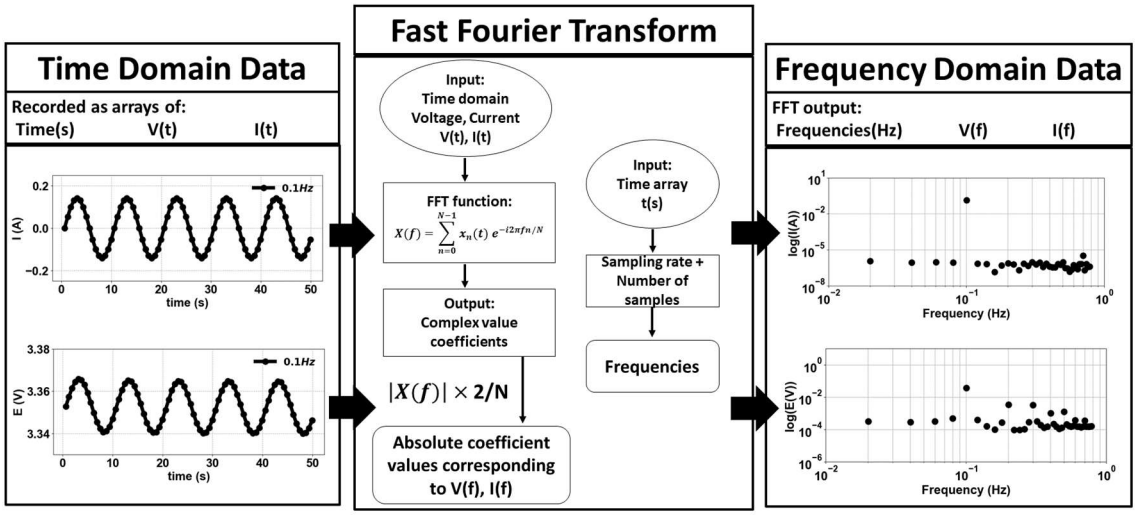

Figure 19. Fourier Transform calculation of time domain excitation and response signal and its representation in the frequency domain, the excitation current signal represent the linear response(top) and the voltage response represent the non-linear case with higher harmonics at the multiple frequency of the fundamental signal(bottom)

For a signal that contains non-linearity, beside the fundamental signal, there are other signals with different amplitudes at the n multiple frequencies of the fundamental signal. For example, at 0.1Hz signal we observe signals at 0.2Hz, 0.3Hz, 0.4Hz …etc. The amplitude of each signal varies at different multiple frequency. However, for non-stationary signals, the amplitude of the higher amplitudes decreases gradually as the frequency increases.

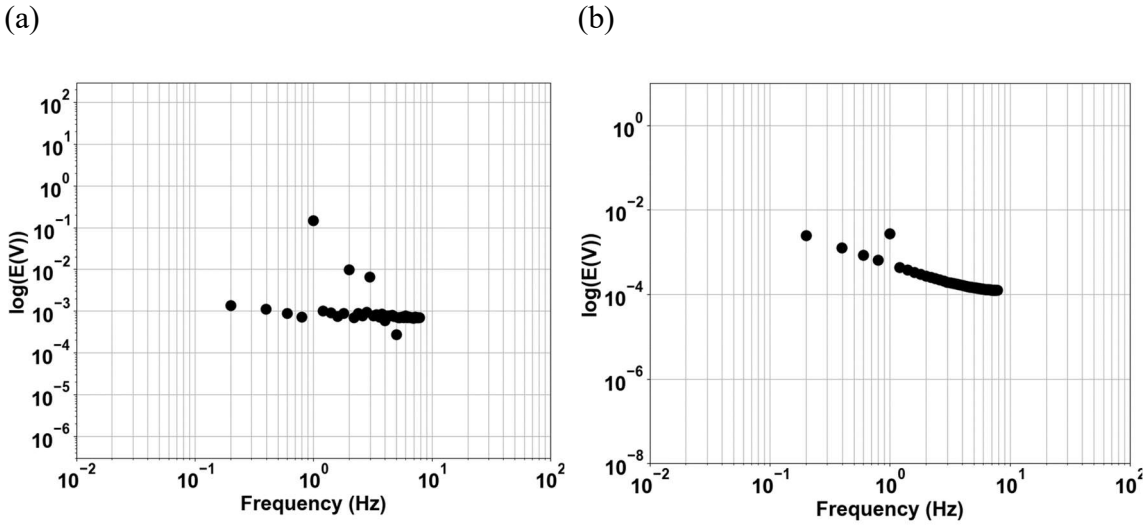

Figure 20. Frequency domain analysis of voltage response signal of (a) Non-linear harmonic response (b) Non-stationary harmonic response

The obtained harmonics amplitude values can be plotted versus frequency x-axis. The plot is called harmonic response spectrum in which the change of the amplitudes of the high order harmonics can be observed as the frequency increase or decrease. The analysis of the spectrum is made to correlate the observed trends to the electrochemical processes.

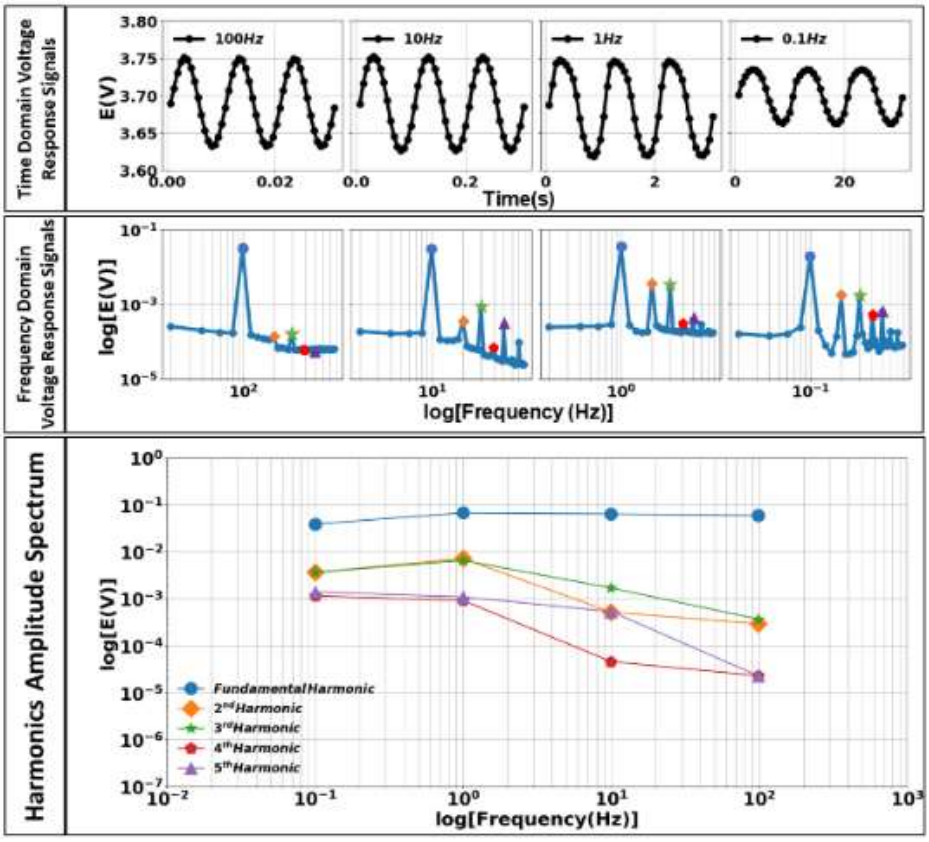

Figure 21. Harmonic response spectrum obtained from the combination of the multiple harmonics in one frequency domain graph

1.5. Modeling Electrochemical Energy Storage Devices

Obtaining knowledge about the capabilities of the EES device is crucial for its application. Various applications such as electric vehicles, intermittent renewable sources or electronics demand diverse capabilities from the used EES devices. These parameters include voltage levels, supplied currents, specific power, capacity and energy density. These are determined by the type of the electrochemical systems and the chemistry of the used device.

Modeling the EES device is achieved through two distinct conditions. The first is modeling the behavior of the EES device for standard conditions such as determining the theoretical capacity, the open circuit voltage of the device or the amount of current that can be provided at certain states-of-charge. This type of modeling is required[21] in determining the specifics of the devices but is impractical for modeling the behavior under real-life applications. The second, is modeling the behavior of the EES under dynamic change/discharge voltages and currents which simulate the real-life application. This type of modeling methodologies mimics the real-life scenarios and gives better understanding about the behavior of the systems. It further provides information regarding the limits of application and its failing circumstances.

In this work, we introduce modeling methodologies that model the EES devices under changing charge/discharge regimes tailored for specific applications such as the fast change in charge/discharge currents caused by driving an electric vehicle in urban areas. These charge/discharge regimes are used for simulating the behavior of the EES device before the assembly for the intended application. The knowledge obtained from the simulations determines whether the device is suitable for such application and further helps in choosing the best device for the tailored application.

In the literature, the dynamic behavior of EES is modeled based on two different approaches. The first is the “First Principle” approach which is based on physics-based equations of the thermodynamics and the kinetics of the systems. This approach shows very accurate results but is built on very complex calculations and numerous adjustable parameters that in many cases require heavy computations and modeling themselves. In this method, the parameters used for the electrochemical process such as the charge transfer resistances are mostly obtained from EIS measurements which makes EIS technique crucial for this method.

The second approach is based on Equivalent Circuit modeling approach in which the system is represented by electric circuit components. As shown previously, electrochemical processes can be modeled by electric circuit components such as resistors and capacitors connected in series or parallel. This approach is simple and does not involve

complex calculations. However, it lacks high accuracy. In this approach, type of circuit components and their values are determined also based on the response to the EIS measurements.

In both approaches, EIS technique plays very important role in determining the parameters used in the models. Determining these parameters involves subjective contribution from the researcher in extracting them from the raw EIS data and in their assignment to the corresponding processes. Though for the same EIS data, different parameter assignments with different values can be made. Moreover, the subjectivity limits the use of the developed modeling method to certain EES systems with certain size and shapes.

To solve the subjectivity problem and to present a modeling method that provide accurate results yet with low computation complexity, a modeling method named Zero-free-parameter was developed by a previous study in our lab. The method is based on EIS technique, free of adjustable parameters and does not use equivalent circuits. It does not involve complex calculations and employs the raw EIS data directly. The method was tested for three separate EES systems, two batteries and a supercapacitor, and provided an accuracy of less than 1% error.

Previous work in our lab modeled systems that were rechargeable single cells. The main aim of the current thesis is to extend the presented modeling approach to other EES systems, including primary Li batteries and arbitrarily combined hybrid battery/supercapacitor systems.

For primary Li batteries, initial challenge is the proper measurement of accurate EIS. Though primary batteries have been employed regularly, literature is lacking proper EIS methodology and reliable data. This is due to the complex electrochemistry of primary batteries and the nonlinear behavior that result from the irreversible chemical reactions. Accurate EIS will be achieved with adjusted procedure that suites the properties of the primary batteries. Moreover, for Li based anode the effect of the Solid Electrolyte Interface should be accounted for in modeling the voltage behavior since it has large effects. the effects are due to the dynamic properties of this interface which varies from Li-ion cells that have stable and static properties. After obtaining the accurate EIS, the application of

the modeling algorithm will follow with adjustments regarding the voltage delay and recovery behaviors.

The modeling methodology will be also extended to hybrid battery/supercapacitor systems. The main challenge in this system is in determining the current distribution among the parallel connected hybrid systems. To overcome this, we develop optimization algorithm which can predict the current distribution and using the Zero-free-parameter method simulate the voltage response of arbitrarily chosen hybrid systems.

The details of the applied method and the algorithm used will be explained and the modeling results with experimental validation will be presented in chapter 3.

1.6. Electrochemical Properties of the Studied Systems:

In this section, the electrochemistry of the studied EES devices and their electrochemical properties are presented. Three devices are studied. The first are primary Lithium batteries. Mainly primary Lithium Thionyl Chloride and Lithium Manganese Dioxide are used. They are heavily characterized by EIS technique and their voltage behavior is modeled. The second systems are Li-ion batteries and the third are supercapacitors. However, secondary Li-ion batteries and supercapacitors are used as a parallel connected hybrid system. These systems are used in the performance modeling study.

1.6.1. Primary Lithium Batteries

Primary batteries represent the main power source for applications where charging is impractical or impossible. They are used as the main EES systems for applications such as, military, space and specialty emergency services. Although they have the disadvantage of non-recharging, they possess the highest gravimetric and volumetric energy density compared to the other types of batteries. Moreover, they have long storage life and operational readiness. They can be carried to remote locations and used instantly, even after long storage.

Primary batteries exist in different chemistries. The most used and the highest performance ones are Li metal based batteries. They are distinguished by their high cell potential higher than 3.0V and hence the highest energy densities. In their anodes, metallic Li is used and different cathode materials are implemented. The usage of metallic Li is what provides the high gravimetric and volumetric energy densities. This is related to its light weight and high reduction potential. We focused in our EIS characterization on mainly two types of Li primary batteries namely, Lithium Thionyl Chloride ($Li/SOCl_2$) and Lithium Manganese Dioxide (Li/MnO_2) batteries which are commercially available and produced by different battery companies.

1.6.1.1. Lithium Thionyl Chloride Battery ($Li/SOCl_2$):

Among Li primary batteries $Li\backslash SOCl_2$ is the most commonly used chemistry, especially for defense applications. It has high energy density, high operating cell voltage, steady voltage over 95% of the discharge, large operating temperature range (-55 to 70 ^oC) and long storage life. It is heavily used in applications ranging from battlefield applications to telecommunication, tracking and actuators for missile systems.

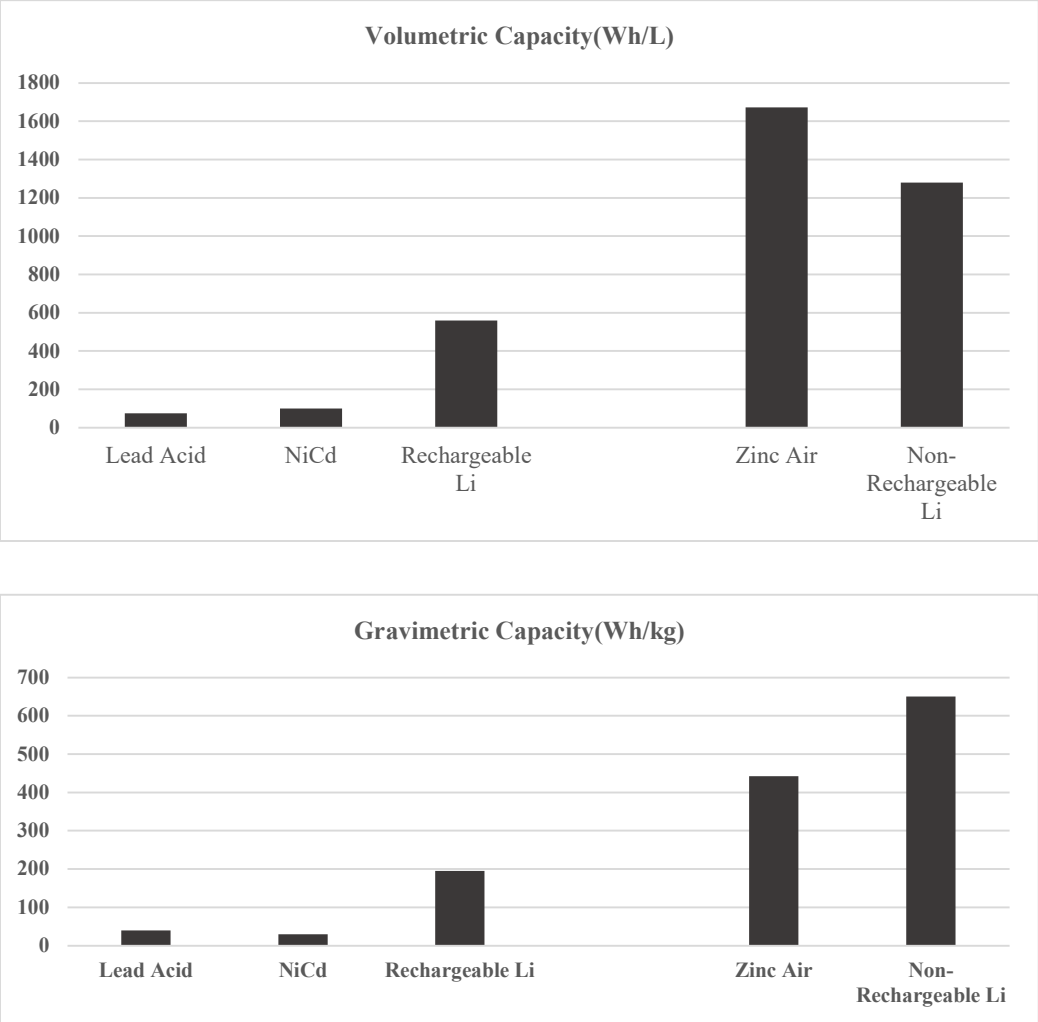

Figure 22. Comparison of primary Lithium batteries to primary and secondary chemistries with respect to volumetric and gravimetric capacity

In Li\$SOCl_2$ batteries, the anode consists of a Li (Lithium metal) foil, the cathode consists of a porous carbon, and the electrolyte is a solution of $LiAlCl_4$ (Lithium Aluminum Tetrachloride) dissolved in $SOCl_2$ (Thionyl Chloride).

The reactions that take place during discharge are:

$$Li_{(s)} \rightarrow Li^{+}_{(dis.)} + e^{-} \qquad \text{Anode reaction}$$

$$4Li^{+}_{(dis.)} + 2SOCl_{2(l)} + 4e^{-} \rightarrow 4LiCl_{(s)} + SO_{2(g)} + S_{(s)} \qquad \text{Cathode reaction}$$

$$4Li_{(s)} + 2SOCl_{2(l)} \rightarrow 4LiCl_{(s)} + SO_{2(g)} + S_{(s)} \qquad \text{Overall}$$

Looking at the overall reaction shown above, the very stable voltage response of the battery during discharge which is shown in the Figure23(a) can be understood. As can be seen, all the reactants and the products are solids or liquids which possess a unity activity except SO_2 which escapes the cell with very small leftover partial pressure. The resulting Nernst equation is then a constant cell potential as long as these reagents exist as shown below:

$$E = E^{o} - \frac{RT}{nF} ln \frac{(a_{LiCl})^4 (a_S)}{(a_{Li})^4 (a_{SOCl2})^2} = 3.6V - \frac{RT}{nF} \ln(1) = \mathbf{3.6V} \qquad \text{Nernst equation}$$

As can be seen from the cell reactions, the reaction on the cathode is irreversible because of the loss of SO_2 in addition to the complicated forms of elemental sulfur. If the reverse reaction is forced by means of a charging current, the possible charge reactions are undefined since SO_2 escapes from the cell. Spectroscopic studies for the formed species with applied currents in the charging direction showed complex reactions. Under conditions where Li and SO_2 is present, mainly SO_2Cl_2, SCl_2 or S_2Cl_2 are shown to form. Under other conditions where Li amount is small, $SOC1_2$ will be oxidized initially,

producing Cl_2 which leads to the formation of SO_2Cl_2. The charging products are all electrochemically inactive, in addition to being hard to predict.

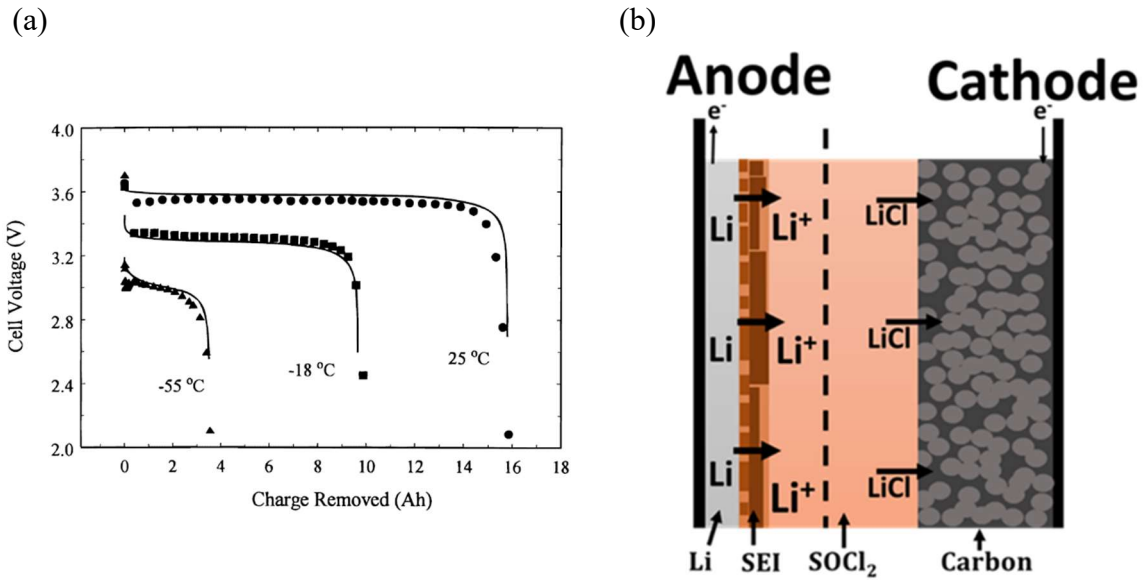

Figure 23. (a) Discharge profile of Li\$SOCl_2$ obtained with permission from [22], (b) Schematic illustration of the structure of Li\$SOCl_2$

A very important phenomenon that takes place in Li primary batteries is the formation of a passivation film at the surface of the Li anode. This film protects the Li metal from the degradation by reacting with active species which cause self-discharge of the battery. In Li\$SOCl_2$ a passivation film consisting of mostly LiCl and other Li compound forming as a result of the reaction between the metallic Li and the electrolyte $SOCl_2$. This layer forms eventually as the anode contact the electrolyte and is responsible for the stability of the Li and prevent the further reaction between the Li and the electrolyte. As we mentioned before, this layer is known among the battery community as the Solid Electrolyte Interface (SEI). It plays very important role in the operation of the cell as will be shown in this work.

The structure of the SEI in Li/$SOCl_2$ is studied in the literature. It is found that it has a two-layer structure, of mostly LiCl crystals, with thin and compact inner layer and thick outer layer. The second layer keeps growing with storage time of the battery.

In Li batteries, the most important property for the SEI is to allow the migration of the Li^+ ions with the prevention of the electrons passage. Unlike the SEI in secondary Li ion batteries in Li/$SOCl_2$, the SEI is destroyed by the migration of the Li^+ ions causing the formation of pores allowing the Li^+ to transport. The pores are closed again by the passivation reaction as the cell is left at open circuit. This dynamic formation and destruction of the SEI has an effect on the cells voltage which will be shown in the voltage modeling section.

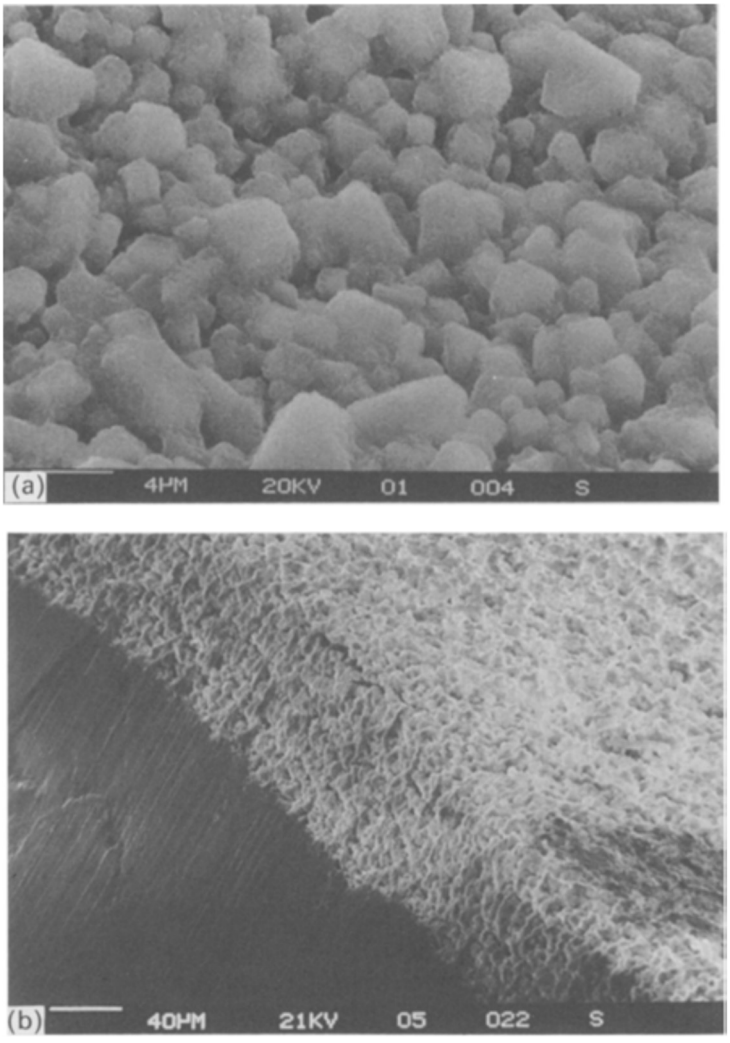

Figure 24. SEM image of the Solid Electrolyte Interface in Li\$SOCl_2$ reproduced with permission from [23]

1.6.1.2. Lithium Manganese Dioxide Primary Battery (Li/MnO_2)

Another type of Li primary battery chemistry is Lithium Manganese Dioxide (Li/MnO_2) which also possesses high energy density. However, its open circuit voltage is less than $Li/SOCl_2$. Its open circuit voltage is between 3.2 to 2.8V depending on the state-of-charge of the cell. It uses Manganese Dioxide (MnO_2) as the cathode material and organic electrolytes of $LiClO_4$ salt in propylene carbonate as electrolyte.

The cell operates by oxidation of the metallic Li at the anode and with intercalation of the oxidized Li^+ at the cathode MnO_2. The reaction of the cell is as follows:

$$xLi_{(s)} \rightarrow xLi^+_{(dis.)} + xe^- \qquad \text{Anode reaction}$$

$$xLi^+_{(dis.)} + MnO_{2(s)} + xe^- \rightarrow Li_xMnO_{2(s)} \qquad \text{Cathode reaction}$$

$$xLi_{(s)} + MnO_{2(s)} \rightarrow Li_xMnO_{2(s)} \qquad \text{Overall}$$

in which x changes from 0 to 1.

The intercalation mechanism causes the open circuit voltage to reduce due to the change in the MnO_2 valance state which is the mixture of Mn(III) and Mn(IV).

In Li/MnO_2 battery, the SEI is more stable and is formed by the reaction of the Li with the organic electrolyte. As the SEI is formed there is no evidence of dynamic behavior of demolition and growth which resembles the $Li/SOCl_2$ battery. This is due to the less reactive nature of the electrolyte.

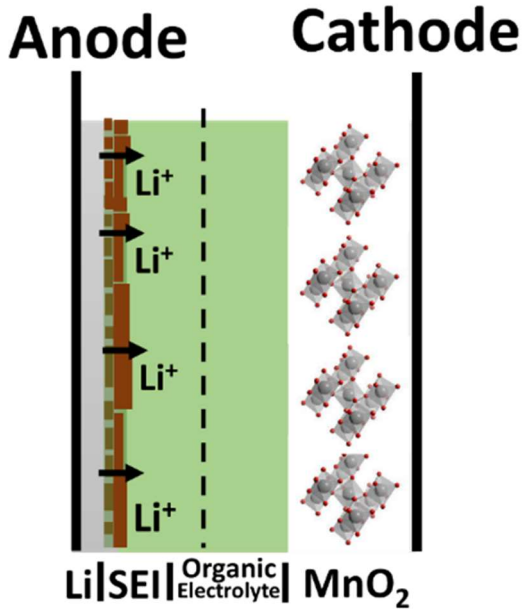

Figure 25. Schematic illustration of the structure of Li\MnO_2 battery

1.6.2. Hybrid Battery/Supercapacitor Systems

To meet the demand of various applications, combination of more than one EES is required. This combination can be done with same or with different kind of EES devices. For example, secondary Li batteries in a battery pack may be electrically connected in parallel in order to increase the pack capacity and meet requirements for power and energy. The nature of a parallel connection means that the voltage over each cell is the same and the applied current is equal to the sum of the individual cell currents. Some examples of real-life application of the parallel connection of the batteries can be found in electric vehicles. In the Tesla Model S (85 kWh) battery pack which uses 74 (3.1 Ah) cylindrical cells to create a parallel unit, and 96 of these units in series. In the Nissan Leaf (24 kWh) the battery pack consists of (33 Ah) cells, with 2 in parallel and 96 in series [24].

In all of these battery packs, the current is assumed to be equally distributed over the parallel connected batteries. However, the variations in internal impedance of the cells results in slight changes in the current distribution among the cells. Differences in current

can change the SoC, temperature, degradation rate of each cell. This means that the parallel connected cells will have different SoC despite being at the same terminal voltage and could degrade at different rates. For such reasons there is a need for a modeling method that understands the behavior of the current distribution, predict the dynamic current response and state the degradation capacity of the parallel connected cells.

Combination of EES can be also done by the hybridization of a battery with a supercapacitor in a parallel connection. This combination broadens the applicability of batteries to higher discharge rates. This is due to the high-power density of the supercapacitors. It is shown that this hybridization is more efficient in supplying the total power in usage of electronics, electric and hybrid vehicles, and uninterrupted power supplies. The emerging advantage of such connection is because supercapacitors have superior cycle efficiency under pulsed load conditions. In these kinds of situations, the supercapacitor acts as a filter or buffer that relieves peak stresses on the battery. They are very suitable for fast charge discharge cycles unlike batteries which operates under relatively slower charge discharge rates.

They have been experimentally demonstrated to exhibit longer operating times when compared to only batteries systems under repetitive high load and high current pulse conditions. These hybrid systems can be used to improve the performance of their applications such as, electric vehicles and intermittent renewable energy sources. Moreover, aiming at high energy densities together with high power densities, hybridization of Li-ion batteries with supercapacitor through parallel connection is been proposed.

The main hindrance in utilizing such hybrid systems is the lack in the understanding of the power distribution among the devices connected in parallel. In the literature, various studies proposed the use of converters and control circuits to manage the power distribution among the hybrid systems. This severely limits the application for not only the reason of added cost, but also due to the reduction in reliability and durability. The used on unmanaged systems is the correct choice to reach their full potential. Though, there is a need for accurate performance modeling methodology which can assess their performance

in realistic scenarios and predict the best combination of batteries and supercapacitor tailored to the application.

In this work, we introduce a semi-empirical modeling methodology which can predict the current distribution and the voltage response of arbitrarily chosen hybrid systems under arbitrary charge/discharge profiles. We present the results of our method validated with experimental measurements for assessment of two different Li-ion battery/supercapacitor hybrid systems under various scenarios.

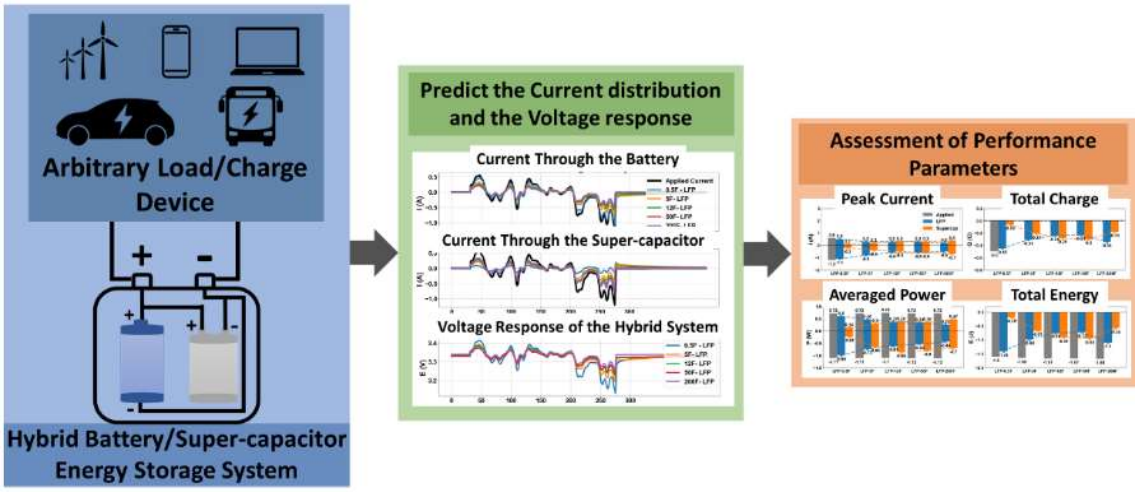

Figure 26. Performance modeling for hybrid battery/supercapacitor systems

1.7. Thesis Outline:

This thesis presents characterization and modeling methods for Li-based batteries and parallel connected battery/supercapacitor hybrid systems of secondary Li-ion batteries and supercapacitors. The thesis is divided into two parts:

In the first part, we focus on utilizing Electrochemical Impedance Spectroscopy (EIS), to deconvolute the electrochemical processes of primary Li metal-based batteries. For this purpose, Galvanostatic-EIS during discharge technique is developed to obtain linear and accurate impedance data. The data is analyzed and assigned to the electrochemical processes of the battery. Next, different electrolyte composition batteries are used to further relate the obtained data to the electrochemical processes. Moreover, temperature-dependent EIS data are obtained to study the kinetic behavior of the electrochemical processes. Finally, non-linear EIS data is analyzed and shown to correlate with the kinetics and the formation of interfaces in the battery.

In the second part, using direct and objective modeling methodology, we apply the information obtained from the EIS to model the performance of primary Li metal-based batteries. We further develop the method to simulate the behavior of hybrid battery/supercapacitor systems under various regimes. The modeling method is experimentally validated and is shown to clarify the parameters for their arbitrary combinations which is crucial in the design and the assembly of these devices.

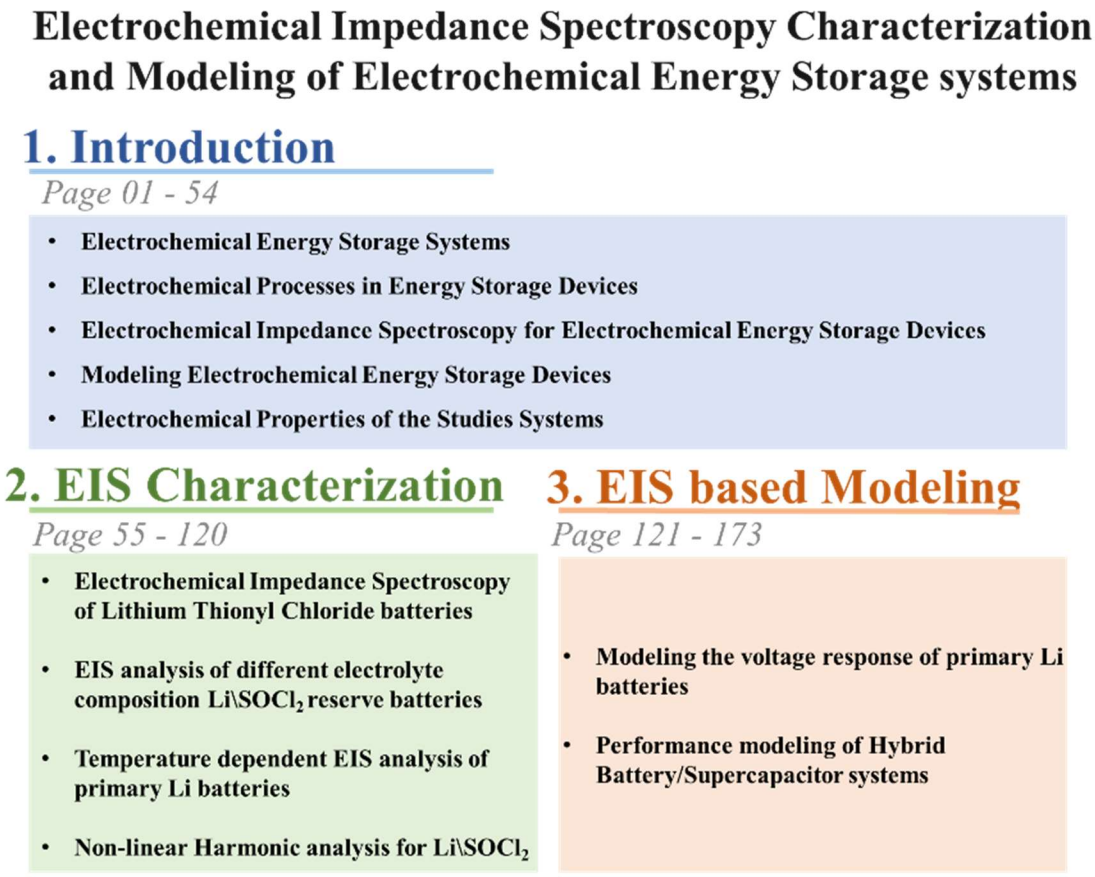

Figure 27. Outline of the thesis

Chapter 2

2. Electrochemical Impedance Spectroscopy Characterization

(This part is also described in

- **Mohammed Ahmed Zabara**, Can Berk Uzundal, and Burak Ulgut, *Linear and Nonlinear Electrochemical Impedance Spectroscopy Studies of Li/SOCl2 Batteries, Journal of The Electrochemical Society, 166 (6) A811-A820 (2019).*
- **Mohammed Ahmed Zabara**, Hasan Göçmez, Akın Karabatak, and Burak Ulgut, *Characterization of Different Electrolyte Composition Lithium Thionyl Chloride Reserve Battery by Electrochemical Impedance Spectroscopy, Journal of The Electrochemical Society, 2021, 168, 050529.*

Reproduced with permission from [25] and [26] from the Journal of the Electrochemical Society, Copyright 2021)

Metallic Li anode batteries possess higher gravimetric and volumetric energy densities compared to Li-ion counterparts. As discussed in chapter 1, Li metal utilization faces several challenges due to unwanted electrochemical processes. Studying and understanding these processes plus the mechanisms taking place at the different interfaces of metallic Li batteries is crucial for overcoming these challenges. Electrochemical Impedance Spectroscopy (EIS) is a powerful, in-situ and non-invasive technique which can be utilized to study these processes.

In this chapter, we will show EIS characterization results for primary Li batteries which use metallic Li as anode. The EIS data is used for modeling studies and for understanding the electrochemical processes of the batteries. Detailed experiments are performed with different types, sizes and geometries of commercial cells, custom made cells, and with temperature-dependent variables.

2.1. Electrochemical Impedance Spectroscopy for Primary Lithium Thionyl Chloride (Li\SOCl$_2$) Battery

Performing accurate and linear Electrochemical Impedance Spectroscopy (EIS) for primary batteries is challenging. The difficulty arises from two reasons:

The first is from the irreversible operation chemistry which lacks well defined charging reaction. EIS is typically performed by exciting the system symmetrically with either a current or potential perturbation around the equilibrium point and measuring the response to such excitation. For batteries, in particular, this requires the applied perturbation signal to oscillate between charge and discharge constantly at different frequencies. For primary batteries, as the experiment proceeds, the discharge side of the experiment decreases the state-of-charge (SoC), where the charge side of the experiment causes undefined reactions. Therefore, the current on the discharge side leads to non-stationarity and the current on the charge side causes non-linearity in the EIS data.

The second, which is seen mostly in metallic Li anodes, is the unstable nature of the Solid Electrolyte Interface (SEI). The use of metallic Li results in the formation of a passivation layer named SEI. Its formation is caused by the spontaneous chemical reaction between Li and electrolyte $SOCl_2$ which starts as soon as they contact. Studies showed the formation of a compact layer right at the electrolyte/Li interface followed by a thicker and denser layer which slowly forms during storage [27][28]. This two-layer structure passivates the anode from further reactions with the electrolyte and helps in its stabilization. However, the passivation layer has drawbacks in the performance of the battery. Unlike the SEI in secondary Li-ion batteries, the thicker part of the passivation layer in Li\$SOCl_2$ demolishes by forming cracks as the cell discharges, allowing the Li to reach the electrolyte, and re-forms again at open circuit [29][30]. This behavior is reflected on the voltage behavior of the battery by causing voltage delay behavior at discharge and recovery after the discharge. This causes the instability in the EIS measurements especially at slow part of the spectrum.

In the literature, there are studies which present EIS data for Li\$SOCl_2$ battery which lacks validation and accuracy. The first publication regarding an impedance study for a complete cell is presented by Hughes et al. [31]. The conditions in which the impedance measurement was performed was mentioned to be galvanostatic in the range of 10 kHz to 1 Hz. Neither values of the excitation signal, nor any DC level were specified. The presented impedance data suffers from clear deviations from ideal behavior in low frequency regions. The presented equivalent circuit model failed to fit the experimental data at the low end of the rather narrow frequency window.

Other studies in the literature utilized Potentiostatic-EIS technique. Popov et al. studied the impedance of the passivation layer at different storage times [32]. The voltage excitation was mentioned to be ±5 mV in amplitude in a frequency range of 10 kHz to 10 mHz. Another study done by Walsh et al. which studied the impedance of the passivation layer to predict the voltage drop in the cell [33]. The excitation signal was ±10 mV and the frequency window between 20 kHz and 50 mHz. The impedance data presented in both studies were dominated by the impedance of the passivation layer and showed an increase as the degree of passivation increased. In both studies, no EIS response was present for the other electrochemical processes.

It should be mentioned that Potentiostatic-EIS cannot provide accurate impedance results for Li\$SOCl_2$ battery, and primary batteries in general, since any positive deviation from the equilibrium would cause undefined reactions that do not represent the operation chemistry of the cell. Moreover, there is no known procedure for getting rid of the passivation layer. The passivation reaction would constantly take place during the measurement.

In order to obtain accurate and linear EIS result at wide range of frequencies, the mentioned two issues should be overcome. First, the impedance measurement has to be done in the discharge mode to ensure that the current does not venture into the ill-defined, irreversible charge reactions of the system. Second, due to the passivation affecting the cell voltage responses, passivation layer should be stabilized before the impedance measurement and should be prevented from re-forming while the measurement is taking place. These conditions can be met by performing Galvanostatic-EIS under discharge.

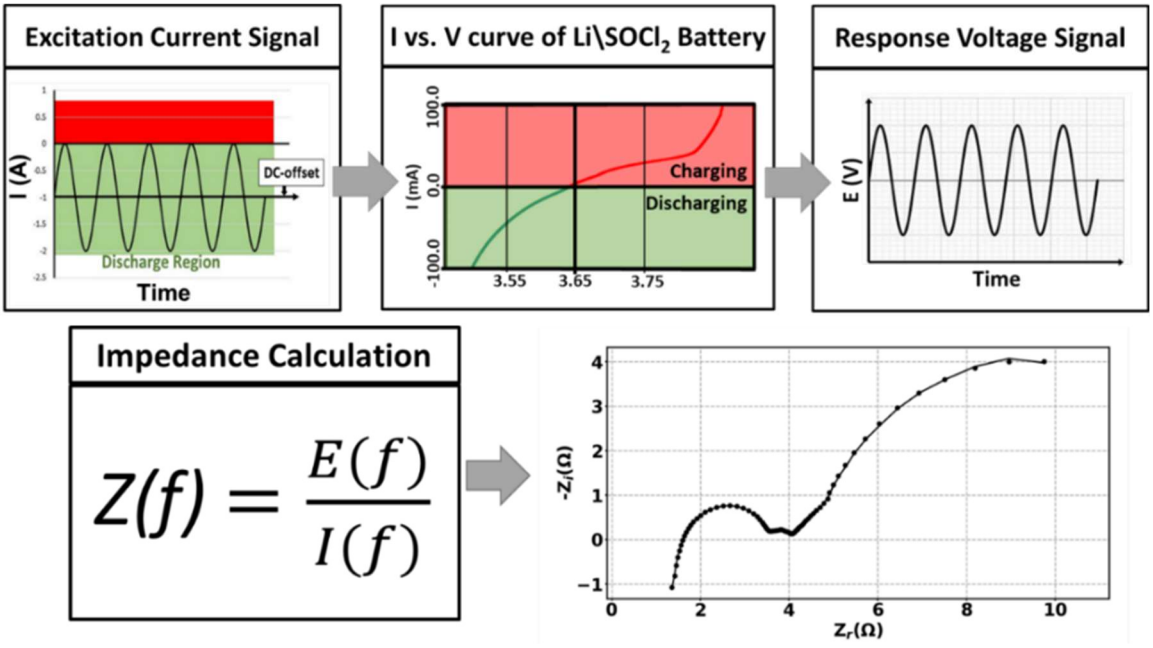

Figure 28. Illustration of Galvanostatic-EIS measurement at discharge which includes the application of a negative DC-offset along the AC excitation

In Galvanostatic-EIS, the excitation Alternating Current (AC) signal is applied along with a negative Direct Current (DC) offset which ensures that no charging currents are imposed on the system. The value of the discharging DC offset is also adjusted to a value that prevents formation of the passivation layer during the measurement.

2.1.1. Galvanostatic-Electrochemical Impedance Spectroscopy at Discharge

In our measurements, we applied a DC-offset along with the AC excitation signals in a Galvanostatic EIS mode. The value of the negative DC offset and the AC excitation were adjusted to ensure no charging currents are imposed on the cell. The values of both DC and AC were adjusted by trial and error until linear and stable data were obtained. Kramers-Kronig compatibility test was used to check for the linearity and the stability. The data was obtained using Gamry Interface 1000E in a frequency window of 10kHz to 1mHz with 10 points per decade or 5 point per decade for D-size cells and a frequency window of 10kHz to 4mHz with 5 points per decade for AA-size cells.

In order to stabilize the passivation layer and hence the voltage of the cell during the measurement, a DC discharge of the same DC offset magnitude was applied before the measurement. The EIS measurement was conducted directly after applying the discharge. Furthermore, a 30 second hold period was applied between the frequencies with the negative DC offset of the measurement to further stabilize the voltage during the measurement.

The cells used in our study were commercially available Li\$SOCl_2$ (SAFT-LSH20) D-size spiral cells and (SAFT- LS 14500) AA-size bobbin cells [34]. The D-size spiral cell has 13Ah capacity with 3.67V open circuit potential and the AA-size bobbin cell has 2.6Ah capacity with 3.67V open circuit potential. The Maximum Recommended Continuous Currents were 1800mA and 50mA for D-size and AA-size respectively. The negative DC offset and the discharge currents were assigned not to exceed these values.

2.1.2. Electrochemical Impedance Results

In conventional EIS measurement, the AC amplitude is the only parameter which influence the results of the measurement. However, in the used technique the DC-offset plays important role in the obtained data. Figure 29 shows the Nyquist diagrams of the obtained EIS data for both D-size and AA-size at three different DC offsets. The frequency range is between (10 kHz – 1 mHz) for the D-size cell while (10 kHz – 4 mHz) for AA-size cell.

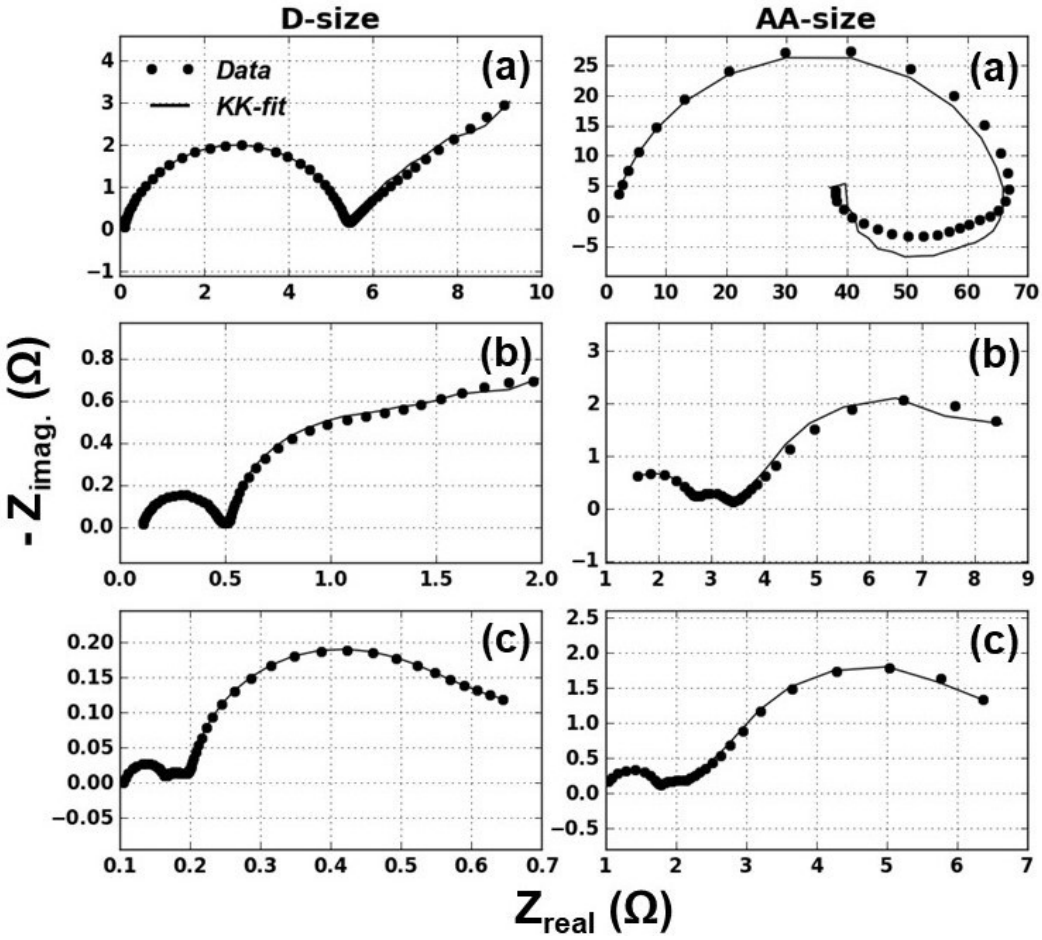

Figure 29. Nyquist diagrams of $LiSOCl_2$ D-size and AA-size cells while discharge with three DC offsets. D-cell (DC offset, AC excitation): a) (-2 mA, 1mA), b) (-10 mA, 5mA) and c) (-50 mA, 5mA). AA-cell (DC offset, AC excitation): a) (-0.5 mA, 0.2mA), b) (-5 mA, 2mA) and c) (-10 mA, 2mA)

In Figure 29 the top two diagrams (shown in a) are for low offset measurements with (-2mA DC, 1mA AC) for D-size cell and (-0.5mA DC, 0.2mA AC) for AA-size at 100% SoC. The middle two diagrams (shown in b) are for moderate offset (-10mA DC, 5mA AC) for D-size and (-5mA DC, 2mA AC) for AA-size cell at 100%SoC. The bottom diagrams (shown in c) are for high offset measurements with (-50mA DC, 5mA AC) for D-size and (-10mA DC, 2mA AC) for AA-size cell at 98% SoC.

In order to study the effect of the passivation layer on the impedance, the layer was not treated for the low DC offset measurements (Figure 29-a) and was treated by discharge prior to EIS measurement for the other two with higher DC offset measurements (Figure 29-b&c). There is a clear difference in the impedance characteristics among the measurements with and without treatment for the passivation layer for either cell. This difference can be related to the high impedance of the passivation layer which dominates over other processes.

The Nyquist diagrams for the passivated cells (Figure 29-a) show comparatively larger impedance values than the de-passivated ones (Figure 29-b&c) with Kramers-Kronig incompatible regions at the lower frequencies. The regions that are incompatible with the Kramers-Kronig relations can be due to the non-linearities or in-stabilities caused by the formation reactions of the passivation layer. However, the high frequency region is compatible with the Kramers-Kronig relations for all cases.

Treatment of the passivation layer by discharge before the measurement causes a decrease in the impedance values as can be seen from Figure 29. Applying higher DC offsets during the measurement was necessary to prevent passivation layer formation during impedance measurement. Nyquist diagrams for the case of no passivation and moderately higher offsets are shown in Figure 29-b. The compatibility with Kramers-Kronig transform is better for these offsets but still deviate at the very low frequency regions. This deviation shows nonlinearity or instability effects of the passivation layer that forms during measurement at this frequency region. Unlike the passivated cells (Figure 29-a), the Nyquist diagrams for the de-passivated cells (Figure 29-b&c) show more than one time-constant region that is compatible with the Kramers-Kronig relations.

Increasing the magnitude of the DC negative offset causes the appearance of three time-constants and shows excellent compatibility with the Kramers-Kronig relations for the full frequency range as shown in Figure 29-c. The first semicircle at the high frequency region between 10kHz and 250Hz, the middle semicircle at mid frequencies between 250Hz and 1Hz, and the third semicircle at the low frequency region between 1Hz to 1mHz. These three semicircles could not be resolved in the previous measurements due to the dominant passivation effects.

2.1.3. Equivalent Circuit Analysis

In order to extract the electrochemical parameters and relate the obtained time constants to the electrochemical processes of the Li\$SOCl_2$ battery, we employed equivalent circuit modeling analysis. We used Constant Phase Elements (CPE) connected to a parallel resistor to represent each time constant of the electrochemical process. A series solution resistor was connected to the three parallel CPE//Resistor circuits. The equivalent circuit is shown in Figure 30(a). The first constant phase element which is dependent on the DC offset is assigned to the process of the SEI which involves the transport of the Li ions through the SEI. The second which shows the smallest impedance values is related to the anodic charge transfer process which is Li oxidation. And the last which has the highest impedance is related to the adsorption of the cell's reaction products on the highly capacitive porous carbon.

(a)

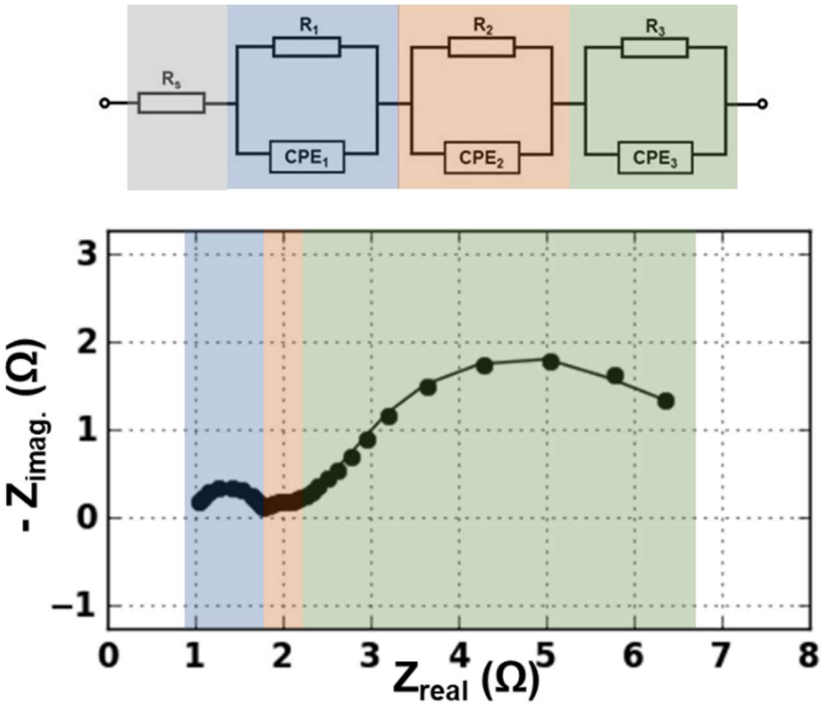

(b)

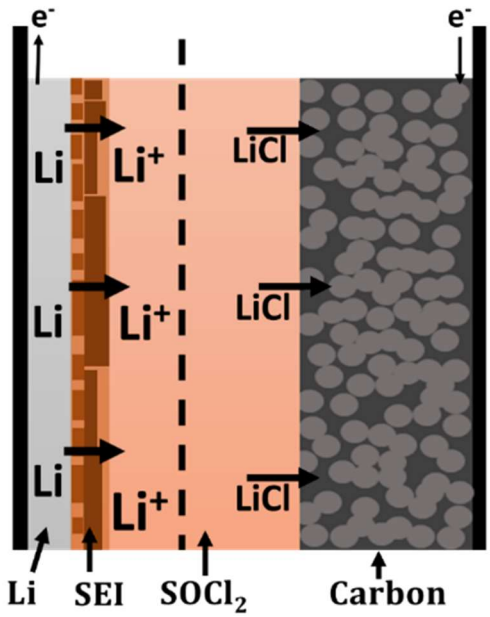

Figure 30. (a) Equivalent circuit model and the Nyquist plot for linear EIS data of Li\$SOCl_2$ battery, (b) Schematic representation of the electrochemical processes of Li\$SOCl_2$ battery

2.1.4. EIS Analysis at Different States-of-Charge

The change in impedance at different SoCs was also investigated. The changes in the parameters of the equivalent circuit models by changing the SoC gave better insight on the behavior of the processes of the battery. The changes can enable us to make speculations about the nature of these three semicircles and their relations to the chemistry of the cell.

Figure 31 shows the EIS vs. %SoC for Li\$SOCl_2$ (100% - 20% SoC) D-size cell and (100% - 45% SoC) AA-size cell. D-size cell measurements were done with (-50mA) DC offset and (5mA) AC while AA-size were with (-10mA) DC offset and (2mA) AC excitation. The frequency range was from 10 kHz to 1 mHz for D-size and 10kHz to 4mHz for AA-size with 5 points/decade for both. D-size cell was discharged with (-300 mA) and AA-size with (-50mA) between the measurements to reach the desired %SoC. These discharge current values allowed for the discharge of the D-size cell until 20 %SoC and 45 %SoC for the AA-size cell. Discharging the cells further resulted in a fast voltage drop below 3.0V indicating the fully discharged state of the cells.

It can be seen from Figure 31 that for both D-size and AA-size cells, the three time-constants appear at all SoCs with differences in size at different SoCs. At 100% SoC the first semicircle at the high frequency region is the largest which shrinks as the SoC decreases. The second semicircle at the middle frequency region on the other hand, is the smallest at 100% SoC and grows by discharging the cell. The size of the third semicircle stays almost constant and decreases at the lower SoCs.

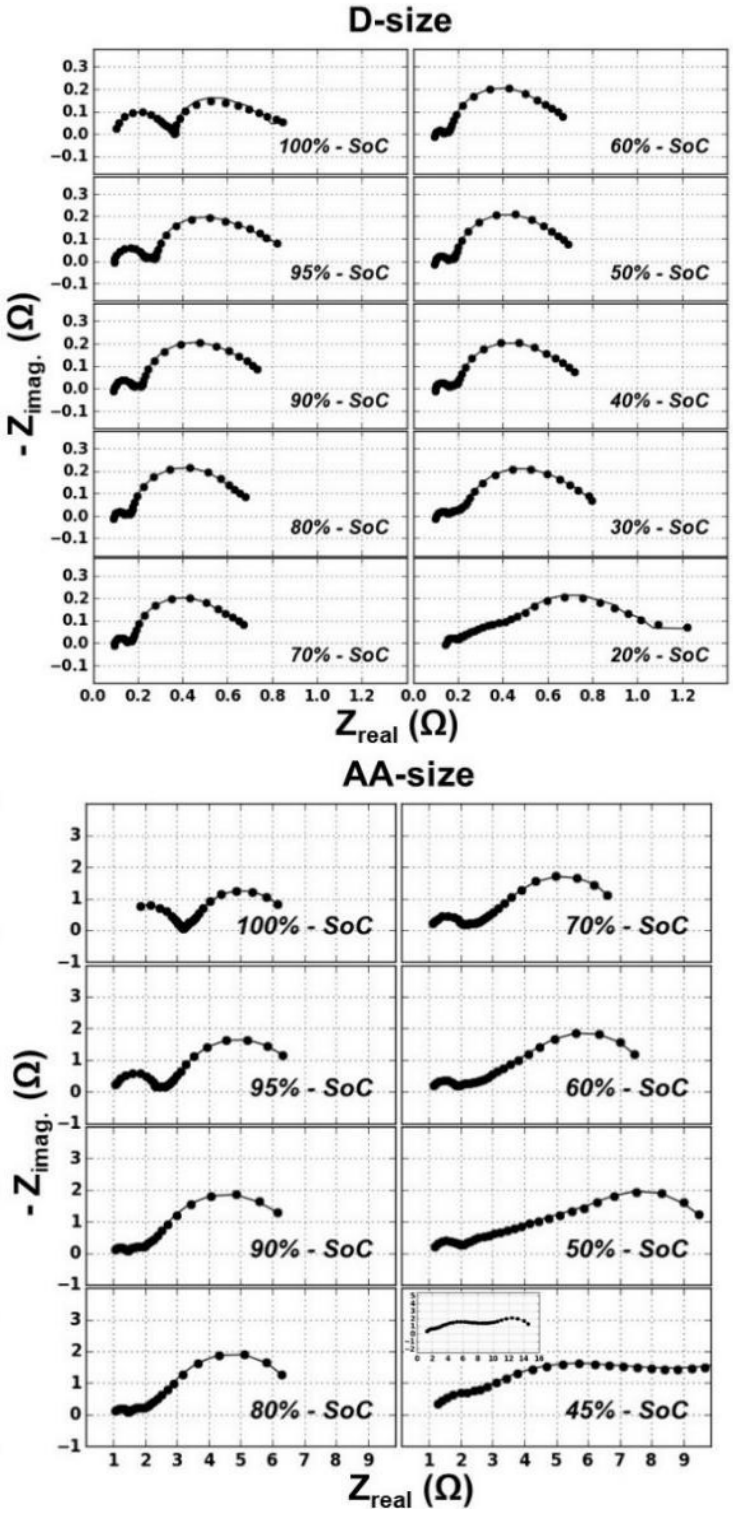

Figure 31. Nyquist diagrams for Li\$SOCl_2$ at different SoCs with Kramers-Kronig compatibility for D-size cell and AA-size cell

For equivalent circuit modeling at different SoC, the values of the model components with their errors are listed in Tables 1 and 2. Figure 32 shows the behavior of the model components vs. SoC with their errors.

Starting from the fully charged state, the electrolyte resistance of the D-size cell was around 100mΩ until 40% SoC which then gradually increased up to 150mΩ at 20% SoC. In the case of the AA-size cell the resistance was around 1.1Ω at the early SoCs and similarly increased to 1.6Ω after 60% SoC. This increase is expected by the depletion of the electrolyte with the discharge of the cell and accumulation of the reaction products.

The values of the parallel resistance of the first semicircle, which lies at the high frequency region, decreases at the first stages of discharge and later shows a constant behavior. At the same time the capacitance increases as the cell discharges. This behavior can be related to the compact Solid Electrolyte Interface (SEI) at the anode which degrades as the cell is discharged, resulting in the drop in the resistance and increase in the capacitance.

On the other hand, the values of the third semicircle, which is found in the low frequency region, shows an increase in the charge transfer resistance and a decrease in the capacitance with discharging the cell. Moreover, the capacitance shows larger values than the other two semicircles. This behavior can be related to the highly porous carbon cathode which adsorb the products of the cell reaction as the cell discharges. The cathode surface area decreases as a result of the adsorption causing a decrease in the capacitance.

Finally, the middle semicircle which shows a gradual decrease followed by an increase in its parallel resistance and an increase in the capacitance followed by gradual decrease, can be related to the Li anode. The consumption of Li as the cell discharges causes a small decrease in the charge transfer resistance at the earlier stages. As the consumption continues, small amounts of Li are left at the later stages resulting in an increase in the charge transfer resistance. The capacitance on the other hand, increases due to the increase in the Li morphology as the cell discharges. The increase in morphology causes high surface area and thus higher capacitance. However, as the cell discharges Li quantity decreases resulting in the observed capacitance decrease.

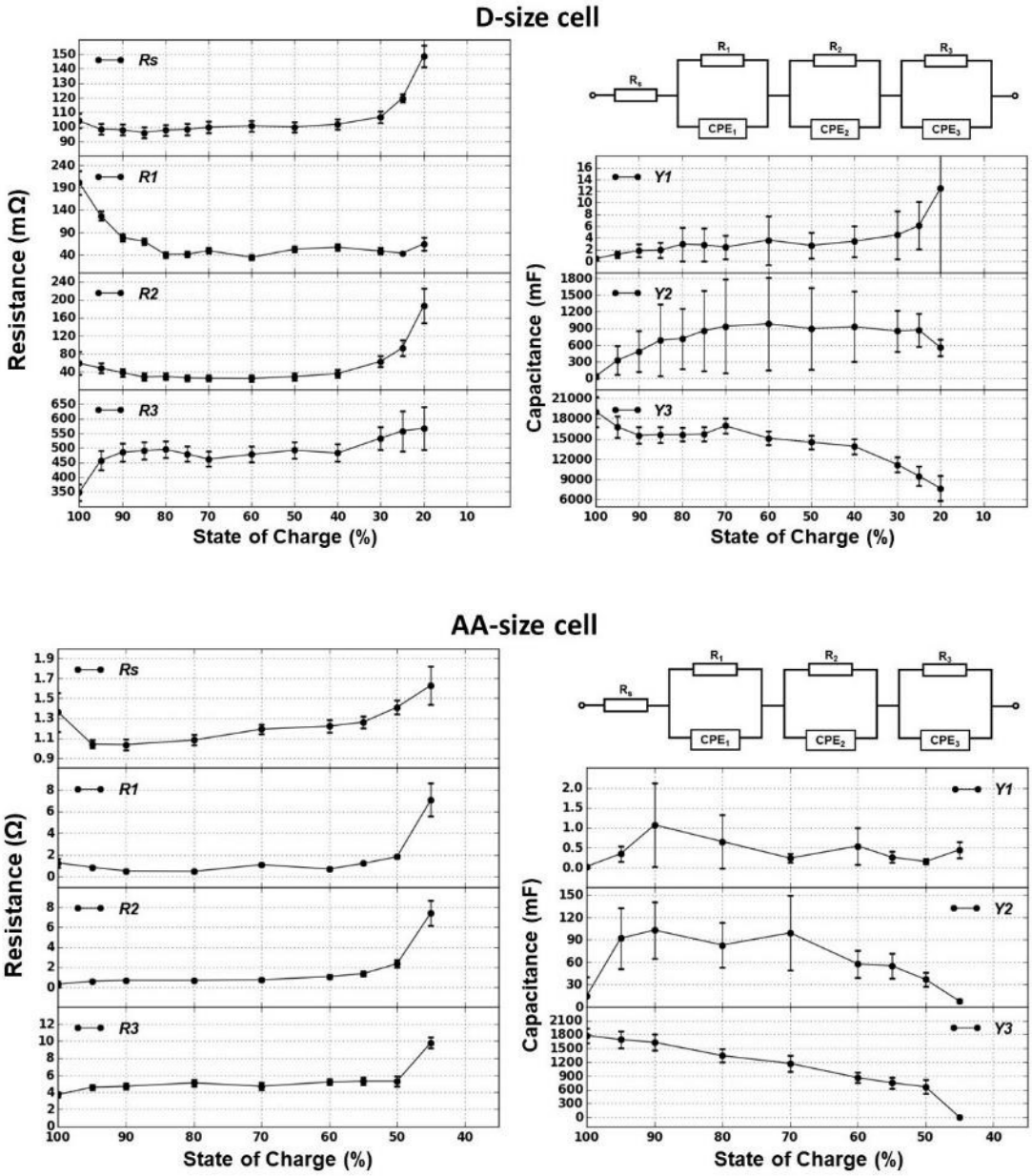

Figure 32. Equivalent circuit model and its components (R_s, R_1, Y_1, R_2, Y_2, R_3, Y_3) vs. SoC for D-size and AA-size cell

Table 1. Parameters of the equivalent circuit model between 100 – 20 %SoC for D-size

%SoC	R_s(mΩ)	R_1(mΩ)	Y_1(mF), α_1	R_2(mΩ)	Y_2(mF), α_2	R_3(mΩ)	Y_3(F), α_3
100	104.1	200.9	0.4, 1.00	58.5	41.2, 0.93	347.3	19.0, 0.93
95	98.5	127.1	1.2, 1.00	47.6	327.1, 0.90	457.2	16.7, 0.91
90	98.0	78.3	1.8, 1.00	37.8	488.4, 0.90	485.0	15.5, 0.90
85	96.1	70.3	1.9, 1.00	27.9	689.2, 0.90	490.6	15.6, 0.91
80	97.8	40.9	2.9, 1.00	29.3	715.7, 0.90	494.7	15.6, 0.92
75	98.3	41.3	2.8, 1.00	25.8	857.0, 0.90	479.3	15.6, 0.92
70	99.8	49.4	2.4, 1.00	25.1	937.9, 0.90	461.5	16.9, 0.92
60	100.7	34.5	3.6, 1.00	24.7	981.7, 0.90	477.4	15.0, 0.90
50	100.0	52.7	2.7, 1.00	28.7	898.1, 0.90	492.1	14.4, 0.90
40	101.8	57.0	3.4, 0.97	35.4	930.4, 0.90	482.3	13.8, 0.90
30	106.8	48.4	4.5, 0.96	62.6	851.6, 0.85	533.2	11.1, 0.85
25	119.6	43.9	6.1, 0.94	92.3	871.2, 0.80	557.9	9.4, 0.80
20	148.7	64.3	12.5, 0.82	186.8	553.9, 0.80	567.3	7.6, 0.80

Table 2. Parameters of the equivalent circuit model between 100 – 45 %SoC for AA-size

%SoC	$R_s(\Omega)$	$R_1(\Omega)$	$Y_1(\mu F)$, α_1	$R_2(\Omega)$	$Y_2(mF)$, α_2	$R_3(\Omega)$	$Y_3(F)$, α_3
100	1.36	1.26	27, 0.97	0.29	14.9, 0.75	3.7	1.78, 0.75
95	1.04	0.86	346, 0.87	0.58	91.9, 0.75	4.6	1.69, 0.79
90	1.04	0.52	1070, 0.78	0.67	102.9, 0.80	4.7	1.63, 0.80
80	1.08	0.48	654, 0.84	0.67	82.9, 0.75	5.1	1.34, 0.75
70	1.19	1.09	236, 0.89	0.72	99.2, 0.75	4.7	1.17, 0.75
60	1.22	0.70	541, 0.82	1.05	57.6, 0.75	5.2	0.86, 0.75
55	1.26	1.21	261, 0.86	1.34	55.0, 0.75	5.3	0.75, 0.75
50	1.41	1.82	152, 0.87	2.33	36.8, 0.75	5.3	0.66, 0.75
45	1.63	7.07	446, 0.75	7.44	7.7, 0.75	9.8	0.001, 0.75

2.1.5. Section Conclusion

Galvanostatic-EIS at discharge for Li\$SOCl_2$ primary batteries results in accurate, linear and stable impedance spectra. It is based on applying a negative DC offset along with the AC excitation signal such that the total current is always negative. The obtained EIS data is a function of the DC offset. High DC offset must be applied during the measurement to minimize the hindrance of the transport of the Li-ions by the SEI. The obtained impedance spectrum between 10kHz and 1mHz showed three time-constants which appeared as three distorted semicircles in the Nyquist plot. Utilizing equivalent circuit model, each semicircle was fit with a charge transfer resistance and a constant phase element. The change in the fitted parameters was investigated by changing the State-of-Charge of the batteries.

As can be seen the correct employment of EIS technique provides insight about the nature of the electrochemical processes of the battery. The analysis with equivalent circuit modeling and with Stat-of-Charge variation determine the nature of the processes and their contributions. However, the assignment here was made with some speculation which required further experimentation and analysis. In the next sections, we will investigate the variation of the EIS data with changing the composition of the electrolyte which will eliminate the speculations and help in assigning the obtained time constants to their corresponding processes.

2.2. Characterization of Different Electrolyte Composition Lithium Thionyl Chloride (Li\SOCl$_2$) Reserve Batteries

In this section, aiming at elucidating the Electrochemical Impedance Spectroscopy (EIS) data and eliminate the speculations used in assigning the electrochemical processes to the time constants obtained, we performed detailed EIS analysis for Li/$SOCl_2$ reserve batteries with two electrolyte compositions. Two cells are used with different electrolyte compositions. The first is made of 100% Thionyl Chloride $SOCl_2$ electrolyte and the second of 75% Thionyl Chloride $SOCl_2$ plus 25% Sulfuryl Chloride SO_2Cl_2 mixture of electrolytes. In both cells, all other components were identical. Through these variations in electrolyte, analysis of the time constants of the EIS data and Equivalent Circuit modeling is performed.

2.2.1. Li\SOCl$_2$ Reserve Battery

The batteries used in this study are Li\$SOCl_2$ reserve primary batteries produced by PILTEK Energy Systems Co. (Ostim Science Park, Ankara/Turkey) with model name 10-10-01 shown in Figure 33(a). Reserve batteries are special purpose primary batteries in which electrolyte is stored separately from the electrodes. Battery can be activated by breaking the ampoule storing the electrolyte. This floods the active cell compartment with electrolyte. Until the activation, battery remains inactive without any ion transfer between electrodes which eliminates capacity loss during shelf life. PİLTEK 10-10-01 model reserve batteries are single cell type battery and liquid electrolyte is stored in breakable glass ampoule. Battery is activated by breaking the ampoule. Two reserve batteries were studied with identical components except for the electrolyte composition inside the ampoule. In the first cell, the electrolyte inside the ampule was filled with 100% Thionyl Chloride ($SOCl_2$). In the second cell, the electrolyte was filled with 75% Thionyl Chloride ($SOCl_2$) and 25% Sulfuryl Chloride (SO_2Cl_2). For the measurement, activation of the cells was achieved by breaking the ampoule which resulted in a jump in the potential of the batteries which is shown in Figure 33 (b and c).

Table 3. Chemical properties of the two electrolytes used

	Thionyl Chloride	*Sulfuryl Chloride*
Boiling point (°C)	79	69
Density at 20°C (kg/m^3)	1.64	1.67
Dielectric constant at 20°C (F·m^{-1})	9.3	10

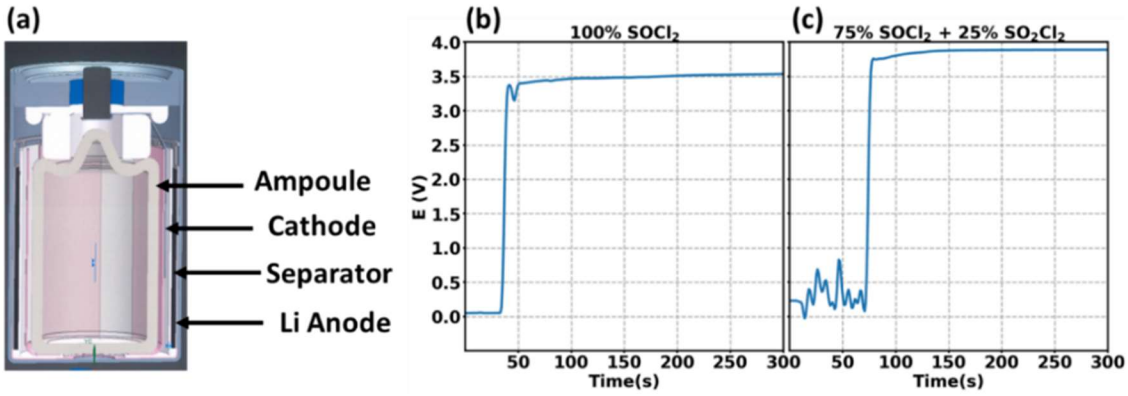

Figure 33. (a) Cross sectional view of PİLTEK 10-10-01 model battery, representing ampoule, Lithium anode layer, separator and other supporting structures. Potential vs. time plots for the reserve battery during activation for (b) 100% $SOCl_2$ electrolyte cell and (c) 75% $SOCl_2$ plus 25% $SO2Cl_2$ mixture electrolyte cell.

2.2.2. Experimental Aspects

Galvanostatic-Electrochemical Impedance Spectroscopy at discharge was employed by Gamry Interface 5000E. EIS was measured at least 24h after the activation of the reserve battery. This duration was necessary for the cells to reach equilibrium and for the open circuit potential to stabilize. After 24h, the open circuit potential for the 100% $SOCl_2$ cell was 3.65V and for the 75% $SOCl_2$ plus 25% SO_2Cl_2 cell was 3.86V. Galvanostatic-EIS

was measured by excitation with Alternating Current (AC) signal on top of a negative Direct Current (DC) signal. The value of the AC and DC signals for 100% $SOCl_2$ cell were 1mA AC and -5mA DC and for the 75% $SOCl_2$ plus 25% SO_2Cl_2 cell were 1mA AC and -7mA DC. These values were assigned by trial and error on bases of compatibility with Kramers-Kronig test. To achieve a more stable potential during the EIS measurement, the cells were discharged for 1 minute with the same DC values applied at the EIS measurement. The frequency window for both cells was between 1MHz to 4mHz with 10 points measurement per decade. The obtained EIS data were tested for linearity and stability by Kramers-Kronig compatibility using the software Gamry Echem Analyst.

2.2.3. Electrochemical Impedance Spectroscopy Results

EIS data for the 100% $SOCl_2$ electrolyte cell measured under two DC-offsets (low = -1mA and high = -5mA) is shown in Figure 34(a). The blue points data is for the measurement done under low DC-offset in which the Li-ion transport through the SEI is hindered. The response for this process appears to have large impedance with large semicircle at the high frequency range and instable response after 100Hz. The red points data is for the same cell but with a high DC-offset measurement which shows a large decrease in the size of the high frequency semicircle. The decrease in the size can be correlated to the easing of Li^+ ion transport though the SEI.

It is also clear that other electrochemical phenomena related to the anode and cathode charge transfer are observed while it is not the case in the low DC-offset. The black curves in Figure 34(a) denote the Kramers-Kronig compatibility of the data. It can be seen that the data for the low DC-offset is compatible at the high frequency range but gives unstable response after 100Hz. Though for the high DC offset data Kramers-Kronig is compatible for all the frequency range.

For 75% $SOCl_2$ + 25% SO_2Cl_2 electrolyte mixture cell, the EIS data are shown in Figure 34(b). Although the behavior is similar to the 100% $SOCl_2$, in which the SEI dominates the impedance response and hinders the kinetics of the cell, the shapes of the semicircles

at the high frequency is different from 100% $SOCl_2$ cell. Here the SEI impedance show two overlapped semicircles indicating the presence of more than one layer. This two semicircles structure is present in both high and low DC-offset data.

For the analysis of the linear high DC-offset data, the overlay of the Kramers-Kronig transformable EIS of 100% $SOCl_2$ electrolyte and 75% $SOCl_2$ + 25% SO_2Cl_2 electrolyte cells is shown in Figure 35. The main distinction is seen at the high frequency region, between 1MHz to 625Hz for 100% $SOCl_2$ cell and 1MHz to 160Hz for 75% $SOCl_2$ + 25% SO_2Cl_2 cell. The 100% $SOCl_2$ cell shows one semicircle indicating the presence of one time constant for charge transfer process or a coating layer whereas, the 75% $SOCl_2$ + 25% SO_2Cl_2 cell shows two semicircles which shows the presence of two charge transfer processes or two layers.

(a)

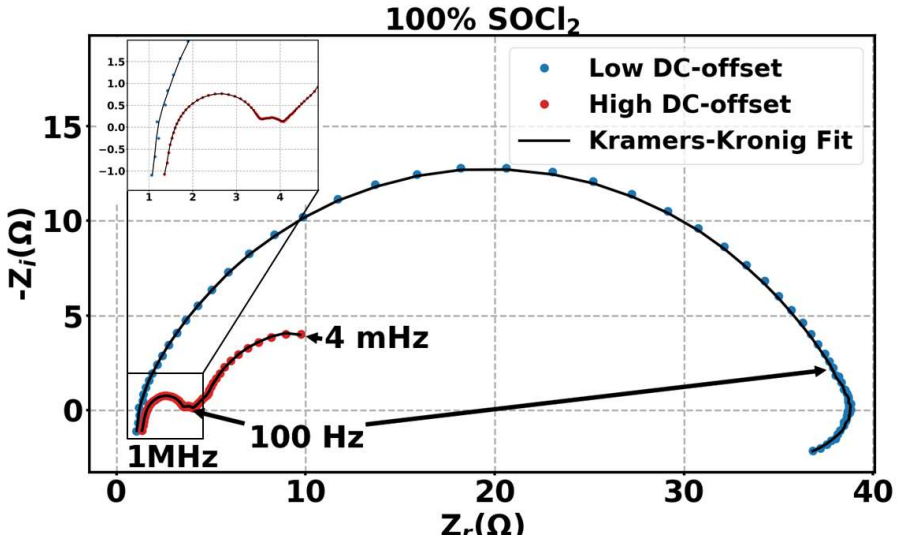

(b)

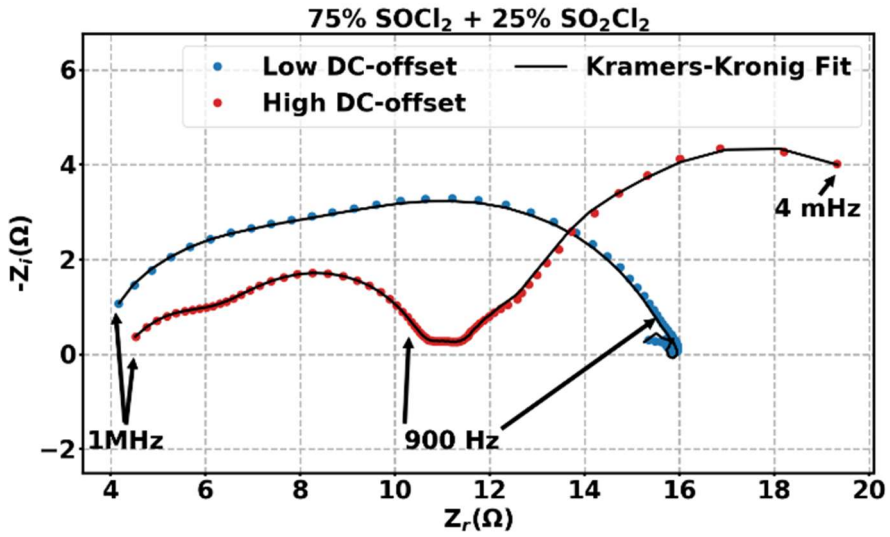

Figure 34. EIS Nyquist plots for the Li/$SOCl_2$ reserve batteries at low and high DC-offset values for (a) 100% $SOCl_2$ electrolyte with DC-offset values (low=-1mA and high=-5mA) and (b) 75% $SOCl_2$ + 25% SO_2Cl_2 electrolyte with DC-offset values (low=-5mA and high=-7mA)

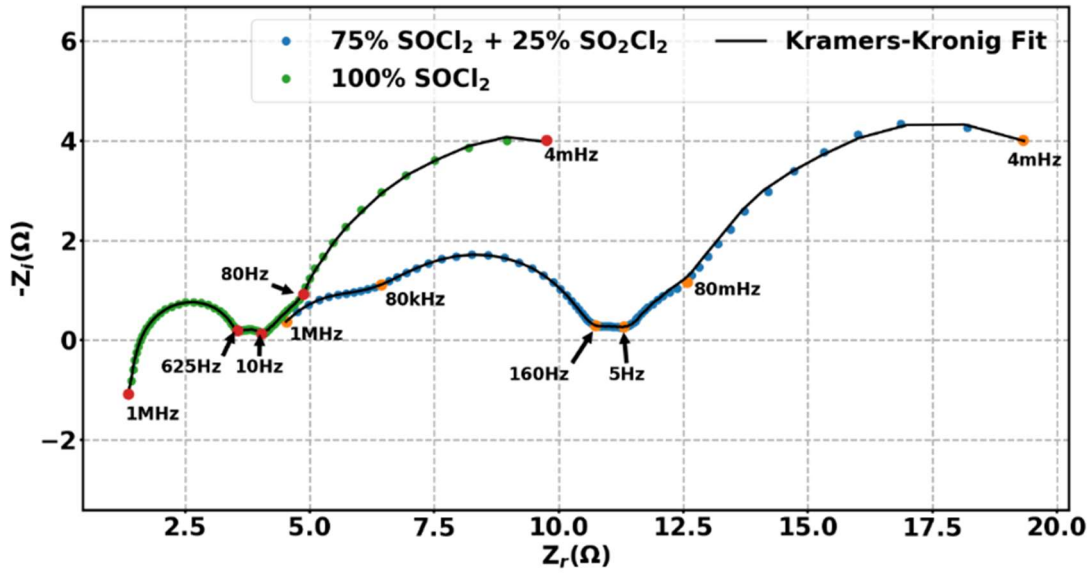

Figure 35. EIS Nyquist plots for the Li/$SOCl_2$ reserve batteries with different electrolyte compositions between 1MHz and 4mHz tested with Kramers-Kronig compatibility

In the literature, many EIS studies including our previous study for the EIS of the Li/$SOCl_2$, suggest that the high frequency time constants belong to the presence of the SEI [35][36]. The data shown in Figure xx support this in which we expect one layer to form for the 100% $SOCl_2$ electrolyte and two layers for the 75% $SOCl_2$ + 25% SO_2Cl_2 electrolyte. The two layers structure can be rationalized by the products formed from the reaction of the metallic Li with the electrolyte mixture. Spectroscopic studies suggest that the passivation reaction of the Li with $SOCl_2$ forms LiCl crystals and SO_2 gas as shown in the following equation [37]:

$$4Li_{(s)} + 2SOCl_{(l)} \rightarrow 4LiCl_{(s)} + SO_{2(g)}$$

In the case of the passivation reaction of Li with SO_2Cl_2 the reaction is assigned to produce different products besides LiCl. As shown in below equations products such as $Li_2S_2O_4$ and Li_2SO_4 are detected at different rates [30]. These products can be related to the formation of two layers in 75% $SOCl_2$ + 25% SO_2Cl_2 electrolyte cells.

$$6Li_{(s)} + 2SO_2Cl_{2(l)} \rightarrow 4LiCl_{(s)} + Li_2S_2O_{4(s)}$$

$$6Li_{(s)} + 2SO_2Cl_{2(l)} \rightarrow 4LiCl_{(s)} + Li_2SO_{4(s)} + S.$$

The other time constants in Figure xx show similar behavior in both cells with small semicircle at the middle frequency region between 650Hz and 10Hz for 100% $SOCl_2$ and 160Hz to 5Hz for $Li_2S_2O_4$ and Li_2SO_4 cell. This small semicircle can be related to the charge transfer at the Li anode (Li oxidation). The difference in frequencies can be related to the effect of the formed SEI on the charge transfer process at the anode. In the two layers structure the time constant appears at lower frequencies due to the high impedance of the SEI which slows down the anode reaction.

At the low frequency region both cells give identical response with two overlapping semicircles. The first is from 5Hz to 80mHz which can be related to the cathodic reaction charge transfer. The second is from 80mHz to 4mHz showing the largest size among the other time constants which can be assigned to the adsorption of the reaction products (LiCl) at the porous carbon which shows large capacitance and hence large RC time constant.

2.2.4. Equivalent Circuit Modeling

Equivalent Circuit (EC) analysis is performed for the obtained EIS to have better clarification for the time constants observed. Figure 36(a) shows the EC fit for the 100% $SOCl_2$ cell and Figure 36(b) shows the fit for 75% $SOCl_2$ + 25% SO_2Cl_2 cell. For both cells Constant Phase Element (CPE) was used to fit the distorted semicircles which did not have ideal RC behavior.

For the EC fits in our data each distorted semicircle was fit with a CPE connected in parallel with a resistor R(R//CPE). For 100% $SOCl_2$ inductive behavior was observed at the highest frequencies which was fitted with an Inductor element L. At the highest frequency point a resistor was fitted to the data which corresponded to the electrolyte resistance R_u. The EC models used are shown in Figure xx and the fitted parameters for the two models are summarized in Table 3.

(a)

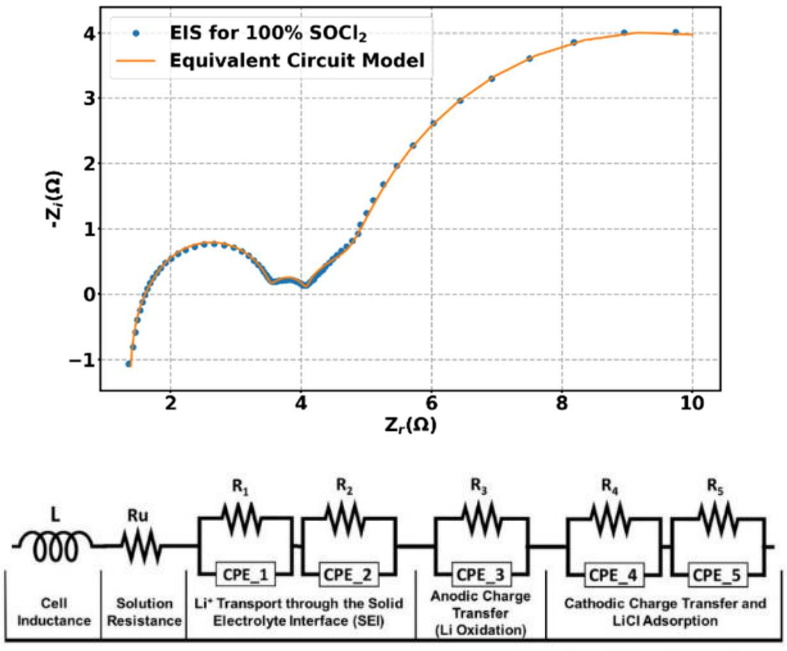

(b)

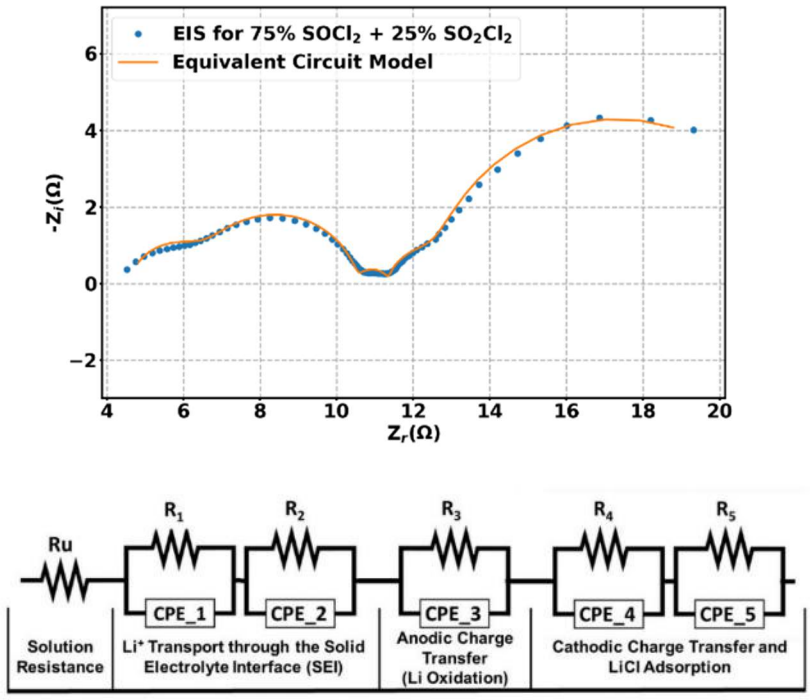

Figure 36. Equivalent Circuit fits overlayed with EIS Nyquist plots for the Li/$SOCl_2$ reserve batteries and the fitted equivalent circuit model for (a) 100% $SOCl_2$ electrolyte cell and (b) 75% $SOCl_2$ + 25% SO_2Cl_2 electrolyte cell

Table 4. Equivalent Circuit parameters and their errors obtained from fitting the models shown in Figure 6 for 100% $SOCl_2$ electrolyte cell and 75% $SOCl_2$ + 25% SO_2Cl_2 electrolyte cell

		100% $SOCl_2$			75% $SOCl_2$ + 25% SO_2Cl_2		
	Circuit Element	**Value**	**Error**	**Time const.**	**Value**	**Error**	**Time const.**
Inductance	**L (H)**	203.2 $x10^{-9}$	15.3 $x10^{-9}$		-	-	
Solution Resistance	**Ru (Ω)**	1.312	0.107		4.587	0.147	
Solid Electrolyte Interface	**R1 (Ω)**	0.384	0.095	0.89 MHz	1.923	0.197	0.40 MHz
	$Y_0$1 (S×s^a)	29.3 $x10^{-7}$	19.7 $x10^{-7}$		12.87$x10^{-7}$	2.71$x10^{-7}$	
	a1	0.933	0		0.902	0	
	R2 (Ω)	1.840	0.069	34.9 kHz	4.061	0.216	18.0 kHz
	$Y_0$2 (S×s^a)	15.59x 10^{-6}	1.63$x10^{-6}$		13.66$x10^{-6}$	2.02$x10^{-6}$	
	a2	0.902	0		0.885	0	
Anodic Charge Transfer	**R3 (Ω)**	0.537	0.067	272 Hz	0.783	0.193	136 Hz
	$Y_0$3 (S×s^a)	6.84 $x10^{-3}$	2.27 $x10^{-3}$		9.39$x10^{-3}$	6.23$x10^{-3}$	
	a3	0.902	0		0.885	0	
Cathodic Charge Transfer	**R4 (Ω)**	0.687	0.116	1.79 Hz	1.205	0.314	1.36 Hz
	$Y_0$4 (S×s^a)	0.813	0.259		0.610	0.291	
	a4	0.884	0		0.920	0	
	R5 (Ω)	9.35	0.61	41.7 mHz	9.649	0.896	47.1 mHz
	$Y_0$5 (S×s^a)	2.56	0.14		2.199	0.253	
	a5	0.900	0		0.920	0	

For 100% $SOCl_2$, the data was fitted with an inductor, a solution resistance and five R//CPE. The CPEs were assigned to the electrochemical processes as follows:

- *Solid Electrolyte Interface* - the first two R//CPEs are assigned to the Li^+ transport through the SEI. The second R//CPE has five times larger resistance than the first one which is consistent with the proposed two layered structure model for the SEI [38]. As proposed by previous studies the SEI has two layers with a compact thin structure at the surface of the Li and a thick porous layer on top of the first layer. Our findings support these models with the obtained resistances.

- *Anodic Charge Transfer* – the third R//CPE was assigned to Li oxidation reaction which show low values of ≈0.5Ω and 6mF.

- *Cathodic Charge Transfer and Transport* – the last two R//CPEs can be assigned to the cathode reaction and the adsorption of the reaction products onto the porous carbon. The last R//CPE is assigned to the adsorption process because of its high capacitive value ≈2.5F representing the adsorption onto the porous carbon while the other is to the reaction of Li^+ with $SOCl_2$.

For 75% $SOCl_2$ + 25% SO_2Cl_2 cell the data are fitted with solution resistance at the highest frequency and five R//CPEs. The assignment of the electrochemical processes to the R//CPEs is the same as the 100% $SOCl_2$ cell with large variation in the time constants and the values of the first two R//CPEs belonging to the SEI.

The value of the resistance at the first R//CPE is five times larger than the 100% $SOCl_2$ cell indicating the presence of thicker layer. Likewise, the second R//CPE has two times the resistance compared to the 100% $SOCl_2$ cell. This increase in the resistances is correlated to what is mentioned previously regarding the formation of two layers from the different reaction products in the electrolyte mixture.

Comparing the time constants of the electrochemical processes in the two cells, we can observe the lower values of time constants for the 75% $SOCl_2$ + 25% SO_2Cl_2 cell for the first three R//CPE and the similar values for the last two. This indicates that the change in the electrolyte only effects the anodic charge transfer and the SEI processes which are

related to the charge and mass transfer of the Li^+. The time constants for the Li^+ transport through the SEI is slower in the mixture electrolyte cell and Li oxidation is also slowed down. The slow down at the anodic processes is related to the multi-component two layers structure of the SEI formed as a result of the mixture of the electrolyte used. As the Li^+ is transported through the SEI the reaction with the electrolyte and the adsorption to the carbon has comparable rates in both cells.

Both cells showed similar EIS response with variations at the high frequency region. The 75% $SOCl_2$ + 25% SO_2Cl_2 cell showed two distorted semicircles while 75% $SOCl_2$ cell showed inductive behavior followed by one distorted semicircle at the very high frequency range (1MHz – 100Hz). This difference is related to the multi-component two layers structure of the SEI at the mixture electrolyte cell. The charge transfer time constants showed slower responses for the mixture electrolyte cell. The obtained data and the performed analysis show the electrolyte composition effect in the formation of the SEI and hence the kinetics of the battery.

2.2.5. Section Conclusion

In this section, the characterization of different electrolyte composition Li\$SOCl_2$ reserve primary batteries was done using EIS. The first cell had 100% $SOCl_2$ electrolyte and the second had 75% $SOCl_2$ + 25% SO_2Cl_2 mixture of electrolytes. Both cells showed similar EIS response with variations at the high frequency region. This difference is related to the multi-component two layers structure of the SEI at the mixture electrolyte cell. Equivalent Circuit analysis using Constant Phase Element connected in parallel to a resistor for each distorted semicircle was performed. The obtained parameters for the first two semicircles at the high frequency region were related to the Li-ion transport through the SEI which had larger values for 75% $SOCl_2$ + 25% SO_2Cl_2 cell. The rest was assigned to the anodic and cathodic charge transfer processes with the largest semicircle assigned to the adsorption of the reaction products on the porous carbon. The charge transfer time constants showed slower responses for the mixture electrolyte cell. The obtained data and the performed analysis show the electrolyte composition effect in the formation of the SEI and hence the

kinetics of the battery. In the following section, we investigate the change in the kinetic parameters of the battery by using Temperature-dependent EIS measurements.

2.3. Temperature Dependent EIS Studies for Li based Batteries

The previous work demonstrated how EIS can be used to elucidate the different charge and mass transport processes in primary Li batteries. In this section, we extend the employment of the EIS technique to study the kinetic and the mechanistic aspects of the observed processes. We utilize temperature-dependent EIS measurements and analyze the obtained results by means of equivalent circuits and Arrhenius relations.

As we have demonstrated, the impedance of the Li-ion transport through the SEI in Li batteries is dominant over the other processes. In the literature, similar observations are made for Li-ion batteries [39][40][41]. It is also proposed, based on temperature-dependent EIS and Arrhenius analysis, that there exist two steps mechanism for the Li-ion transport through the SEI. The first, is the solvation/de-solvation of the Li-ion from the electrolyte. The second, is the migration of the Li-ions through the porous structure of the SEI with the first to be the more dominating process [42][43][44].

Furthermore, simulation studies which used physics-based models were developed to simulate the EIS response of the SEI based on the two-structure model and two-steps mechanism for the Li-ion transport through the SEI. The simulation results presented is in agreement with the experimental results showed in the previous sections. The first, is two-time constants at the high frequency region related to the charge transfer processes of the Li-ions transport through the SEI. The second, is a diffusion response at the lower frequencies for the Li-ion transport through the electrolyte. The third, is a time constant for the Li oxidation process at the mid frequency region [13][45].

In this section, we will investigate EIS response of the SEI formed on the Li anode in the Li based commercial primary batteries. We will use Lithium Thionyl Chloride ($Li/SOCl_2$) and Lithium Manganese Dioxide (Li/MnO_2) which have different SEI structures. We will present detailed investigation of temperature-dependent EIS data at wide range of temperatures and at different States-of-Charge (SoC). Moreover, Arrhenius analysis is made where applicable for the electrochemical process of the battery.

2.3.1. Temperature-Dependence in the Electrochemical Impedance for Primary Li Batteries

The impedance of the electrochemical processes in batteries are hugely affected by the variation in temperature. As was presented in the introduction chapter, both thermodynamic (voltage) and kinetic (charge transfer resistances) parameters are temperature dependent. The charge transfer resistance of an electrochemical processes decreases as the temperature increases. For example, the decrease in the battery impedance is utilized in Li-ion batteries in fast charging applications. The Li-ion battery pack in an electric vehicle is heated to around 60C prior fast charging to increase the rate of charging and allow more current to pass [45].

Figure 37 shows the change in the EIS of the Li/$SOCl_2$ battery at various temperature from -15C to 65C. The impedance values show a large decrease as the temperature increase. However, the change in the impedance values is different for each electrochemical process. The most noticeable change is observed in the processes at the high frequency region. Detail investigation is made to understand these changes by means of equivalent circuit modeling and Arrhenius relations.

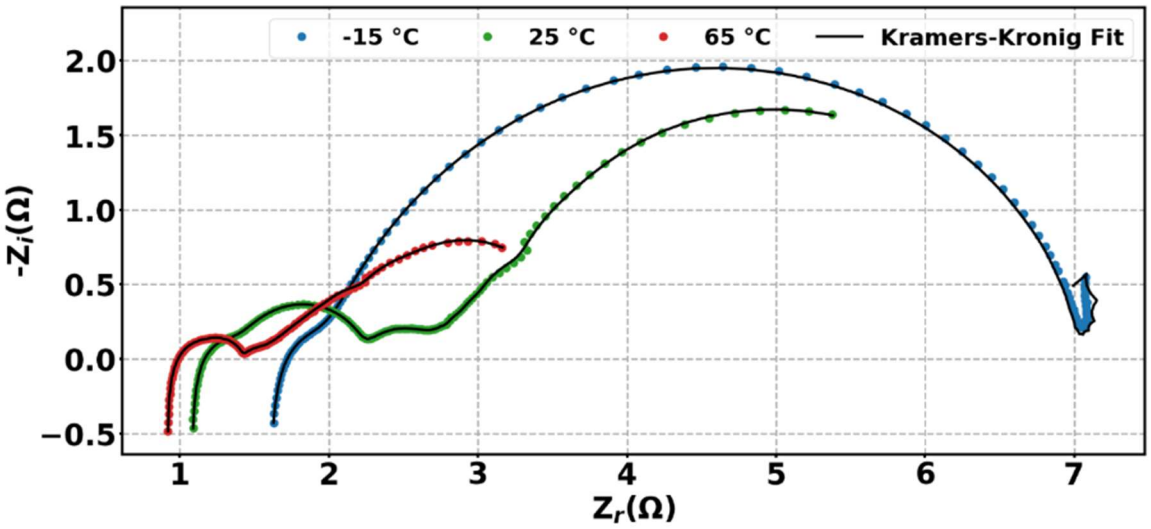

Figure 37. Temperature-dependent EIS of Li\$SOCl_2$ at 90% SoC with -10mA DC-offset and 2mA AC excitation at 65, 25 and -15 ºC

2.3.2. Comparison between EIS of Lithium Thionyl Chloride (Li\SOCl$_2$) and Lithium Manganese Dioxide (Li\MnO$_2$)

The Nyquist plots of Li/SOCl$_2$ and Li\MnO$_2$ at 90% SoC and 25C are shown in Figure 38. For Li/SOCl$_2$, as we have concluded in the previous sections, the EIS response can be analyzed for three frequency regions with each region corresponding to electrochemical process:

- *High frequency region (1MHz – 100Hz):* after an inductive behavior at the very high frequencies, we observe two semicircles with different in size. These two time-constants are assigned to the transport of the Li-ion through the two-layer SEI.

- *Middle frequency region (100Hz – 1Hz):* this region is assigned to the anodic reaction namely, Li oxidation.

- *Low frequency region (1Hz – 1mHz):* one semicircle is observed at the lower frequencies which is related to the cathodic charge transfer reaction namely the adsorption of the reaction products on the porous carbon.

For the Li\MnO$_2$ cell, the response is similar to the Li/SOCl$_2$ at the high and the middle frequency regions but varies at the low frequency region. This is expected since the cathode chemistry is different. The cathodic electrochemical process is based on the Li-ion intercalation into MnO$_2$ which is not observed in the Nyquist response except at very low frequencies which is difficult to measure due to the instability of the battery at such low frequencies <1mHz.

The similar behavior at the high and the middle frequency is related to the usage of the same anode active material, metallic Li. However, due to the usage of organic electrolyte in Li\MnO$_2$ cell, the SEI structure and morphology is different from Li/SOCl$_2$ cell. The transport of the Li-ion through the SEI will have different Activation energies and investigating these changes will enable us to gain insight into this process. Moreover, we will study the change that different SEI causes in the anodic process which is the oxidation of Li.

(a)

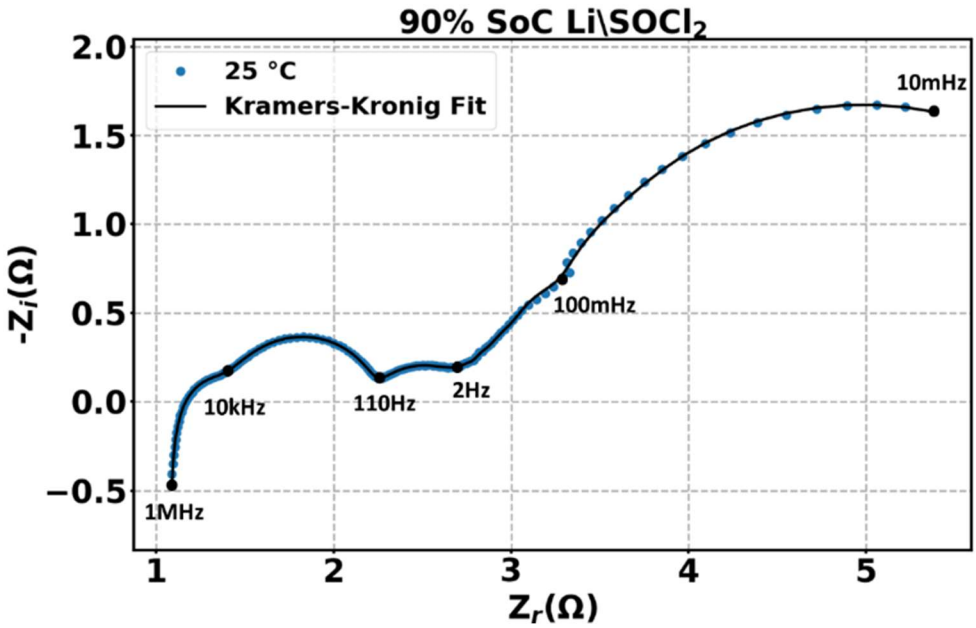

(b)

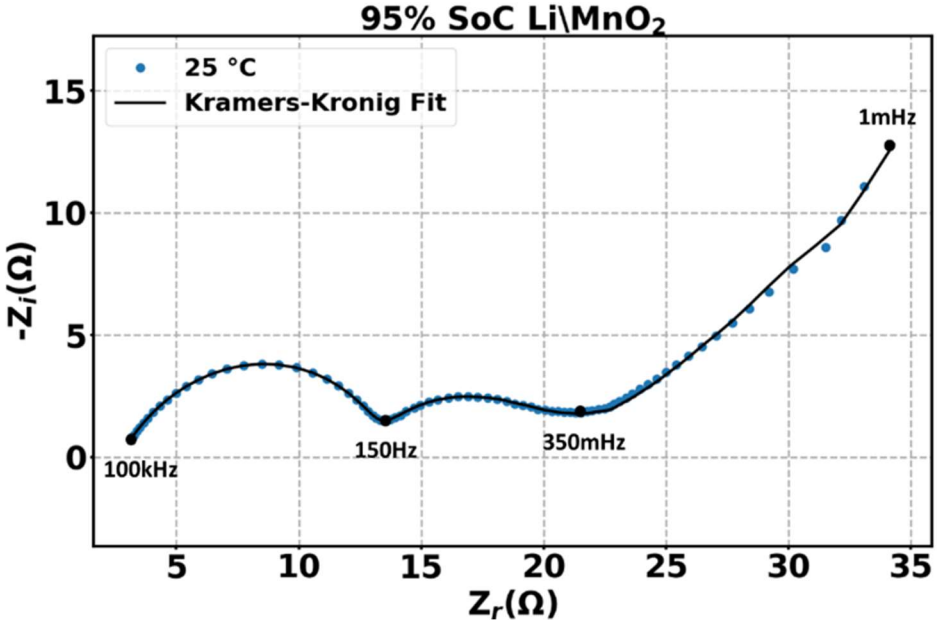

Figure 38. Nyquist plots of (a) $Li/SOCl_2$ from 1MHz to 10mHz (b) Li/MnO_2 from 1MHz to 1mHz at room temperature.

2.3.3. Experimental Design

The temperature-dependent (T-dependent) EIS experiments were performed in a temperature range from -15ºC to 65ºC. The temperature was measured using a thermocouple which was placed in a custom-made insulating chamber. Thermoelectric cooler (Peltier device) was placed on one side of the chamber to provide the required cooling. The Peltier device was able to cool the temperature to 5ºC. Further cooling was done by placing a beaker with liquid Nitrogen in which the temperature was controlled manually. Higher temperatures (25ºC – 65ºC) were achieved by placing heating stripes in which the heating was controlled by controlling the voltage source. At the higher temperatures, the temperature inside the chamber was stabilized by the Peltier device.

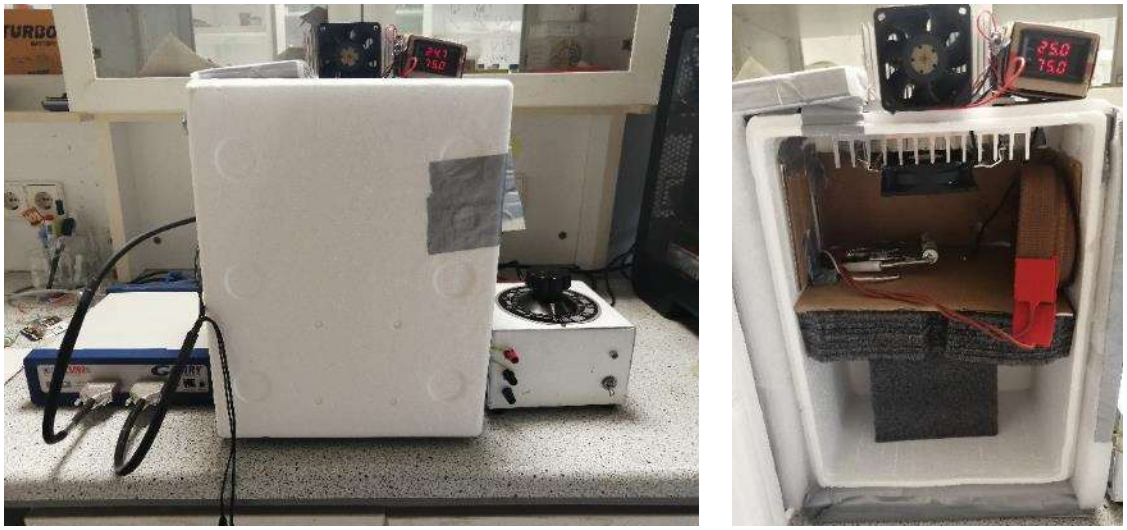

Figure 39. Home-made temperature chamber used for the T-dependent experiments

The studied cells were places inside the chamber before the EIS experiments which was also connected to Gamry 5000E instrument. The EIS measurements were performed after bringing the temperature of the chamber to the desired value and waiting at that temperature for at least 10 minutes. Galvanostatic-EIS at discharge was performed for the cells. The experiments were performed on both Li\$SOCl_2$ and Li\$MnO_2$ batteries.

Li\$SOCl_2$ (SAFT- LS 14500) AA-size bobbin cell with 2.6Ah capacity and 3.67V open circuit potential and Li\$MnO_2$ (Panasonic LM2023) coin cell with 2mAh capacity and 3.20V open circuit potential were used.

2.3.4. T-dependent Electrochemical Impedance Spectroscopy Results for Lithium Thionyl Chloride (Li\$SOCl_2$)

Figure 40 shows the Nyquist plots of the EIS of the 90% SoC Li\$SOCl_2$ cell at temperatures between -15ºC to 65ºC with 10ºC intervals. As can be seen, there is a large decrease in the impedance of the cell by increasing the temperature. For temperatures below 15ºC, only linear data for two semicircles are observed at the high frequency region. This is related to the change in the impedance and the time constants of the processes by changing the temperature. The kinetics of the processes is slowed down by the decrease in the temperature which results in impedance increase and in appearance at slower frequencies. For the rest of temperatures five semicircles are observed which are assigned to the anodic, cathodic and SEI processes.

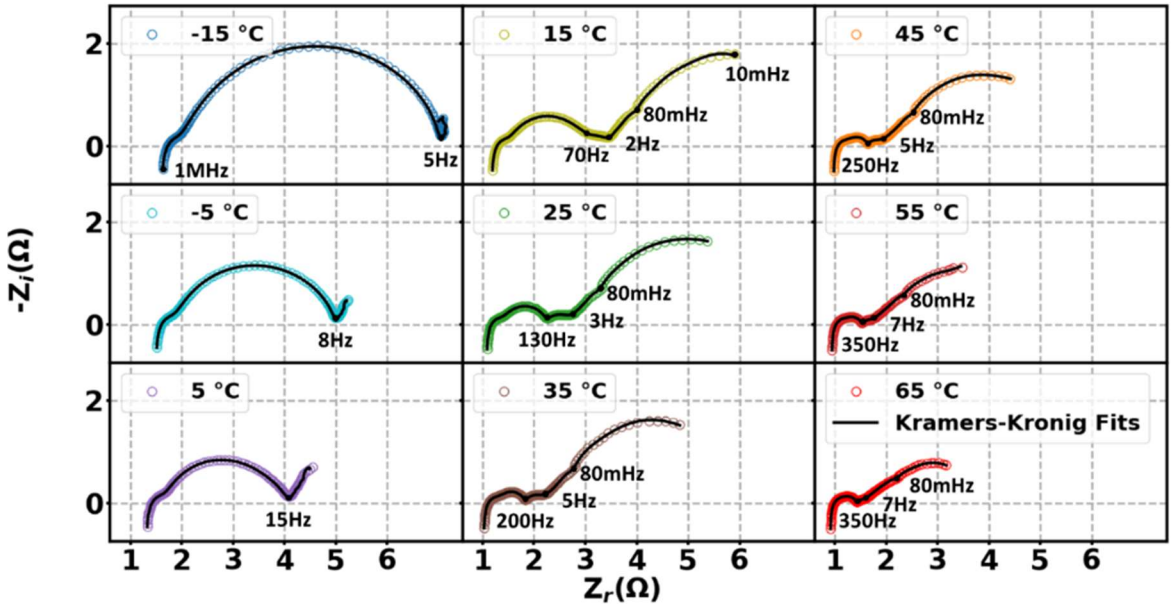

Figure 40. Nyquist plots of the Temperature-dependent EIS for Li\$SOCl_2$ at 90% State-of-Charge

The high frequency region which is observed in all temperatures is assigned to the processes of Li-ion transport through the SEI. This region is the most effected by the temperature variation which shows the high temperature dependence of the corresponding electrochemical processes. This region shows inductive behavior followed by small and large semicircles. The time constants of the two semicircles shift to higher frequencies as the temperature increases. Both real and imaginary impedance values decrease as the temperature increases.

The middle frequency region shows one semicircle which is assigned to the anodic charge transfer processes. This region is observed for temperatures above 15ºC which shows small temperature dependence in both time constant and impedance.

The low frequency region which is also observed above 15ºC shows two semicircles which are assigned to the cathodic charge transfer and mass transport of the reaction products. There is also small temperature dependence in the impedance and the time constants.

To have better insight about the variations in the resistive and the capacitive nature of the observed change in the semicircles, we utilized equivalent circuit analysis. The details of the equivalent circuit analysis are presented in the following section.

2.3.5. Equivalent Circuit Analysis for Li\SOCl$_2$ T-dependent EIS Data

The high frequency region showed inductive behavior followed by two distorted semicircles which is fitted with an inductor, solution resistor and two Constant Phase Elements (CPE) connected in parallel to a charge transfer resistor shown in Figure 41(a). The first R//CPE corresponds to the electrochemical processes of Li-ion transport through the first layer of the SEI which is known to be thin and compact [46]. The R//CPE is for the Li-ion transport through the second and thicker layer of the SEI. It is observed that Li-ion transport impedance and kinetics through the second layer is more temperature dependent than the first one. The change in the parameters of the fitted equivalent circuit with the change in temperature is shown in Figure 41(b) and listed in Table 4.

(a)

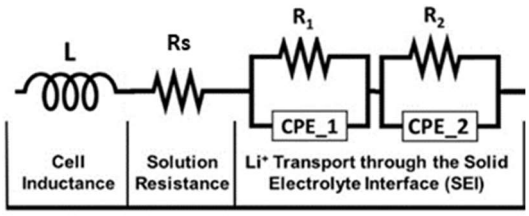

(b)

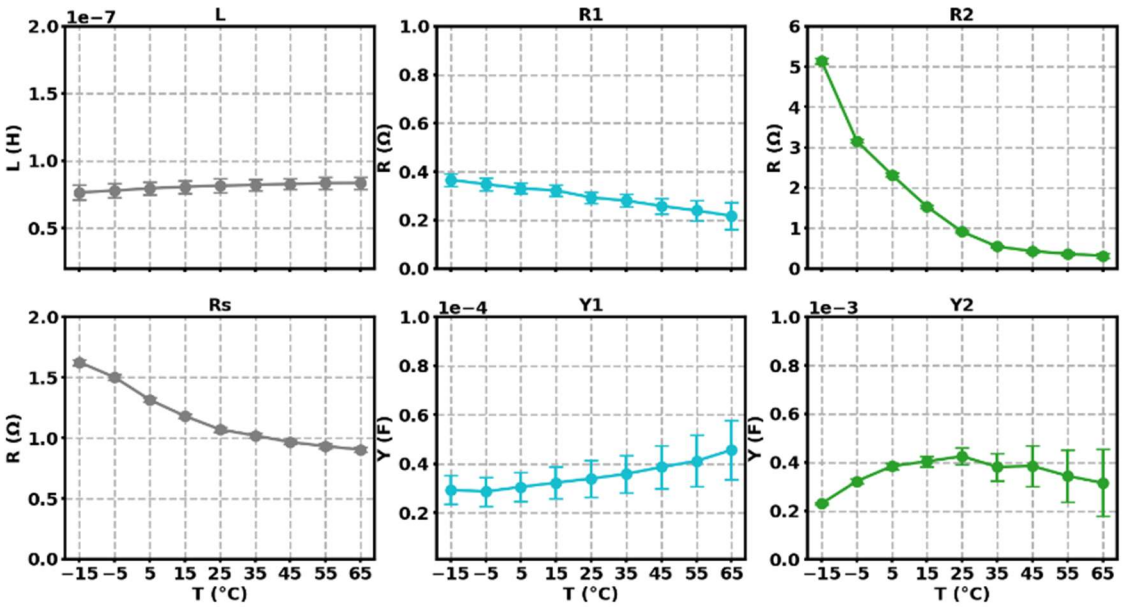

Figure 41. (a) Equivalent circuit model fitted to the high frequency region of the T-dependent EIS data, (b) Variation in the equivalent circuit parameters with error range by the temperature change

The equivalent circuit analysis shows small increase in the inductance of the cell and a decrease in the solution resistance as temperature increases. The decrease in the solution resistance is related to the increase in the kinetic energy of ions as the temperature increases which facilitate the movement of ions in the solution resulting in better conductance. The decrease in the value of the resistance is sharper moving from -15ºC to 25ºC which reduced its rate from 25ºC to 65ºC.

Table 5. Equivalent circuit parameters for the T-dependent EIS at high frequency region

T(ºC)	Rs(Ω)	R1 (Ω)	Y_01 (S×s^a)	a1	Time Const. (s)	R2 (Ω)	Y_02 (S×s^a)	a2	Time Const. (s)
-15	1.62	0.37	2.93×10^{-5}	0.85	1.07×10^{-5}	5.14	2.30×10^{-4}	0.83	1.18×10^{-3}
-5	1.50	0.35	2.86×10^{-5}	0.85	9.90×10^{-6}	3.16	3.22×10^{-4}	0.81	1.02×10^{-3}
5	1.31	0.33	3.05×10^{-5}	0.85	1.01×10^{-5}	2.32	3.84×10^{-4}	0.81	8.93×10^{-4}
15	1.18	0.32	3.22×10^{-5}	0.85	1.04×10^{-5}	1.53	4.04×10^{-4}	0.82	6.21×10^{-4}
25	1.07	0.29	3.39×10^{-5}	0.85	9.90×10^{-6}	0.91	4.25×10^{-4}	0.82	3.86×10^{-4}
35	1.02	0.28	3.58×10^{-5}	0.85	1.00×10^{-5}	0.54	3.81×10^{-4}	0.83	2.07×10^{-4}
45	0.96	0.26	3.86×10^{-5}	0.85	9.90×10^{-6}	0.43	3.85×10^{-4}	0.82	1.65×10^{-4}
55	0.93	0.24	4.11×10^{-5}	0.85	9.80×10^{-6}	0.36	3.44×10^{-4}	0.82	1.25×10^{-4}
65	0.90	0.22	4.56×10^{-5}	0.85	9.90×10^{-6}	0.31	3.15×10^{-4}	0.82	9.86×10^{-5}

The equivalent circuit analysis for the two semicircles at the high frequency region shows different trends as the temperature change. These two semicircles are assigned to Li-ion transport through the two-layer structure of the SEI. The first thing which is noticed is the different behavior of the time constant of the processes as the temperature increases. For the first semicircle, the time constant is almost constant showing value around 1.00×10^{-5}s which indicated that the kinetics of this processes is temperature independent. However, for the second semicircle, the time constant shows constant decrease as the temperature increases. As can be seen from Table 4, the time constant is around 1.18×10^{-3}s at -15ºC and is 9.86×10^{-5}s at 65ºC. This huge change indicated the high temperature dependence of this processes to the temperature change.

The high temperature dependence is also observed in the fitted charge transfer resistance values which shows a large decrease from -15ºC to 35ºC followed by low decrease from 35ºC to 65ºC. This change in the decrease rate indicated the existence of more than one mechanism for the charge transfer or the presence of more than one processes at the same frequencies. This is also observed in the fitted capacitive values of the CPE which shows increase from -15ºC to 25ºC and a decrease going to 65ºC.

The fitted charge transfer resistance for the first semicircle shows almost a linear decrease by increasing the temperature with a corresponding capacitive increase in the fitted CPE.

The middle frequency region which is assigned to the Li oxidation at the anode, is fitted with charge transfer resistance connected in parallel to a CPE. The trends of the fitted values to the temperature change are shown if Figure 42 and listed in Table 5. As can be seen, except of values at 15ºC, there is a decrease in the charge transfer resistance and corresponding capacitive increase as the temperature increase. The rate of change in the fitted values is almost linear.

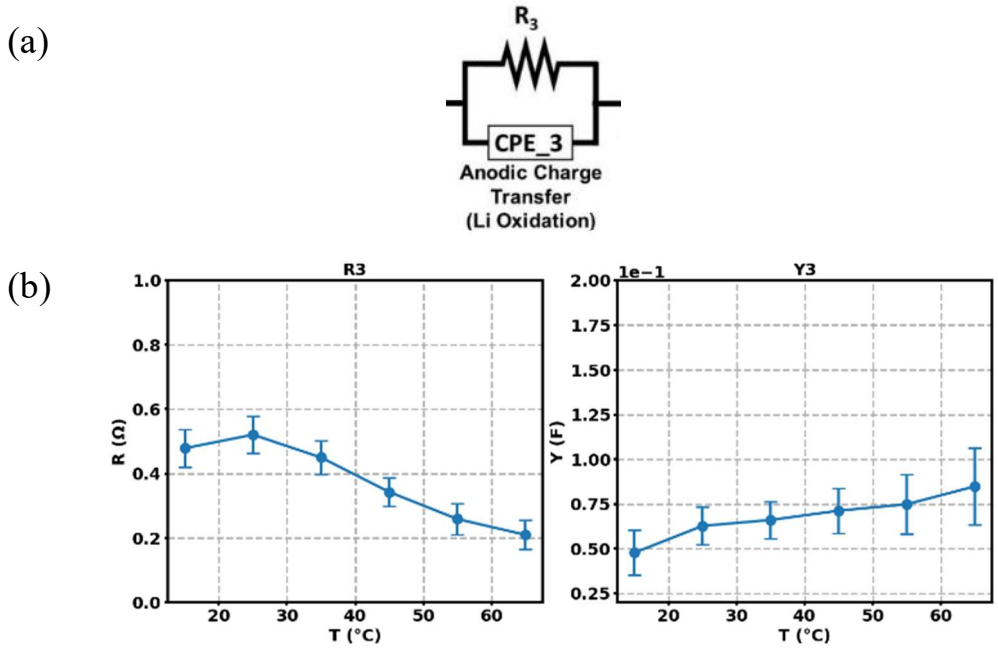

Figure 42. (a) Equivalent circuit model fitted to the middle frequency region of the T-dependent EIS data, (b) Variation in the equivalent circuit parameters with error range by the temperature change

The time constant values are showing a decrease by the increase in the temperature which indicates the increase in the kinetics of Li oxidation as the temperature increases.

Table 6. Equivalent circuit parameters for the T-dependent EIS at mid frequency region

T(C)	R3 (Ω)	$Y_0$3 (S×s^a)	a3	Time Const. (s)
15	0.48	4.78×10^{-2}	0.83	2.29×10^{-2}
25	0.52	6.28×10^{-2}	0.83	3.27×10^{-2}
35	0.45	6.61×10^{-2}	0.82	2.97×10^{-2}
45	0.34	7.13×10^{-2}	0.83	2.45×10^{-2}
55	0.26	7.49×10^{-2}	0.83	1.94×10^{-2}
65	0.21	8.49×10^{-2}	0.83	1.79×10^{-2}

The low frequency region which seems to show two semicircles is actually one semicircle with deviations between 150 to 70 mHz. The deviation is instrumental artifact that results from the generation of the excitation signal. This was confirmed by control experiments in dummy cells. The semicircle was fitted with one R//CPE equivalent circuits assigned to the cathodic charge transfer processes.

The charge transfer resistance shows a decrease in increasing temperature with corresponding almost constant capacitive behavior in the fitted CPE. The time constant values show small decrease as the temperature increase indicating the small temperature dependence of the adsorption processes.

(a)

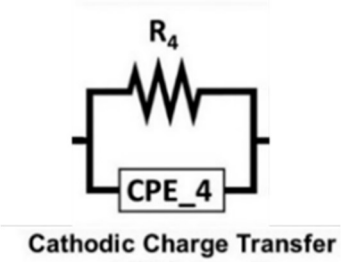

(b)

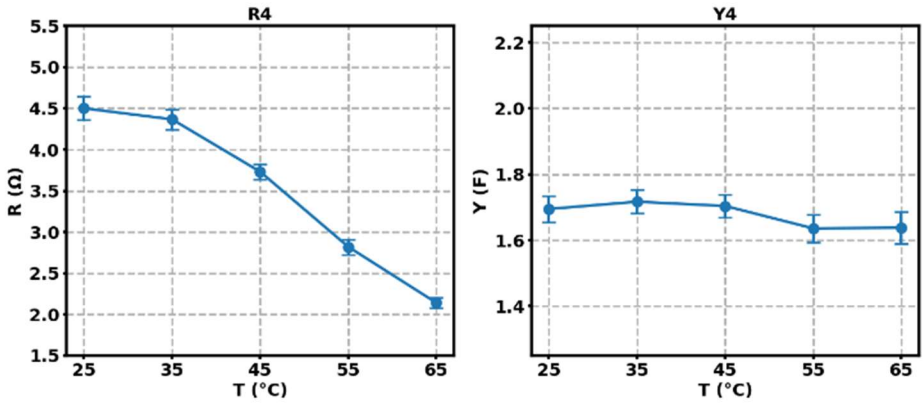

Figure 43. (a) Equivalent circuit model fitted to the low frequency region of the T-dependent EIS data, (b) Variation in the equivalent circuit parameters with error range by the temperature change

Table 7. Equivalent circuit parameters for the T-dependent EIS at low frequency region

T(C)	R4 (Ω)	$Y_0$4 (S×s^a)	a4	Time Const. (s)
25	4.50	1.69	0.8	7.6
35	4.36	1.71	0.8	7.5
45	3.73	1.70	0.8	6.4
55	2.82	1.63	0.78	4.6
65	2.14	1.63	0.75	3.5

2.3.6. Arrhenius Analysis

Kinetic information such as the activation energy (E_a) of the electrochemical processes can be obtained by means of Arrhenius equation. From the fitted resistance values of the electrochemical processes, only the resistance of the second semicircle assigned to the Li-ion transport through the SEI shows a large decrease as the temperature increases. the large decrease indicates the existence of an exponential relation between the resistance and the temperature. The logarithmic reciprocal of the resistance is drawn versus the reciprocal of the temperature to investigate the Arrhenius relation. As can be seen from Figure 44, the data shows two trends with increasing the temperature. At low temperatures (-15ºC – 35ºC) there is a linear trend which is fitted with a slope. However, with the increase in the temperature there is deviation from the slope. The difference in the trends indicate the existence of two temperature dependence for the Li-ion transport process through the second layer of the SEI. The activation energies obtained from the linear slopes are 29 ± 5 kJ/mol.

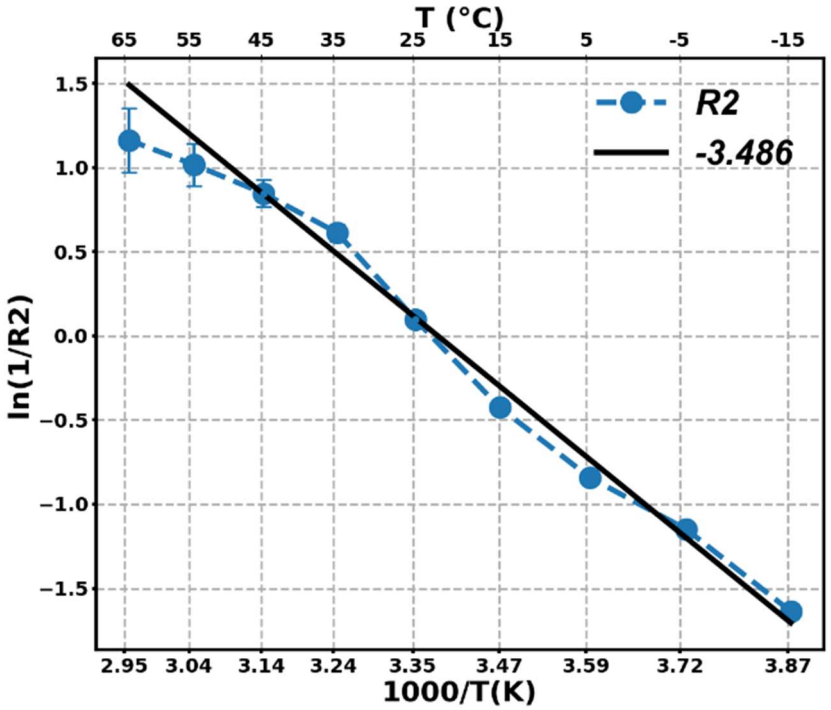

Figure 44. Arrhenius plot for charge transfer resistance of the second semicircle R_2

2.3.7. Variations by Changing States-of-Charge

The equivalent circuit analysis was performed at different States-of-Charges (SoC) of the Li\$SOCl_2$ battery. The trends observed are similar for all SoC. The observations for the equivalent circuit parameters for 100%, 90%, 70% and 50% SoC are as follows:

- *Inductance (L)*: the inductance of the cell decreased by decreasing the SoC of the battery.
- *Solution resistance (Rs)*: the solution resistance increased as the SoC decreased due to the depletion of the electrolyte $SOCl_2$ coupled with the accumulation of the reaction products LiCl. At 50% SoC the resistance is showing a large increase at low temperatures.
- *Li transport through SEI:* the first charge transfer resistance R1 shows similar values with low T-dependent behavior for all SoCs except at 50% SoC which displays high T-dependent behavior. The change in the temperature dependence at 50% SoC is also observed for the second charge transfer resistance R2. The change at 50% SoC can be associated with the change in the structure of the SEI.

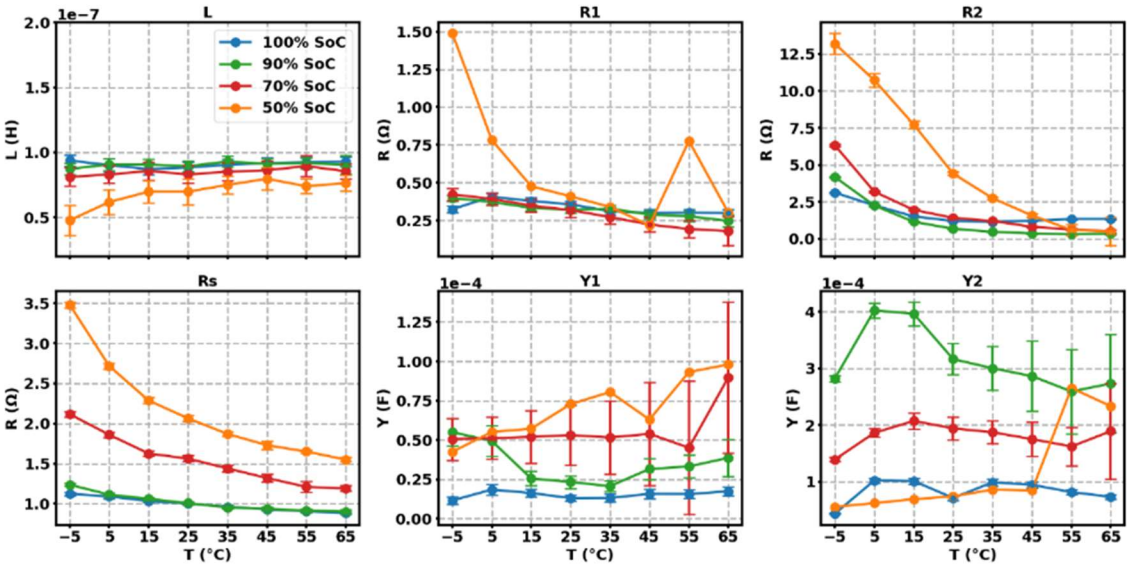

Figure 45. Change in the equivalent circuit parameters by changing State-of-Charge for the high frequency region

- *Li oxidation*: the charge transfer resistance R3 for the anodic processes is showing an increase as the cell is discharged. The increase can be related to the depletion in the metallic Li anode. The capacitive values of the parallel CPE are the highest at 90% SoC and lowest at 50% SoC. The high capacitive value at 90% SoC is related to the high amount of Li which starts to deplete as the cell discharges and hence show a decrease in the capacitive values.

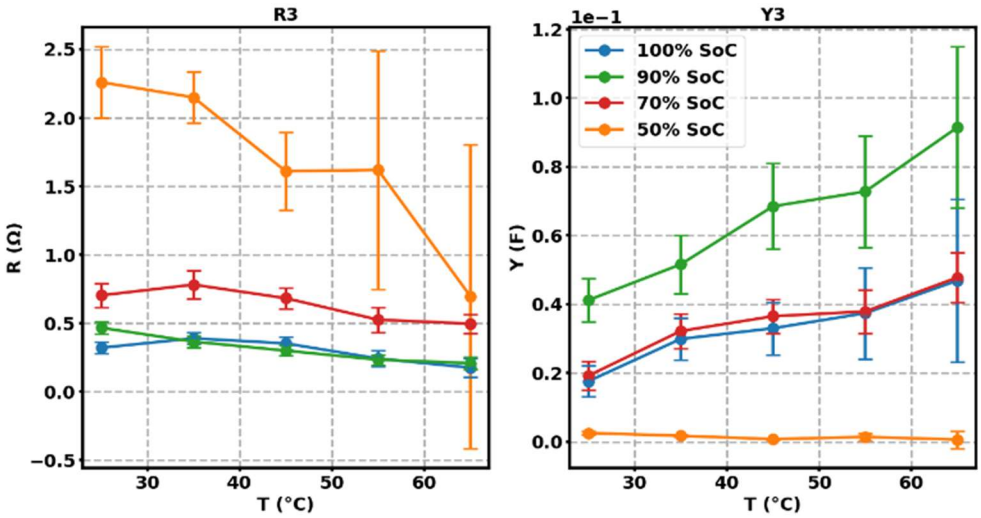

Figure 46. Change in the equivalent circuit parameters by changing State-of-Charge for the middle frequency region

- *Cathodic charge transfer:* the cathodic charge transfer resistance R4 is showing a huge decrease in the parallel CPE capacitive value as the cell is discharged. This is due to the accumulation of the reaction product LiCl at the pores of the carbon cathode which causes the decrease in the porosity of the cathode showing the large decrease in the capacitive value.

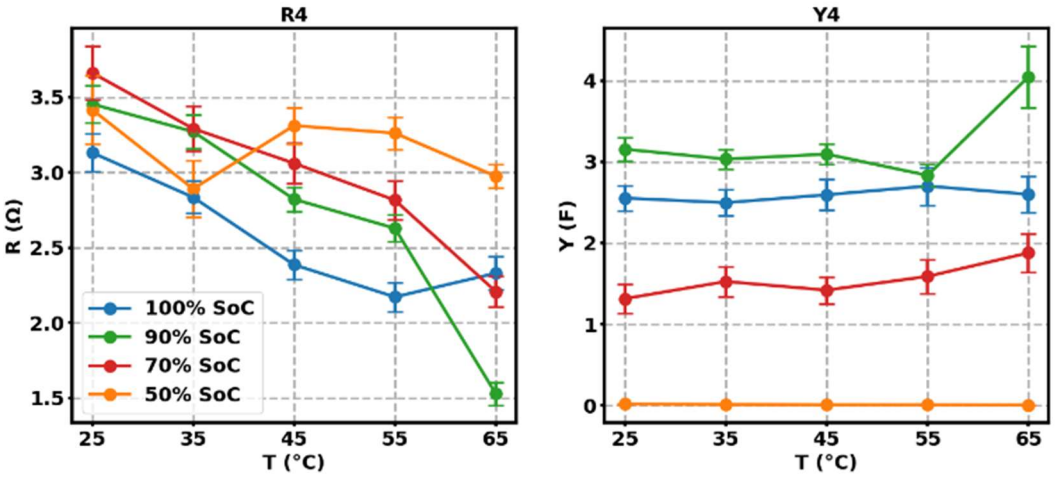

Figure 47. Change in the equivalent circuit parameters by changing State-of-Charge for the low frequency region

- *Arrhenius plots for R2*: the Arrhenius relation of the R2 is plotted for the different %SoC. Except for the 100% SoC the values of the activation energies are similar. The activation energies are 10.8 kJ/mol, 28.9 kJ/mol, 31.3 kJ/mol, 28.8kJ/mol for 100, 90, 70 and 50% SoC respectively.

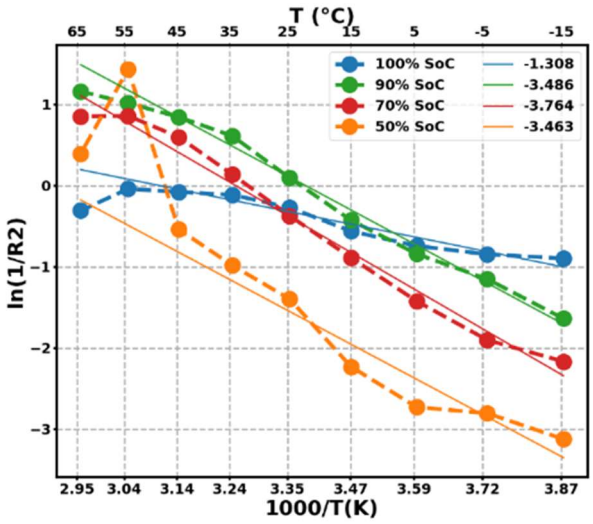

Figure 48. Arrhenius plots for charge transfer resistance of the second semicircle R2 at different %SoC

2.3.8. T-dependent Electrochemical Impedance Spectroscopy Results for Lithium Manganese Dioxide (Li\MnO$_2$)

For the intention of conforming the observed EIS temperature dependence in Li based batteries and in order to further investigate the effect of changing the type of electrolyte and hence the structure of the SEI, we performed temperature dependent EIS analysis for Lithium Manganese Dioxide (Li/MnO$_2$) battery.

The T-dependent EIS measurements were performed between 1MHz and 100mHz which shows two overlapped semicircles at the high frequency region and one semicircle at the mid frequency region. The low frequency region showed deviations in the Kramers-Kronig compatibility test due to the presence of instability in the data.

Similar to Li/SOCl$_2$ there is a high temperature dependence in the EIS especially at the high frequency region which is assigned to the Li-ion transport through the SEI. The decrease in the value of the impedance and the time constants as the temperature increases is comparably larger than the Li/SOCl$_2$. This is related to the different structures of the SEI each cell has. The SEI in Li/MnO$_2$ is known to be stable and formed by various organic and inorganic products of the undesired reaction of Li with the organic electrolyte and the inorganic salt. on the other hand, the SEI in Li/SOCl$_2$ is dynamic and mostly formed by LiCl crystals from the reaction of Li with SOCl$_2$.

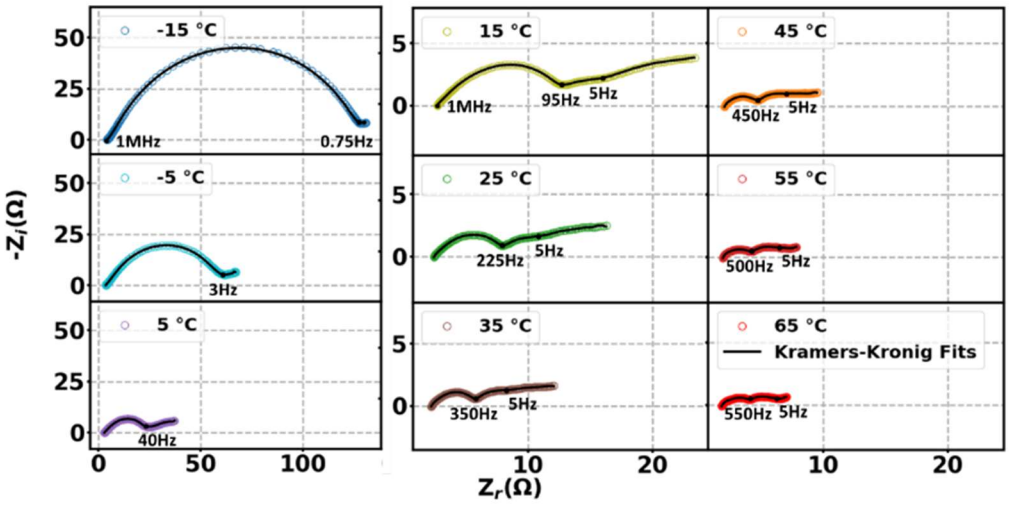

Figure 49. Nyquist plots of the T-dependent EIS for Li\MnO$_2$

2.3.9. Equivalent Circuit Analysis for Li\MnO$_2$ T-dependent EIS Data

The equivalent circuit analysis for the T-dependent EIS data for the Li\MnO$_2$ battery was performed to compare the behavior the charge transfer resistances of the electrochemical processes of the battery. For the high and middle frequency regions, we utilized the same equivalent circuits used for Li\SOCl$_2$.

The high frequency region was fitted with inductor where applicable followed by solution resistance connected in series with two R//CPE circuits. The R//CPE are assigned for the Li-ion transport through the SEI. The Nyquist plots of the EIS data show one semicircles which indicates the existence of one time-constants.

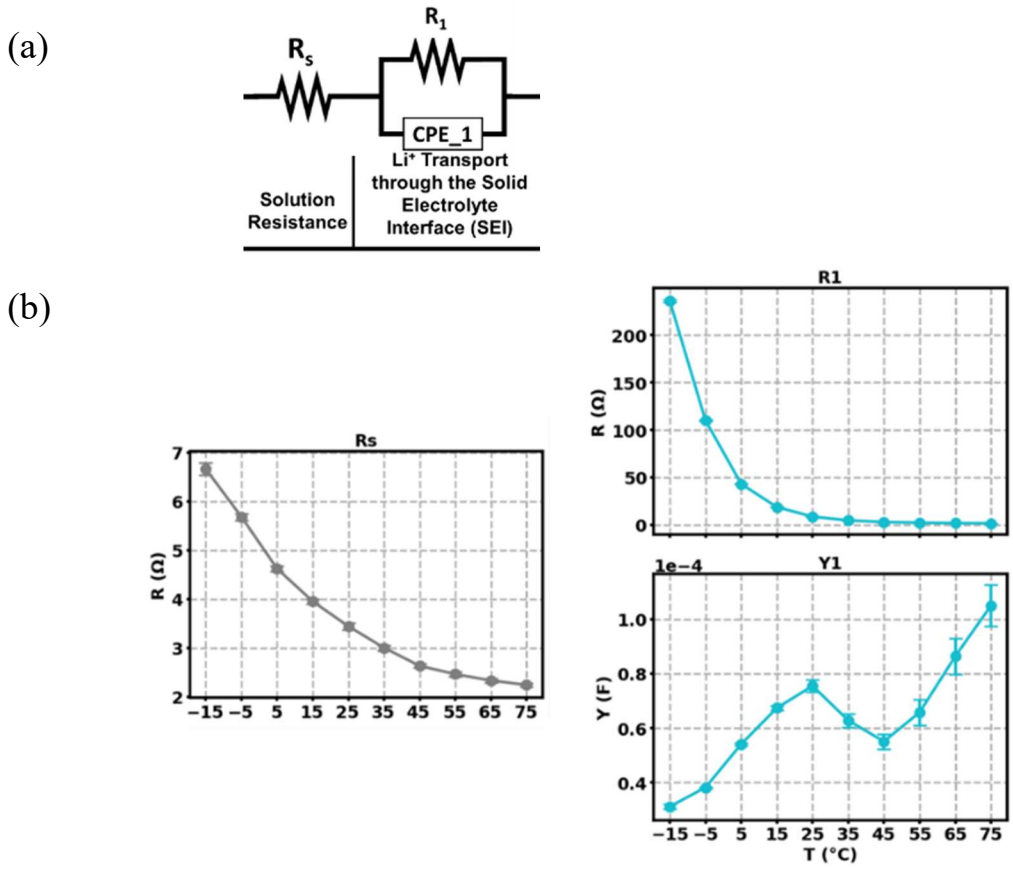

Figure 50. (a) Equivalent circuit model fitted to the high frequency region of the T-dependent EIS data, (b) Variation in the equivalent circuit parameters with error range by the temperature change

The fitted charge transfer resistance shows large decrease as the temperature increases indicating the high temperature dependence. The large temperature dependence for the second semicircle was also observed for Li\$SOCl_2$ chemistry. The Li-ion transport through the SEI is highly temperature dependent.

Table 8. Equivalent circuit parameters for the T-dependent EIS at high frequency region

T(C)	Rs(Ω)	R1 (Ω)	$Y_0$1 (S×s^a)	a1	Time Const. (s)
-15	6.66	235.5	3.12×10^{-5}	0.81	7.35×10^{-3}
-5	5.67	110.0	3.82×10^{-5}	0.81	4.21×10^{-3}
5	4.62	42.9	5.41×10^{-5}	0.78	2.33×10^{-3}
15	3.95	18.6	6.74×10^{-5}	0.77	1.25×10^{-3}
25	3.43	8.5	7.55×10^{-5}	0.76	6.45×10^{-4}
35	3.00	4.5	6.28×10^{-5}	0.77	2.85×10^{-4}
45	2.62	2.8	5.51×10^{-5}	0.77	1.55×10^{-4}
55	2.46	2.0	6.58×10^{-5}	0.76	1.35×10^{-4}
65	2.33	1.6	8.64×10^{-5}	0.75	1.43×10^{-4}

The semicircle observed for the middle frequency region is assigned to the Li oxidation charge transfer processes which shows small decrease in the time constants. The charge transfer resistance shows a decrease as the temperature increases. As was observed in Li\$SOCl_2$, there is no significant temperature dependence in these processes.

(a)

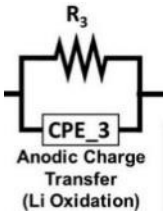

(b)

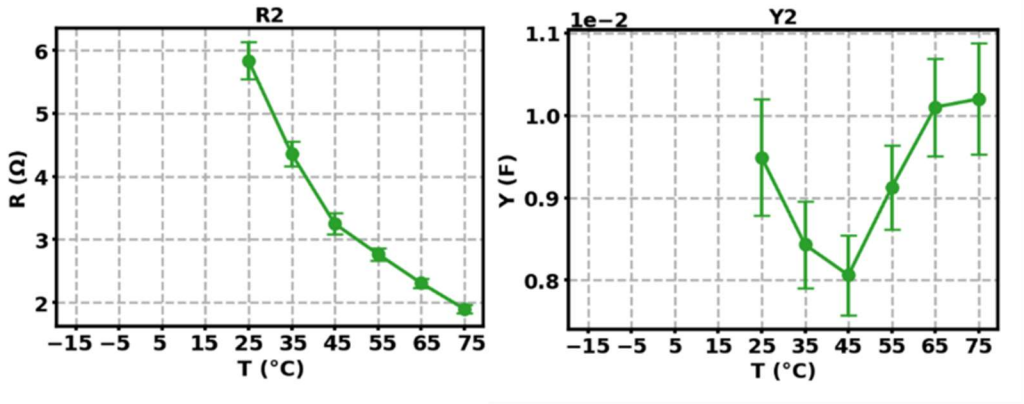

Figure 51. (a) Equivalent circuit model fitted to the middle frequency region of the T-dependent EIS data, (b) Variation in the equivalent circuit parameters with error range by the temperature change

Table 9. Equivalent circuit parameters for the T-dependent EIS at mid frequency region

T(C)	R3 (Ω)	Y_03 ($S \times s^a$)	a3	Time Const. (s)
25	5.84	9.49×10^{-3}	0.77	5.54×10^{-2}
35	4.362	8.43×10^{-3}	0.77	3.68×10^{-2}
45	3.253	8.06×10^{-3}	0.77	2.62×10^{-2}
55	2.773	9.13×10^{-3}	0.76	2.53×10^{-2}
65	2.311	1.01×10^{-2}	0.75	2.34×10^{-2}

2.3.10. Arrhenius Analysis for Li/MnO_2

Comparable to what we observed in Li/$SOCl_2$ battery, the Arrhenius plot of the highly temperature dependent charge transfer resistance R_1 shows also two behaviors for two temperature ranges. The low temperature range (-15ºC – 25ºC) shows linear behavior with the Arrhenius relation while the high temperature range (25ºC – 65ºC) deviates from linearity. The activation energy calculated form the linear region is 53 ± 5 kJ/mol which is larger than the Li\$SOCl_2$ one ≈30 ± 5 kJ/mol.

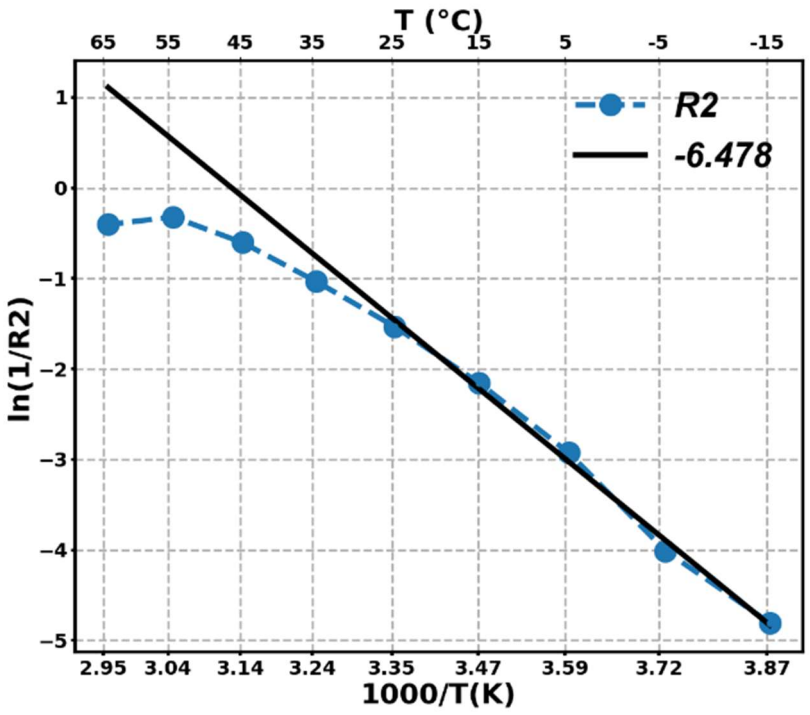

Figure 52. Arrhenius plot for charge transfer resistance of the first time constant R1 in Li\MnO_2 T-dependent EIS

This Arrhenius and non-Arrhenius behavior is observed for the two SEI chemistries. It is in agreement with the two steps mechanisms in the Li-ion transport through the SEI. The first mechanism is the migration of the Li-ions through the solid phase of the SEI and the second is the solvation of the Li-ion in the electrolyte. The existence of the two mechanisms which have different temperature dependencies results in the two behaviors with the

Arrhenius relation. The migration of Li-ions through the solid state SEI can be linked to the lower temperature dependence behavior since migration current densities are linearly related to temperature [47]. The solvation process of Li-ions is assigned to the highly temperature behavior which follows the linear Arrhenius relation. Several modeling and computational studies presented results that the solvation of Li-ions in Li-ion batteries requires high activation barriers (≈40 kJ/mol) which are higher than the activation barrier for the migration of Li-ions through the SEI [48][49]. Although the studies in the literature were made for Li-ion batteries having graphite anodes which are based in intercalation anodic processes, the results we observed for metallic Li anodes are similar with different activation energies. The change in activation energies is due to the different structure of the SEI and the type of electrolyte in the Li\$SOCl_2$ and Li\$MnO_2$ cells we studied.

2.3.11. Section conclusion

The investigation of temperature dependence of the impedance response of the electrochemical processes in Li primary batteries was performed in this section. The Temperature-dependent Electrochemical Impedance Spectroscopy (T-dependent EIS) response showed an overall decrease in impedance and time constant values as the temperature increases. The degree of temperature dependence was different for the battery's electrochemical processes.

The high frequency EIS response showed high degree of temperature dependence. The impedance response in this region is assigned to the Li-ion transport processes through the Solid Electrolyte Interface (SEI). The EIS response showed two time-constants represented by two semicircles in the Nyquist plot. The two semicircles are related to the two-layer structure of the SEI.

We obtained the change in the resistive and capacitive behavior of this processes by fitting the EIS response to a charge transfer resistance connected in parallel to a Constant Phase Element (CPE). The resistance of the second semicircle showed the highest temperature dependence with high resistive values at low temperatures (-15ºC – 5ºC). Furthermore, the temperature dependence decreased as the temperature went above 35ºC. The time-constant

of this processes was low at low temperatures which increased drastically as the temperature increased. This increase in the time-constant indicated the increase in the process's kinetics as the temperature increased.

The logarithmic reciprocal of the resistance values was plotted against the temperature to investigate the Arrhenius behavior and to obtain the activation energy of the processes. The plot showed linear behavior at lower temperatures (-15ºC – 35ºC) and deviated at higher temperatures. The observed Arrhenius and non-Arrhenius behavior for the resistance values of the same impedance response indicated the existence of two mechanism for the Li-ion transport process.

The same region was investigated for different chemistry of metallic Li based battery Lithium Manganese Dioxide (Li\$MnO_2$). The resistive behavior of the same processes showed identical Arrhenius behavior at lower temperatures with deviations at high temperatures. There was also an increase in the value of the calculated activation energy which was related to the more stable structure of the SEI in Li\$MnO_2$ chemistry.

The observed two temperature dependence for the same processes in both Li\$SOCl_2$ and Li\$MnO_2$ chemistries supports what was presented in the literature for the Li-ion transport mechanisms through the SEI in Li-ion batteries. It is proposed that Li-ion is transported by the migration of Li-ion through the solid state SEI followed by the solvation of the Li-ion into the electrolyte.

The T-dependent EIS response of the other processes showed low temperature dependence. The middle frequency region which is assigned to the anodic charge transfer (Li oxidation) gave one semicircle which was fitted with a resistance and a CPE. The values of the resistance showed gradual decrease with corresponding capacitive increase as the temperature increased. Similar behavior was observed for the low frequency region which showed two semicircles with low degree of temperature dependence.

2.4. Non-linear Harmonic Analysis for Primary Lithium Thionyl Chloride (Li\SOCl$_2$) Battery

The Electrochemical Impedance data of primary Li batteries, except for narrow range of excitation amplitudes, suffers from non-linearity and non-stationarity which show incompatibilities with Kramer-Kronig test. The analysis of this behavior is performed in an attempt to understand the source of these behaviors and to relate them to the electrochemical processes of the battery.

Non-linear harmonic analysis involves the analysis of the voltage response signals in the frequency domain. It has been used in the literature to investigate the nonlinear characters of different electrochemical systems. Large perturbation excitation is used to obtain insight about the nonlinear processes in the studied system by the analysis of the response signal as a function of frequency. Darowicki et al. published a review which described the application of the harmonic analysis to study activation reactions, simple diffusion systems and corrosion systems [50]. They emphasized that harmonic analysis can be very useful in studying the kinetics of electrode processes simultaneously with EIS. Later Bosch et al. developed a new technique named Electrochemical Frequency Modulation which utilizes two sine waves of different frequencies as excitation and analyzes the response in frequency domain for nonlinear characteristics [51]. They showed that this technique can be used for instantaneous corrosion rate measurements under various corrosion conditions. Other corrosion studies utilized harmonic analysis to study the rate of corrosion for different systems [52][18].

Harmonic analysis was also utilized to investigate nonlinear processes in fuel cells. It was used for the diagnosis of dehydration, flooding and CO-poisoning processes as well as monitoring oxygen concentration and operation status of PEM fuel cells [19].

More recently, harmonic analysis was used for Li-ion batteries. Krewer et al. investigated the relation of the excitation signal amplitude to the observed harmonics for different types of Li-ion batteries. Temperature dependence and aging of the battery was related to the obtained harmonic responses. Moreover, studies on Li plating showed the ability of its

detection utilizing harmonic analysis along with EIS [53]. In another study, Schwartz et al. utilized harmonic analysis for Li-NMC batteries with moderate-amplitude excitation signals. They presented second harmonic spectra for the response signal at different SoCs and with aging of the cells along with the EIS. They showed how second harmonic at the low frequency regions can provide information about diffusion and charge transfer symmetry [54].

In this section, we show how non-linear harmonic analysis can be used to study the electrochemical processes in Li\$SOCl_2$ batteries. We will show that the passivation of metallic Li anodes as a nonlinear process is directly related to higher harmonic responses in the EIS. Furthermore, we investigate the behavior of the harmonics by applying high amplitude excitation signals. The harmonics will be also studied by variation of the State-of-Charge of the cell and under various temperatures.

2.4.1. Experimental Aspects of Non-linear Harmonic Analysis

As we mentioned in the introduction chapter, non-linear harmonic analysis is performed by transforming the time-domain voltage response signals into the frequency-domain. This was achieved by Fast Fourier Transform (FFT) of the separately recorded voltage signals. The measurement script was modified to simultaneously measure the impedance of the system and record the time domain voltage response at each frequency. The Fourier transforms were done within SciPy v0.15.1 fft module with Spyder v2.3.5.2 as the developing environment.

Figure xx. shows a generic frequency domain description of both current excitation and voltage response signals, both obtained in a non-averaged fashion in the time domain. After FFT, both signals are plotted as a function of the harmonic index. The zeroth position corresponds to the DC offset followed by the first, second and third harmonic etc. The first harmonic is typically referred to as the fundamental. The fundamental harmonic on the current corresponds to the AC excitation signal. The other harmonics have negligible values that correspond to the noise level of the instruments' signal generator. In a particular

case where a nonlinear voltage response is observed, the voltage response shows a DC offset at the zeroth position corresponding to the voltage of the battery as well as the expected fundamental harmonic, in addition to finite amplitudes over the noise floor of the instrument at the higher harmonics. The higher harmonics are the result of nonlinear behavior of the system and their presence preclude a Kramers-Kronig compatible EIS measurement.

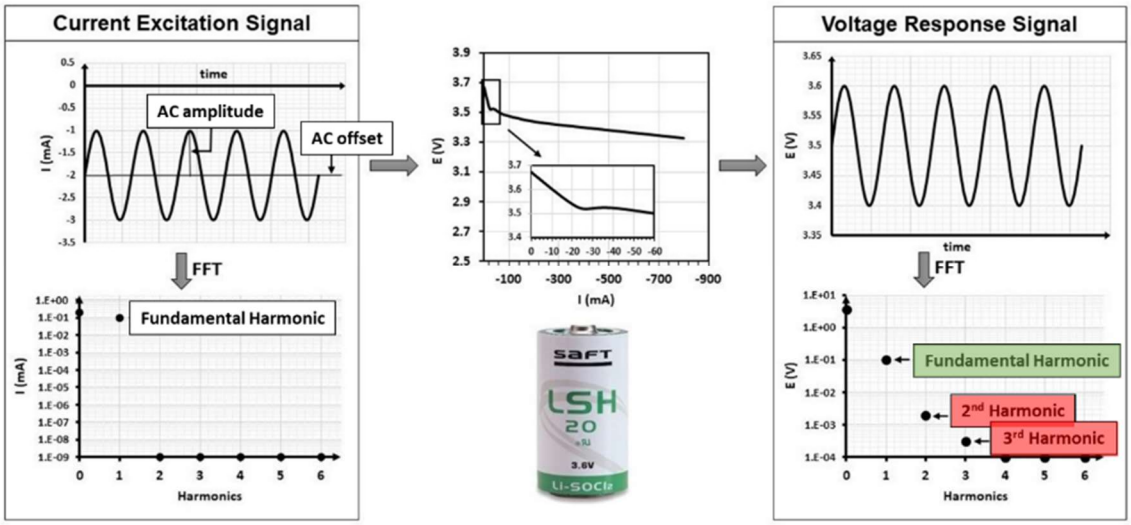

Figure 53. Galvanostatic-EIS while discharge method and harmonic analysis. Time and frequency domain of the current excitation signal (left) and voltage response signal (right).

In performing harmonic analysis, we first ensured that there are no nonlinear contributions from the instrument or the applied excitation signal. This was achieved by constructing a dummy cell with the equivalent circuit components that are chosen to be as close as possible to the fit results of the D-size cell at 80% SoC. The dummy cell was composed of one resistance connected in series to three resistor and capacitor in parallel combinations. G-EIS was performed with the same parameters used for the D-size cell and the harmonics of the voltage response signals were analyzed. The resulting EIS is shown in Figure 54(a). As can be seen from the Nyquist diagram, the dummy cell impedance resembles the

Li\$SOCl_2$ with three distinctive regions. The harmonics of the voltage response signal is also shown in Figure 54(b) in which only the principal occurs between (10^{-3} – 10^{-4} V) with other harmonics at a negligibly low level between (10^{-6} – 10^{-7} V).

This result shows that there are no harmonics coming from the instrument or as a result of the amplitude of the applied excitation signal when the sample is linear. The distinction between the harmonic spectra of the dummy cell and for the Li\$SOCl_2$ cells is the higher noise level. The higher noise level is expected due to the electrochemical reactions taking place during the discharge of the cell which does not exist in the passive components of the dummy cell.

The analysis of the excitation signals are also shown in Figure 54(c). The fundamental harmonic which represents the AC excitation signal is shown with the resulting harmonics up to its fifth multiple. It is clear from Figure xx for both cells that only the fundamental signal at (10^{-3} A) is present with the others at levels that are five orders of magnitude lower (10^{-8} A) which is the noise level of the measurement. The AA-size harmonics spectrum shows higher noise level than the D-size due to the smaller DC offset and AC excitation signals used. This analysis demonstrates that there cannot be any harmonics in the response signal forming as a result of our excitation signal.

(a) (b)

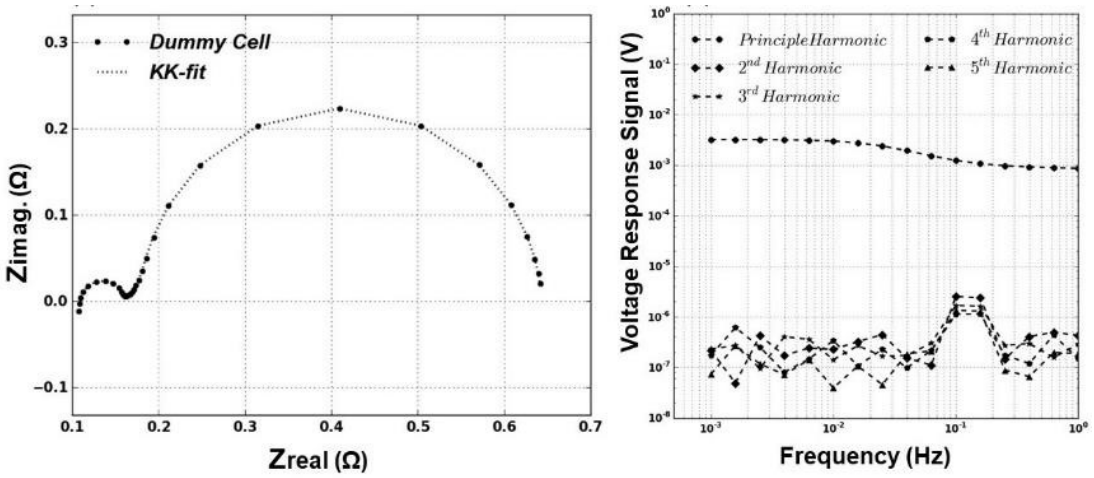

(c)

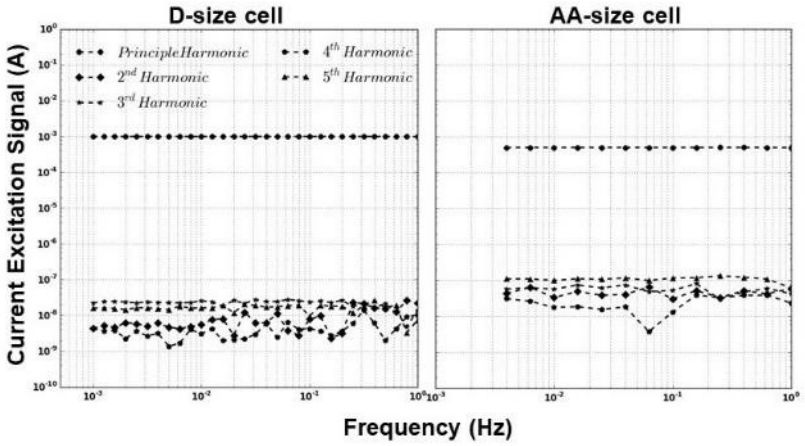

Figure 54. (a)Nyquist diagram for the dummy cell measured with 5mA AC excitation, (b)Harmonic spectrum for the voltage response of the dummy cell, (c) Harmonics spectra for the current excitation signals for both D and AA size cells

2.4.2. Non-linear Harmonics in Li\SOCl$_2$ Batteries

Here we analyze the frequency domain harmonics obtained by transforming the time domain voltage response of the impedance measurements of the Li\SOCl$_2$ battery which was shown in section 2.1. The measurements were obtained with low and high amplitude

DC-offsets. Harmonic analysis of the voltage response signals for low DC-offset measurements (passivated) and low DC-offset measurements (de-passivated) D-size and AA-size cells are presented in Figure 55. Harmonic spectra for measurements in which the cell is passivated are shown in Figure 55(a). Spectra for measurements with passivation treated cells and with moderate and high negative DC offset are shown in Figure 55(b and c) respectively.

The harmonic spectra show linear behavior for the measurements where passivation was treated and a high negative DC offset was applied, see Figure 55(c). The response contains the fundamental harmonic component at (10^{-3}) with remaining harmonics at negligible levels (10^{-5}) for both cells.

The nonlinear responses shown in Figure 55(a) were obtained for both cells while maintaining a high degree of passivation. The response contained the principal harmonic accompanied with appreciable amplitudes of the second harmonic. The remaining harmonics were at undetectable amplitudes. We refer this behavior to the passivation effect on the anode. The presence of the passivation layer during the measurement causes nonlinear behavior which results in the appearance of the second harmonic.

The second nonlinear response was observed for the cells in which the passivation layer was treated before the measurement but moderate DC offsets were applied during the measurement, see Figure 55(b). In this case, the second harmonic shows appreciable amplitudes at the lower end of the frequency range (<10mHz) for the D-size cell and at frequencies lower than (<1Hz) for AA-size cell. This analysis shows that the moderate offset was not high enough to prevent passivation layer formation while the measurement is being performed.

One concern about the harmonic response is regarding the drift. Voltage drift would also manifest itself in the harmonic response, especially in the low frequency region. As can be seen in figure 55(b) for both cells, the lower frequency harmonics are larger, slowly decaying towards the higher frequencies. This drift is due to the passivation layer forming through the experiment and is not visible in the high or low offset cases since the

passivation layer is not present or always present in the high and low offset cases respectively.

It should be mentioned that the change in the voltage of the cells during the measurement due to the applied DC offset was not enormous. This is related to the unique chemistry of the Li\$SOCl_2$ which shows very stable voltage throughout discharge. The calculated voltage drifts for the measurement where passivation layer is present was 50mV for D-size and 30mV for AA-size cells. The voltage drift for passivation treated cells with moderate DC offset was 70mV for D-size and 30mV for AA-size cells while less than 2mV drift was observed for the high DC offset measurements.

Voltage drifts of the measured voltage signal at 4mHz for all measurements also show small values. Drift of 2.5mV was observed for both passivated cells. 3.8mV and 7.5mV were seen for D-size and AA-size cells respectively with moderate DC offset whereas less than 1mV for high DC offset measurement for both cells. These values were not corrected prior to FFT for the harmonic analysis.

These results show the ability of harmonic analysis as well as the accurate measurement of EIS for Li\$SOCl_2$. They demonstrate the ability of SEI (passivation) layer detection using the harmonic analysis accompanied with the EIS of the cell and especially highlights that the nonlinear part of the impedance response contains information regarding the SEI.

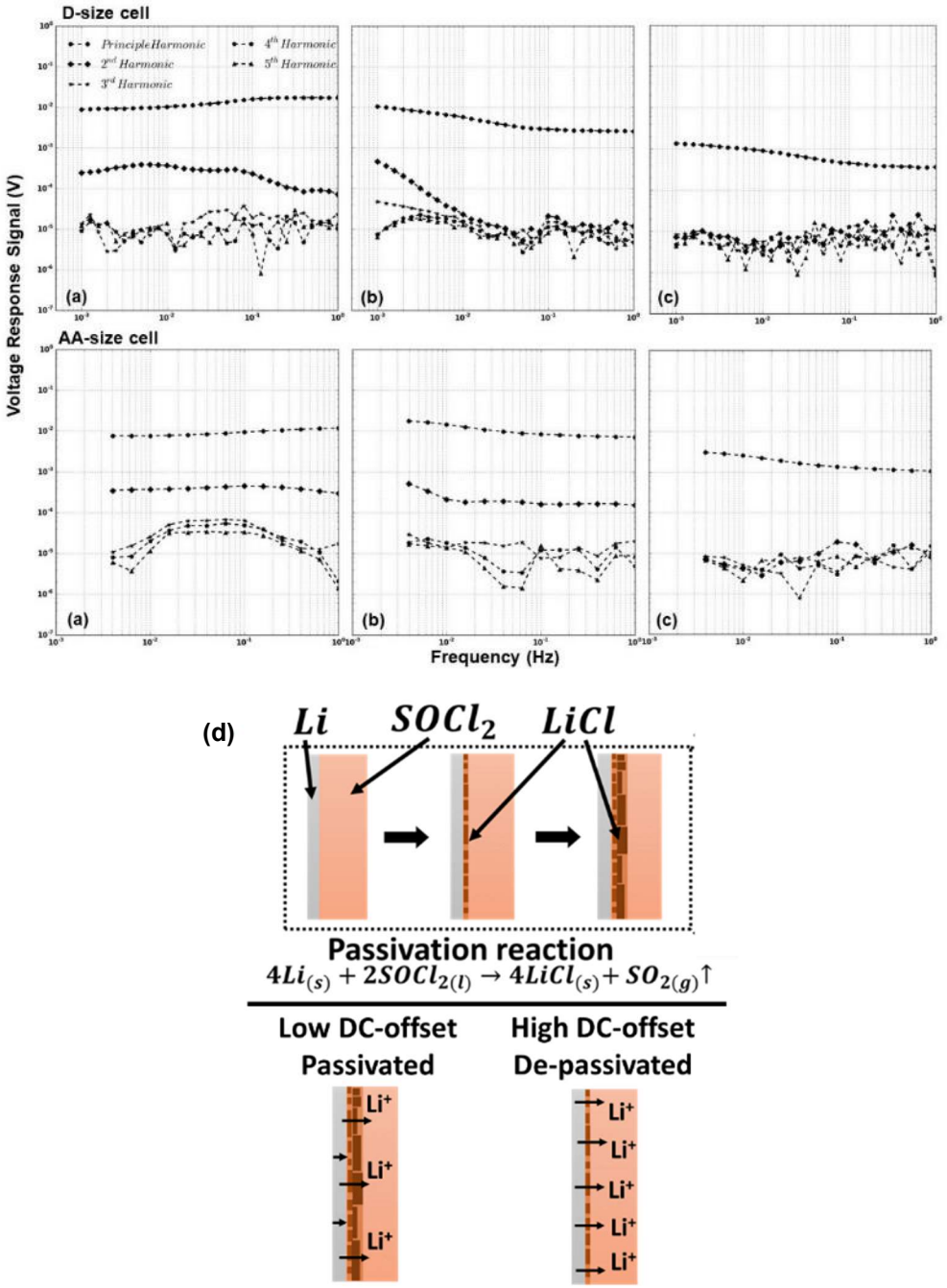

Figure 55. Harmonics spectrum for the voltage response signal from 1Hz to 1mHz for D-size cell and from 1Hz to 4mHz for AA-size cell. (a) passivated cell (D-size: -2mA, AA-size: -0.1mA), (b) moderated DC-offset (D-size: -10mA, AA-size: -5mA), (c) high DC-offset (D-size: -50mA, AA-size: -10mA) (d) Schematic representation of the passivation processes and the high and the low DC-offset effect on the passivation layer

2.4.3. Harmonic Analysis with High AC-Amplitude Excitations

The harmonic spectra which are shown in previous section were as a function of DC-offset. Their presence was related to the degree of the passivation of the cell. Further harmonic responses can be obtained by changing the AC parameters of the excitation signal. Higher AC amplitudes can be utilized to obtain non-linear harmonics. The excitation can be done at Open Circuit Potential (OCP) which will force the cell to undefined charging reactions or with DC-offset as was utilized to obtain linear EIS. The undefined charging reactions cause the non-linear response which shows distortions in the voltage response signals. The DC-offset causes the change in the voltage level of the cell which results in voltage drift. Both behaviors are demonstrated in Figure xx.

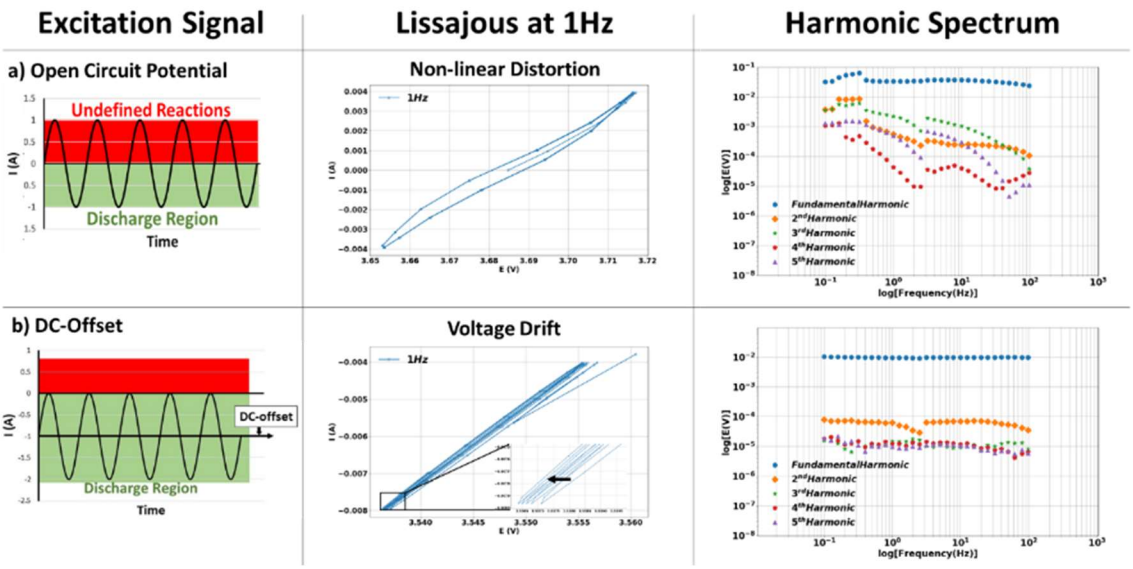

Figure 56. Harmonic analysis for excitation at open circuit and with DC-offset

It should be taken into consideration that the high AC amplitudes also cause a drift in the voltage response which causes a mixed non-stationary and non-linear behavior. The separation of each behavior is hard to achieve without further mathematical treatment. As shown in Figure 56, the non-linear behavior is observed with distortion in the Lissajous

plot which shows high amplitudes of harmonic signals at the full frequency range. On the other hand, the non-stationary behavior which involve voltage drift shows an increase in the amplitude of the second harmonic signal. the investigation of the behavior of these harmonics is done with variation of the AC and DC signals.

The analysis of the harmonics by variation of the AC excitation amplitudes at OCP is shown in Figure 57. The values of the harmonics show increase as the AC excitation amplitude increases. The increase is seen for all harmonics at the full frequency range. The increase in the harmonic levels reaches constant value after 5mA. This behavior is originating from the positive excitation of the Li\$SOCl_2$ battery which caused undefined reactions that increase the distortion of the voltage response signal as the amplitude of the excitation is increased.

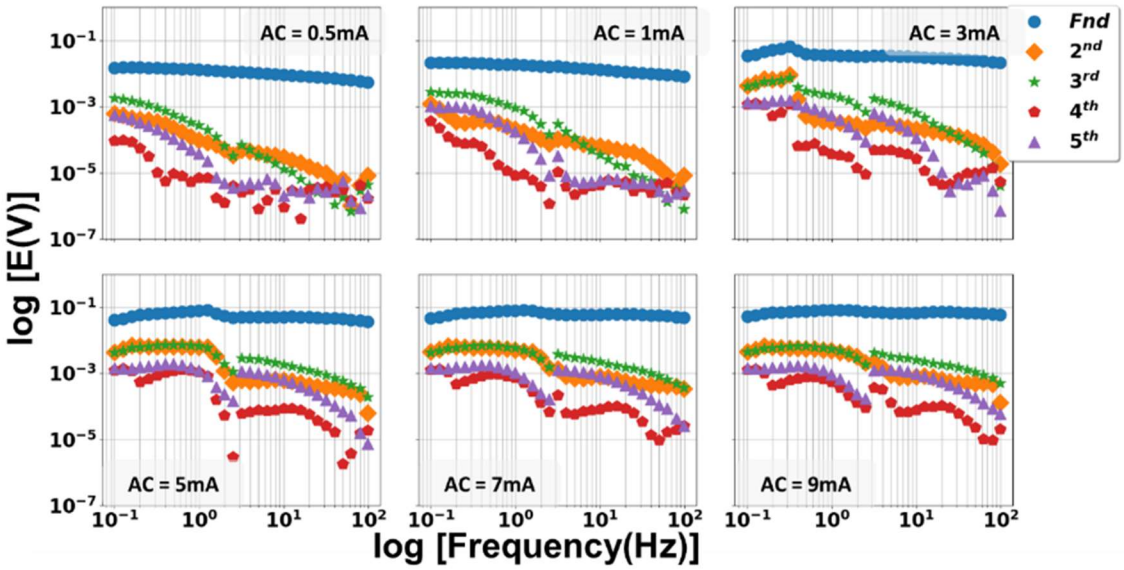

Figure 57. Harmonic spectra for excitation at Open Circuit Potential with increasing the excitation AC amplitude

The analysis of the harmonics was also obtained for the variation of the DC-offset amplitudes at similar AC excitation 0.5mA. The results show opposite behavior to the AC amplitudes. The harmonics decreases as the DC-offset increases. It is observed that linear behavior is obtained after 5mA of DC-offset amplitude. These results support the idea that the harmonics obtained for the nonlinear behavior of the Galvanostatic-EIS measurements for Li\$SOCl_2$ cells are caused by the passivation reaction of the anode. The higher the DC-offset applied the more the passivation reaction causing the non-stationarity in inhibited. However, the noise level of the voltage response increases at the high DC-offset values. The increase in the noise level indicates the application of abusive parameters to the cell.

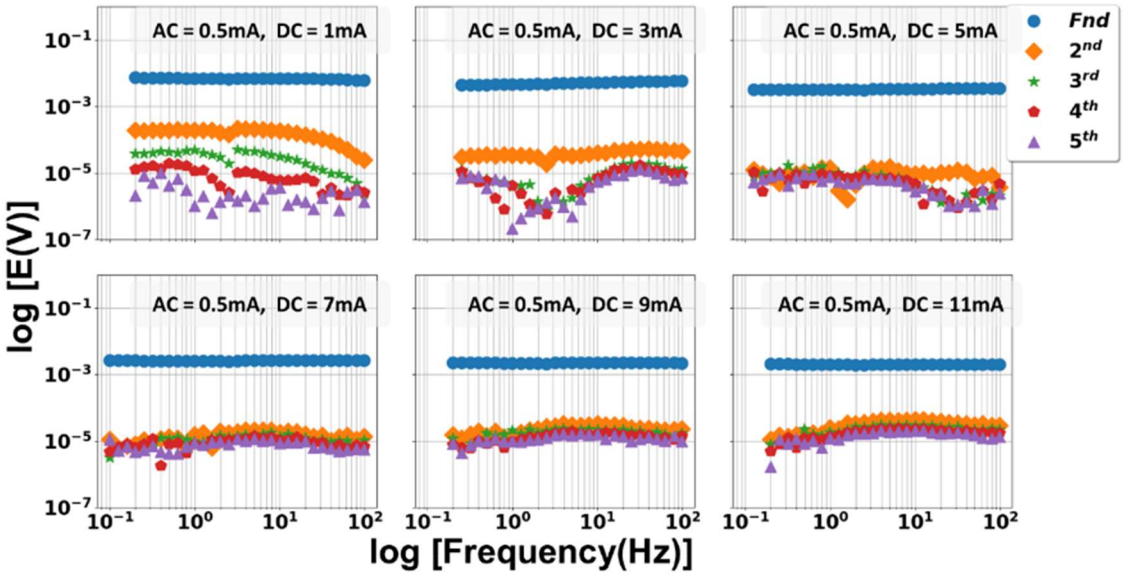

Figure 58. Harmonic spectra for AC excitation of 0.5mA with increasing the amplitude of the DC-offset

2.4.4. Analysis of the Harmonics by Temperature Variation

We have shown previously that the kinetics of the electrochemical processes increases and their impedance decreases as the temperature of the cell increases. The temperature dependence is also observed for the obtained harmonics. Figure 59 (a) shows the results of excitation at Open Circuit Potential which shows the decrease in the harmonics as the

temperature increases. The same trend is observed for the excitation with DC-offset. The harmonics are inversely proportional with temperature. However, the level of the harmonics is decreased more at the OCP excitation. This indicated that the temperature dependence is more effective for the non-linear processes than for the non-stationary behaviors.

(a)

(b)

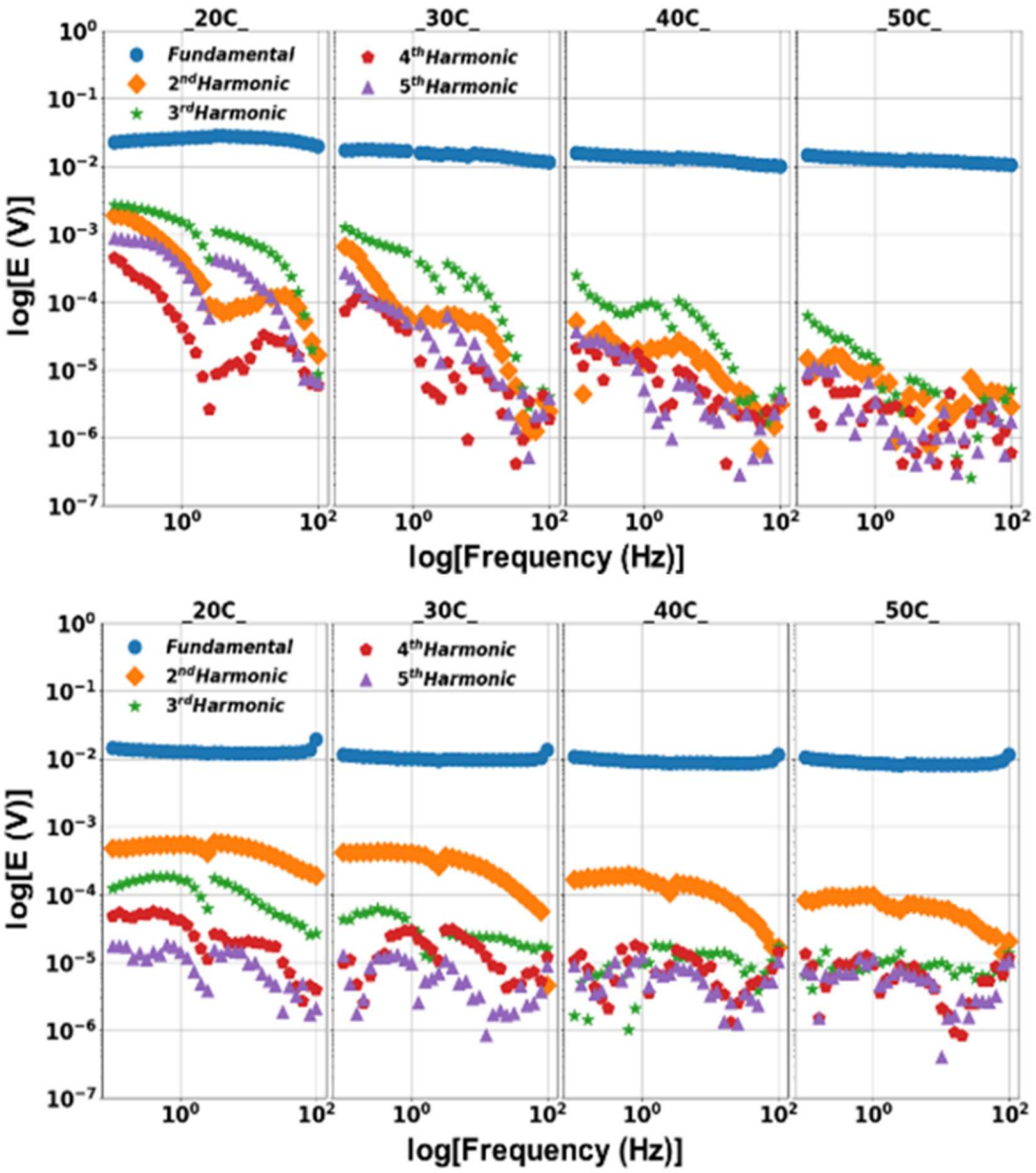

Figure 59. Change in the Harmonic spectra as the temperature increases for (a) Excitation with open circuit potential, (b) Excitation with DC-offset

The harmonics at OCP excitation almost decrease to the noise level at 50ºC whereas the second harmonic is persistence for the DC-offset excitation at the same temperature. This result can be related to the origin of the harmonics at each excitation. In the DC-offset excitation, the non-linear response caused by the voltage drift is the result of the chemical passivation reaction. The reaction kinetics increases as the temperature increases which will cause the decrease in the voltage drift level. However, the voltage drift will be persistence even at high reaction rate due to the continuous passivation reaction.

In the OCP excitation, the large decrease in the non-linear response can be related to the change in the temperature dependent electrochemical processes of the cell. We have shown in the T-dependent EIS studies for the Li\$SOCl_2$ battery that the increase in the temperature of the cell causes the decrease in the impedance of the processes. As a result, the decrease in the impedance will cause a decrease in the voltage harmonic amplitude since the impedance and the voltage are directly proportional by Ohm's low.

2.4.5. Analysis of the Harmonics by State-of-Charge Variation

The Harmonic analysis shows also variations by changing the State-of-Charge (SoC). Figure 60 shows the harmonic spectra for 90, 70, 40 and 20 SoCs. As can be seen the amplitudes of the harmonics differ at each state of charge. There is no linear trend for the variation. The harmonics show high amplitudes at 90 SoC which decreases going to 70 SoC. This decrease is expected since the decrease in the amount of the electrolyte decreases the degree of the passivation reaction in the Li anode. The harmonics response increases as the SoC decreases, though there is a difference in the shapes of the harmonics moving toward the lower SoCs.

The difference is on the constant increase in the harmonic amplitudes as the frequency decreases in the lower SoCs. The harmonics at the high SoCs did not show this constant increase. This difference can be related to the origin of the harmonics obtained. The constant increase is known to be related to the non-stationarity in the signal which is

expected as the SoC decreases. The stability of the voltage at the lower states of charge is low due to the depletion of the cell's components.

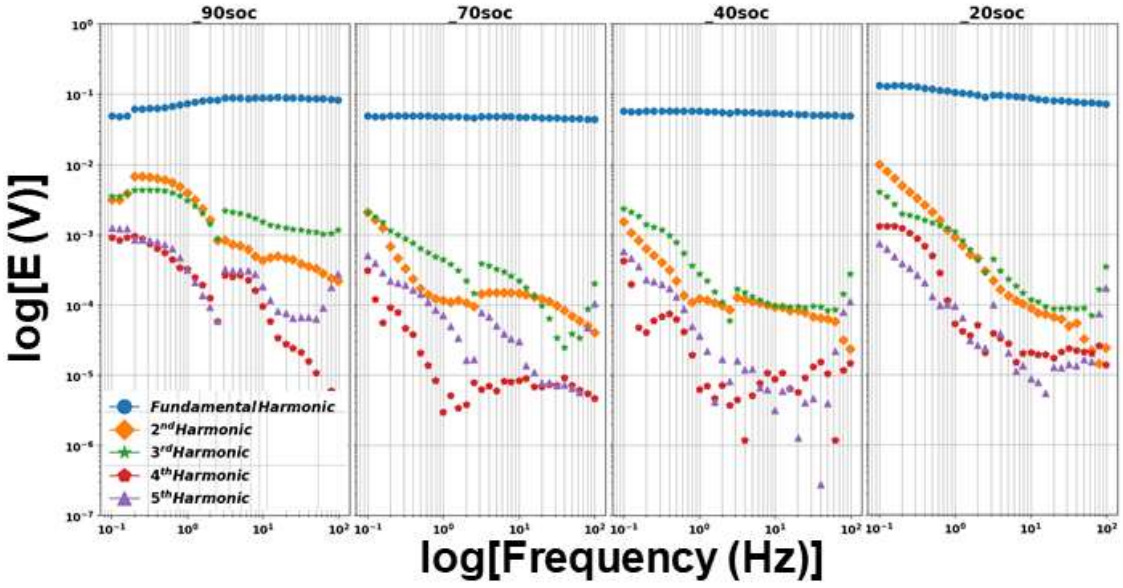

Figure 60. Change in the Harmonic spectra as the State-of-Charge decreases

2.4.6. Section Conclusion

In this section we analyzed the non-linear response of the Electrochemical Impedance data for the Lithium Thionyl Chloride (Li\SOCl$_2$) battery by means of non-linear harmonic analysis. The transform of the time domain voltage response signal to the frequency domain was achieved by Fast Fourier Transform. The results showed higher harmonics response for the EIS data obtained from the passivated cells. The origin of the harmonics was related to the effect of the passivation reaction on the voltage stability of the cell. The passivation reaction caused voltage drifts which appeared as second harmonic signals in the non-linear harmonic spectra.

The investigation of the harmonics was also achieved through the excitation with higher AC signals at Open Circuit Potential (OCP) and different amplitude of DC-offset. The excitation at OCP showed distortions in the Lissajous plots and high amplitude for almost

all harmonics. However, the DC-offset excitation showed mostly an increase in the second harmonic amplitudes. Investigation in the relation of the excitation amplitudes and the obtained harmonics amplitudes was also achieved. The results showed the increase in the harmonics level as the amplitudes of the AC excitation signals increase. The increase in the level of the harmonics was related to the non-linear response from the undefined reactions caused by the positive excitation of the cell. Conversely, the level of harmonics for the DC-offset excitation showed inverse proportional with the increase in the amplitude which support the relation of these harmonics to the passivation of the cell.

Finally, the temperature and the State-of-Charge dependence of the harmonics was investigated. The results show the decrease in the level of the harmonics as the temperature increases which is related to the decrease in the impedance of the processes. The direct relationship between the impedance and the voltage response results in the decrease in the harmonic amplitude levels as the temperature increases. Moreover, the harmonics did not show direct relationship with the SoCs of the battery. Instead, the harmonics level showed higher values at the highest and the lowest SoCs. However, the shape of the harmonic was different in the harmonic spectra. At lower SoC, the harmonics showed constant increase as the frequency decreased which was related to the instability of the voltage levels at the low SoC of the battery.

Chapter 3

3. Zero-Free-Parameter Electrochemical Impedance Spectroscopy based Modeling of Electrochemical Energy Storage Systems

(This part is also described in

- **Mohammed Ahmed Zabara** and Burak Ulgut, *Electrochemical Impedance Spectroscopy based voltage modeling of Lithium Thionyl Chloride (Li\SOCl2) primary battery at arbitrary discharge, Electrochimica Acta 334 (2020) 135584*
- **Mohammed Ahmed Zabara**, Can Berk Uzundal, and Burak Ulgut, *Performance Modeling of Unmanaged Hybrid Battery/Super-capacitor Energy Storage Systems, Journal of Energy Storage 43 (2021) 103185*

Reproduced with permission from [55] and [56] Copyright 2021)

As was mentioned in the introduction chapter, Zero-free-parameter modeling methodology is very accurate in determining the dynamic voltage response of the Electrochemical Energy Storage systems under any desired regime. The method is based on the Electrochemical Impedance Spectroscopy (EIS) of the systems. It has been shown to accurately determine the voltage response of single cells of secondary batteries and supercapacitor [57][58]. In this chapter, we will show the applicability of the method to primary batteries and hybrid combination of secondary Battery/Supercapacitor systems.

Briefly, the steps of the modeling approach are summarized in Figure 61 which is explained in details in Ozdemir et al. [57] along with its error analysis [58]. First, the desired current profile is transformed to the frequency domain by Fast Fourier Transform (FFT). Second, accurate EIS of the system is measured and multiplied by the current response in the frequency domain. As a result, we will have the voltage response of the system in the frequency domain. Finally, the voltage response is inversely transformed to the time domain by (iFFT) and a DC response of the voltage is added at the State-of-Charge of the system.

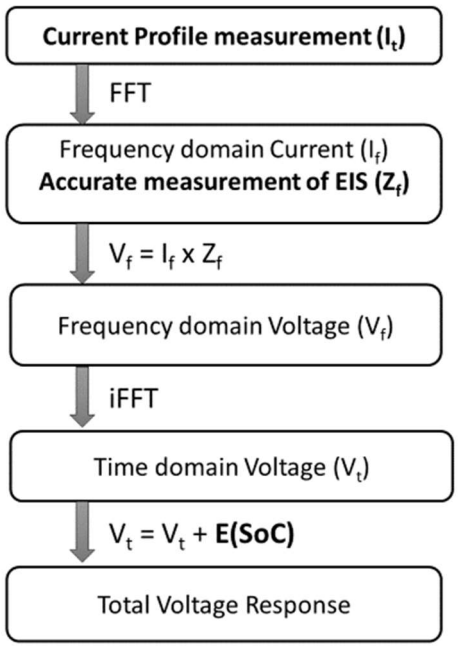

Figure 61. Zero-free Parameter Modeling Steps, bold highlighted steps are measurements other steps are mathematical operations

In this chapter, method will be developed further and employed in modeling the voltage response of the characterized primary Li batteries, Lithium Thionyl Chloride (Li\$SOCl_2$) and Lithium Manganese Dioxide (Li\$MnO_2$). The development will involve the correction for the voltage recovery and delay behaviors caused by the effect of the Solid Electrolyte Interface. Afterwards, we will also develop and employ the method to simulate the current distribution and the voltage response of the hybrid Li-ion battery supercapacitor systems. The method will be enhanced by an optimization algorithm which will optimize for the current distribution among the systems which will enable for the voltage calculation. We will also present performance metrics to evaluate for the combination of the systems at different conditions.

3.1. Voltage Modeling of Li\$SOCl_2$ battery

Even though, understanding their voltage behavior under several discharge conditions is crucial for its correct implementation, literature is very scarce in modeling studies for Li primary batteries. Modeling studies performed are one- and two-dimensional first-principle methods in which the voltage behavior of the cell is predicted at constant discharge [59][60][61]. The number of free parameters in these models cast doubt on the validity of the approaches. Moreover, modeling Li primary batteries under constant discharge does not contribute in understanding their response to real-life discharge regimes which include discharge currents with various amplitudes.

In this section, we will demonstrate how the voltage of primary Li\$SOCl_2$ battery can be predicted under different dynamic discharge regimes using Electrochemical Impedance Spectroscopy (EIS) based model. We employ Zero-free-parameter modeling methodology which is free of adjustable parameters and uses the impedance data as is. We further improve the modeling methodology by doing the necessary corrections for the deviations caused by the formation and breakdown of the passive layer. These corrections are required for lithium anodes used in the primary batteries as compared to the alloys used in the secondary batteries. Additionally, we study the voltage response of the cell at different States-of-Charge (SoC). We first employ the method to Li\$SOCl_2$ battery in which the SEI

(passivation of Li anode) has negative effects on the voltage response. Then to show the applicability of the method to other chemistries of primary Li batteries, we perform the same procedure for Lithium Manganese Dioxide (Li\MnO_2) battery.

3.1.1. Effects of the Solid Electrolyte Interface on the Voltage Response of Li\$SOCl_2$ battery

As presented in chapter 2 regarding the EIS characterization of primary Li, the impedance of the transportation of Li-ions through the Solid Electrolyte Interface (SEI) plays important role in the operation of the battery further influencing the voltage behavior of the battery. In Li\$SOCl_2$, the effect is severely seen at the initial operation in which the transport of the Li-ions is inhibited by the SEI. The transport of the Li-ions requires the destruction of the SEI which open pathway for the Li-ion to diffuse and reach the electrolyte [46]. This process causes a voltage delay response which is shown in Figure xx. After operation, the demolished parts in the SEI allow for the reaction between Li and the electrolyte $SOCl_2$ forming crystals of LiCl. This reaction is known as the passivation reaction. This process causes the voltage recovery behavior in which the voltage increases slowly to reach the open circuit potential level which is also shown in Figure 62.

This effect is the result of metallic Li utilization in very reactive medium such as $SOCl_2$. In simulating the voltage response of the battery to a specific charging discharging regime this behavior should be taken into consideration which as shown in Figure xx has different degrees at different discharge currents.

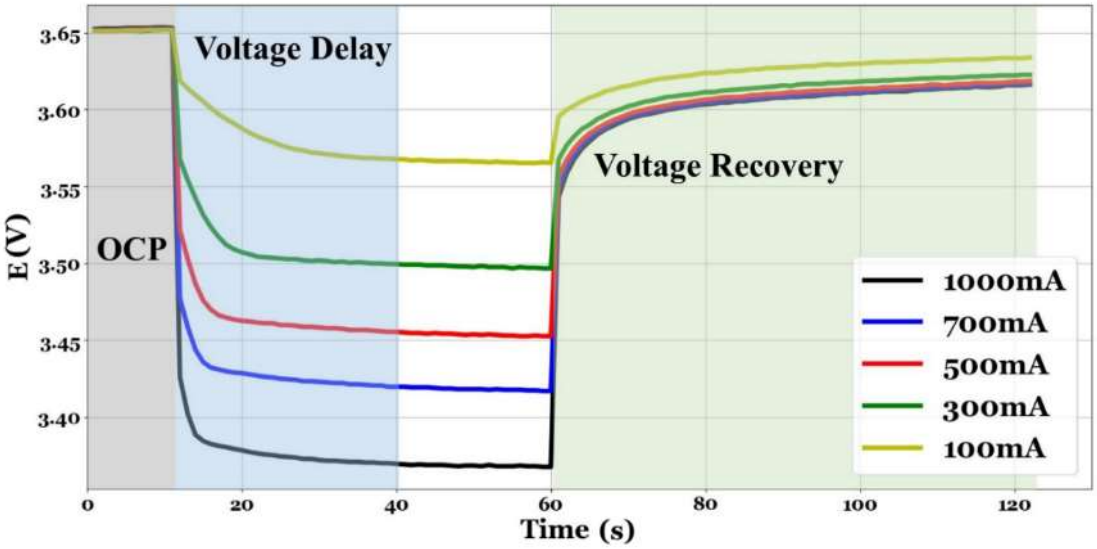

Figure 62. Voltage response of Li\$SOCl_2$ at OCP + constant discharge currents ranging from 100mA to 1A followed by zero current

3.1.2. Experimental Measurements and Modeling Methodology

In this section, the experimental measurements which represent the inputs of the modeling method, the steps of the method and the specification of the used cells are explained.

3.1.2.1. Electrochemical Impedance Spectroscopy Measurements

EIS measurements were done in a galvanostatic mode at discharge. Direct Current (DC) is applied along with the Alternating Current (AC) excitation signal as shown in Figure 64 (Input[1]). Gamry Interface 1000E was used for obtaining the EIS data. In all EIS measurements, -50mA DC offset was used along with 5mA AC excitation signal. The measurement script was adjusted to measure the impedance at the required frequencies. The frequency window was linearly spaced between 0.5Hz to 940µHz which was obtained from the FFT output of the current profiles. The highest frequency in the window is half of the sampling rate (1 second) and the lowest is the inverse of the length of the profile. The total time for EIS measurement was 26,316 seconds. For the state of charge (SoC)

experiments, each EIS measurement discharged the cell by 2.7% of the nominal capacity. The cell was discharged with -100mA between the EIS measurements in a controlled manner. This allowed for the investigation of the EIS until 30% SoC in which cutoff voltage (2.5V) was reached.

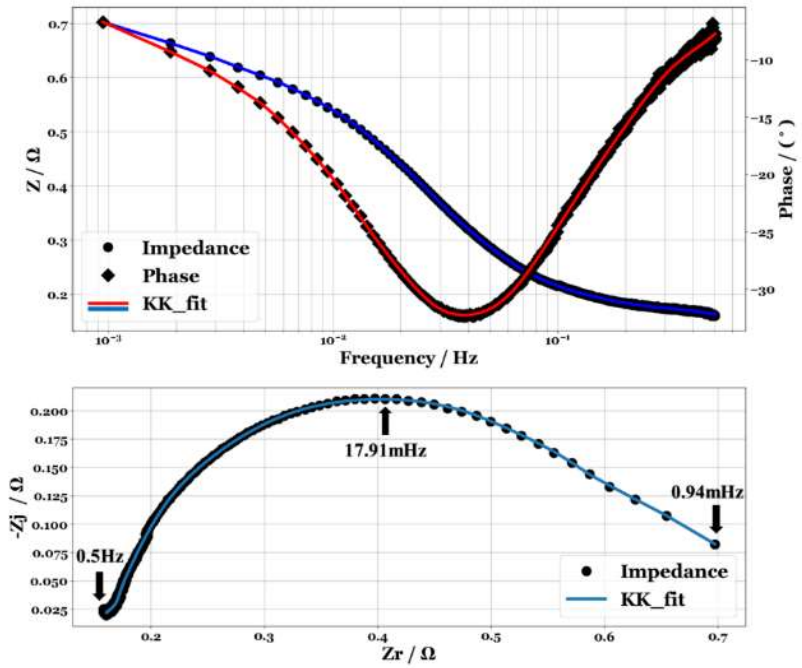

Figure 63. Bode and Nyquist plots for the EIS of Li\$SOCl_2$ at 85% SoC at the corresponding frequencies of the discharge current profile, Kramers-Kronig test is applied to check for the linearity and stability of the obtained data

3.1.2.2. Modeling Methodology

The steps of the modeling process are shown in Figure xx. In the process, the first step after obtaining the EIS (Input[1]) of the cell is to Fast Fourier transform (FFT) the current profile (Input[2]). The second step is to multiply the impedance values by the current values at every frequency of interest. This result, according to Ohm's law, in the voltage response of the cell at the frequency domain. Inverse-FFT is performed to the frequency domain voltage response to obtain the time domain voltage response of the cell. Finally, correction

of the voltage response for the voltage recovery caused by the passivation reaction is done to obtain the accurate voltage response.

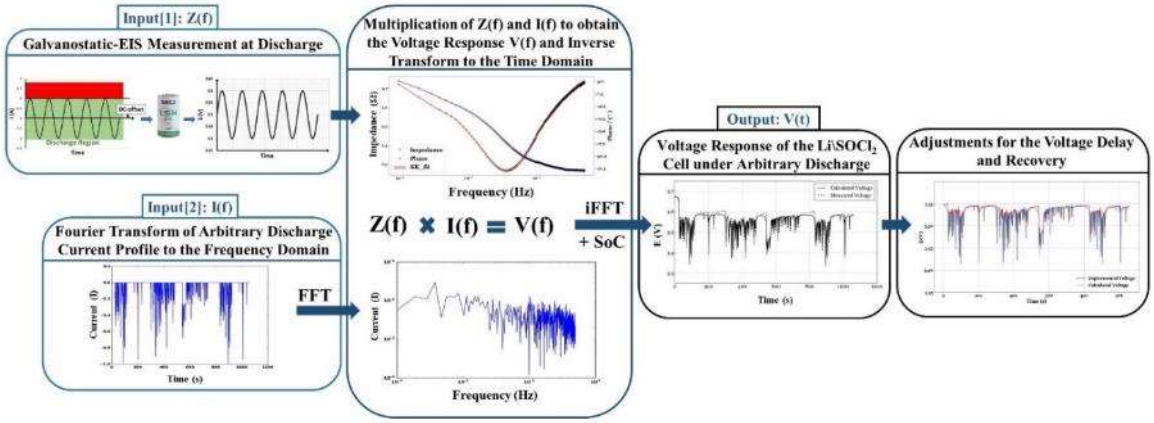

Figure 64. EIS-based modeling methodology for predicting the voltage response of Li\$SOCl_2$ cell at arbitrary discharge. Input(1) is the EIS measurement of the cell, Input(2) is the arbitrary discharge profile. The Output is the time domain voltage response for the applied profile.

3.1.2.3. Primary Li Batteries

Commercially available Li/$SOCl_2$ and Li/MnO_2 batteries were used. For Li/$SOCl_2$ (SAFT-LSH20) D-size spiral cells were used in all the measurements. The cell has 13Ah capacity with 3.67V open circuit potential. For Li/MnO_2 batteries (Maxell CR2032) coin cell was used with 220mAh and 3.0V open circuit potential.

3.1.2.4. Current Profiles

The current profiles were chosen from published Environmental Protection Agency (EPA) profiles [62]. The first is Heavy Duty Urban Dynamometer Drive Schedule (HDUDDS) and the second is Highway Fuel Economy Test Drive Schedule (HighwayFET). These

profiles are published as arrays of speeds in time domain. Obtaining the time domain current profile from the speed time domain profile was done by calculating the local accelerations as simple two-point finite differences. Accelerations were normalized to have the highest acceleration level to be unity. The power is assumed to be directly proportional to the current drawn from the batteries. Because this study explicitly employs primary batteries, charging currents were replaced with zeros. The maximum discharge current amplitude was adjusted to -500mA as shown in Figure 65. In the initial modeling results, a DC-offset was applied along the current profiles to prevent the cell from falling into voltage recovery behavior caused by the passivation of the anode at open circuit. The experimental voltage response for the current profiles were recorded by Gamry Interface 1000E using adjusted measurement script.

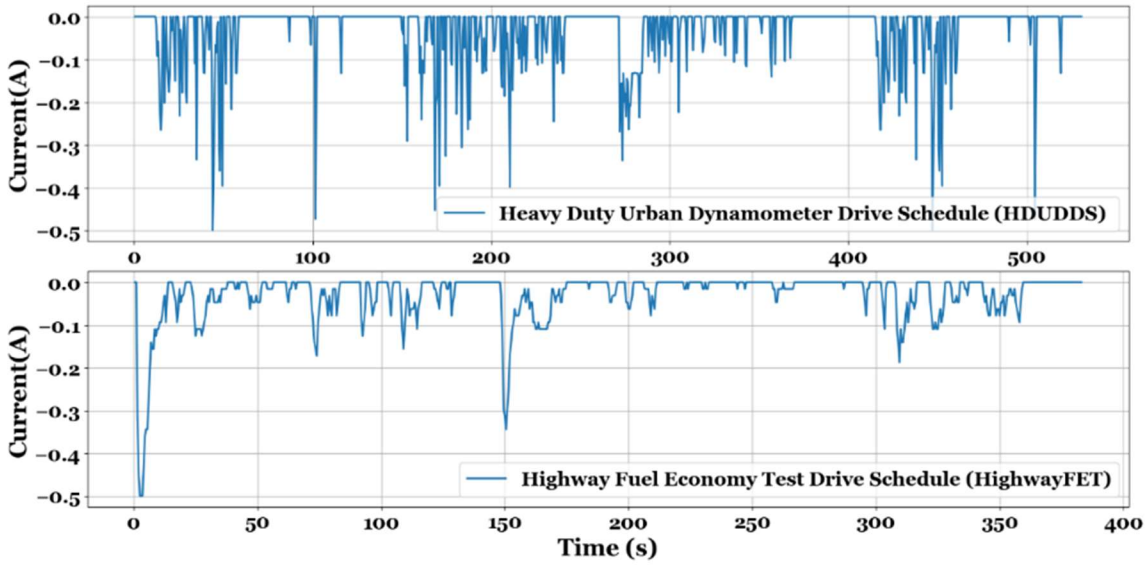

Figure 65. Environmental Protection Agency current profiles, Heavy Duty Urban Dynamometer Drive Schedule (HDUDDS) [Up] and Highway Fuel Economy Test Drive Schedule (HighwayFET) [Bottom], charging currents were replaced with zero currents to suit primary battery conditions

3.1.3. Voltage Response with DC-offset

First, we employed the method to the battery with the current profiles recorded under a DC-offset. The aim of the DC-offset was to minimize the effect of the voltage recovery caused by the passivation reaction of the SEI. The calculated and the experimentally measured voltage response of the Li\$SOCl_2$ to the HDUDDS and HighwayFET current profiles with the DC offset are shown in Figure xx and Figure xx respectively. The starting voltage is around 3.55V due to the applied DC-offset. As can be seen, there is good overlay between the calculated and the experimentally measured values. The proportional errors for both profiles which are shown in Figure 66 and Figure 66 (bottom) are less than 1% for both profiles.

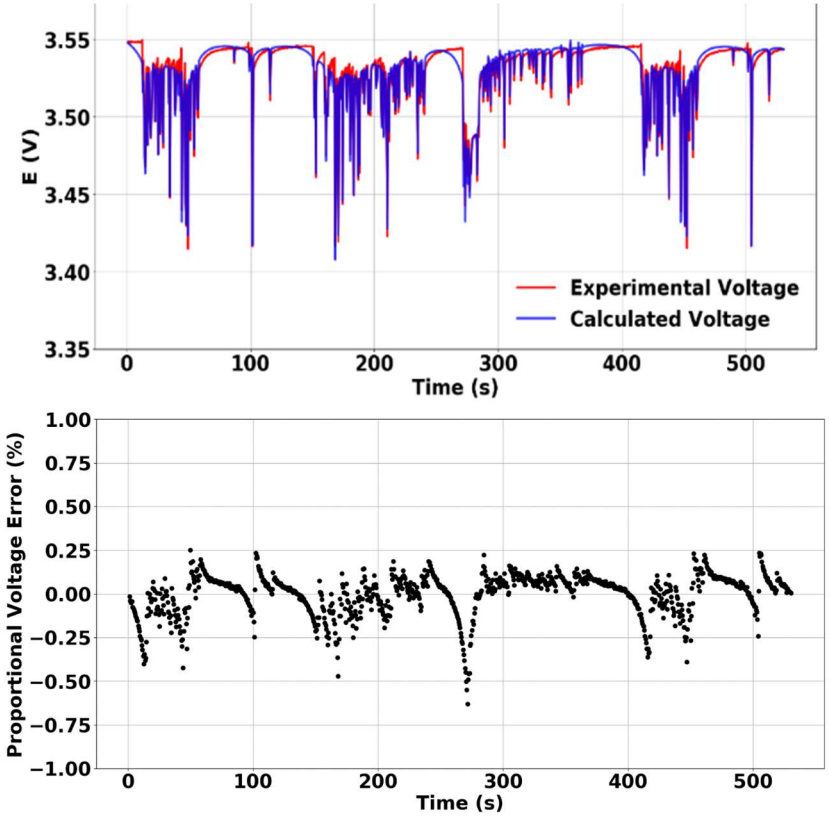

Figure 66. Calculated and measured voltage responses (Up) and percent proportional voltage error for the calculated voltage response (Bottom) of the Li\$SOCl_2$ cell plus -50mA DC-offset for HDUDDS.

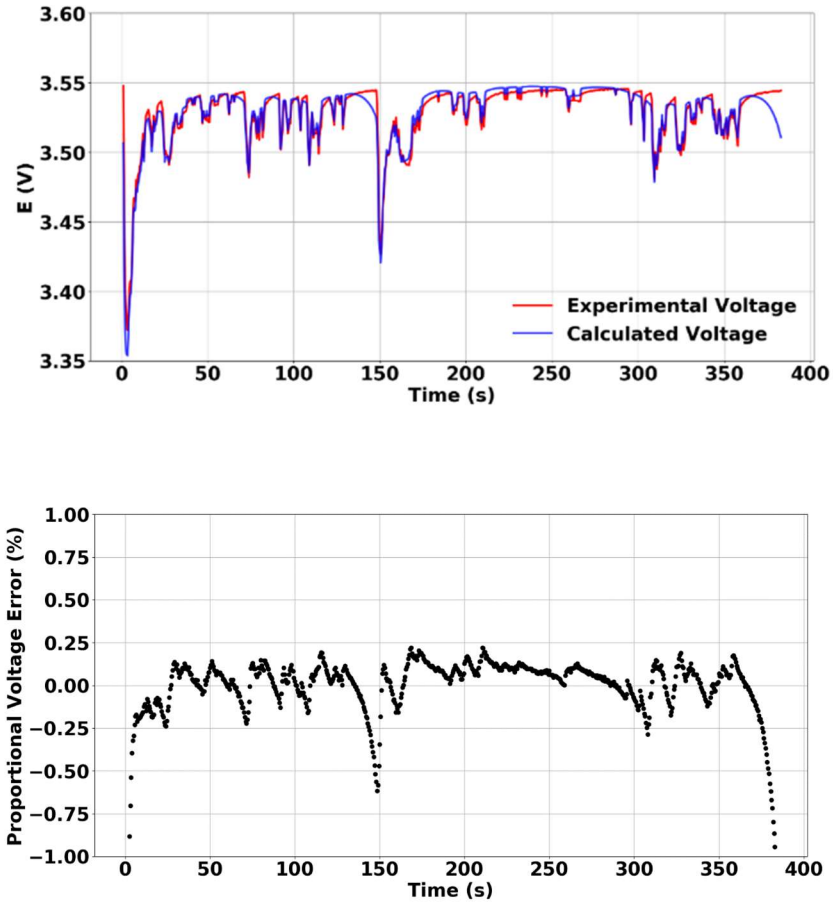

Figure 67. Calculated and measured voltage responses (Up) and percent proportional voltage error for the calculated voltage response (Bottom) of the Li\$SOCl_2$ cell plus -50mA DC-offset for HighwayFET.

3.1.4. Voltage response at Open Circuit Potential

Although there is good agreement between the experimental and the simulated results for the current profiles obtained with a DC-offset, the voltage response of the battery starting from the Open Circuit Potential (OCP) is required. For that we performed the same procedure starting from the OCP without application of any DC-offsets.

The voltage response at OCP results showed higher proportional errors which can be seen in the overlay of the calculated and the experimental voltages shown in Figure 68 and Figure 69. As can be seen, the simulated voltages deviate from the experimental ones at zero current segments which is related to the voltage recovery caused by the passivation reaction. During zero current (recovery), the calculated voltage stays roughly constant at a certain voltage while the measured increases with time. This deviation at the zero currents should be corrected by adjustments in the voltage response specifically at these regions based on the voltage calculated from the calibration data.

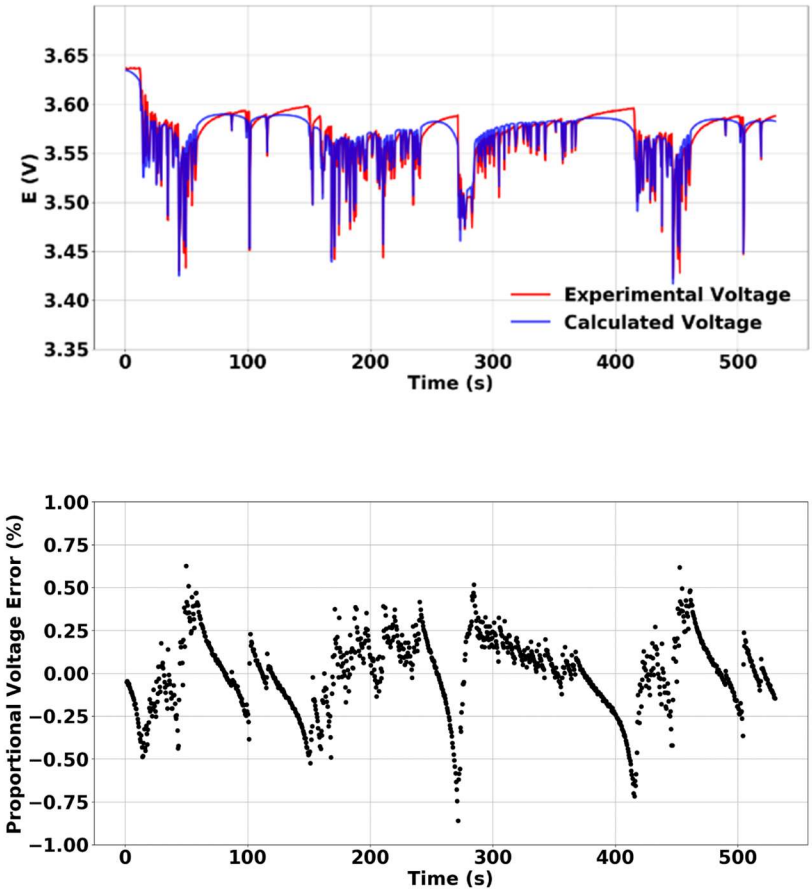

Figure 68. Calculated and measured voltage responses (Up) and percent proportional voltage error for the calculated voltage response (Bottom) of the Li\$SOCl_2$ cell for HDUDDS.

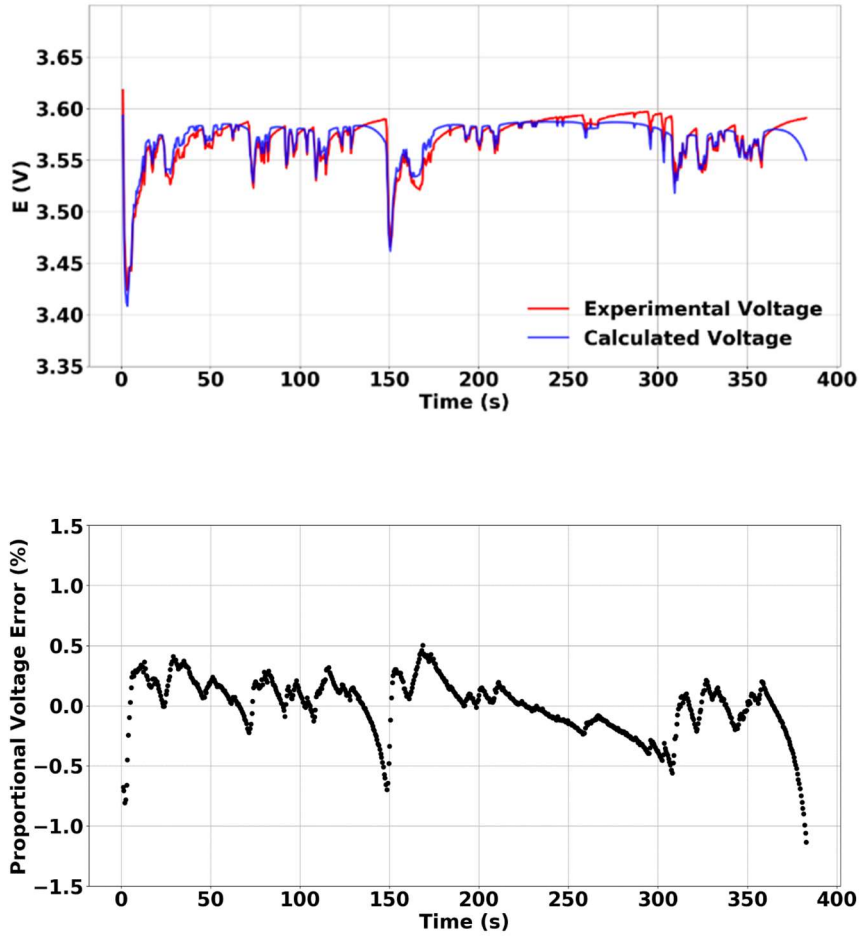

Figure 69. Calculated and measured voltage responses (Up) and percent proportional voltage error for the calculated voltage response (Bottom) of the Li\$SOCl_2$ cell for HighwayFET.

3.1.5. Correction for the Voltage Recovery Behavior

The recovery treatment was performed by first recording the voltage response of the cell at different discharge currents followed by open circuit potential for calibration. The voltage recovery curves obtained from these voltage responses were averaged to one curve and then normalized. The curve was fitted to a mathematical function using scipy.optimize.curve_fit script [63] in Spyder 3.3.3, which could predict the voltage

recovery behavior as a function of time. The parametrized function was used to calculate the required voltage recovery correction in the last step in the modeling procedure which corrects for the voltage response at zero currents.

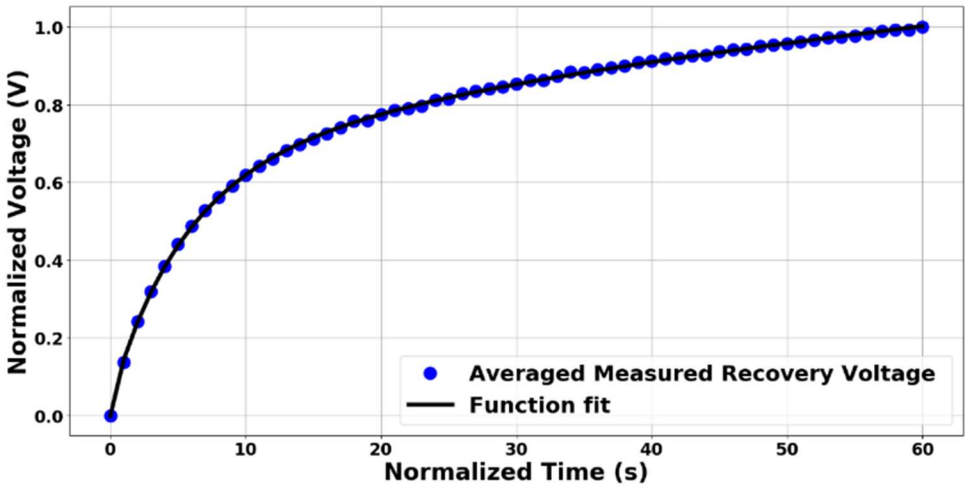

Figure 70. fitting curve for the averaged and normalized voltage recovery response

The mathematical function used for fitting the curve is shown below, which predicts the normalized voltage response as a function of time:

$$V(t) = a\sqrt{t} + be^{-ct} + d$$

where, a = 0.065, b = -0.502, c = 0.176 and d = 0.500.

This function was chosen with a generic diffusion and a capacitive relaxation in mind. Using a square root of time to model a generic diffusion response and a single-exponential relaxation function to model a capacitive decay. This function was used to correct for the voltage response at the regions of zero current.

The corrections in the voltage response at the voltage recovery regions resulted in a better agreement with the experimentally measured voltage response. The corrected voltage responses are shown in Figure xx and xx along with the uncorrected and the experimentally

measured ones. The proportional error graphs demonstrate a decrease in the error levels particularly at zero current regions where voltage recovery exists.

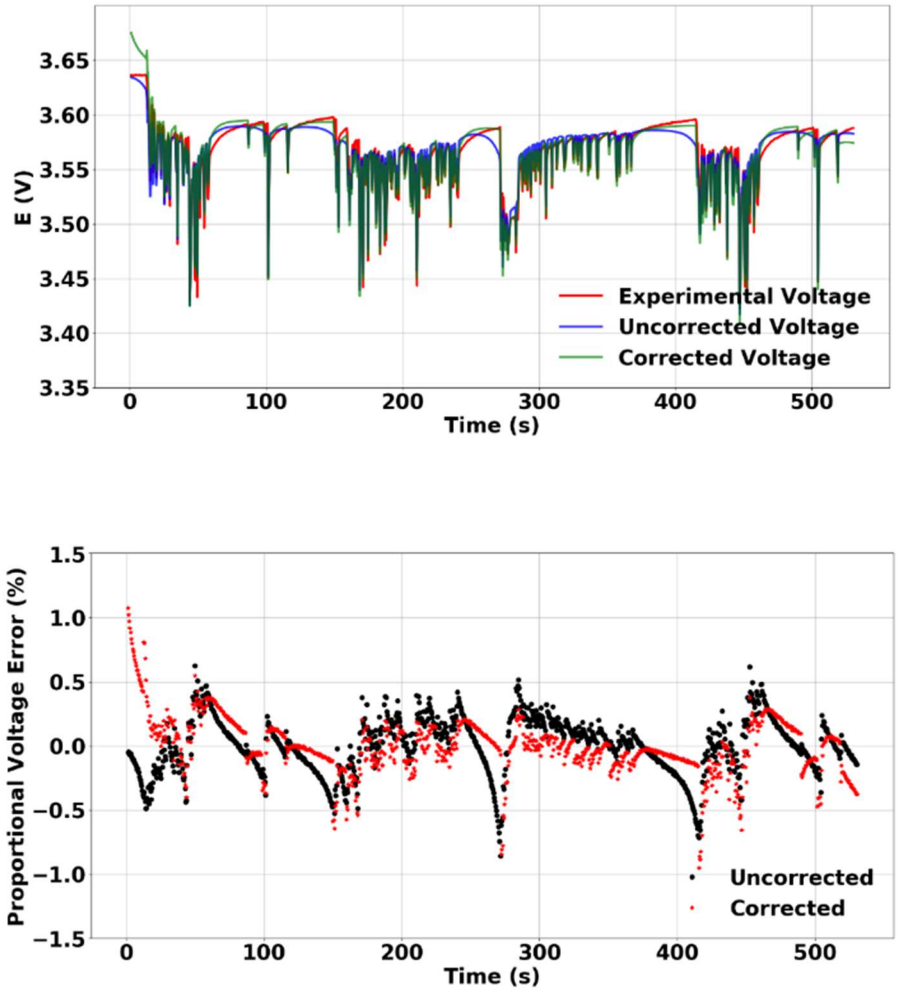

Figure 71. Calculated and measured voltage responses (Up) and percent proportional voltage error for the calculated voltage response (Bottom) after applying recovery correction for HDUDDS

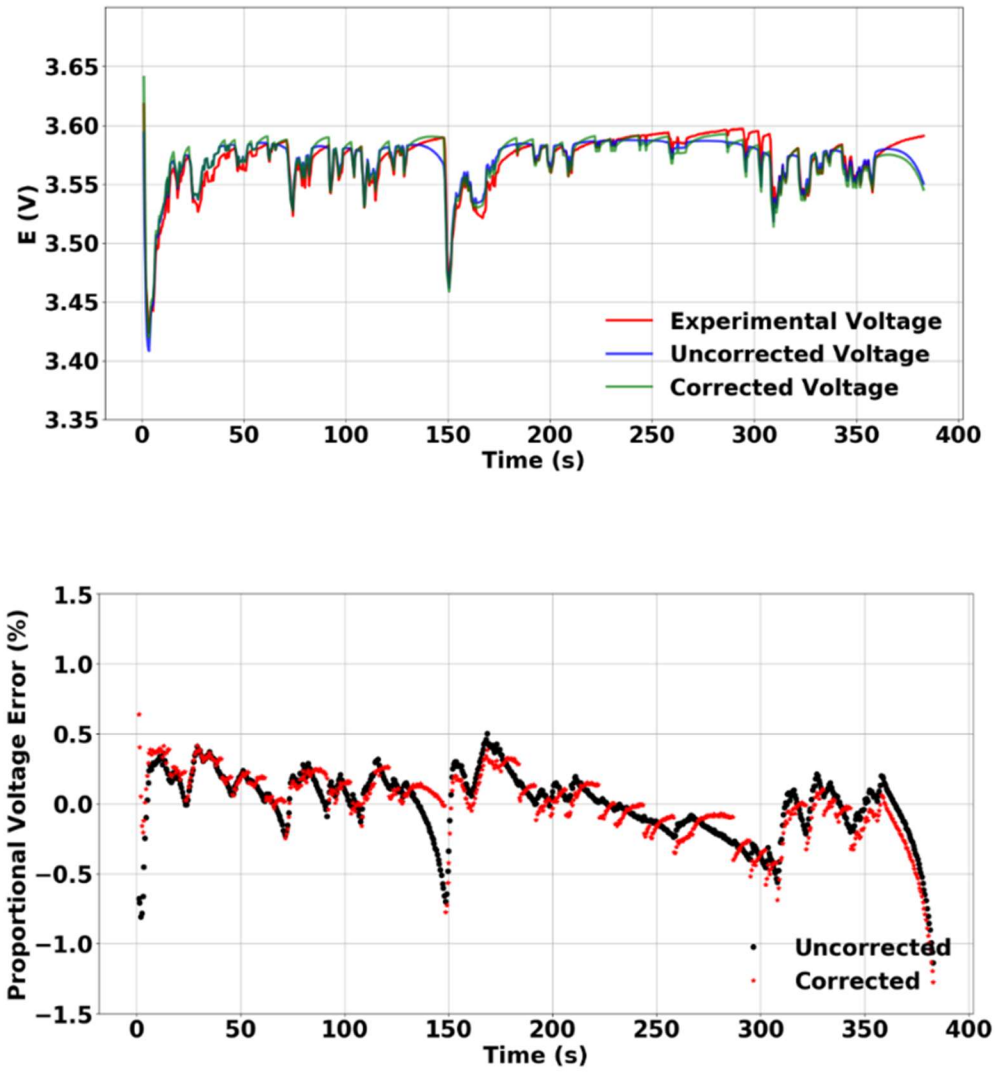

Figure 72. Calculated and measured voltage responses (Up) and percent proportional voltage error for the calculated voltage response (Bottom) after applying recovery correction for HighwayFET.

3.1.6. Voltage Response at Different States-of-Charge

Investigation of the voltage response of the Li\$SOCl_2$ battery at different States-of-Charge (SoC) was done by applying the same method for fully charged battery and with levels of discharged batteries until 30% SoC. The Nyquist plots of the EIS at different SoC are

shown in Figure xx. The distorted semicircle shows itself at all the SoC with small shifts in the transition frequency. The impedance spectrum at the high and the low SoC in Figure xx show deviations in the Kramers-Kronig compatibility test which indicates the presence of instabilities or nonlinearities. At high SoC the deviations are caused by the intense passivation reaction due to the high amount in electrolyte ($SOCl_2$) which decreases by discharge. On the other hand, at the low SoC voltage instability causes the deviations. The rest of the impedance data in Figure 73 show better compatibility with the Kramers-Kronig indicating the stability and the linearity of the obtained EIS.

The calculated and the experimentally measured voltage responses for the two profiles are shown in Figure 74. There is good overlap for the calculated and the measured voltage profiles at all SoC as can be also seen from the proportional error profiles shown in Figure 75. The deviations in the impedance data from the Kramers-Kronig compatibility at high and low SoC reflect themselves in the voltage responses as can be seen in the voltage profiles and the proportional error at 100, 95 and 35 %SoC shown in Figure 74 and 75. However, the rest SoC data show better voltage responses with lower proportional errors.

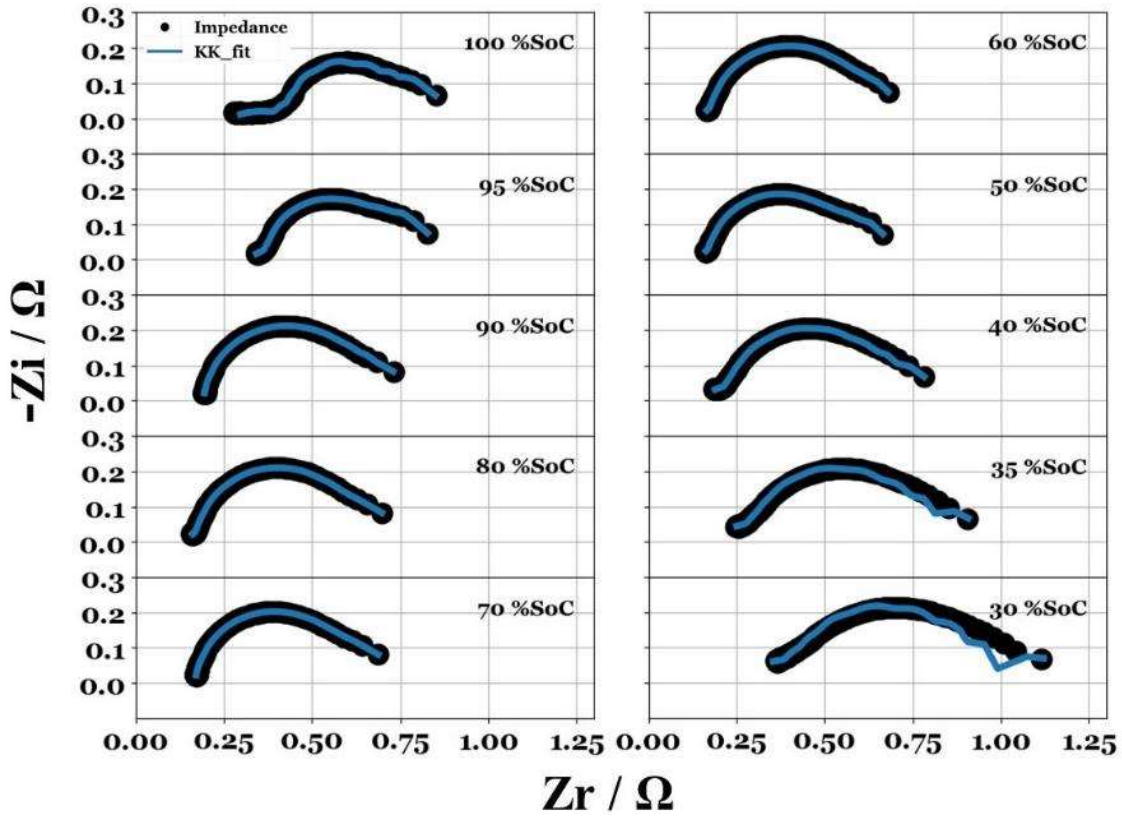

Figure 73. Nyquist plots for the EIS of Li\$SOCl_2$ battery from 100% to 30% states of charge

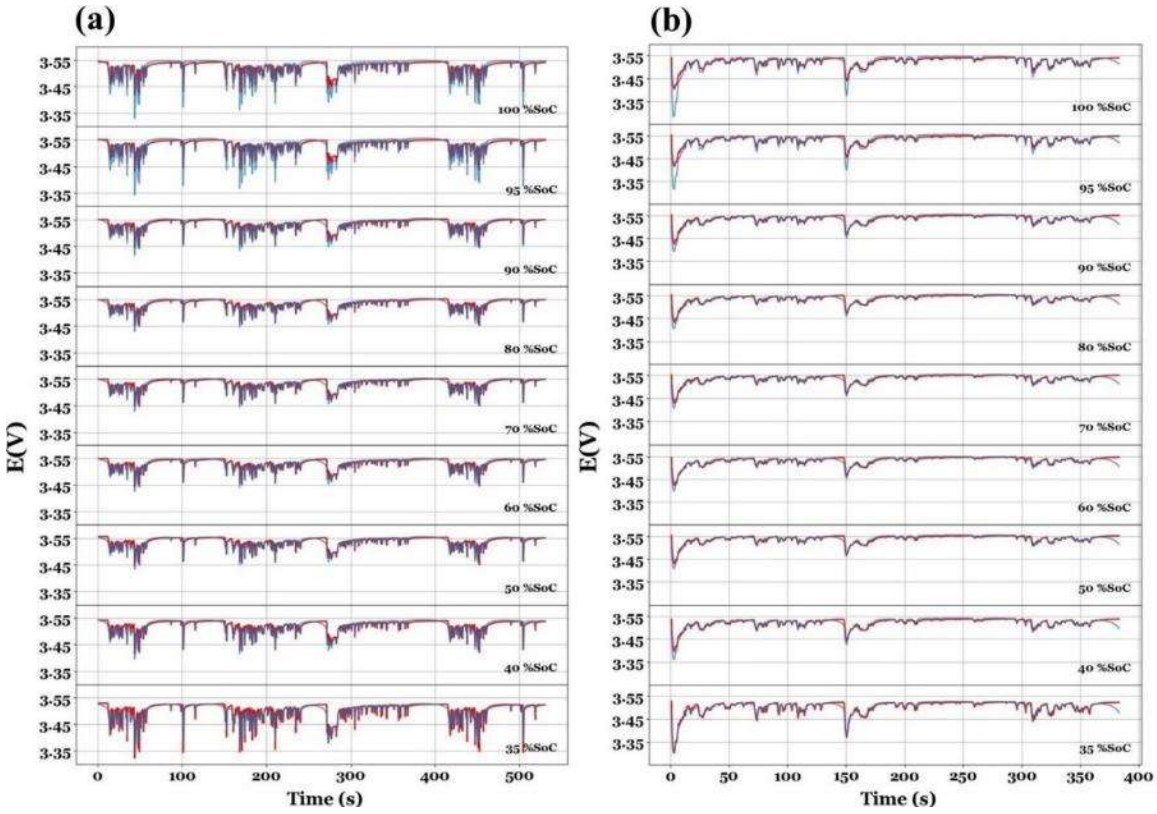

Figure 74. Calculated and experimentally measured voltage responses at different SOC for (a)HDUDDS and (b) HighwayFET

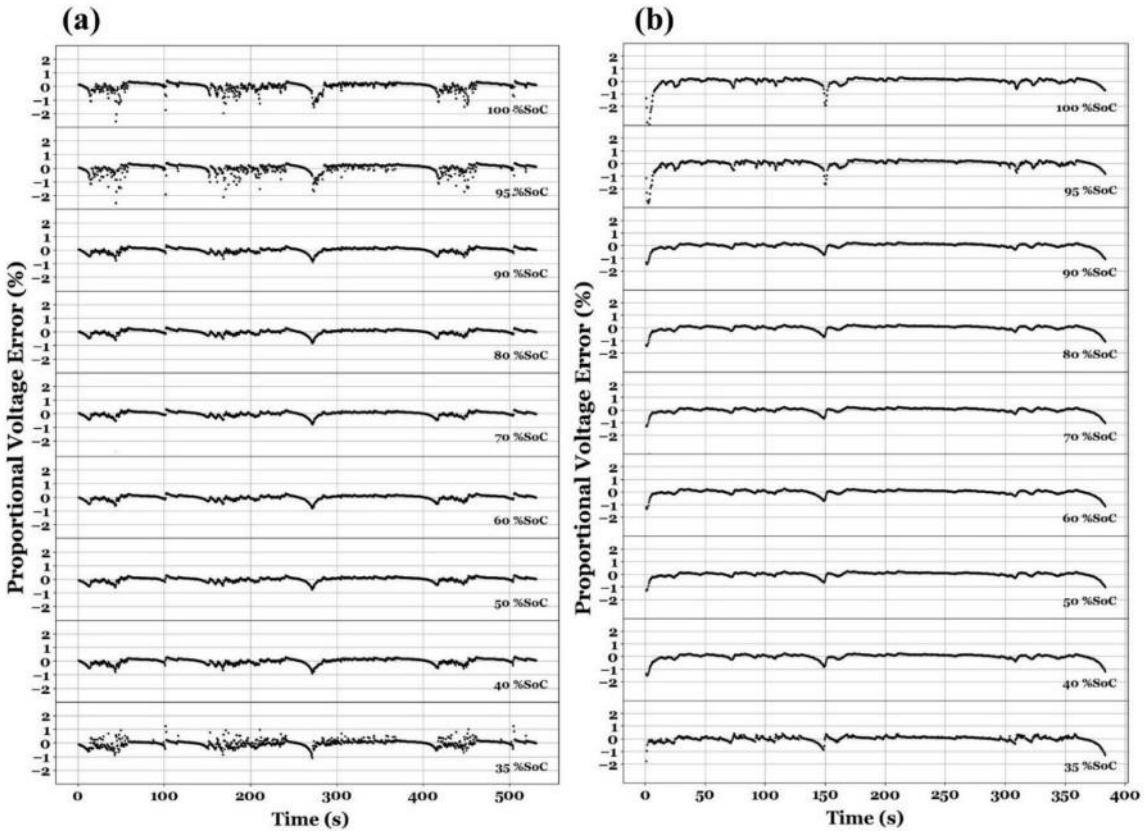

Figure 75. Percent proportional voltage error for (a)HDUDDS and (b) HighwayFET at different SoC

3.1.7. Application to Li\MnO_2 Battery

To demonstrate the applicability of the used modeling methodology in predicting the voltage behavior of other primary batteries, Lithium Manganese Dioxide (Li/MnO2) primary coin batteries were used. The same procedure was applied with the current profiles maximum amplitude adjusted to -10mA to account for change in capacity. The results are shown in Figure 76 in which decent overlap between the experimentally measured and the calculated voltage with less than 0.3% proportional error are observed.

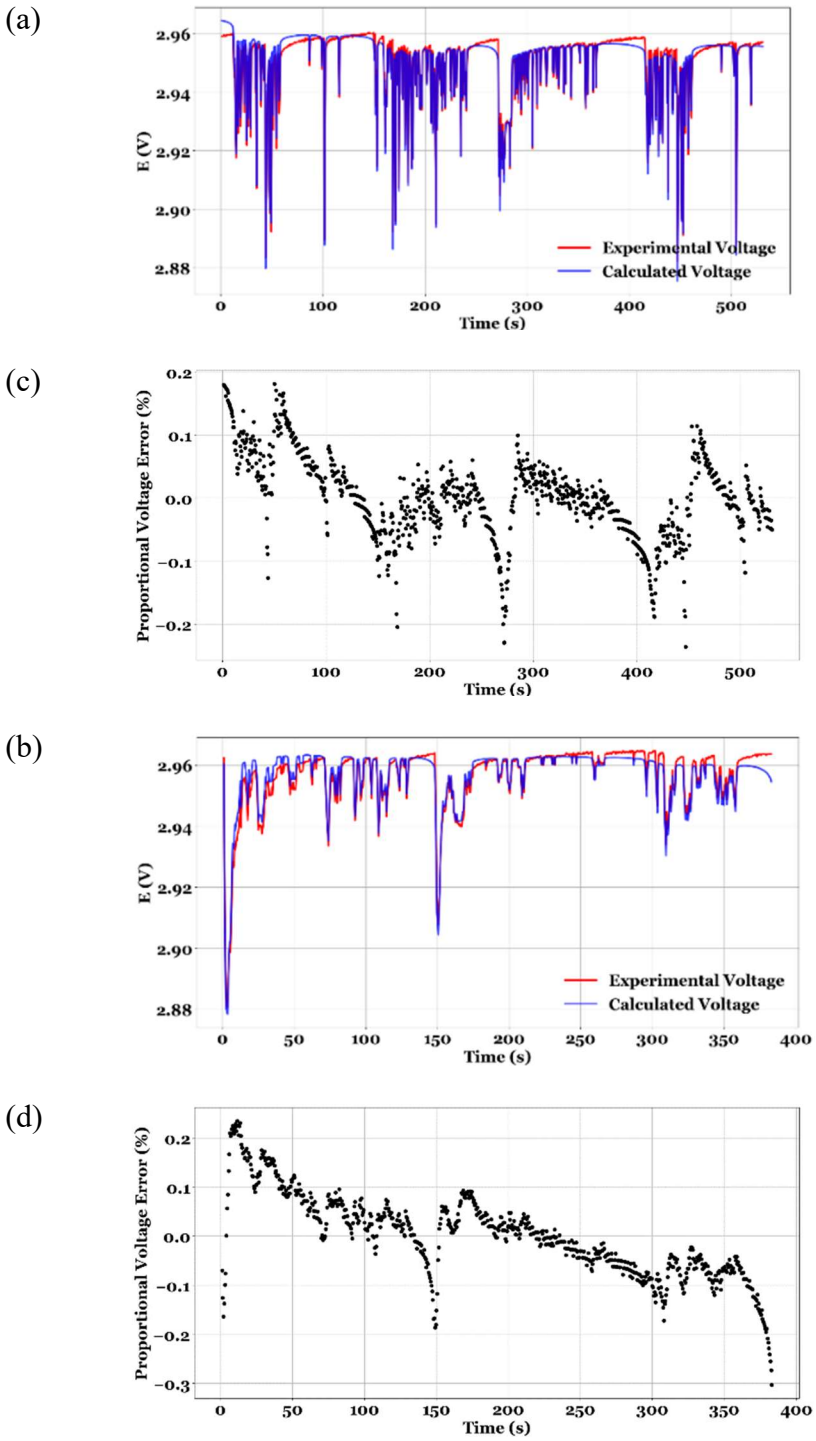

Figure 76. Calculated and Measured voltage response of Li/MnO2 primary battery under (a) HDUDDS and (b) HighwayFET discharge profiles. Proportional voltage error for (c) HDUDDS and (d) HighwayFET

3.1.8. Section Conclusion

EIS based modeling methodology was employed and developed to predict the voltage behavior of the Li\$SOCl_2$ and Li\$MnO_2$ under arbitrary discharge. The modeling methodology showed accurate results for predicting the voltage response with less than 1% proportional errors. The small deviations were influenced by the Li-ion transport through the Solid Electrolyte Interface (SEI). The continuous formation and destruction (passivation reaction) of the SEI at the surface of the anode Li resulted in voltage delay and recovery behavior. We minimized the deviations by calibrating the behavior of the voltage under the passivation effect and correcting the voltage response according to mathematical fits.

Investigation of the voltage response at different States-of-Charge (SoC) was also achieved. Higher errors were observed at the 100 – 95 % SoC due to the deviations in the impedance results caused by the strong passivation. However, the response was accurate for the rest of the SoC with less than 1% proportional error. Finally, the method was also applied to Li/MnO_2 primary battery which predicted the voltage response with less than 0.3% proportional error without the correction for voltage recovery behavior. The deviations caused by the SEI in Li/MnO_2 chemistry is negligible due to the less reactive nature of the electrolyte.

The accurate modeling results presented for both batteries demonstrate the applicability of the modeling methodology to predict the voltage behavior of primary batteries at arbitrary discharge regimes.

3.2. Performance Modeling of Battery\Supercapacitor Hybrid Energy Storage Systems

We mentioned in chapter 1 that the combination of battery/supercapacitor systems in parallel connection offers the advantages of both devices and mitigates the negative effects of quick changes or high levels of charge and/or discharge of the high-power-density applications. Li-ion batteries are considered the state-of-the-art electrochemical energy storage devices used widely in transportation, electronics and stationary applications. However, due to limitations of the underlying electrochemical properties, they suffer from capacity degradation and reduced cycle life if used under high power density conditions. Supercapacitors on the other hand, possess high power density with 10-times larger cycle life than Li-ion batteries. However, their energy density is low and are much smaller than Li-ion batteries. The hybridization of secondary Li-ion batteries with supercapacitors has the highest energy and power density potential among other systems.

Many studies investigated the positive effect of hybridization. For example, White et al. did an experimental characterization of the battery supercapacitor power systems under pulse current loads [64]. Their results showed an increase in the energy available from battery as the pulse duty increased. There is also an increase in the available capacity and current. other studies investigated the efficiency and applicability of a battery supercapacitor used in in different. The results showed a potential for the significant extension of the battery life and the effectiveness of the reduction of peak battery current [65][66]. These studies proved the advantages of using battery/supercapacitor systems and rise the significance of understanding and modeling their behavior in different conditions.

The parallel connection of Li-ion battery to a supercapacitor allows the current to be distributed among both devices and the voltage on the terminals to be equal. Understanding the current distribution behavior is crucial for utilizing such systems.

In the literature, various studies proposed the use of converters and control circuits to manage the current distribution among the components of the hybrid systems [67][68][69]. This severely limits the application for not only the reason of added cost, but also due to

the reduction in reliability and durability [70]. Unmanaged hybrid systems are the better configuration of hybridization for maximized performance tailor-made for given use cases. Achieving their full performance requires understanding of the power distribution under various conditions and combinations. This requires an accurate performance modeling methodology which can assess their performance in realistic scenarios and predict the best combination of batteries and supercapacitor tailored to the application.

In this section, we develop our modeling methodology to predict the current distribution and the voltage response of battery/supercapacitor hybrid systems under arbitrary charge/discharge profiles. We will present modeling results for the assessment of hybrid systems under real life scenarios. We will validate the modeling methodology with experimental measurements for two different Li-ion battery chemistries, namely Lithium Iron Phosphate (LFP) and Lithium Vanadium Pentoxide (LVO), connected in parallel to wide range of supercapacitors. Finally, we outline several design rules for hybrid storage systems for different use cases.

3.2.1. Modeling Studies for Unmanaged Hybrid Battery\Supercapacitor Systems

In the literature, the performance of unmanaged hybrid systems was simulated by means of equivalent circuit models where a combination of voltage source, resistors, and capacitors are used for the simulation. Ragone plots were implemented to evaluate their performance under pulse discharge current [64][70]. As another approach, Sikha et al. presented a one-dimensional mathematical model for the simulation of Li-ion and 10F system under pulse current profile [71]. The study also used Ragone plots for the comparison of the energy densities of the systems before and after the hybridization. However, the presented modeling studies did not provide a comparison for hybrid systems under real life scenarios with application oriented current profiles. Moreover, the equivalent circuit models are dependent on the subjective inputs in its parameter determination [72][73]. The strength of any modeling method relies on its good agreement with the experimental measurement and in minimizing the number of free parameters.

Therefore, there is a need for a modeling methodology that can accurately predict the performance of battery/supercapacitor hybrid systems under real life scenarios and employs objective approaches that don't require human interpretation.

We believe that Zero-free-parameter Electrochemical Impedance Spectroscopy (EIS) based modeling methodology is suitable for modeling battery/supercapacitor hybrid systems. It can provide accurate results in predicting voltage and current behavior of these system under arbitrary load. However, the challenge here is in calculating and measuring the current distribution response among the components.

For the calculation, we develop an optimization algorithm which can optimize with the help of the previously developed modeling method the values of the current distributed among the battery/supercapacitor systems.

For the measurement, we design and utilize sensitive current sensors that are able to sense the small current changes resulting from the parallel connection of the devices.

After the development of the modeling method and the measurement set-up, we validate the obtained results for two Li-ion battery chemistries connected to different supercapacitors. We test the method for three different charge/discharge regimes.

Next, we extend the applicability of the method to simulate the response of battery/supercapacitor hybrid systems with supercapacitors having any capacitance value. This is achieved by simulating the EIS response of the specified supercapacitor with equivalent circuit models.

Finally, we introduce performance metrics such as, peak currents, averaged power distribution and total energy distribution along with cost considerations which helps in determining the best Li-ion supercapacitor combination for tailored application.

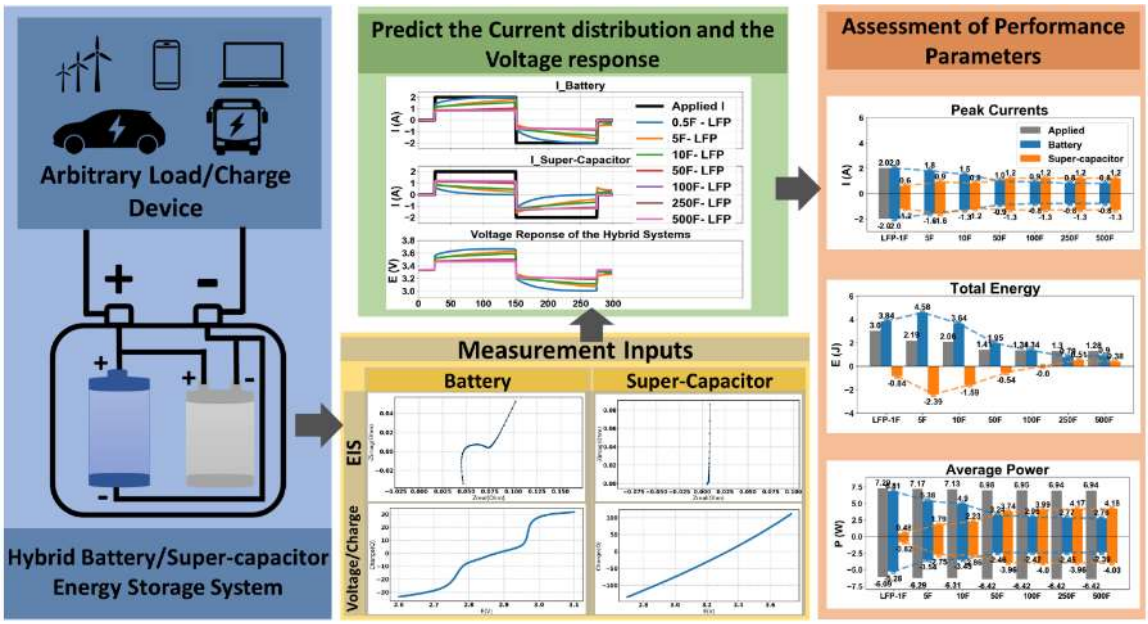

Figure 77. An overview of the performance modeling methodology of battery/supercapacitor hybrid system under arbitrary load/charge profile. First the current distribution and the voltage response are predicted from Electrochemical Impedance spectrum and equilibrium charge/voltage lookup tables then performance parameters are obtained to determine the best combination of battery/supercapacitor hybrid system

3.2.2. Modeling Methodology

As mentioned above, to model parallelly connected hybrid systems, the current distribution and the voltage response should be calculated. To accurately model current distributions across hybrid systems, a Differential Evolution (DE) algorithm is incorporated to iteratively optimize the current distribution for hybrid systems. DE is chosen because of its ability to solve non-differentiable functions by its stochastic direct search and its convergence properties [74].

3.2.2.1. Differential Evolution algorithm for current distribution optimization

The system modeled in this paper is best posed as a multi-variable nonlinear optimization problem as each point in the time series shown constitutes a variable to optimize. Given that majority of the current profiles involve sudden jumps, whose numerical derivatives are not well defined, most gradient descent-based algorithms are ill-suited for the problem with our current cost function. Instead, a stochastic minimizer, called Differential Evolution (DE), developed by Storn and Price [74] was used for all optimizations run in this work. Owing to its robust implementation, the readily available Scipy implementation [75] of the algorithm was used. To minimize the effect of our initial guesses, all minimizations were run starting from random initial currents. To ensure proper convergence, each minimization shown in the article was run in triplicates. The DE routine finds the optimal current across each energy storage device under two constraints. The first is, as hybrid storage devices are connected in parallel, the sum of currents across the individual arms needs to be equal to the total current passing through the stack. The total current is the current applied to the hybrid system for the tailored application. The second is, the voltages of the individual arms are always required to be equal. The voltage here is calculated utilizing the electrochemical impedance of the components which is explained in Zero-free-parameter voltage calculation section.

DE utilizes D-dimensional parameter vectors as a population of individuals for each generation. In our case, the components of the vectors are the currents passing through each component $I_{battery}$ and $I_{supercapacitor}$.

The two constraints are implemented as follows:

- For the current restraint, the current through the supercapacitor is defined as the total current minus the current through the battery at every point. This decreases the number of parameters to be optimized, while also maintaining the constraint.

$$I_{supercapacitor}[t] = I_{total}[t] - I_{battery}[t]$$

- The voltage constraint is used as the cost function to be minimized. That is:

$$Cost\ Function = \sum_{t} \left| E_{battery}[t] - E_{scapacitor}[t] \right|$$

For a given current profile, the zero free parameter model can accurately model the voltage response. If the current over each arm of a hybrid system is known, the zero free parameter model can be used to calculate the voltage response. Thus, modelling the hybrid stack turns into a question of finding the optimal current distributions.

After generating the population, the first step in DE is called mutation in which new parameter vectors are generated by adding the weighted difference between two population vectors to a third vector. After mutation, the mutated vector's parameters are mixed with the parameters of another predetermined vector in a step called crossover. If the resultant vector yields a lower cost function value than the target vector the latter is replaced by the new vector. This last operation is called selection. The DE steps of mutation, crossover and selection is repeated until a maximum number of generations is reached.

Starting from an initial guess of currents over each arm, we can use the Zero-free-parameter model to calculate the voltage response of each arm. Since in a parallel connection the voltage over the two arms is equal, we can use these calculated voltages to find the optimal current distribution in an iterative fashion. The objective of the iteration is to slowly change the initial guess for the current such that the objective function (the difference between the two voltages as calculated by zero-free-parameter model) is minimized.

3.2.2.2. Zero-free-parameter voltage calculation

To obtain the voltage response of the hybrid components, zero-free-parameter method is used [57]. The main computation is in obtaining the voltage of each hybrid device at the frequency domain based on Ohm's law using the EIS data:

$$E_i'(f) = I_i(f) \times Z_i(f)$$

Where $Z_i(f)$ is the impedance of the device (i), which can be a battery or a supercapacitor, obtained from the EIS measurement at the corresponding frequencies and $I_i(f)$ is the current values of the applied current profile in the frequency domain obtained from the Fourier transform of the chosen current profile for specific application:

$$I(t) \overset{FFT}{\Longrightarrow} I(f)$$

The calculated voltage response is then converted from the frequency domain to the time domain using inverse Fourier transform:

$$E_i'(f) \overset{iFFT}{\Longrightarrow} E_i'(t)$$

The final step is to add the equilibrium charge/voltage values $E_i(Q)$ which are obtained from look up tables collected for each system. The final result is the voltage at the State-of-Charge of the component:

$$E_i'(t) + E_i(Q) = E_i(t)$$

This method is used to calculate the total voltage of the hybrid system which is used for predicting the current distribution among the hybrid components. There exists a difference between the total measured voltage of the measurement set-up and the terminal voltage of the components. This difference is related to the stray resistance which is the resistance of the current at paths of the measurement set-up. To compensate for this voltage difference, we have measured the EIS of each component at the terminals and while connected to the measurement set-up which included the stray resistance. For calculation of the total voltage of the hybrid system, the EIS data of the component with the stray resistances were used.

3.2.3. Experimental Measurements

The experimental part of the study involved the measurement of the inputs of the modeling methodology. Two inputs required which are, the EIS measurements and the Charge/Voltage maps record of each device. Furthermore, for the experimental validation

the current distribution and the voltage response of each hybrid system needed to be measured. This required the design and the built of measurement set-up which is shown in this section.

3.2.3.1. Batteries and Supercapacitors:

Modeling methodology was tested for two hybrid systems with two Li-ion chemistries and wide range of supercapacitors. The systems and their parameters are as follow:

LFP/Supercapacitor - Lithium Iron Phosphate (LFP) 18650 size battery with 1500mAh capacity and 3.2 V nominal voltage was used at 100% State-of-Charge. The cell was connected to supercapacitor with 1, 10, 25, 100 and 400F. The maximum voltage of the supercapacitor was 2.7V which is lower than the voltage of the LFP. To increase the voltage of the supercapacitor, we connected two identical supercapacitors in series which resulted in increasing the maximum voltage to 5.2V. However, the series connection resulted in decreasing the capacitance of the identical supercapacitor to half. As a result, LFP/0.5, 5, 12, 50, 200F systems were studied.

LVO/Capacitor - Lithium Vanadium Pentoxide (LVO) coin battery with 20mAh capacity and 3.0 V nominal voltage. LVO cell was connected to capacitors with 10mF and 20mF capacitance. The maximum voltage of these capacitors was 6.3V.

3.2.3.2. Electrochemical Impedance Spectroscopy Measurements:

EIS data of the batteries and the supercapacitors were obtained in potentiostatic mode using Gamry Interface 5000. The measurement script was adjusted to obtain the linearly spaced EIS spectra with the user defined parameters. In a typical measurement, excitation amplitudes of 5mV were applied between 50 and 0.2 Hz with 0.2 Hz sampling.

Potentiostatic EIS was performed for the batteries and the supercapacitors at the open circuit potential with 0.2 linearly spaced frequency between 50 – 0.2 Hz. The Nyquist plots

for LFP and 0.5, 5, 12, 50, 200F Supercapacitors are shown in Figure 78 and LVO and 10mF, 20mF are shown in Figure 79. The Kramers-Kronig compatibility test was performed to check for the stability and the linearity of the obtained data.

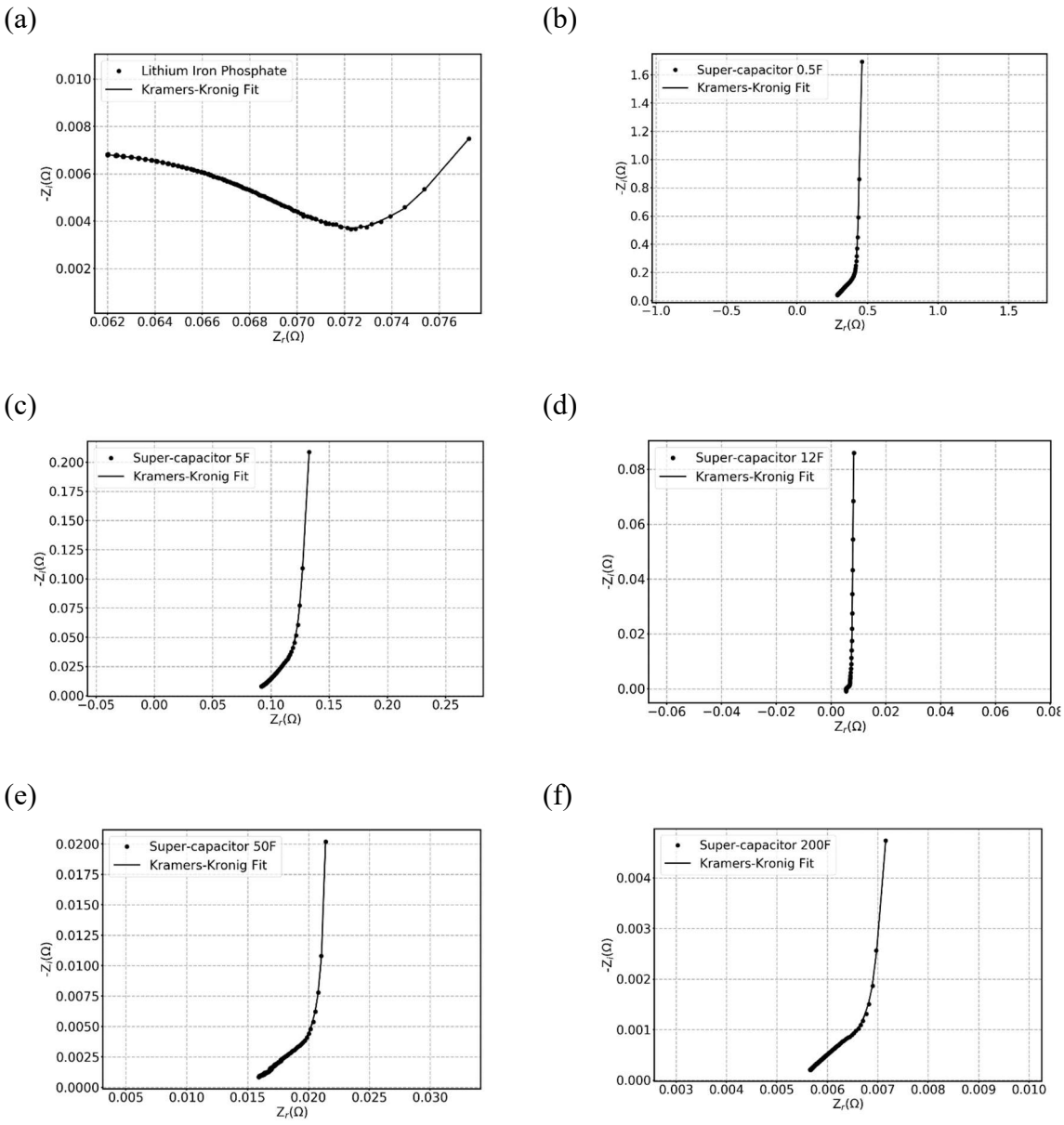

Figure 78. EIS of (a)Lithium Iron Phosphate, (b)0.5F, (c)5F, (d)12F, (e)50F and (f)200F with 5mV AC excitation at Open Circuit Potential from 50 to 0.2 Hz

(a)

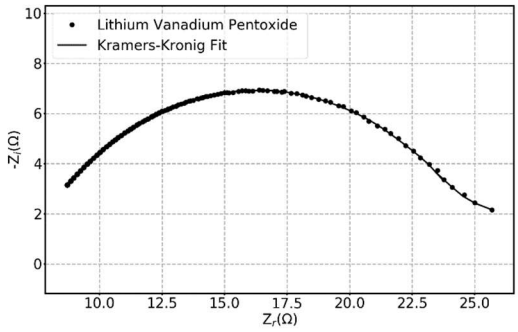

(b) (c)

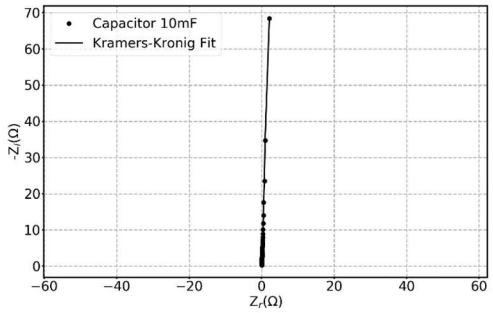

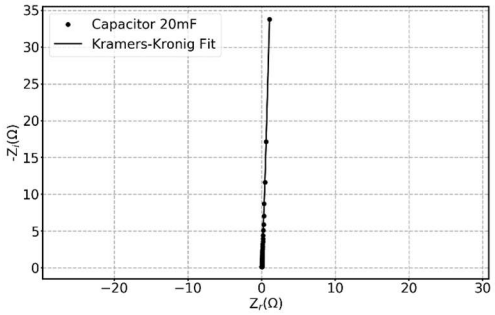

Figure 79. EIS of (a)Lithium Vanadium Pentoxide, (b)10mF and (c)20F with 5mV AC excitation at Open Circuit Potential from 50 to 0.2 Hz

3.2.3.3. Electrochemical Impedance Spectroscopy Simulations:

EIS data was simulated for supercapacitors with capacitance ranging from 1F to 500F using a transmission line model (Bisquert Open) [76]. For a given intended capacitance, the transmission line model had two input parameters which are, the solution resistance R_u, and the series pore resistance R_m. The EIS data of 1, 10, 25, 100 and 400F supercapacitors were used to parametrize the transmission line model. This parametrized model was used to determine the appropriate values of R_u and R_m for the EIS simulations.

The EIS of the Super-capacitor is hard to simulate with simple capacitor or even Constant Phase Elopement model. For simulating the EIS for the Super-capacitor systems we used Transmission Line model shown in Figure 80(a) which is used to model the impedance of highly porous systems. The model composes of several parallel and serially connected elements namely Rm, Rk, qm, L and Ru, where Rm represent the resistance of the electrolyte within the pore which is different from the electrolyte resistance Ru. Rk is the resistance of the charge transfer at pore which in our case was set to 1 x$10^{13}\Omega$ since there is no charge transfer for the capacitor. A constant phase element qm reflect the capacitance of the Supercapacitor with components of Y and the exponent a which was set to 1. L represents the depth of the pore which is taken as unity in our model.

The EIS data shown in Figure 78. was fitted with this model and the parameters (Rk and Ru) obtained with their errors are shown in Table 9. The obtained parameters were drawn versus the capacitance and by using linear regression and capacitance dependent power function was obtained as shown in Figure 80(b). this equation was used to simulate EIS of any intended Supercapacitors capacitance. Examples of the simulated EIS for 5, 50, 100, and 500F are shown in Figure 81.

(a)

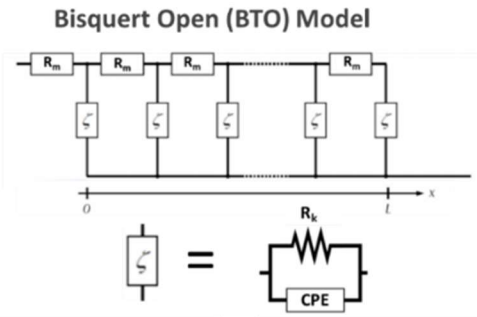

(b)

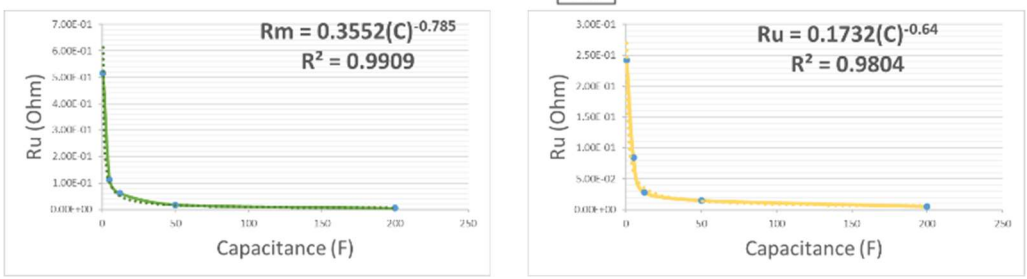

Figure 80. (a) Transmission Line Equivalent Circuit model, (b) Rm and Ru vs. Capacitance obtained from the fits of the Bisquert Open model to the EIS data of Super-capacitor

Table 10. Parameters of the transmission line mode used to simulate the EIS response for the Supercapacitors

	L(m)	Rm(Ω)		Rk(Ω)	Y(S×s^a)		a	Ru(Ω)	
SC (F)	**Value (Fixed)**	**Value**	**Error**	**Value (Fixed)**	**Value**	**Error**	**Value (Fixed)**	**Value**	**Error**
0.5	1	0.5160	0.0080	1 x10^{13}	0.466	0.009	1	0.24250	8.56 x10^{-4}
5		0.1120	0.0030		3.746	0.120		0.08476	2.55 x10^{-4}
12		0.0610	0.0020		10.180	0.307		0.02822	8.86 x10^{-5}
50		0.0180	0.0006		39.150	1.739		0.01528	4.33 x10^{-5}
200		0.0050	0.0002		169.10	10.02		0.00547	1.50 x10^{-5}

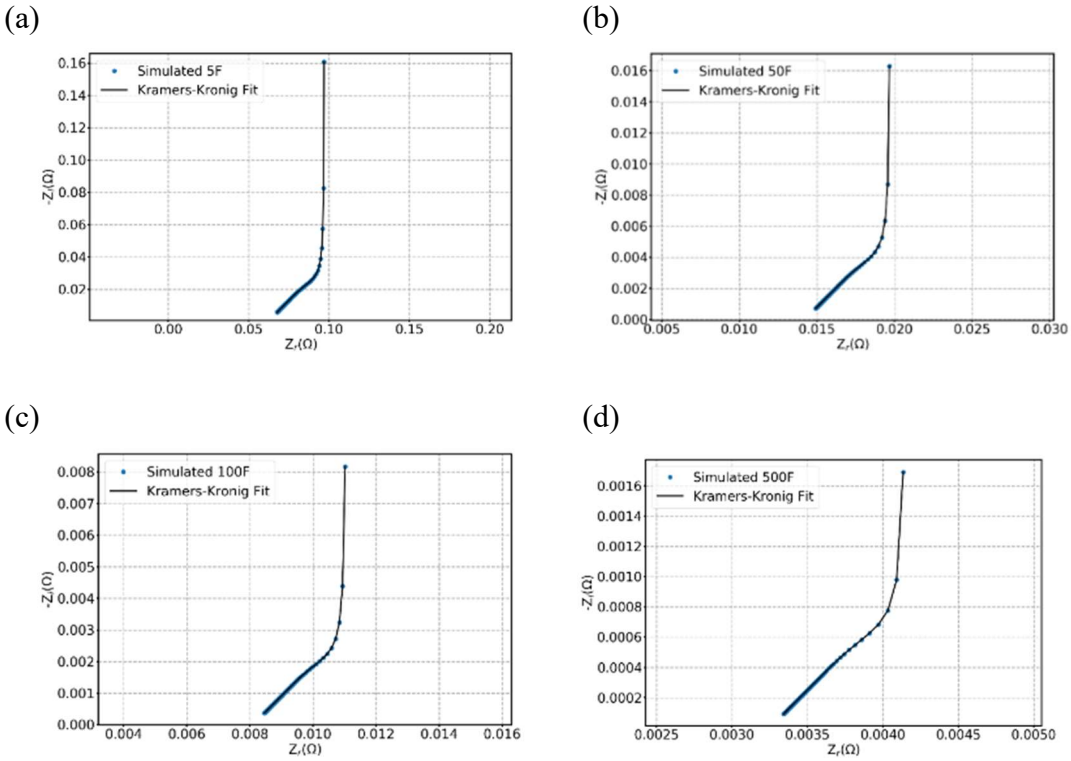

Figure 81. Simulated EIS data for (a)5F, (b)50F, (c)100F, (d)500F simulated by Bisquert Open Transmission Lines model

3.2.3.4. Charge/Voltage maps

The voltage behavior vs. charge maps were obtained by charging each device at low currents. LFP was charged with 1mA from 2.8 to 3.8V. LVO was charged with 500µA from 2.4 to 3.4V. Supercapacitors with capacitance from 0.5 to 200F were charged with 1mA and with capacitances between 10mF to 100mF by 100µA.

The charge/voltage map for simulated supercapacitors was calculated using:

$$V = \frac{Q}{C}$$

Where V is the supercapacitor's potential in Volts, Q is the charge in Coulomb and C is the capacitance in Farads. The voltage of the supercapacitor at Q = 0 was assigned to the Open Circuit Potential of the hybrid system which correspond to the zero current in the applied current profiles.

3.2.3.5. Current Distribution Measurement Set-up

To validate the predicted current distribution and voltage response obtained by the modeling method, we constructed a measurement set-up. The setup can simultaneously measure the individual currents passing over the hybrid devices and the voltage at their terminals. The current measurements were done using Hall effect transducers to circumvent the added impedance of shunt resistors. Given the resistance of an energy storage device (~mΩ), the added shunt resistance in series to an energy storage device would dominate the measured response. Further, as the current levels investigated approaches greater than 1 A, the resistance of the shunt resistor is liable to thermal drifts. The circuit for the current measurement is provided in supplementary materials (SM4)**.** The voltages from the current sensors and the voltages at the terminals of the hybrid components were measured using a DAC (NI USB-6229). The DAC was controlled with Python 3.5 using the NI-DAQmx package under Scientific Python Developing Environment (Spyder 2.3.5.2) [75]. The current profiles were applied to the hybrid systems

connected to the measurement set-up by Gamry Interface 5000. An in-house written script was used to apply the current values of the intended profiles at the specifies sampling rate.

For accurate measurement of current we used LTSR 6-NP current transducers which are Hall effect-based transducers with accuracy of ±0.2%. The sensors required a reference voltage of 5V and had an output offset of 2.5V. We designed a circuit shown in Figure 82(a) which consists of an Operational amplifier used for the correction of the output offset and a Zener diode that serves as a 5V reference. The current transducers were connected in series with the battery or the Supercapacitor as shown in Figure 82(c). The output signal of the transducers is in voltage which was filtered using RC filters and calibrated to the corresponding current value which is shown in Figure 82(b).

(a) (b)

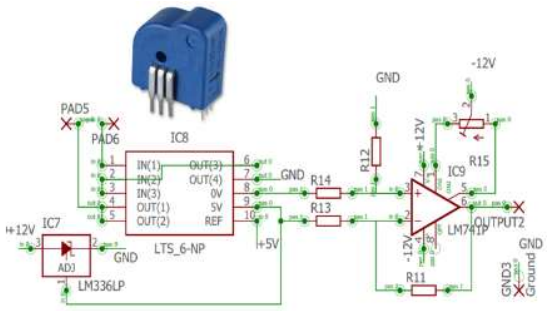

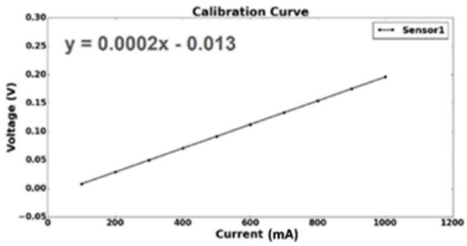

(c)

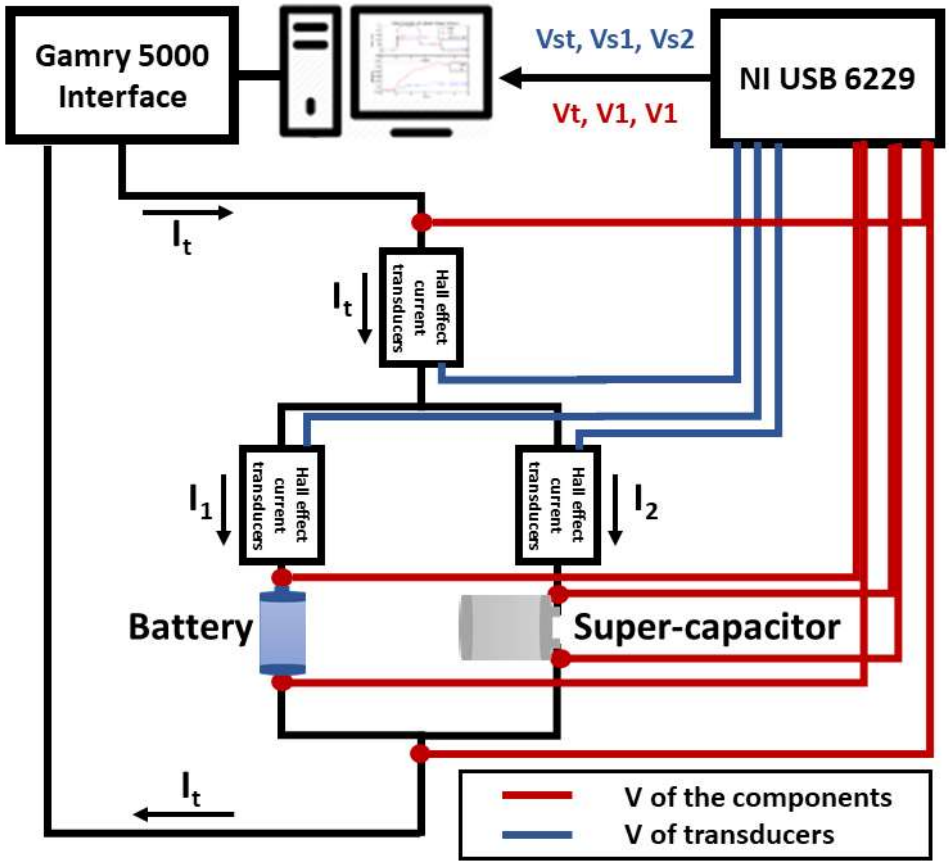

Figure 82. (a) Hall effect current transducers circuit, (b) Calibration curve for the transducers, (c) Data acquisition and current profile application

3.2.3.6. Current Profiles

Three current profiles were chosen to test the modeling method with three distinct charge/discharge scenarios. The first scenario is a slow charge/discharge which is named as profile-1. The profile demonstrates the slow response to current depths of fixed time periods. The slow profile is specifically picked to test our methodology since long plateaus are the toughest for our algorithm [58]. The second scenario is a fast-fluctuating profile demonstrating the fast response of the system at various current depths which is named as profile-2. This profile was obtained from Worldwide Harmonized Light Vehicle duty cycle published by United Nations Economic Commission for Europe [77]. The third scenario is a charge/discharge square wave which was used to study the symmetric response of the hybrid systems while further straining our algorithm. The three profiles are shown in Figure83. For LFP/Supercapacitor systems the current amplitude was adjusted to range between 0.5C to 2C for profile-1 and maximum of 1C for profile-2. For LVO/Capacitor systems the maximum current was adjusted not to exceed 1.5C for both profiles.

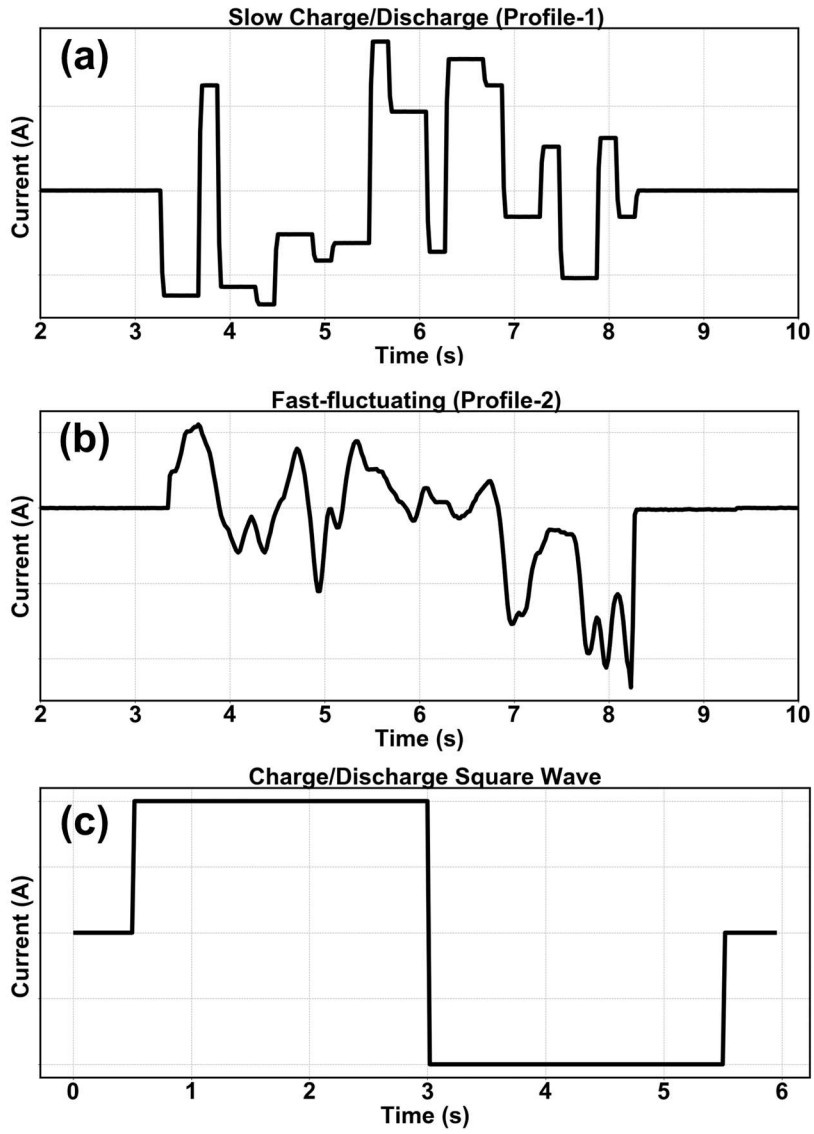

Figure 83. Current profiles applied to study the performance of the hybrid systems (a) Slow charge/discharge (Profile-1), (b) Fast-fluctuating (Profile-2), (c) Charge/discharge square wave

3.2.4. Lithium Iron Phosphate\Supercapacitor Hybrid Systems

The developed method was first validated with experimental measurements for two Li-ion battery/Supercapacitor systems under profile-1 and profile-2. For these systems the EIS and charge/voltage measurement inputs were obtained experimentally. Here, we will first show the accuracy of the modeling method compared to experimental measurements. Then results from simulated supercapacitor systems are shown followed by our suggestions for optimal performance under various use-cases for the hybrid devices.

In Figure 84, the overlay of simulated and experimentally measured current distribution and voltage responses and proportional error plots of hybrid LFP/supercapacitor with 0.5F and 200F systems are shown. As can be seen, the simulations and the experimentally measured data agree within 2% in all cases and 1% in majority of the cases. The agreement between the experimentally measured and the simulated results in both profiles demonstrates the high accuracy of the method to predict the current distribution and to determine the voltage response of the LFP/supercapacitor systems.

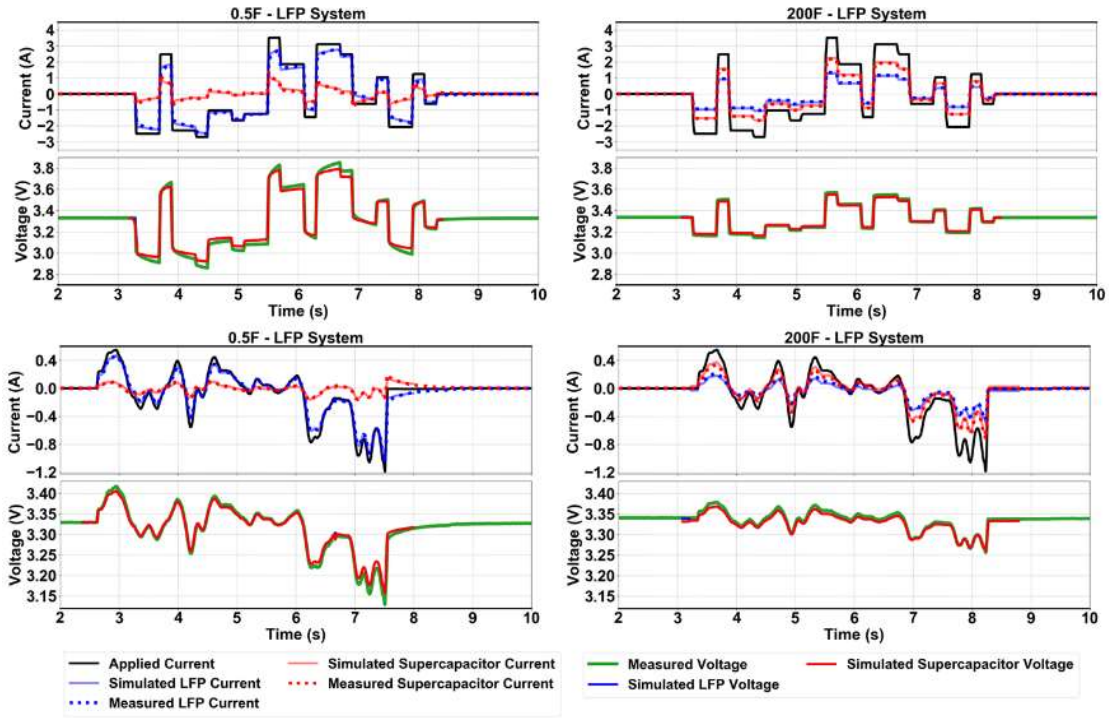

Figure 84. Overlays of simulated and experimentally measured current distributions and voltage responses for parallel-connected Lithium Iron Phosphate (LFP) battery and supercapacitors of 0.5F and 200F under profile-1 (top) and profile-2 (bottom). In the current response, black lines represent the total applied current, blue lines are the current passing through the LFP and the red lines are for the supercapacitor. Voltage response shows the measured voltage in green lines and the simulated voltage in red and blue lines resulting from the applied current profile.

3.2.5. Lithium Vanadium Oxide\Capacitor Hybrid Systems

The method was also successful in predicting the current distribution and the voltage response of small capacity hybrid systems but with higher proportional percent error. In Figure 85. the overlay of simulated and experimentally measured results with proportional error plots of parallel-connected Lithium Vanadium Pentoxide (LVO) battery and two capacitors (10mF, 20mF) are shown. The raise in the percent error is due to the decrease in the device's capacity and the amplitudes of the current applied.

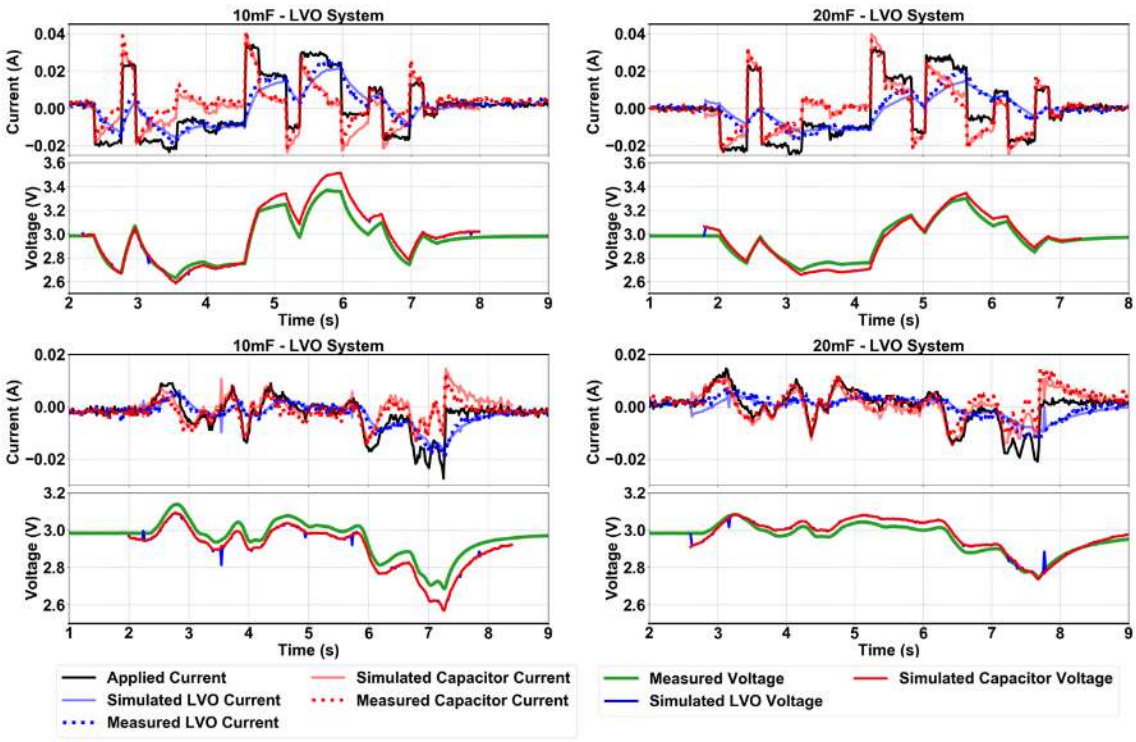

Figure 85. Overlays of simulated and experimentally measured current distribution and voltage response of Lithium Vanadium Pentoxide (LVO) battery and 10mF and 20mF capacitors under current profile-1(top) and profile-2(bottom).

3.2.6. Lithium Iron Phosphate\Simulated Supercapacitor Hybrid Systems

Having demonstrated the high accuracy of the developed methodology, we set out to investigate simulated hybrid systems. In Figure 86 simulations for square wave profile for LFP and simulated supercapacitors hybrid systems are shown. The simple square wave profile helps in visualizing the effect of capacitance on the current distribution and the voltage response of LFP/supercapacitor hybrid systems. For the charging pulse, the current is passing heavily through the LFP when hybridized with 5 and 10 F. The charging pulse is almost shared equally at 50F and then is mostly passing through 100 and 500F. In all systems the take-off current is shared by both LFP and the supercapacitors. Progressing through the pulse, the current passing through the supercapacitor arm decreases at 5 and 10F while the current passing through the LFP increases. This is due to the low capacity of

5 and 10F supercapacitors at this current level. When hybridized with higher capacitances (50, 100 and 500F), the take-off current favors the supercapacitor. The current over the supercapacitor arm also remains higher than the LFP arm. The current over the supercapacitors decrease over time for 50 and 100F but is almost constant for 500F. The above observations are consistent with the increase in the capacitance of the supercapacitors. It is important to note that although there is a large increase in the capacitance going from 100 to 500F there is no big increase in the current passing through the supercapacitor. In this case the current is limited by the impedance of the supercapacitors and the stray resistance.

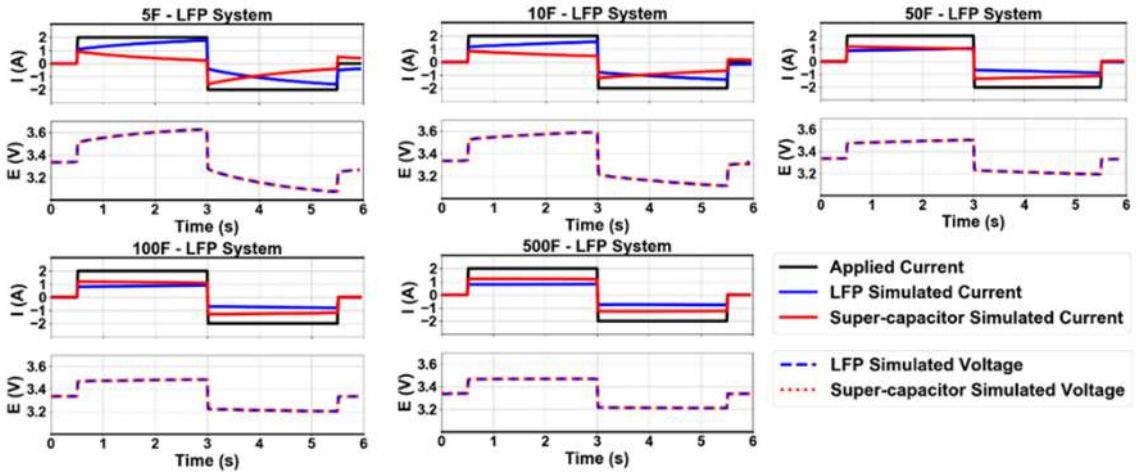

Figure 86. Simulated current distribution and the voltage response of LFP and simulated supercapacitor (5F, 10F, 50F, 100F and 500F) hybrid system under a square wave profile of 2A followed by -2A current pulses

The discharge pulse is applied directly after the charging pulse. At the current jump, from 2A to -2A, the current is mostly drawn from the supercapacitors. The current over the supercapacitors then decreases for 5 and 10F and is overtaken by the LFP while the current over the supercapacitor remains higher for 50, 100 and 500F at all times. After the pulse,

although the total current is zero, the LFP charges the 5 and 10F supercapacitors to reach equilibrium which is not observed for higher capacitances 100 and 500F.

The voltage response of the system displays a decrease in the pulse amplitudes as the capacitance increases. This is related to the decrease in impedance as the capacitance increases. The shape of the voltage response to the current pulse also varies where it shows an increase in voltage at charge and a decrease at discharge for 5, 10 and 50F and almost stays at constant voltage for higher capacitances.

3.2.7. Performance Evaluation for the Hybrid Systems

The performance of the hybrid system varies with changing the capacitance. To facilitate the assessment of their performance, we assigned performance parameters which provide information to best combine and optimize the hybrid systems. We define the metrics to be used to evaluate the hybrid systems as follows:

- *Peak Current* is the maximum current that passes through the battery and the supercapacitor.
- *Average Power Distribution* defined as the sum of the power through the applied current profile divided by the number of sampling points.

  $$\hat{P} = \frac{\sum_{i=1}^{n} P_i}{n}$$

  where $P_i = E_i \times I_i$
- *Total Charge Distribution* defined as the sum of the charges obtained from the integration of the current distribution through time.

  $$Q_T = \int_0^t I(t)dt$$
- *Total Energy* obtained from the integration of the total power through the time of the current profile applied.

  $$E_T = \int_0^t P(t)dt$$

The trends in these metrics vs. the capacitance can be used to understand the systems performance. These trends can also be used to find tailored hybrid systems for various use cases (as demonstrated by their unique current profiles). Figure 87(b) shows the extracted performance metrics for LFP/Supercapacitor (5,10, 50, 100 and 500F) hybrid systems under the square wave profile shown in Figure 87(a). The trends are as follows:

Peak Current _ Although the pulse was applied for 2.5 seconds, we can assign the peak current as the maximum point reached by the current of each system. Taking this into consideration, we can see that the peak current decreases for the LFP and increases for the supercapacitor from 5 to 50F. It then remains constant with increasing the capacitance. This is related to the stray impedance of the hybrid system.

Average Power Distribution and *Total Charge Distribution* _ Evaluating the total charge and the average power provides clearer trends as the capacitance increases. The charge and the average power distribution increase for the supercapacitor matched with a decrease in the LFP by increasing the capacitance. However, the increase is non-linear in which it flattens after 50F.

Total Energy _ The total energy distribution shows the sum of the energy from the two pulses. It shows positive values when any component charges and negative if it discharges. The total energy shows positive values for the LFP with a decreasing value as the capacitance increases. In the case of the supercapacitors, it discharges at 5, 10 and 50F with decrease in the total energy and charges at 500F with zero total energy at 100F.

Performance parameters are also analyzed separately for the charge and the discharge pulse shown in Figure 87(c and d). Benefits of unmanaged hybridization in providing rapid response and protecting the battery at such fast changes is observed at the discharged pulse where the current jump from 2A to -2A is taking place. Supercapacitor is clearly acting as a buffer and protects the battery from the fast change in the current. In the charging pulse both the battery and the supercapacitor almost share the charge, power and energy equally at around 50F but at the discharge pulse, due to the fast change, supercapacitor is more effective even at lower capacitances.

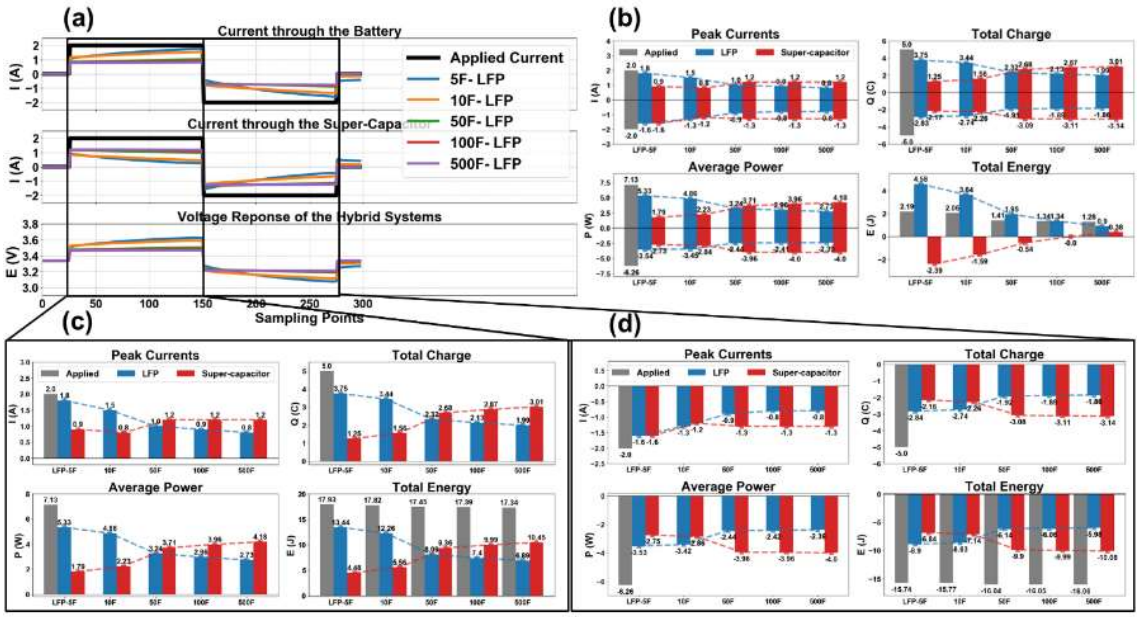

Figure 87. (a) Simulated current distribution and the voltage response of LFP and simulated supercapacitor (5F, 10F, 50F, 100F and 500F) hybrid system under a square wave profile of 2A followed by -2A current pulses. Performance parameters: Peak Current, Total Charge, Average Power, and Total Energy for the simulated systems under (b) Total square wave profile, (c) Charging pulse, (d) Discharge pulse.

The analysis is done for the other profiles which represent real life scenario applications with the profiles shown previously for profile-1 and 2. In Figure 88 and 89. we show examples of parameter analyses for the entire profiles and from specific regions. Parameters calculated using the entire profile show complex trends due to the summation over various current depths and rates. However, analysis of sub-regions provides intuitive trends to understand the behavior of the systems.

Peak Current _ Peak current passing through the LFP decreased by increasing capacitance of the parallel connected supercapacitor. The lower peak current is preferred for batteries. A hybrid system with a large enough supercapacitor is expected to result in a longer cycle life for the battery by avoiding Li plating [78]. For instance, in applications where batteries encounter bursts of current for short durations, a 10F or higher supercapacitor in parallel

to the LFP is predicted to be beneficial for cycle life. The extended cycle life would serve to benefit applications such as GSM and other portable electronics. However, the rate of peak current decrease is not linear. The decrease is high moving from 0.5F to 10F which is around 600mA, but the effect is lowered moving to higher capacitances. It only decreases by 300mA moving from 10F to 200F.

Average Power Distribution _ The power distribution is almost following a linear trend with increasing the capacitance in which the power is heavily supplied by the battery for the low capacitances and heavily by the supercapacitor in the high capacitances. The power is equally shared for the capacitance value between 12F and 50F in both profiles.

Total Energy and Charge Distribution _ Comparing the energy and charge distribution, more charge and energy is shared by the supercapacitor by increasing the capacitance. It is observed that almost equal distribution is obtained for LFP-50F hybrid system. In the case of LFP-0.5F system, although the applied current pulse results in negative total energy for the region shown in Figure 88 (c), the 0.5F capacitor shows positive energy distribution. This shows that the capacitor is causing extra load on the LFP resulting in faster discharge of the LFP which should be avoided.

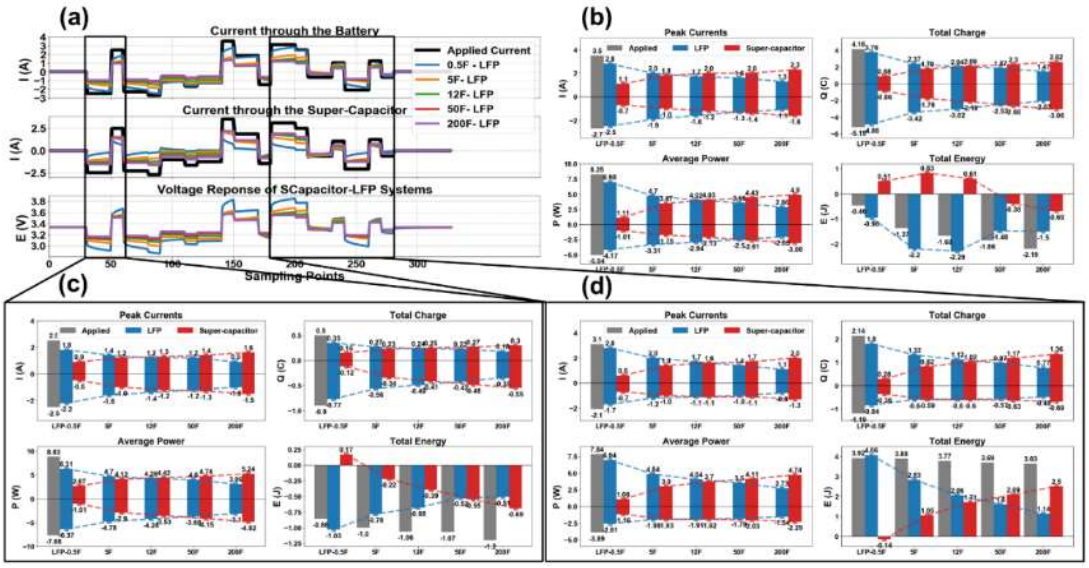

Figure 88. (a) Current profile-1, Performance parameters: Peak Current, Total Charge, Average Power, and Total Energy for different LFP-0.5, 5, 12, 50 and 200F systems for (b) All the profile, (c) First region, (d) Second region

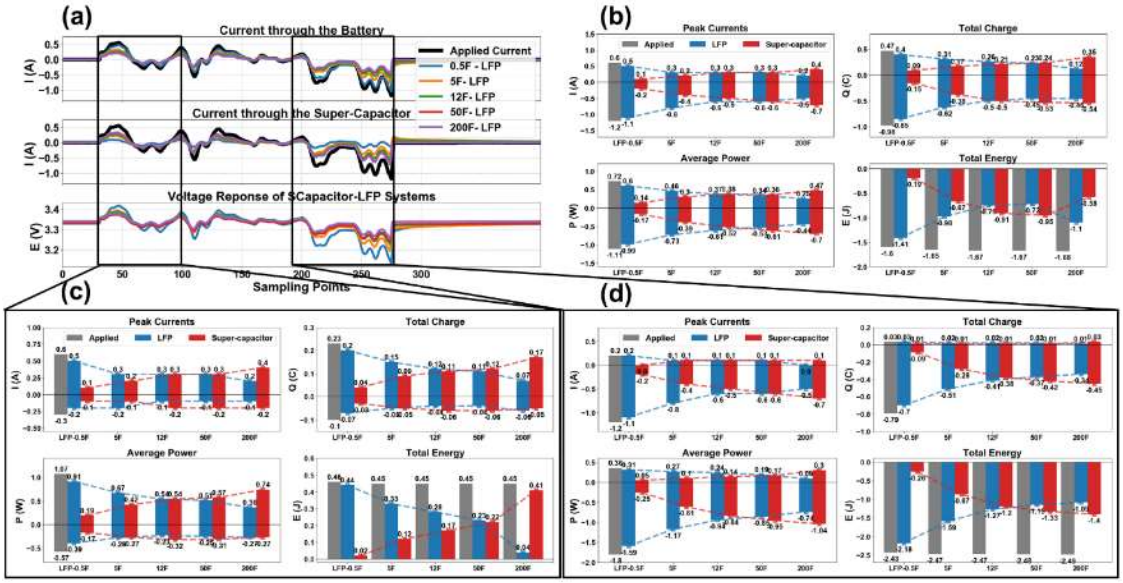

Figure 89. (a) current profile-2, Performance parameters: Peak Current, Total Charge, Average Power, and Total Energy for different LFP-0.5, 5, 12, 50 and 200F systems for (b) All the profile, (c) First region, (d) Second region

3.2.8. Evaluations Including Cost and Size

Evaluation of performance under the employed current profiles exhibits the advantages of the battery/supercapacitor hybrid system. However, in choosing the capacitance of the supercapacitor, other limitations such as cost and size of the supercapacitor should be considered. A comparison of the gained performance and these limitations is made to find the optimal combination for any tailored application. For such comparison a summary of the percent reduction of the metrics for the LFP and the cost of the hybrid systems are provided in table xx.

In applications where size is very crucial such as, cell phones and portable electronics, choosing the smallest supercapacitor that can deliver desired level of performance is chosen. In this case, the targeted supercapacitors are the ones with low capacitances. For example, LFP\Supercapacitor hybrid systems under profile-1 have 20%, 43% and 51% reduction in positive peak currents for 0.5F, 5F and 12F respectively. If 40% decrease in the peak current is enough, a supercapacitor with 5F is the best combination for the LFP under profile-1. Nevertheless, this is also dependent on the applied profile. For instance, in the case of the same LFP\Supercapacitor system but under profile-2 the reduction of the positive peak current is 17%, 50% and 50% for 0.5F, 5F and 12F. As can be seen there is large increase between 0.5F and 5F and no increase at 12F which indicate that supercapacitors with less than 5F are the better choice for hybridization with LFP used under profile-2.

The other limiting factor is the cost of the hybrid system which has great importance while designing any hybrid system. Mass transportation and stationary applications may not have limits in the size of the supercapacitor but the cost is certainly important. If we assume that the cost per kWh of Li-ion battery is 400$/kWh and supercapacitor is 2500$/kWh [79][80]; hybridization of LFP with 0.5F will have an increase in the cost by 0.26% while for 200F the increase is 105%. Comparing the increase in the cost percentages with the increase in the performance for each combination in the hybrid systems, we find a linear increase in the cost since it is related to the capacity of the supercapacitors but a nonlinear increase in the performance metrics. For example, under profile-1 the reduction in the positive peak

current of the LFP hybridized with 50F is 54% while it is 63% for 200F. However, the increase in the percent cost is 26.4% for the 50F and 105.5% for the 200F. This large increase in the cost is not matched by an increase in the performance which indicates the importance of such analysis in determining the best combination of the battery/supercapacitor hybrid systems.

Table 11. Capacity and Cost in dollars calculated for LFP and used Supercapacitors

Cell	Capacity (Wh)	Cost ($)
LFP	4.8	1.92
0.5F	0.002	0.005
5F	0.020	0.050
12F	0.048	0.121
50F	0.202	0.506
200F	0.810	2.025

Table 12. Summary of the reduced percent values for the LFP performance metrics under Profile-1

	Reduction in the LFP metrics						
Super capacitor (F)	**Peak Current (%)**		**Charge (%)**		**Power (%)**		(%cost increase*)
	Positive	**Negative**	**Positive**	**Negative**	**Positive**	**Negative**	
0.5	**20.0**	**7.4**	**9.6**	**6.4**	**15.3**	**17.3**	0.26
5	**42.8**	**29.6**	**43.0**	**34.1**	**43.0**	**34.3**	2.63
12	**51.4**	**40.7**	**50.9**	**41.8**	**51.2**	**41.7**	6.32
50	**54.2**	**51.9**	**55.0**	**51.3**	**56.8**	**50.4**	26.36
200	**62.8**	**59.3**	**64.6**	**61.1**	**65.3**	**59.3**	105.46
*Percent Increase in Cost with respect to LFP cost							

Table 13. Summary of the reduced percent values for the LFP performance metrics under Profile-2

Supercapacitor (F)	Reduction in the LFP metrics						(%cost increase*)
	Peak Current (%)		**Charge (%)**		**Power (%)**		
	Positive	**Negative**	**Positive**	**Negative**	**Positive**	**Negative**	
0.5	**16.7**	**8.3**	**14.9**	**13.3**	**16.7**	**10.8**	0.26
5	**50.0**	**33.3**	**34.0**	**36.7**	**36.1**	**34.2**	2.63
12	**50.0**	**50.0**	**44.7**	**49.0**	**48.6**	**45.0**	6.32
50	**50.0**	**50.0**	**51.1**	**54.1**	**52.8**	**52.3**	26.36
200	**66.7**	**58.3**	**74.5**	**53.1**	**65.3**	**60.4**	105.46
*Percent Increase in Cost with respect to LFP cost							

3.2.9. Section Conclusion

In this section we demonstrated how the performance of unmanaged hybrid battery/supercapacitor systems can be evaluated using Electrochemical Impedance Spectroscopy based approach. The procedures of the methodology included the prediction of the current distribution among the parallelly connected hybrid systems with the total voltage response. Optimization algorithm named Differential Evolution is incorporated along with the developed Zero-free-parameter to iteratively optimize the current distribution for hybrid systems and to calculate the voltage response. The method was tested for two different Li-ion battery chemistries under three distinct charge/discharge regimes.

The modeled results were validated with experimental measurements. A measurement set-up was designed and constructed which enabled for the accurate measurements of the current distribution among the hybrid systems. The overlay of the simulated and the experimental measurements showed high accuracy for all systems with less than 2% proportional errors and 1% for most systems.

We extended the modeling method to include simulations of the battery/supercapacitor hybrid systems with any intended capacitance for the supercapacitors. This was achieved

through the simulation of the Electrochemical Impedance response for the supercapacitors with equivalent circuit models.

The performance of the hybrid systems was evaluated by performance metrics such as peak currents, average power and energy distribution associated with respect to the gains in cost, size and mass of the added supercapacitor. The evaluation gave insight regarding the advantages gained by the combination of supercapacitor in certain capacitance range. Moreover, it showed that evaluation of the performance under dynamic charge/discharge regimes can provide information regarding the limitations and the gained compensations which cannot be obtained by the evaluation under constant charge/discharge conditions.

Therefore, the modeling methodology we introduced and verified for hybrid systems are an invaluable tool for studying different scenarios regarding not only existing but also potential devices that can be hybridized in an unmanaged setting. It can bridge the gap between real life applications of the hybrid systems and the experimental complexities, especially if paired with a data driven approach. We envision further studies that focus on the predictive nature of the model to extract exhaustive design rules for applications such as grid scale storage, electric vehicles and consumer electronics.

Conclusion

This work presents significant contributions in EIS characterization of primary Li batteries. It shows how EIS is a powerful tool to study and understand different electrochemical processes in non-destructive and in-situ measurements. It also contributed in utilizing the impedance response in predicting the voltage of these batteries under arbitrarily load. Further it showed how the extension of the EIS based modeling method can predict the performance of different battery supercapacitor hybrid systems.

In the chapter 2, we first present linear and stable EIS results of Li\$SOCl_2$ batteries utilizing Galvanostatic EIS at discharge measurement. Impedance parameters related to the anodic, cathodic and Solid Electrolyte Interface (SEI) are obtained and analyzed for different battery geometries and at wide range of States-of-Charge. The domination of the SEI impedance response is observed and suppressed through the application of higher DC-offset levels.

Second, the impedance response is further investigated through change in the electrolyte composition. The investigation shows variation in the high frequency region assigned to the SEI and the anodic processes while the low frequency region related to the cathodic process doesn't show any variation. The high frequency region time constant is assigned to the Li-ion transport through the SEI and the second time constant to Li oxidation.

Third, temperature-dependent EIS is utilized to extract kinetic parameters of the observed processes. The procedure is applied for Li\$SOCl_2$ and Li\$MnO_2$. The results show the high temperature dependence for Li-ion transport through the SEI while small dependence for the anodic and cathodic processes. Furthermore, the Arrhenius analysis shows deviation from linearity at the high end of the temperature range. The conclusion can be made for the existence of more than one process for the transport of the Li-ions through the SEI. Yet, investigation of different Li battery chemistries with different electrolytes and cell

geometries is needed to better understand the temperature dependence of the Li-ion transport through the formed SEI.

Finally, Non-linear Harmonic Analysis is utilized for the non-linear EIS response of the Li\$SOCl_2$ battery. The results show the existence of higher order harmonics for the responses dominated by the SEI impedance. Non-linearities are observed by the excitation of the battery at the open circuit potential and with applying a DC offset. Both results show the existence of higher order harmonics with different amplitudes. However, the obtained harmonics are a mixture of non-linearity and non-stationarity responses. The distinction of each response is not applicable for most cases. The investigation of the harmonic responses utilizing linear systems such as dummy cells with same resistance and capacitance values for the studies systems needs to be done to eliminate the artifacts. Further, the correlation of the observed harmonics to the electrochemical phenomena is still to be investigated and the same response is to be observed for other Li battery chemistries.

In chapter 3, we applied Zero-free-parameter model to predict the voltage response of primary Li batteries and the performance of unmanaged secondary Li-ion batteries supercapacitor hybrid systems.

First, the method is developed to compensate for the voltage delay phenomena which is unique for the utilization of metallic Li anodes. The voltage delay behavior is added through mathematical equation obtained from linear regression of the voltage delay behavior at different discharge currents. The results show high accuracy with less than 1% error for both Li\$SOCl_2$ and Li\$MnO_2$ batteries.

Second, the modeling methodology is extended to predict both the voltage behavior and the current distribution in unmanaged hybrid battery/supercapacitor systems. The current distribution is the result of connecting battery/supercapacitor in parallel connection. This distribution is calculated using differential evolution optimizing algorithm. The calculated currents are used to predict the voltage response utilizing the impedance of each system. The method is tested for two different Li-ion battery chemistries under three distinct charge/discharge regimes. The modeled results are validated with experimental

measurements which showed high accuracy for all systems with less than 2% proportional errors and 1% for most systems.

We further extend the model to include simulations of potential combinations with any intended supercapacitor is achieved through the simulation of its EIS response through equivalent circuit models. Then using the current distribution and the voltage response different design parameters can be calculated to determine the best combination of specific battery to various supercapacitors. Additionally, cost and volume constraints can be included to give insight about the gains obtained from each combination.

The presented modeling method demonstrates its predictive potential for different chemistries under various charge\discharge regimes. Further studies combined with artificial intelligence can focus on the predictive nature of the model to extract exhaustive design rules for applications such as grid scale storage, EVs and consumer electronics.

Ultimately, this thesis presents that EIS can be used as an analysis and a prediction tool for metallic lithium anode containing battery chemistries with detailed examples.

Bibliography

[1] Z. Yang *et al.*, "Electrochemical energy storage for green grid," *Chemical Reviews*, vol. 111, no. 5. American Chemical Society, pp. 3577–3613, 11-May-2011.

[2] A. G. Olabi, C. Onumaegbu, T. Wilberforce, M. Ramadan, M. A. Abdelkareem, and A. H. Al – Alami, "Critical review of energy storage systems," *Energy*, vol. 214, p. 118987, Jan. 2021.

[3] S. Koohi-Fayegh and M. A. Rosen, "A review of energy storage types, applications and recent developments," *Journal of Energy Storage*, vol. 27. Elsevier, p. 101047, 01-Feb-2020.

[4] L. W. Chong, Y. W. Wong, R. K. Rajkumar, R. K. Rajkumar, and D. Isa, "Hybrid energy storage systems and control strategies for stand-alone renewable energy power systems," *Renewable and Sustainable Energy Reviews*, vol. 66, pp. 174–189, Dec. 2016.

[5] P. V. Kamat, "Lithium-Ion Batteries and Beyond: Celebrating the 2019 Nobel Prize in Chemistry – A Virtual Issue," *ACS Energy Letters*, vol. 2019, no. 8, pp. 2757–2759, 2019.

[6] O. C. Esan, X. Shi, Z. Pan, X. Huo, L. An, and T. S. Zhao, "Modeling and Simulation of Flow Batteries," *Advanced Energy Materials*, vol. 10, no. 31, p. 2000758, Aug. 2020.

[7] G. Pacchioni, "Superelectrodes for supercapacitors," *Nature Reviews Materials 2019 4:10*, vol. 4, no. 10, pp. 625–625, Sep. 2019.

[8] "Electrochemical Methods: Fundamentals and Applications, 2nd Edition | Wiley." [Online]. Available: https://www.wiley.com/en-us/Electrochemical+Methods%3A+Fundamentals+and+Applications%2C+2nd+Edition-p-9780471043720. [Accessed: 13-Sep-2021].

[9] J. O. Bockris and A. K. N. Reddy, *Volume 2 Modern Electrochemistry*. Springer US, 1973.

[10] Wu Xu *et al.*, "Lithium metal anodes for rechargeable batteries," *Energy & Environmental Science*, vol. 7, no. 2, pp. 513–537, Jan. 2014.

[11] X. Zhang, A. Wang, X. Liu, and J. Luo, "Dendrites in Lithium Metal Anodes:

Suppression, Regulation, and Elimination," *Accounts of Chemical Research*, vol. 52, no. 11, pp. 3223–3232, Nov. 2019.

[12] M. E. Orazem and B. Tribollet, *Electrochemical Impedance Spectroscopy*. Hoboken, NJ, USA: John Wiley & Sons, Inc., 2008.

[13] A. Wang, S. Kadam, H. Li, S. Shi, and Y. Qi, "Review on modeling of the anode solid electrolyte interphase (SEI) for lithium-ion batteries," *npj Computational Materials*, vol. 4, no. 1, p. 15, Dec. 2018.

[14] M. Winter, "The Solid Electrolyte Interphase – The Most Important and the Least Understood Solid Electrolyte in Rechargeable Li Batteries," *Zeitschrift für Physikalische Chemie*, vol. 223, no. 10–11, pp. 1395–1406, Dec. 2009.

[15] E. Peled, D. Golodnitsky, and G. Ardel, "Advanced Model for Solid Electrolyte Interphase Electrodes in Liquid and Polymer Electrolytes," *Journal of The Electrochemical Society*, vol. 144, no. 8, p. L208, Aug. 1997.

[16] A. J. Bard and L. R. Faulkner, *Electrochemical Methods: Fundamentals and Applications, 2nd Edition | Wiley*. 2008.

[17] M. Kiel, O. Bohlen, and D. U. Sauer, "Harmonic analysis for identification of nonlinearities in impedance spectroscopy," *Electrochimica Acta*, vol. 53, no. 25, pp. 7367–7374, Oct. 2008.

[18] R. Vedalakshmi, S. Manoharan, H. W. Song, and N. Palaniswamy, "Application of harmonic analysis in measuring the corrosion rate of rebar in concrete," *Corrosion Science*, vol. 51, no. 11, pp. 2777–2789, 2009.

[19] T. Kadyk, R. Hanke-Rauschenbach, and K. Sundmacher, "Nonlinear frequency response analysis of PEM fuel cells for diagnosis of dehydration, flooding and CO-poisoning," *Journal of Electroanalytical Chemistry*, vol. 630, no. 1–2, pp. 19–27, May 2009.

[20] F. Fasmin and R. Srinivasan, "Review—Nonlinear Electrochemical Impedance Spectroscopy," *Journal of The Electrochemical Society*, vol. 164, no. 7, pp. H443–H455, May 2017.

[21] A. González-Cortés, "Electrochemical Impedance Spectroscopy," in *Agricultural and Food Electroanalysis*, Chichester, UK: John Wiley & Sons, Ltd, 2015, pp. 381–419.

[22] M. Jain, G. Nagasubramanian, R. G. Jungst, and J. W. Weidner, "Analysis of a Lithium/Thionyl Chloride Battery under Moderate-Rate Discharge," *Journal of The Electrochemical Society*, vol. 146, no. 11, p. 4023, Nov. 1999.

[23] P. Chenebault, D. Vallin, J. Thevenin, and R. Wiart, "Properties of surface layers formed on lithium in Li-SOCl2 cells: synergetic effect of SO2 and LiAl(SO3Cl)4,"

Journal of Applied Electrochemistry, vol. 18, no. 4, pp. 625–632, Jul. 1988.

[24] M. J. Brand, M. H. Hofmann, M. Steinhardt, S. F. Schuster, and A. Jossen, "Current distribution within parallel-connected battery cells," *Journal of Power Sources*, vol. 334, pp. 202–212, 2016.

[25] M. A. Zabara, C. B. Uzundal, and B. Ulgut, "Linear and Nonlinear Electrochemical Impedance Spectroscopy Studies of Li/SOCl 2 Batteries," *Journal of The Electrochemical Society*, vol. 166, no. 6, pp. A811–A820, 2019.

[26] M. A. Zabara, H. Göçmez, A. Karabatak, and B. Ulgut, "Characterization of Different Electrolyte Composition Lithium Thionyl Chloride Reserve Battery by Electrochemical Impedance Spectroscopy," *Journal of The Electrochemical Society*, vol. 168, no. 5, p. 050529, May 2021.

[27] R. Gangadharan, P. N. N. Namboodiri, K. V. Prasad, and R. Viswanathan, "The lithium—thionyl chloride battery — a review," *Journal of Power Sources*, vol. 4, no. 1, pp. 1–9, Jan. 1979.

[28] V. E. Kazarinov and V. S. Bagotzky, "Properties of a passivating film on the surface of lithium electrodes," *Journal of Power Sources*, vol. 20, no. 3–4, pp. 259–263, Jul. 1987.

[29] A. Leef and A. Gilmour, "Voltage delay in lithium non-aqueous battery systems," *Journal of Applied Electrochemistry*, vol. 9, no. 6, pp. 663–669, Nov. 1979.

[30] G. Razzini, S. Rovellini, F. Alessandrini, B. Di Pietro, and B. Scrosati, "The lithium-sulfuryl chloride battery: Discharge behaviour," *Journal of Power Sources*, vol. 5, no. 3, pp. 263–271, 1980.

[31] M. Hughes, S. A. G. R. Karunathilaka, N. A. Hampson, and T. J. Sinclair, "The impedance of the lithium-thionyl chloride primary cell," *Journal of Applied Electrochemistry*, vol. 13, no. 5, pp. 669–678, Sep. 1983.

[32] R. E. Popov, B. N. Zhang, E. C. Darcy, E. C. White, "Impedance Spectroscopy as a Nondestructive Health Interrogation Tool for Lithium-BCX Cells," *Journal of The Electrochemical Society*, vol. 140, no. 11, p. 3097, 1993.

[33] F. Walsh, M. Pozin, A. Cherniy, and K. Tikhonov Jr., "Characterization of lithium-thionyl chloride cells by impedance techniques," *Journal of Power Sources*, vol. 97–98, no. 98, pp. 714–718, Jul. 2001.

[34] LSH, "LS, LSH | Saft Batteries." [Online]. Available: https://www.saftbatteries.com/products-solutions/products/ls-lsh. [Accessed: 15-Oct-2018].

[35] T. Osaka, D. Mukoyama, and H. Nara, "Review—Development of Diagnostic Process for Commercially Available Batteries, Especially Lithium Ion Battery, by

Electrochemical Impedance Spectroscopy," *Journal of The Electrochemical Society*, vol. 162, no. 14, pp. A2529–A2537, 2015.

[36] M. A. Zabara, C. B. Uzundal, and B. Ulgut, "Linear and nonlinear electrochemical impedance spectroscopy studies of Li/SOCl<inf>2</inf> batteries," *Journal of the Electrochemical Society*, vol. 166, no. 6, 2019.

[37] S. Dallek, "Exothermic Reactions among Components of Lithium-Sulfur Dioxide and Lithium-Thionyl Chloride Cells," *Journal of The Electrochemical Society*, vol. 128, no. 3, p. 508, 1981.

[38] M. B. Mogensen and E. Hennesø, "Properties and Structure of the LiCl-films on Lithium Anodes in Liquid Cathodes," *Acta Chimica Slovenica*, vol. 63, no. 3, pp. 519–534, Sep. 2016.

[39] F. Single, B. Horstmann, and A. Latz, "Theory of Impedance Spectroscopy for Lithium Batteries," *Journal of Physical Chemistry C*, 2019.

[40] L. Benitez and J. M. Seminario, "Ion Diffusivity through the Solid Electrolyte Interphase in Lithium-Ion Batteries," *Journal of The Electrochemical Society*, vol. 164, no. 11, pp. E3159–E3170, 2017.

[41] T. R. Jow, S. A. Delp, J. L. Allen, J.-P. Jones, and M. C. Smart, " Factors Limiting Li + Charge Transfer Kinetics in Li-Ion Batteries ," *Journal of The Electrochemical Society*, vol. 165, no. 2, pp. A361–A367, 2018.

[42] K. Xu, Y. Lam, S. S. Zhang, T. R. Jow, and T. B. Curtis, "Solvation sheath of Li+ in nonaqueous electrolytes and its implication of graphite/electrolyte interface chemistry," *Journal of Physical Chemistry C*, vol. 111, no. 20, pp. 7411–7421, 2007.

[43] Y. Yamada, F. Sagane, Y. Iriyama, T. Abe, and Z. Ogumi, "Kinetics of lithium-ion transfer at the interface between Li 0.35La0.55TiO3 and binary electrolytes," *Journal of Physical Chemistry C*, vol. 113, no. 32, pp. 14528–14532, 2009.

[44] S. Shi *et al.*, "Direct calculation of Li-ion transport in the solid electrolyte interphase," *Journal of the American Chemical Society*, vol. 134, no. 37, pp. 15476–15487, 2012.

[45] J. Huang *et al.*, "Editors' Choice—Review—Impedance Response of Porous Electrodes: Theoretical Framework, Physical Models and Applications," *Journal of The Electrochemical Society*, vol. 167, no. 16, p. 166503, 2020.

[46] R. V. Moshtev, Y. Geronov, and B. Puresheva, "The Primary Passive Film on Li in SOCl2 Electrolyte Solutions," *Journal of The Electrochemical Society*, vol. 128, no. 9, p. 1851, Sep. 1981.

[47] K. Xu, "'Charge-Transfer' Process at Graphite/Electrolyte Interface and the

Solvation Sheath Structure of Li[sup +] in Nonaqueous Electrolytes," *Journal of The Electrochemical Society*, vol. 154, no. 3, p. A162, 2007.

[48] "/Rt E T," *Electrochemistry*.

[49] Y. Yamada, Y. Iriyama, T. Abe, and Z. Ogumi, "Kinetics of lithium ion transfer at the interface between graphite and liquid electrolytes: effects of solvent and surface film," *Langmuir*, vol. 25, no. 21, pp. 12766–12770, 2009.

[50] K. Darowicki and J. Majewska, "Harmonic analysis of electrochemical and corrosion systems - a review," *Corrosion Reviews*, vol. 17, no. 5–6, pp. 383–400, Jan. 1999.

[51] R. W. Bosch, J. Hubrecht, W. F. Bogaerts, and B. C. Syrett, "Electrochemical Frequency Modulation: A New Electrochemical Technique for Online Corrosion Monitoring," *CORROSION*, vol. 57, no. 1, pp. 60–70, Jan. 2001.

[52] W. Durnie, R. De Marco, A. Jefferson, and B. Kinsella, "Harmonic analysis of carbon dioxide corrosion," *Corrosion Science*, vol. 44, no. 6, pp. 1213–1221, Jun. 2002.

[53] N. Harting, N. Wolff, and U. Krewer, "Identification of Lithium Plating in Lithium-Ion Batteries using Nonlinear Frequency Response Analysis (NFRA)," *Electrochimica Acta*, vol. 281, pp. 378–385, Aug. 2018.

[54] M. D. Murbach, V. W. Hu, and D. T. Schwartz, "Nonlinear Electrochemical Impedance Spectroscopy of Lithium-Ion Batteries: Experimental Approach, Analysis, and Initial Findings," *Journal of The Electrochemical Society*, vol. 165, no. 11, pp. A2758–A2765, 2018.

[55] M. A. Zabara and B. Ulgut, "Electrochemical Impedance Spectroscopy based voltage modeling of lithium Thionyl Chloride (Li\SOCl<inf>2</inf>) primary battery at arbitrary discharge," *Electrochimica Acta*, vol. 334, 2020.

[56] M. A. Zabara, C. B. Uzundal, and B. Ülgüt, "Performance modeling of unmanaged hybrid battery / supercapacitor energy storage systems," *Journal of Energy Storage*, vol. 43, no. January, p. 103185, 2021.

[57] E. Özdemir, C. B. Uzundal, and B. Ulgut, "Zero-Free-Parameter Modeling Approach to Predict the Voltage of Batteries of Different Chemistries and Supercapacitors under Arbitrary Load," *Journal of The Electrochemical Society*, vol. 164, no. 6, pp. A1274–A1280, Apr. 2017.

[58] B. Ulgut, C. B. Uzundal, and E. Özdemir, "Analysis of errors in zero-free-parameter modeling approach to predict the voltage of electrochemical energy storage systems under arbitrary load," in *ECS Transactions*, 2017, vol. 77, no. 11, pp. 99–104.

[59] T. I. Evans, T. V. Nguyen, and R. E. White, “A Mathematical Model of a Lithium/Thionyl Chloride Primary Cell,” *Journal of the Electrochemical Society*, vol. 136, no. 2, pp. 328–339, 1989.

[60] M. Jain, “Analysis of a Lithium/Thionyl Chloride Battery under Moderate-Rate Discharge,” *Journal of The Electrochemical Society*, vol. 146, no. 11, p. 4023, 1999.

[61] R. M. Spotnitz, G. S. Yeduvaka, G. Nagasubramanian, and R. Jungst, “Modeling self-discharge of Li/SOCl2 cells,” *Journal of Power Sources*, vol. 163, no. 1, pp. 578–583, Dec. 2006.

[62] O. US EPA, “Dynamometer Drive Schedules.” .

[63] “scipy.optimize.curve_fit — SciPy v1.3.0 Reference Guide.” [Online]. Available: https://docs.scipy.org/doc/scipy/reference/generated/scipy.optimize.curve_fit.html. [Accessed: 23-Sep-2019].

[64] R. A. Dougal, S. Liu, and R. E. White, “Power and life extension of battery-ultracapacitor hybrids,” *IEEE Transactions on Components and Packaging Technologies*, vol. 25, no. 1, pp. 120–131, Mar. 2002.

[65] G. Sikha and B. N. Popov, “Performance optimization of a battery-capacitor hybrid system,” *Journal of Power Sources*, vol. 134, no. 1, pp. 130–138, Jul. 2004.

[66] L. Gao, R. A. Dougal, and S. Liu, “Power Enhancement of an Actively Controlled Battery/Ultracapacitor Hybrid,” *IEEE Transactions on Power Electronics*, vol. 20, no. 1, pp. 236–243, Jan. 2005.

[67] L. Gao, R. A. Dougal, and S. Liu, “Active power sharing in hybrid battery/capacitor power sources,” in *Eighteenth Annual IEEE Applied Power Electronics Conference and Exposition, 2003. APEC ’03.*, 2003, vol. 1, pp. 497–503.

[68] S. Hajiaghasi, A. Salemnia, and M. Hamzeh, “Hybrid energy storage system for microgrids applications: A review,” *Journal of Energy Storage*, vol. 21, no. August 2018, pp. 543–570, 2019.

[69] B. Wang *et al.*, “Current technologies and challenges of applying fuel cell hybrid propulsion systems in unmanned aerial vehicles,” *Progress in Aerospace Sciences*, vol. 116, no. April, p. 100620, Jul. 2020.

[70] L. Kouchachvili, W. Yaïci, and E. Entchev, “Hybrid battery/supercapacitor energy storage system for the electric vehicles,” *Journal of Power Sources*, vol. 374, no. November 2017, pp. 237–248, Jan. 2018.

[71] G. Sikha, R. E. White, and B. N. Popov, “A Mathematical Model for a Lithium-Ion Battery/Electrochemical Capacitor Hybrid System,” *Journal of The*

Electrochemical Society, vol. 152, no. 8, p. A1682, 2005.

[72] A. Seaman, T.-S. Dao, and J. McPhee, "A survey of mathematics-based equivalent-circuit and electrochemical battery models for hybrid and electric vehicle simulation," *Journal of Power Sources*, vol. 256, pp. 410–423, Jun. 2014.

[73] C. Zou, L. Zhang, X. Hu, Z. Wang, T. Wik, and M. Pecht, "A review of fractional-order techniques applied to lithium-ion batteries, lead-acid batteries, and supercapacitors," *Journal of Power Sources*, vol. 390, pp. 286–296, Jun. 2018.

[74] R. Storn and K. Price, "Differential Evolution - A Simple and Efficient Heuristic for Global Optimization over Continuous Spaces," *Journal of Global Optimization*, vol. 11, no. 4, pp. 341–359, 1997.

[75] P. Virtanen *et al.*, "SciPy 1.0: fundamental algorithms for scientific computing in Python," *Nature Methods*, vol. 17, no. 3, pp. 261–272, 2020.

[76] J. Bisquert, "Influence of the boundaries in the impedance of porous film electrodes," *Physical Chemistry Chemical Physics*, vol. 2, no. 18, pp. 4185–4192, Sep. 2000.

[77] "A reference book of driving cycles for use in the measurement of road vehicle emissions | TRL."

[78] M. R. Palacín and A. De Guibert, "Batteries: Why do batteries fail?," *Science*, vol. 351, no. 6273. American Association for the Advancement of Science, pp. 1253292–1253292, 05-Feb-2016.

[79] P. K. S. Roy, H. B. Karayaka, Y. Yan, and Y. Alqudah, "Size optimization of battery-supercapacitor hybrid energy storage system for 1MW grid connected PV array," *2017 North American Power Symposium, NAPS 2017*, 2017.

[80] P. K. S. Roy, H. B. Karayaka, Y. Yan, and Y. Alqudah, "Investigations into best cost battery-supercapacitor hybrid energy storage system for a utility scale PV array," *Journal of Energy Storage*, vol. 22, no. July 2018, pp. 50–59, 2019.